A hybrid additive manufacturing framework for the multi-phase fabrication and in-line characterization of functional devices

A thesis submitted for the degree of
Doctor of Philosophy



Lukas Fieber
Corpus Christi College

February 19, 2020

Supervised by
Prof P. S. Grant & Dr C. Huang

A thesis presented to the *Department of Materials*
in partial fulfillment of the requirements for the degree of
Doctor of Philosophy at the *University of Oxford*.

Declaration of originality

All of the research presented was carried out by the author in the *Department of Materials* at the *University of Oxford* between October 2016 and September 2019 under supervision of Prof P. S. Grant & Dr C. Huang. The project was primarily funded by the UK Engineering and Physical Sciences Research Council (EPSRC) in alignment with the theme *Manufacturing the Future*, with the majority of experimental work being conducted at the Begbroke Science Park. The work is original and where work from others has been included it has been clearly referenced and acknowledged. No part of this thesis has been submitted or accepted for any other degree at this university or elsewhere.

Lukas Fieber
Oxford – February 19, 2020

Copyright declaration

The copyright of this thesis rests with the author. Unless otherwise indicated, its contents are licensed under a *Creative Commons* attribution – non commercial international license (CC BY-NC 4.0). Under this license you may share (copy and redistribute the material in any medium or format) and adapt (remix, transform, and build upon the material) provided you give appropriate credit, provide a link to the license, and indicate if changes were made. You may do so in any reasonable manner, but not in any way that suggests the author endorses you or your use. You may not use the material for commercial purposes.

Abstract

Multi-material, multi-technology (MMMT) manufacturing systems combine or *hybridize* the benefits of individual fabrication and characterization techniques into a single manufacturing platform. In particular MMMT systems based on additive manufacturing (AM) technologies offer new opportunities for increased design freedom and additional functionality. However, the realization of the potential of AM-based MMMT systems is held back by the lack of accessible, affordable and reconfigurable hybrid-AM systems.

In this thesis, a novel, extendable hybrid-AM framework/concept is introduced. A corresponding, modular machine has been designed and built from the bottom-up. Detailed insights into the design considerations, operating principles, associated digital workflows and potential applications are discussed. The machine provided design freedom and *in-line* functionality previously unachievable. These aspects are then demonstrated through the: (1) AM of functional, form-factor free energy storage devices (supercapacitors, EDLC's) in a single, automated multi-material operation; and (2) measurement of a material property distribution (the local dielectric permittivity (ε_r) in 3D) within printed parts as they are being formed. Careful consideration was given to the underlying materials- and AM processing-science. The supercapacitor behaviour was assessed through a range of electrochemical and other characterization techniques, and provided encouraging energy storage behaviour. A ring-shaped supercapacitor was fabricated in a single manufacturing operation, unachievable by conventional manufacturing. Non-destructive, *in-line* permittivity data was reconstructed into three dimensional (3D) dielectric "images" of a printed object, and techniques to understand and improve the spatial resolution are presented.

The research aimed to accelerate the integration of functional devices in product manufacture (in particular for applications with irregular volume/shape and mass-customization requirements), accelerate the design-make-test cycle for functional devices through insight in device conformance to intended design (*in-line* quality control), and provide a versatile hybrid-AM environment for further research.

Keywords: Additive Manufacturing, 3D Printing, Hybrid-AM, Energy Storage Devices, Capacitors, RF, In-line Characterization, Dielectric Imaging.

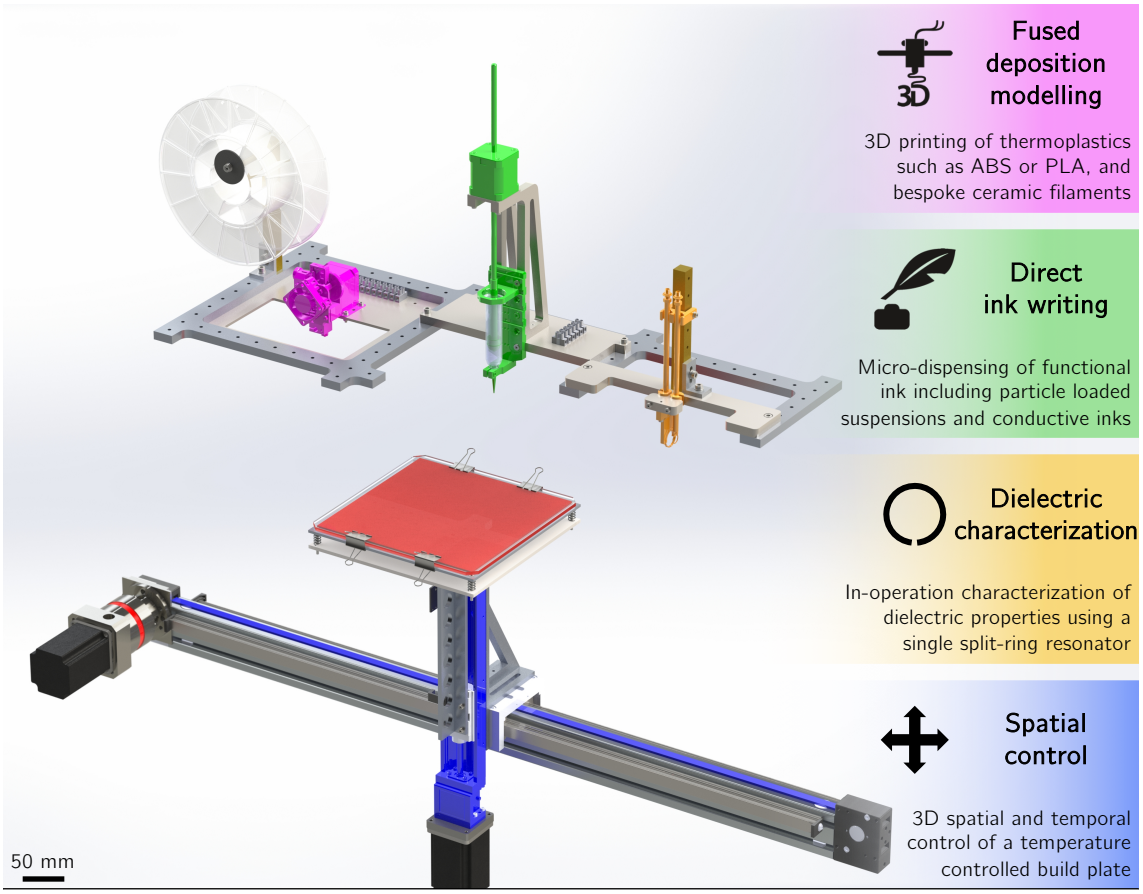

Figure i: A render of the multi-functional, lab-scale hybrid additive manufacturing machine that was designed and built by the author. The machine played a central role while investigating hybrid additive manufacturing (hybrid-AM) concepts and applications. Operating principles and design considerations are discussed in detail throughout this thesis.

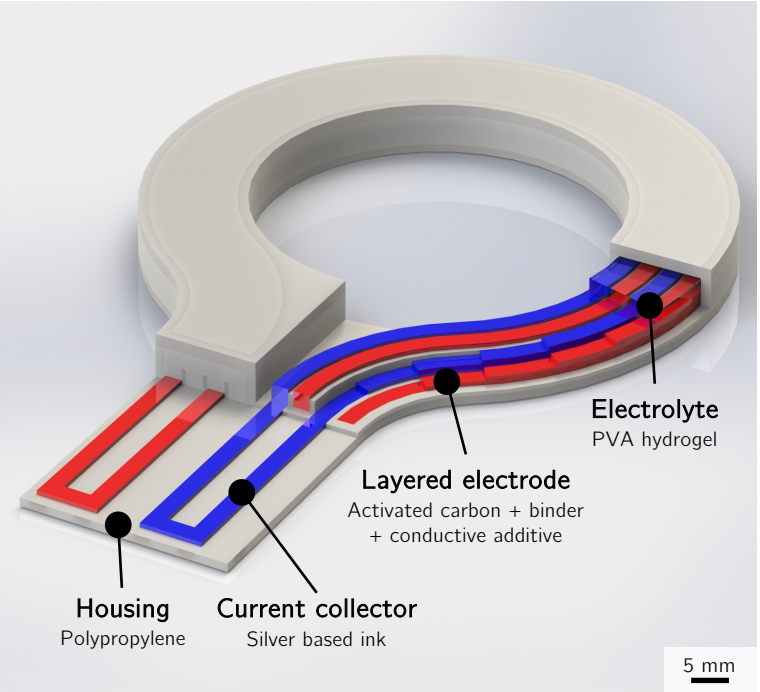

Figure ii: A render of the free-form energy storage device (supercapacitor, EDLC) that was printed in a single, automated *hybrid-AM* manufacturing operation. The device was fabricated in approximately 30 min, and was fully functional *as-printed*. Manufacturing considerations and the electro-chemical performance of such devices is discussed in detail in this thesis.

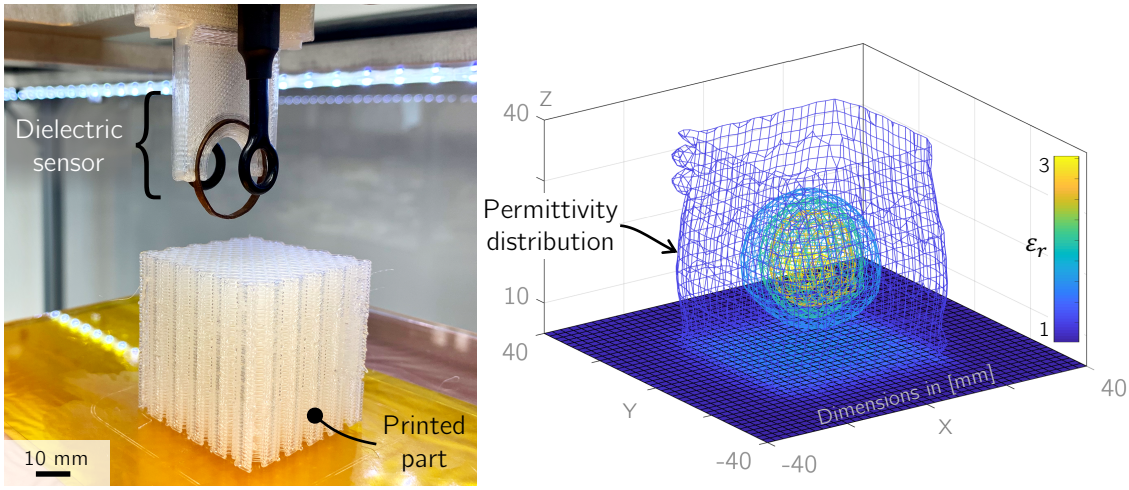

Figure iii: A photograph of the non-destructive, dielectric imaging sensor which was integrated *in-line* with additive manufacturing, alongside a resulting 3D map showing the internal distribution of a deliberately varying material property (dielectric permittivity, ε_r). Detailed insights into the imaging principle, data processing/analysis and limitations are provided in this thesis.

Publications and presentations

Parts of the work presented in this thesis have been published elsewhere, or presented at conferences. An index is provided here:

Scientific publications

- L. Fieber, J. D. Evans, C. Huang, P. S. Grant, Single-operation, multi-phase additive manufacture of electro-chemical double layer capacitor devices, *Additive Manufacturing* 28 (August) (2019) 344–353. doi:10.1016/j.addma.2019.05.001
- L. Fieber, S. Bukhari, Y. Wu, P. S. Grant, In-line measurement of the dielectric permittivity of materials during additive manufacturing and 3D data reconstruction, *Additive Manufacturing* 32 (March) (2020) 101010. doi:10.1016/j.addma.2019.101010
- L. Fieber, P. S. Grant, C.2 Capacitors in *Current state of 3D printing technologies & materials*, submitted to the editor on 10/05/2019.

Conference presentations

- L. Fieber, C. Huang, P. S. Grant, Single-step printing of encapsulated supercapacitors, Oral and poster presentation at the *5th International Symposium on Enhanced Electrochemical Capacitors ISEECap'17*, Friedrich-Schiller University Jena, Germany, 10–14 July 2017.
- L. Fieber, C. Huang, P. S. Grant, Single-step additive manufacture of rationally designed supercapacitors, Oral presentation at *Materials Research Society spring meeting & exhibit MRS Spring 2018*, Pheonix, USA, 2-6 April 2018.
- L. Fieber, S. Bukhari, C. Huang, P. S. Grant, A hybrid additive manufacturing framework for the multi-phase fabrication and in-operation characterization of functional devices, Poster presentation at *STFC Early Careers Research Conference 2019*, Abingdon, UK, 18-19 March 2019.
- L. Fieber, S. Bukhari, C. Huang, P. S. Grant, Hybrid additive manufacturing: multi-phase fabrication and in-line characterization, Oral presentation at the *30th Annual International Solid Freeform Fabrication Symposium*, University of Texas, USA, 12-14 August 2019.

Acknowledgements

First and foremost, thank you Patrick for your trust and guidance throughout the last 3 years. It's been a pleasure to work together, to conceptualize more ideas than we could implement and to challenge your perception of how many *in-sentence* lists and sub-sub-sub headings are acceptable in a publication. You provided me with ample opportunities to explore and learn, present at conferences and chase ideas that at first may have seemed too ambitious – thank you!

I would like to thank all of my colleagues and friends who supported me in Oxford. In particular, I would like to thank my fellow group members Jack, Kylee, Sarah and Alasdair for bringing life to Begbroke. Thank you Syed, Ann and Enzo for providing useful advice at all times. And thank you Robin, Gideon and Greg for your support in constructing the apparatus enabling the work in this thesis.

I would like to thank all of my friends who filled the last years with fun and those who helped justify my travels. Thanks Alex and Sam for unforgetable Corpus-Queens-Oriel exchanges. Thank you to everyone who made CCC feel like the home that it was. Ross, thank you for being the perfect friend to share a flat with, never bringing work home and helping to keep Il Principe profitable. And thank you Sumant, Nick and Wai-Tong for getting me in a position to start this DPhil.

Finally, I would like to thank my parents and brother for 24 years of continuous support, for enabling all of this, and also for providing some competition in the ongoing *Fieber-Globetrotter-Race*.

Contents

Abstract **vii**

Preface **xix**

0.1 Principal motivation xix
0.2 Objectives xx
0.3 Structure of this thesis xxi
0.4 Terms and abbreviations xxii

I

Hybrid additive manufacturing framework

1 Introduction: Hybrid additive manufacturing **3**

1.1 Manufacturing in 2019 3
1.2 Additive manufacturing 5
1.3 Hybrid manufacturing systems 9
1.4 Objectives for Part I 12

2 Hybrid additive manufacture framework, system and workflow **13**

2.1 The framework 13
2.2 Principal design specifications for a hybrid AM system 16
2.3 Hybrid-AM workflow 17

3 Adaptive printing host **19**

3.1 The printing host in context 20
3.2 Design requirements and implementation 23
3.3 Software architecture 25
3.4 Software operation 33
3.5 Summary of the printing host 38

4 Modular microelectronics **39**

4.1 The microelectronics system in context 40

4.2 Design requirements and implementation . . . 43
4.3 Architecture of the microelectronics system . . . 45
4.4 Prototyping and assembly . . . 51
4.5 Summary of the microelectronics system . . . 53

5 Engineering design, manufacture & assembly 55
5.1 Purpose and functionality of the hybrid-AM machine . . . 56
5.2 Design requirements and implementation . . . 56
5.3 Overview of the hybrid-AM machine . . . 58
5.4 Engineering design . . . 59
5.5 Part manufacture and assembly . . . 68
5.6 Calibration . . . 72
5.7 Summary of the hybrid-AM machine functionality . . . 73

6 Conclusions & outlook: Hybrid-AM 75

II

Multi-phase AM for energy storage applications

7 Introduction: Energy storage 79
7.1 Capacitor technology . . . 79
7.2 Electro-chemical double layer capacitors . . . 82
7.3 The challenge of manufacturing EDLCs . . . 86
7.4 The promise of AM for the manufacture of EDLCs . . . 88
7.5 Objectives for Part II . . . 91

8 Materials & methods 93
8.1 Materials & ink preparation . . . 93
8.2 Manufacturing sequence . . . 94
8.3 Cell characterization . . . 96

9 Results & discussion 99
9.1 Overview of results . . . 99
9.2 Key materials and processing considerations . . . 100
9.3 Characterization of as-printed EDLCs . . . 109
9.4 Cell configuration . . . 113

10 Conclusions & outlook: AM of EDLCs 117

III

In-line characterization of dielectric properties

11 Introduction: Electro-magnetic characterization **121**
11.1 Characterization of material properties in AM . . . 121
11.2 Additive manufacturing of radio frequency devices . . . 123
11.3 Electro-magnetic characterization techniques . . . 123
11.4 Objectives for Part III . . . 124

12 Materials & methods **125**
12.1 Hybrid-AM . . . 125
12.2 Electro-magnetic characterization techniques . . . 128
12.3 Simulation . . . 130

13 Results & discussion **133**
13.1 Overview of results . . . 133
13.2 Measurement: In-line sampled frequency map . . . 135
13.3 Deblurring: Improving spatial resolution . . . 147
13.4 Extraction: Interpreting the resonant frequency . . . 150

14 Conclusions & outlook: In-line characterization **153**

15 Research summary: Parts I to III **155**

Afterword **157**

A Conceptualization of the hybrid additive manufacture machine **159**

B Technical documentation **163**
B.1 Risk assessment . . . 163
B.2 Bill of materials . . . 164
B.3 Engineering drawings . . . 165
B.4 Control circuit diagrams . . . 174
B.5 Calibration of functional modules . . . 177

Bibliography **179**

Preface

0.1 Principal motivation

Additive manufacturing (AM), the process of fabricating parts *layer-by-layer* [1], is no longer only a tool for *rapid prototyping*, but is finding applications across the value chain in virtually all industries. AM may provide unprecedented design freedom, product-mix flexibility and facilitate democratized, distributed manufacturing for some goods. In tandem with emerging technologies associated with Industry 4.0, the Internet of Things (IoT), real-time data analytics and artificial intelligence (AI), remarkable technological advancements and applications involving AM have been demonstrated, such as true-to-life organ replicas with integrated sensors for surgical planning [2], and high-performance gas turbine blades *printed* from a nickel-based alloy [3].

The transformative potential of AM has by no means been exhausted and we are merely beginning to understand the impact fabricating parts *additively* as opposed to *subtractively* may have. The following fields of AM, and their respective research questions, were the principal motivation for this thesis: (i) hybrid-AM – can we *mix-and-match* different AM technologies to exploit their individual benefits? What advantages would a truly *modular* or *reconfigurable* AM environment bring? And what would this look like? How would a control-system for multiple, *hybridized* AM techniques work? What challenges arise when *printing* using various technologies?; (ii) functional devices – can we fabricate *functional* devices using only AM techniques? For example, can we *print* an energy storage device such as a battery or capacitor? And would printing such devices bring any benefit?; (iii) quality control – to what extent have quality control methods for AM been established? Does fabricating parts *layer-by-layer* bring any opportunities for new forms of quality control or materials characterization? Can we characterize the internal material properties of a part as it is being printed? Could the information gathered for one layer, be used intelligently to correct or adapt the next layer to achieve a better quality print? This thesis investigates these issues and provides new approaches, insights and materials processing technology; where open questions remain, ideas for future work are presented.

0.2 Objectives

The narrative structure and principal objectives/work-packages are outlined below:

Part I – Hybrid additive manufacturing framework

(a) **Construct a versatile hybrid-AM system** – to design, build and commission a modular, lab-scale multi-material, multi-technology (MMMT) manufacturing system (hardware, software & workflows) to facilitate research in hybrid additive manufacturing (hybrid-AM).

Part II – Multi-phase additive manufacture for energy storage applications

---

(b) **Investigate *multi-phase* AM processing science** – to develop quantified understanding of underlying material extrusion additive manufacturing (MEAM) processing-science, such as melt and extrusion dynamics, extrudate spreading as well as bonding processes between successive layers, to enable *multi-phase* AM, i.e. the layer-by-layer deposition of solid-liquid-gel combinations;

(c) **Print a complete energy storage device** – to fabricate a functioning, form-factor free electro-chemical energy storage (EES) device in a single, automated manufacturing operation using MEAM techniques, to characterize the arising electro-chemical performance, and compare with conventional approaches.

Part III – In-line characterization of dielectric properties

(d) **Engineer a non-destructive dielectric probe** – to engineer, characterize and apply a non-destructive, non-contact probe to measure the dielectric permittivity of as-printed materials *layer-by-layer*, suitable for direct integration *in-line* with MEAM processes; and

(e) **Demonstrate 3D dielectric imaging** – to demonstrate proof-of-concept for the real-time, non-destructive acquisition of dielectric data during AM (in three dimensions), providing quantified insight into the internal distribution of the local dielectric permittivity within a printed part.

0.3 Structure of this thesis

Figure iv schematically illustrates the structure of this thesis. Each part is comprised of an introduction providing context, a review of relevant literature and key objectives, followed by an outline of the research/development conducted, and finally a summary of the key scientific contributions or findings as well as an indication of further research opportunities.

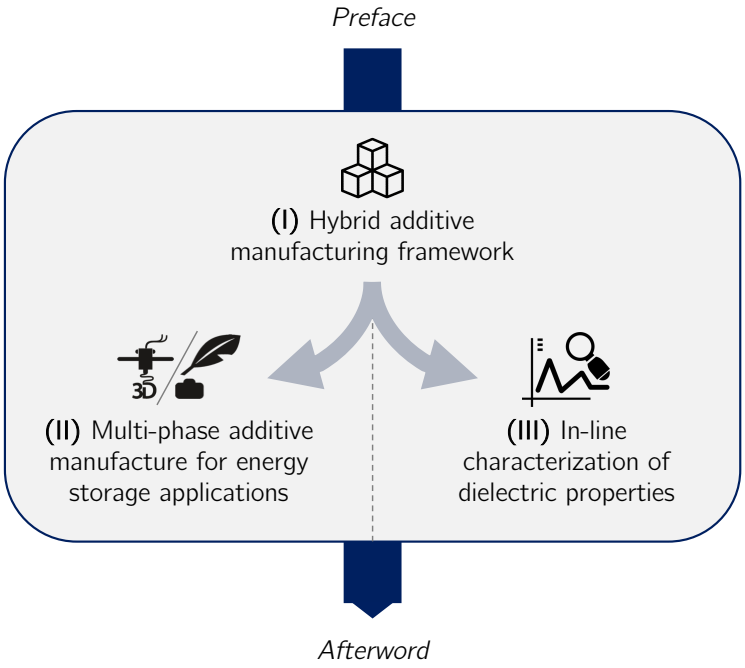

Figure iv: A schematic illustration of the structure of this thesis.

0.4 Terms and abbreviations

C capacitance
L inductance
R internal radius
V voltage
$\dot{\gamma}$ shear rate
μ viscosity
μ_r magnetic permeability
ν scan rate
ϕ_e working potential
ε_r dielectric permittivity
$\vec{\mathbf{E}}$ **field** electric field
$\vec{\mathbf{H}}$ **field** magnetic field
f_0 resonant frequency
g air gap
h thickness
i current
n refractive index
q probe-sample separation distance
w ring width
ABS acrylonitrile butadiene styrene
BN boron nitride
$BaTiO_3$ barium titanate
CNF carbon nanofibre
CNT carbon nanotube
Fe_3O_4 iron oxide
GO graphene oxide
IPA isopropyl alcohol
KCl potassium chloride
KOH potassium hydroxide
$LiFePO_4$ lithium ferrophosphate
NMP N-Methyl-2-pyrrolidone
Ni nickel
PC polycarbonate
PEEK polyether ether ketone
PET polyethylene terephthalate
PE polyethylene
PLA polylactic acid
PP polypropylene
PTFE polytetrafluoroethylene
PVA polyvinyl alcohol
PVDF polyvinylidene fluoride
Pt platinum

1D one dimensional
2D two dimensional
3D three dimensional
3DP three-dimensional printing
AI artificial intelligence
AM additive manufacturing
BJ binder jetting
BOM bill of materials
CAD computer aided design
CAM computer aided manufacture
CCCD constant current charge/discharge
CDLP continuous digital light processing
CNC computer numerical control
CPS cyber-physical system
CV cyclic voltammetry
DED direct energy deposition
DfAM design for additive manufacturing
DfM design for manufacture
DIW direct ink writing
DLP digital light processing
DLW direct laser write
DMLS direct metal laser sintering
DOD drop on demand
DR dynamic range
e-3D embedded 3D printing
EBAM electron beam additive manufacturing
EBM electron beam melting
EDL electric double layer
EDLC electro-chemical double layer capacitor
EES electro-chemical energy storage
EIS electro-chemical impedance spectroscopy
EM electro-magnetic
EPSRC UK Engineering and Physical Sciences Research Council
ESR electrical series resistance
ESW electro-chemical stability window
FEM finite elements model
FFF fused filament fabrication
GUI graphical user interface
H&S health and safety
HiSLIP high-speed LAN instrument protocol
HL holographic lithography
IDE integrated development environment
IEC International Electrotechnical Commission

IJP inkjet printing
IoT Internet of Things
LED light emitting diode
LENS laser-engineered net shaping
Li-ion lithium ions
MEAM material extrusion additive manufacturing
MJM multijet modelling
MMMT multi-material, multi-technology
MMST multi-material, single-technology
NC numerical control
NRW Nicolson-Ross-Weir
OEE overall equipment efficiency
OOP object oriented programming
PμSL projection micro stereo-lithography
PAC printed active composites
PEMA printed electrode membrane assembly
PID proportional-integral-derivative
PML perfectly matched layer
PoC proof-of-concept
PSF point spread function
PWM pulse width modulation
QC quality control
R & D research and development
RF radio frequency
SEM scanning electron microscopy
SL stereo-lithography
SLA stereolithography
SLM selective laser melting
SLP selective laser printing
SLS selective laser sintering
SMA SubMiniature version A
SMMT single-material, multi-technology
SPDR split post dielectric resonator
SRR split ring resonator
STL standard tesselation language
TTL transistor transistor logic
USB universal serial bus
UV ultraviolet
VISA virtual instrument software architecture
VNA vector network analyzer
WIP work in progress
XRT X-ray tomography

Part I
Hybrid additive manufacturing framework

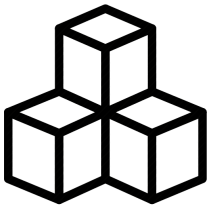

Summary

In the wake of established additive manufacturing (AM) processes and technologies lie so-called *hybrid-AM* techniques. With the ambition to *hybridize* or *unify* the individual strengths of different *additive* (and also *subtractive*) techniques, the potential opportunities of hybrid-AM may be significant: from supply chain simplification through single-operation manufacture, to additional *in-line* functionality such as real-time characterization of material properties *during build*. However, research and development in hybrid-AM concepts and technologies is held back by a lack of accessible, affordable and reconfigurable hybrid-AM systems. Here, the challenges, trends and opportunities for high-value manufacturing in 2019 are described, with a focus on the transformative potential of *AM* and *hybrid-AM*. A novel hybrid-AM framework/concept is then introduced. As proof-of-concept, a corresponding machine is designed and built from the *bottom-up*, with modularity/extensibility at its core. Detailed insights into the design considerations, operating principles, associated work-flows and *digital threads*, alongside potential applications are discussed. The tools and methods developed in Part I form the basis for the research conducted in Parts II and III.

1

Introduction: Hybrid additive manufacturing

1.1 Manufacturing in 2019 3
1.2 Additive manufacturing 5
1.3 Hybrid manufacturing systems 9
1.4 Objectives for Part I 12

1.1 Manufacturing in 2019

Disruption The manufacturing sector is experiencing significant disruption: expanding in emerging economies, in which global consumerism is met by low-wage, low-cost mass production [4]; and shrinking in developed economies, where innovation and flexibility have been identified as key remaining drivers of growth [5, 6]. The legacy sector has been characterized by complex, established production processes, requiring large financial and labor investments, making it chronically difficult for innovation to flourish. Traditionally, manufacturing development has been reserved for big players (e.g. Ford, Toyota and 3M) tackling incremental challenges associated with mass production, waste reduction and overall production efficiency. However, today's technological advancements, particularly in robotics and data-collection/analysis, may provide platforms to radically accelerate the rate of manufacturing/product innovation necessary to tackle primary challenges the sector is facing.

Challenges The manufacturing sector faces severe socio-economic challenges, including: (a) an increasingly competitive manufacturing-scape with radical new business models (service oriented architecture, network communication at production level [7]); (b) a demographic change in the workplace (e.g. skilled labor shortage in the USA [8]); (c)

cyber-security threats (e.g. Stuxnet superworm attacking shop-floor programmable logic controllers [9], 42 % of organizations worldwide were affected by cyber-attacks in the first half of 2018 [10]); and (d) increased market demand volatility (e.g. through fluctuating customer demand paired with imposed tariffs and unpredictable foreign policy [5]). Technological challenges include those relating to: (e) high energy consumption and carbon emissions; (f) multi-material, multi-operation device fabrication (e.g. of functional devices); (g) process flexibility (e.g. shortened product life cycles and small batch sizes); (h) data integration (e.g. a rapid increase in IoT devices contributing to the heterogeneity, speed and quantity of data generated at production level [11]); and (i) a desire for increased production transparency [12].

Industry 4.0 To address the aggregate of these challenges (a-i, described in detailed surveys elsewhere [11]), a wave of industrial digitization and virtualization, termed *industry 4.0*, has emerged. It involves the application of advanced cyber-physical systems (CPSs) at production and logistics level to bring new value and services for customers and organizations [11]. Differentiating such advanced, *smart* systems from conventional manufacturing approaches is the coordination of information, automation, computation, software, sensing, and networking [7]. 80 % of high-value manufacturers believe concepts related to *industry 4.0* will help address the current challenges [12]. Nevertheless, the societal impact of such systems remains controversial, and will require further attention/discussion.

Manufacturing mega-trends Increasing investments in research and development (R & D), innovation and integrated technologies are being made in the manufacturing sector (an expected 40 billion EUR in IoT technologies in 2020, compared to 10 billion in 2015 [13]). Some of the current, industry-wide trends include [14]:

(a) **smart manufacturing** – real-time data analytics, leveraging connected equipment (IoT, CPS systems) with smart sensors and actuators [11, 12] (e.g. real-time work in progress (WIP) tracking [15] or predictive maintenance [16]);

(b) **flexible manufacturing** – unprecedented change-over times in hybrid manufacturing systems facilitating economical, very low production volumes alongside the sending of files across the world, not parts; and

(c) **collaboration** – increased connectivity allowing for multi-party, flexible solutions (global partnerships) as opposed to conventional linear manufacturing contracts.

Amongst the most promising manufacturing technologies, are *additive manufacturing (AM)*, and *hybrid* manufacturing solutions, discussed in detail hereafter.

1.2 Additive manufacturing

Additive manufacturing (AM), or *3D printing*, is proving to be an innovation driver, transforming the way we think about manufacturing and its interaction with the value-chain [17]. AM may be defined as *"the process of joining materials to make parts from three dimensional (3D) model data, usually layer upon layer"* [1] and contrasts to/complements traditional formative (e.g. injection molding) or subtractive methods (e.g. CNC milling). Figure 1.2.A schematically illustrates the difference between *additive* and *subtractive* methods. Comprehensive reviews of the materials [18], methods [19], challenges [20] and applications [21] related to AM are frequently published. Additive methods can fabricate an ever-expanding palette of material classes, primarily: polymers [22], metals [23] and ceramics [24]. The technologies are frequently categorized into seven groups [1]: material extrusion, powder bed fusion, vat photo-polymerization, material jetting, binder jetting, sheet lamination, and direct energy deposition. Table 1.2.A provides an overview of common AM technologies and materials.

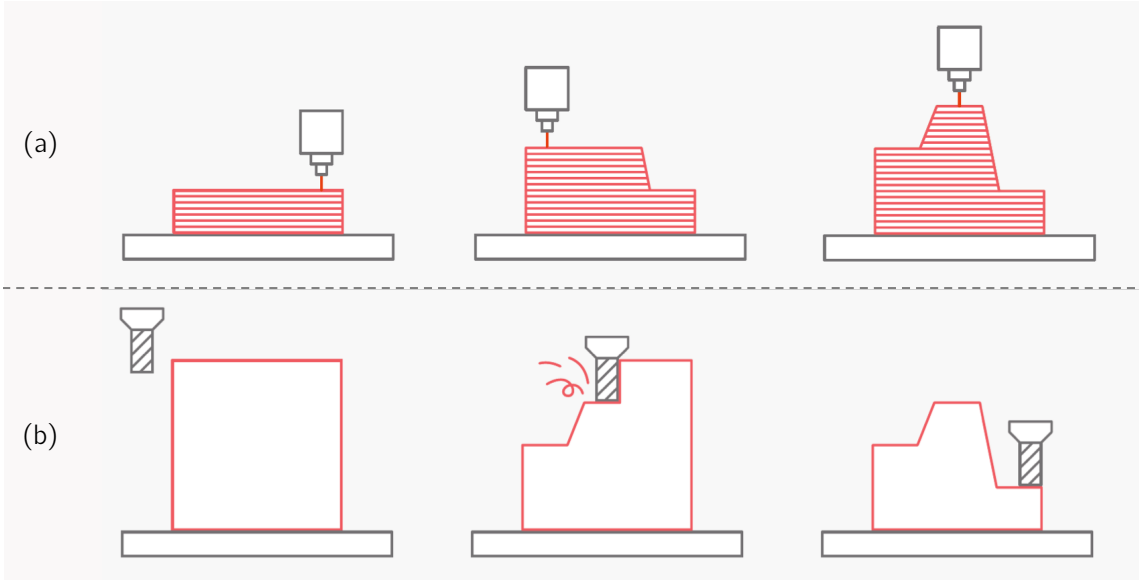

Figure 1.2.A: A schematic representation of (a) *additive* manufacturing and (b) *subtractive* manufacturing. Adapted from [25].

AM category	Example technologies	Common materials
 Material extrusion	Fused filament fabrication (FFF) Direct ink writing (DIW) or robocasting Embedded 3D printing (e-3D)	Thermoplastics Composites
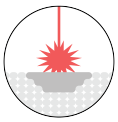 Powder bed fusion	Selective laser melting (SLM) Direct metal laser sintering (DMLS) Selective laser sintering (SLS) Electron beam melting (EBM)	Metal Ceramic Plastic
 Vat photo-polymerization	Stereolithography (SLA) or (SL) Digital light processing (DLP) Continuous digital light processing (CDLP) Selective laser printing (SLP) Projection micro stereo-lithography (PμSL) Holographic lithography (HL)	Thermoset plastic
 Material jetting	Inkjet printing (IJP) Three-dimensional printing (3DP) Multijet modelling (MJM) Drop on demand (DOD)	Plastic Metal Wax
 Binder jetting	Binder jetting (BJ)	Gypsum Sand Metal Plastic
 Direct energy deposition	Laser-engineered net shaping (LENS) Electron beam additive manufacturing (EBAM)	Metal

Table 1.2.A: An overview of common AM process categories, example technologies and common materials. Note: sheet lamination has been excluded; thumbnails adapted from [25].

Additive workflow In its simplest form, the AM workflow entails: (1) product design (conceptualization, computer aided design (CAD) and conversion to a surface geometry, i.e. standard tesselation language (STL) file), (2) *slicing*, or path planning (consideration of geometry, print-presets, material properties and system parameters to generate a machine executable `g-Code` file), (3) machine calibration (homing, offsets, first layer, etc.), (4) build/fabrication (typically layer-by-layer), (5) removal and clean-up, (6) post-processing (e.g. thermal- or ultraviolet (UV)-curing), and (7) quality control and application. Maintaining the integrity and coherency of the associated *digital thread* (i.e. the flow of digital data/files from design to inspection) is crucial in exploiting all the benefits AM technologies may provide (e.g. to be able to use *big-data* algorithms to pre-emptively spot design or manufacturing defects).

Impact of AM Mature AM technologies, such as polymer fused filament fabrication (FFF) or metal selective laser melting (SLM), have already had wide-reaching impact, in particular in areas of [26]: (a) rapid prototyping (e.g. accelerated design cycles and associated time to market through direct manifestation of product designs i.e. from CAD to part within hours [27]); (b) design freedom (e.g. simple fabrication of complex internal/overhanging features alongside topological optimization, organic shapes/structures and cellular structures [28]); and (c) customization (e.g. allowing economical customer co-creation i.e. mass-customization through toolless production [29]). Furthermore, AM is having an impact on: (d) risk mitigation (e.g. minimal financial burden of faulty designs when compared to bespoke molds, tooling or jigs [25]); (e) resource efficiency (e.g. waste reduction/optimized material usage [30], repeatability, tireless 24/7 fabrication and minimal labor costs); (f) decentralization of manufacturing (e.g. disruptive business models/implementation frameworks [31, 32] and rationalization of inventory/logistics [33]); (g) complexity reduction (e.g. component consolidation [34]); (h) democratization of manufacturing (e.g. allowing amateurs to design/fabricate products [35]); (i) collaboration (e.g. open-source projects [36]); and (j) legal as well as security concerns (e.g. intellectual property implications [37]).

Innovation frontiers Technological advancements in microelectronics, robotics, AI, sensors, etc. and the expiration of patents (e.g. [38] in 2009) have led to a surge in research and development (R & D) efforts related to AM. Industrial and academic efforts are tightly linked, through for example the *High Value Manufacturing* catapult scheme in the UK [39], the *America Makes* innovation institute in the USA [40] or the *Frauenhofer AM Alliance* in Germany [41]. Multi-national corporations, such as Siemens, GE and HP, have entered the AM market, and are bringing with them significant R & D efforts [42]. Some of the main innovation frontiers include: (a) advanced materials for AM (e.g. carbon fibre

loaded filaments [43]), (b) new AM processes (e.g. embedded 3D printing (e-3D) [44]), (c) supply-chain integration (e.g. reduced inventory and streamlined logistics [45]), (d) design optimization (i.e. the exploration of light-weighting and organic shapes [46]), (e) economic viability (e.g. lead-time reduction and aftermarket repairs/spare parts [47]), (f) software development (i.e. to cope with the specific requirements of AM [48]), and (g) *4D printing* (i.e. fabrication of parts which change characteristics after they have been printed [49]). At the time of publication, in 2019, the key industries at the forefront of adopting/innovating AM technologies are aerospace, medical and automotive [42].

The AM landscape The AM landscape can generally be divided into hardware manufacturers (e.g. Stratasys or Markforged), software vendors (e.g. Autodesk or Ansys), materials/feedstock suppliers (e.g. Dupont or BASF), post-processing solutions (e.g. Klaeger or PostProcess), quality and inspection solutions (e.g. Faro or Sigma Labs) and research institutions (e.g. Fraunhofer or MTC) [42]. Knowledge is often shared and discussed in open-source online forums [35], not least due to a self-replicating rapid prototyping machine *Rep-Rap* [36]. The consumer market is dominated by XYZprinting, Monoprice, Prusa Research, Wanhao and Flashforge when considering units sold in 2018 [50]. MakerBot, Ultimaker, MarkForged and Formlabs also offer popular desktop printers. Notable AM suppliers with mature technologies for industrial applications (primarily metal based) include Stratasys, EOS, GE additive, 3D systems, Siemens and HP. The list of suppliers offering advanced AM technologies is constanlty expanding/evolving [42].

Limitations of AM Despite the rapid advances in AM technologies, disadvantages include: (a) single-material ability – most AM systems are still only capable of fabricating single-material parts (e.g. to achieve complex geometrical and even structural components, but thus far rarely *functional* products); (b) extensibility – available AM solutions offer virtually no after-market customizability or extensibilty; and (c) mechanical properties – especially tensile properties, fatigue life and ductility are typically lower than conventional counterparts. Furthermore, current AM technologies suffer from: (d) anisotropy – the layer-by-layer nature of AM processes inherently results in anisotropic functionality and stength (usually weakest/poorest perpendicular to the print planes); (e) quality control and reliability – the lack of experience/a comprehensive database to predict and simulate material behaviour of parts fabricated by AM limits their use in critical area or demands costly *complete* or 100 % inspection (i.e. every production part needs to be inspected); (f) reluctance to change – adoption of this radical manufacturing technology faces reluctance to change/slow adoption in some industries [51]; and (g) throughput – the *layer-by-layer* or even *spot-by-spot* methods used in AM may result in very low production throughput when compared to traditional methods such as injection molding or forging.

1.3 Hybrid manufacturing systems

Principal motivation To fabricate complex parts, multiple manufacturing operations[1] are often required. Conventionally, such manufacturing processes are comprised of cascaded, discrete machining operations (e.g. cell manufacturing [52]). Such sequential arrangements systematically prevent the exploitation of potentially advanced interactions between individual processes. Recently (since ∼2012), *hybrid-AM* systems have gained traction [53] to address these issues and promise, among other things: (a) efficiency improvements – radical operational waste reduction (so-called *muda*) through low changeover costs; (b) single-operation manufacture – unison of multi-operation fabrication and what used to be post-processing; (c) additional functionality – incorporation of in-operation metrology and other advanced functionality [54]; (d) multi-material fabrication – two or more dissimilar materials (e.g. metal + polymers) distributed with a designed composition achieving multiple functionalities or enhanced performance [55, 56]; (e) enhanced flexibility – integrated value chain networks with unseen product-mix flexibility [57]; and (f) reactive manufacture – dynamic, *smart* process parameter adjustment based on real-time data collection/analytics [58].

Architecture and definition Hybrid additive manufacturing systems (hybrid-AM systems) may draw on the benefits of multiple, complementing fabrication techniques (e.g. the toolless production principle of AM and the high throughput/surface finish of subtractive/formative fabrication [59–62]). An illustrative example of a metal-based hybrid-AM system is shown in Figure 1.3.A. A range of systems with varying levels of technological maturity and market penetration exist, and may be classified as *single-* or *multi-material* and *single-* or *multi-technology*. Note, hereafter only *integrated*, fully automated and primarily polymer-based systems with at least one MEAM technology will be considered.

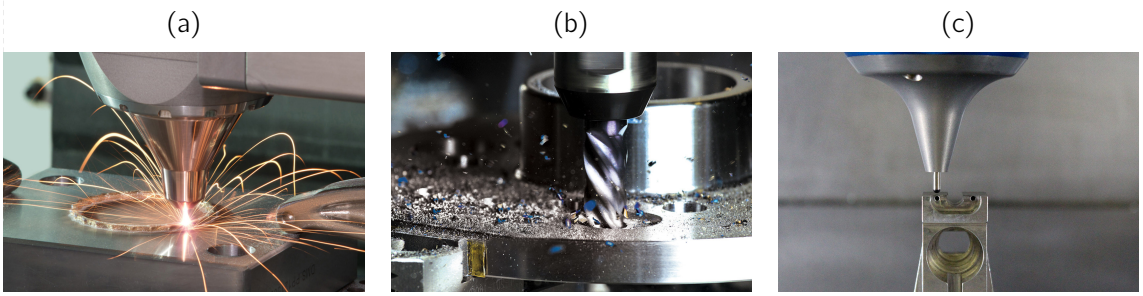

Figure 1.3.A: Example of a hybrid manufacturing system incorporating (a) additive and (b) subtractive manufacture as well as (c) in-operation inspection/metrology [59].

[1] *manufacturing operation*: an activity or activities performed by a single machine, person or both

Single-material, multi-technology The principal benefit of single-material, multi-technology (SMMT) systems is to allow for single-operation manufacturing and the associated higher overall equipment efficiency (OEE), i.e. the reduction of transfer and assembly times through the unison of multiple manufacturing operations. A variety of SMMT manufacturing systems have been proposed (primarily for metal parts [61]), such as direct energy deposition (DED) combined with computer numerical control (CNC) milling, and inspection methods [59], SLM and precision milling [63, 64] and ultrasonic AM with CNC subtractive [65].

Multi-material, single-technology The principal benefit of multi-material, single-technology (MMST) systems is enhanced design freedom: MMST systems allow for multi-material gradients i.e. region-specific, user-defined material properties to create products not possible through single-material processes. Notable research developments related to MMST systems include: (a) FFF systems – the use of dissolvable materials for the fabrication of geometrically complex/overhanging structures and easy removal of support structures [66, 67], the exploration of production speed concepts by combining multiple FFF heads to print variable layer or trace thicknesses [68], the coaxial or sequential deposition of fibres (e.g. kevlar or carbon) for fabricating reinforced composites [69, 70], and the use of needle valves for more precise multi-material flow control [71]; (b) stereolithography (SLA) systems – a rotating vat carousel to exploit the high resolution of SLA but prevent vat contamination issues [72]; (c) inkjet systems – printing of embedded electronic circuits [73, 74], proof-of-concept multi-material demonstrators such as printed active composites (PAC) or origami-like structures [75], and demonstration of blending colours to achieve over 360,000 material combinations for printing multi-coloured objects [76]; (d) laser-engineered net shaping (LENS) systems – the fabrication of functionally graded metal parts (e.g. stainless steel 316L and Stellite Grade 12 Co-Cr alloy [77]); and (e) binder based systems – the control of binder concentration affecting local mechanical properties [78].

Multi-material, multi-technology Manufacturing systems that are capable of processing multiple materials using a variety of additive technologies are still at their infancy [79]. Nevertheless, the principal benefit expected from emerging MMMT systems is to provide additional manufacturing and part functionality, including: (a) the fabrication of parts with superior material properties (hardness, corrosion resistance, thermal conductivity), (b) printed functionality such as bioactivity [79], and (c) the exploitation of complex interactions between manufacturing technologies and materials such as controlled chemical reactions upon deposition. An overview of MMMT concepts for increased component functionality has been published elsewhere [80]. Notable research developments related

to polymer-based MMMT systems include: (a) multi-direct ink writing (DIW)/FFF – an AI enhanced *all-in-one* bio-printer [81] and conductive ink printing for integrated circuits [82, 83]; (b) modular manufacturing systems – interchangeable functional modules such as laser, FFF and CNC machining on flexible gantries [84]; (c) SLA and DIW – single-operation fabrication of arbitrary functional electronic circuits [85]; (d) DIW and pick/place – fabrication of electronic circuits using pre-fabricated electric devices [86]; and (e) in-operation characterization – machine vision assisted, reactive fabrication allowing the integration of auxiliary objects [87].

Limitations of current hybrid-AM systems Hybrid-AM systems remain immature and suffer from a host of challenges/limitations relating to:

(a) **software & control** – (explored further in Section 3.1.1) current manufacturing software (printing hosts, slicers, CAD/computer aided manufacture (CAM), etc.) is frequently regarded as proprietary technology, and as such protected commercially, reserving development to resource intensive firms and hindering wide-spread adoption/development/extension. The academic, open-source counterparts lack standardization in language (python, C/C++, Java, MATLAB, etc.) and platform (Arduino, Raspberry pi, etc.) alongside user friendliness;

(b) **material interfaces** – the material properties of parts fabricated by AM are not well understood. As such, predicting the multi-material interfaces and properties of parts fabricated by hybrid-AM processes remains a challenge;

(c) **complexity & agility** – the complexity, cost and size of current hybrid-AM systems, in particular metal-based systems, result in a lack of flexibility and accessibility for widespread R & D purposes. Furthermore, existing hybrid-AM systems are often simply an aggregate of existing printers, susceptible to interfacing issues, as opposed to a bottom-up designed system. The back-end of common AM machines prevents adaption or manipulation;

(d) **design freedom** – design for additive manufacturing (DfAM) is still in its infancy [88, 89], not to mention design for MMMT hybrid-AM systems. Systematic frameworks have been proposed to help engineers organize complex material and machine-related resources in the design process [56], but are still immature and have not found wide-spread adoption [28, 56, 90]. Furthermore, a lack of design knowledge and infrastructure is hindering the freeform advantage of hybrid-AM systems to be fully exploited (e.g. CAD software is still based on, and promotes, traditional methods like *extrude* (billet material) or *rotate* (lathe));

(e) **collaboration** – as high-value manufacturers move up the value-chain, to focus on technologically advanced industries and products, the required complexity of manufacturing solutions is likely to exceed the capabilities which can be provided by a single vendor [91]. As such, a manufacturing paradigm shift towards a more open-source, collaborative or modular manufacturing-scape, harnessing the latest developments from a wide range of adjacent, complementing fields, is required; and

(f) **universality** – the often praised universality of AM machines has by no means been achieved. The endless permutations of users, technologies and applications related to hybrid-AM systems will likely prohibit the development of a universal hybrid-AM system [92].

1.4 Objectives for Part I

While developments in hybrid-AM systems are advancing in industry, a lack of open-source, freely available hybrid-AM solutions, alongside the limitations outlined in Section 1.3, are limiting research outcomes related to hybrid-AM at lab-scale/in academia. As such, the primary objectives for Part I of this thesis are:

(a) **develop a modular manufacturing concept** – to conceptualize a hybrid additive manufacturing framework (hybrid-AM framework) with modularity, extensibility, multi-functionality and automation as core principles. The framework must consider associated workflows/data transfers as well as necessary interfaces;

(b) **construct a versatile hybrid-AM system** – to design, build and commission a modular, lab-scale MMMT manufacturing system (hardware, software & workflows) to facilitate research in hybrid-AM. The hybrid-AM system should act as proof-of-concept for objective (a), and be specifically capable of, but not limited to, multi-material additive manufacturing and in-line characterization to facilitate the objectives of Parts II and III;

2

Hybrid additive manufacture framework, system and workflow

2.1 The framework 13
2.2 Principal design specifications for a hybrid AM system 16
2.3 Hybrid-AM workflow 17

2.1 The framework

Concept Figure 2.1.A schematically shows an overview of the new overarching, conceptual hybrid-AM framework. The framework is comprised of horizontal *functions* (control, mechatronics and mechanical) and vertical *modules* (e.g. fabrication or characterization). A selection of *modules* were chosen for proof-of-concept (PoC) purposes, in particular to demonstrate multi-material and *multi-phase*[1] fabrication (see Part II of this thesis for an application), alongside the demonstration of *in-line*[2] characterization (see Part III for an application). In principle, the number and functionality of *modules* is not limited, however in practice the mechanical design (described in Section 5) of the hybrid-AM system will restrict the number of *modules*. It should be noted, that all *modules* (e.g. FFF) have corresponding elements in all *functions* (e.g. tailored control algorithms, a designated micro-electronics system and a physical extrusion head), represented as the nodes of the matrix in Figure 2.1.A. The aggregate of each *function* across all *modules* forms the basis of *system components*, which are discussed in detail hereafter:

[1] fabrication using materials in at least 2 different states of matter (phases), e.g. solids and liquids.
[2] integrated within an existing manufacturing operation, i.e. does not require a seperate operation.

- **control** (see Section 3) – a *printing host* to provide the logic and data manipulation/analysis/etc. behind the hybrid-AM system;
- **mechatronics** (see Section 4) – a motherboard as interface between control and mechanical *functions*; and
- **mechanical** (see Section 5) – the hybrid additive manufacturing machine (hybrid-AM machine), i.e. the physical fabrication system.

Novelty Unlike conventional, cascaded/sequential manufacturing, the hybrid-AM framework is characterized by modularity and interconnectivity as core principles. The framework provides a novel, reconfigurable and extensible approach to digital fabrication and characterization. For example, the unification of all *control functions* in a single, *modular printing host* (described in detail in Section 3) may provide a platform to facilitate smart and reactive manufacture *by design*. Parts II and III of this thesis bring out and exploit these aspects explicitly.

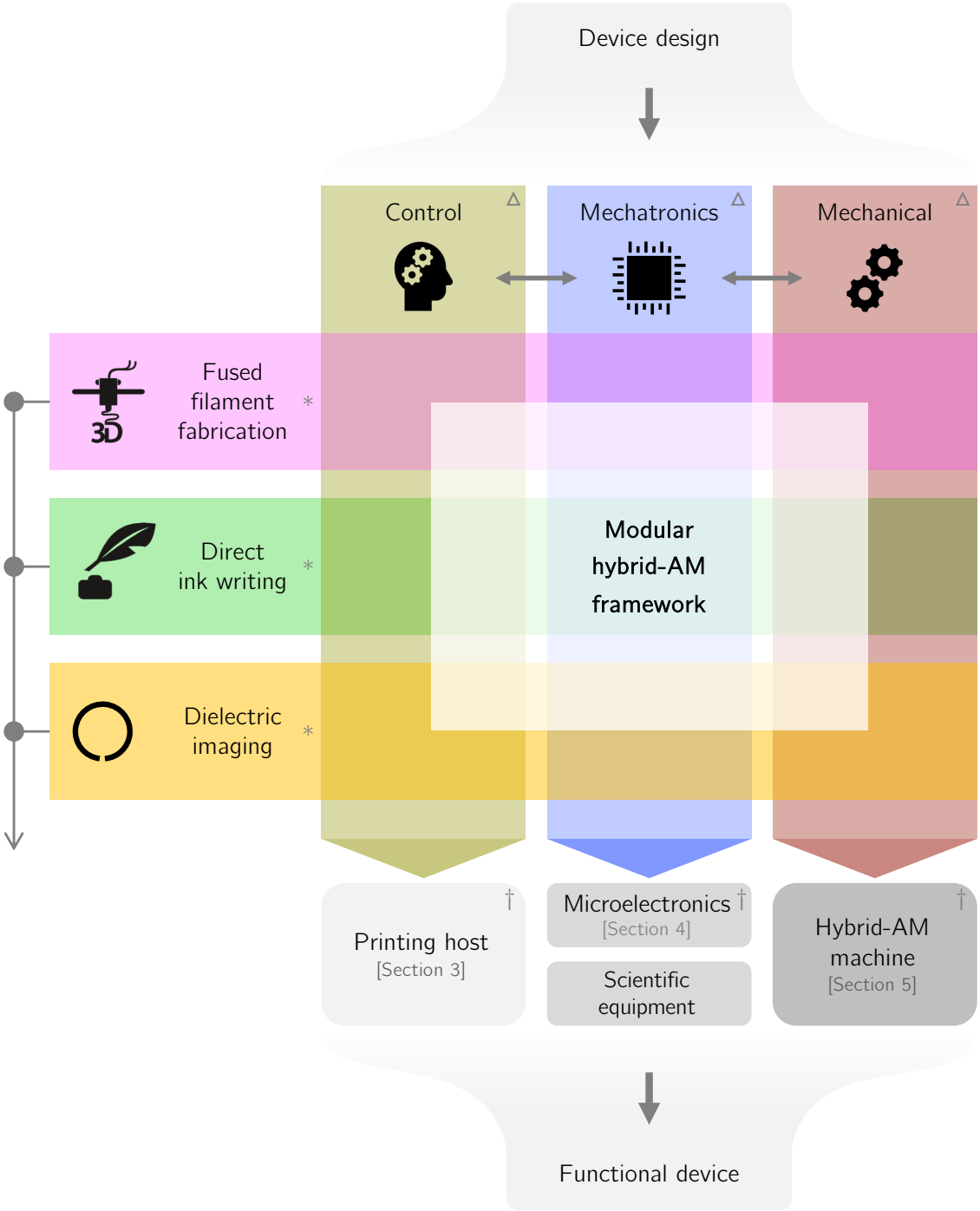

Figure 2.1.A: A schematic overview of the modular hybrid-AM framework showing the interaction of a selection of *modules* (FFF, DIW and dielectric imaging, indicated by *), *functions* (control, mechatronics and mechanical, indicated by △) and *system components* (printing host, motherboard, and hybrid-AM machine, indicated by †).

2.2 Principal design specifications for a hybrid AM system

Table 2.2.A outlines a selection of requirements that guided the design process of the hybrid-AM system. The principal challenge lies in coordinating motion and functionality through software interfaces (control systems), mechatronic systems and mechanical mechanisms. Modularity, versatility and robustness were considered to be the most important attributes of the hybrid-AM system.

Hybrid-AM system requirements

Non-functional	Automated	allow system capabilities to operate with a minimum of human assistance
	Maintainable	design for easy fault finding and repair
	Reconfigurable	allow for the easy, modular extension of system capabilities, *by design*, to meet needs for materials science/engineering research
	Operable	designed for ease of use by an engineer
	Reliable	repeatable, reliable operation of all functional modules
	Safe	operation in strict adherence to H&S requirements
	Standardized	provision of detailed engineering drawings for all components, and the use of commercially available parts where possible
Functional/ technical	User friendly	provide a simple graphical user interface (GUI) to guide the user throughout AM (i.e. from g-Code generation to fabrication/characterization)
	Multi-material	allow for multi-material, multi-technology (MMMT) fabrication of complex 3D assemblies
	Integration	support the integration of 3rd party scientific equipment (e.g. sensors, probes, measuring equipment, etc.)
	Host-based	rely on a host-computer for processing and control to allow for e.g. *reactive* or *smart* AM
	Logging	keep an accessible record of all manufacturing related parameters for debugging and retrospective data analysis
	Spatial control	allow 3D spatial/temporal manipulation in orthogonal axes X, Y and Z over a build volume $\geq 100 \times 100 \times 100\,\text{mm}$

Table 2.2.A: A selection of non-functional and functional/technical design requirements for the hybrid-AM system.

2.3 Hybrid additive manufacturing workflow

Step-by-step Figure 2.3.A depicts a simplified, functional flowchart of the hybrid-AM workflow including a visualization of the *digital thread* (data transfers and processes, software and file types). Detailed flowcharts for individual *system components* are provided in the corresponding sections: printing host (see Section 3), microelectronics (see Section 4) and hybrid-AM machine (see Section 5). The workflow relied on a *host-based*[3] control approach and in its simplest form, with reference to labels in Figure 2.3.A and excluding more complicated feedback loops, the workflow entailed:

- **Device design** – (1) conceptualization of a part or device (e.g. functional or multi-material); (2) articulation and quantification of design specifications; (3) detailed 3D device design in CAD software (i.e. multi-part assembly with respect to a mutual origin); (4.1) exporting of a simplified surface geometry to meet the requirements of slicing software (e.g. in `.STL` format); (4.2) definition of fabrication or *print* parameters such as material, speed, temperatures, etc. in designated slicing software (e.g. in `.INO` format for Slic3r v1.3.0). Finally, from 4.1 and 4.2, the slicing software could (5.1) calculate a layer-by-layer tool path and generate a chronological list of machine commands i.e. the `g-Code`.

- **Printing host** – (5.2) definition of module specific parameters through the printing host graphical user interface (GUI); from 5.1 and 5.2, (6) manipulation of the original `g-Code` to reflect module specific parameters and finally; (7) numerical control (NC)/communication with the hybrid-AM system.

- **Microelectronics** – (8.1) the firmware on a microcontroller interpreted the machine command and in conjunction with (8.2) interpreting the current system status, decided which action to make (e.g. if the command was to reach a desired temperature, the firmware cross-checked the current temperature and decided to heat up or cool down accordingly); (9) module specific *break-out boards*[4] amplified the logic signal from the microcontroller in 8 to power the hybrid-AM machine.

- **Hybrid-AM machine** – (10.1) an analog signal caused actuation (e.g. stepper motor motion) while (10.2) sensors reported back to the microcontroller or other scientific equipment; (11) multi-material parts were fabricated layer-by-layer; and (12) could then be extracted for (13) application and testing.

- **Printing host (post-processing)** – (14) throughout production, the system status 8.2 was logged and could influence NC in 7; (15) production and characterization data (e.g. from scientific equipment) was analyzed and visualized.

[3] relies entirely on a single *host* computer/processor to coordinate all processes
[4] bundled, electrical components on a modular, replaceable motherboard

Software requirements It follows that the minimum software requirements for implementing the described hybrid-AM workflow were: (a) CAD software – to design/generate 3D parts and assemblies; (b) a slicing engine – to generate layer-by-layer tool-paths and machine interpretable lists of commands (`g-Code`); (c) a printing host – to communciate with the hybrid-AM system; and (d) microcontroller firmware – to interpret and execute commands from the printing host. Mature, commercially available software was used for the *device design* stages i.e. SolidWorks 2017 as CAD engine, and Slic3r v1.3.0 as slicing engine. A bespoke printing host (see Section 3) was developed *bottom up* to satisfy the system requirements outlined in Section 2.2. An existing, open-source firmware (Repetier v0.92.9) was modified (see Section 4.3.1) to meet system requirements.

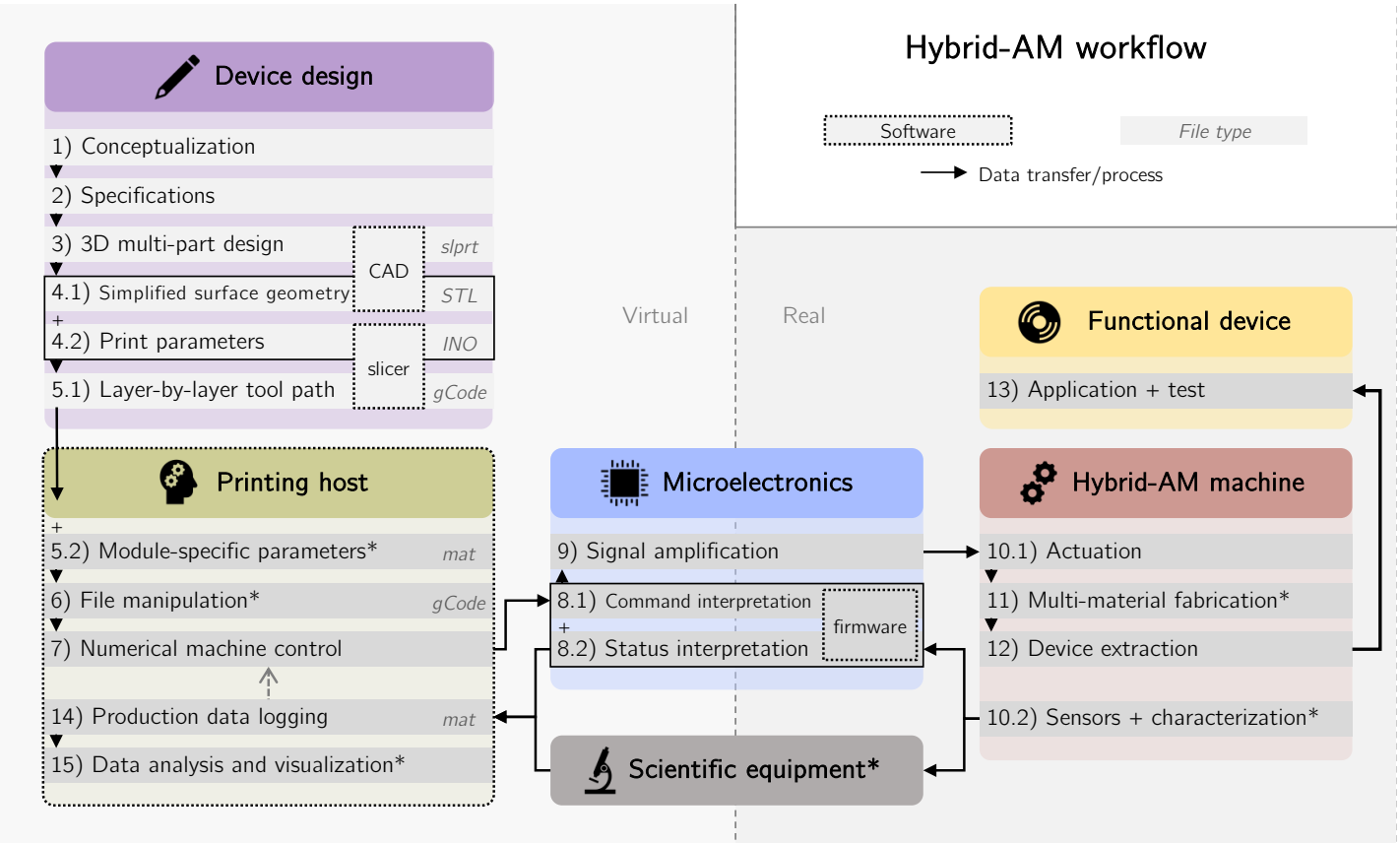

Figure 2.3.A: Functional flowchart of the hybrid-AM workflow. Note: * indicates steps which differ significantly from conventional AM workflows.

3

Adaptive printing host

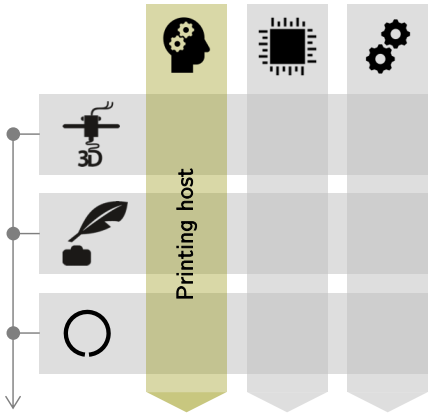

Figure 3.0.A: The printing host within the hybrid-AM framework.

3.1 The printing host in context 20
3.1.1 Purpose and functionality 20
3.1.2 Literature review 21
3.2 Design requirements and implementation 23
3.3 Software architecture 25
3.3.1 The graphical user interface 27
3.3.2 Callbacks and functions 28
3.3.3 Properties 30
3.4 Software operation 33
3.4.1 Initialization of the printing host 34
3.4.2 Print preparation 34
3.4.3 During build 35
3.4.4 Data analysis 37
3.5 Summary of the printing host 38

Section 3 outlines the design considerations for an adaptive 'printing host', providing logic and control functionality across all 'modules' of the hybrid-AM system. The printing host described here is a piece of computer software that acted as interface between the user/engineer and the microelectronics system described in Section 4. The printing host is interchangeably referred to as the hybrid-AM app. The reasoning behind key decisions and selections is given, and may provide a design guide that could be followed by other researchers.

3.1 The printing host in context

3.1.1 Purpose and functionality

The *printing host* sent, received and logged commands or queries to/from microelectronics systems of ancillary devices (e.g. relating to the hybrid-AM machine or attached scientific equipment such as a vector network analyzer (VNA), see Figure 2.3.A for context). It provided a computer-based platform for the user/engineer to interact with all *system components* of the hybrid-AM framework. Additionally, the printing host allowed for: (a) debugging of machine commands and queries (i.e. the `g-Code`), (b) manual machine control (e.g. for calibration purposes), (c) production data logging/analysis (i.e. storing a record of machine motions and responses), and (d) visualization of fabrication and characterization processes.

Inputs The primary inputs to the printing host were: (a) user interaction with the GUI (e.g. clicking of buttons or entering of parameters), (b) arrays of machine commands (layer-by-layer tool paths or `g-Code` from slicing software i.e. label 5.1 in Figure 2.3.A), (c) system calibration parameters (e.g. travel speeds and tooling off-sets), and (d) print settings (e.g. extruder or build-plate temperatures).

Outputs The primary outputs of the printing host were: (a) a real-time GUI (visualizing machine commands/returns and system status), (b) communciation with the microelectronics system, and (c) a log of production and characterization data (e.g. hot-end temperature profiles or a temporal/spatial record of the state of actuators).

3.1.2 Literature review

Printing hosts A wide variety of open-source and proprietary printing hosts are available. Many printing hosts integrate the functionality of a *slicer*[1], by either calling on external slicing engines such as *CuraEngine* [93], *Slic3r* [94] and *Skeinforge* [95] or by providing their own proprietary slicing engine such as *Eiger* [96] and *Preform* [97]. Common printing hosts for AM include: *ReplicatorG* – simple, based on the *Skeinforge* [98]; *Simplify3D* – compatible with most desktop printers [99]; *Repetier host* – freeware, supports remote access [100]; *Ultimaker Cura* – open source, compatible with most desktop printers [101]; *Printrun* – python based [102]; *Octoprint* – open source, optimized for wireless communication [103]; and *Siemens NX* or *Autodesk Netfabb* – proprietary, mainly for metal AM including advanced design optimization, build preparation, AM simulation and CNC operations [104, 105]. Initial attempts at designing and implementing printing hosts for bespoke hybrid-AM systems have been reported and are often based on *Lab-VIEW*[2]. For example: an overall process management system linking existing fabrication control software (multi-SLA based on *buildstation 4.0* [72]), the control of a MMST hybrid-AM system (multi-FFF controlled by *FDMotion* [68]), and the control of both fabrication and characterization methods (e.g. FFF and imaging techniques using *Fabricator* [87]).

Limitations of current printing hosts Sophisticated, open source printing hosts (i.e. with an accessible, modifiable backend[3]) designed specifically for hybrid-AM systems do not exist. Some of the main limitations of current printing hosts include:

(a) **modularity** – software does not reflect the desired modularity and extensibility of next generation hybrid-AM systems and is often optimized for a single use-case only (e.g. FFF processing only);

(b) **live control (packaging)** – typically printing hosts send batches of commands to a microelectronics system local on the machine, in the form of *packages*, until a pre-specified buffer is full. This implies that the printing host does not necessarily know exactly at which point of execution (i.e. command line) the microcontroller/-machine is, resulting in a *lag* between sending a command and its execution. This systematically prevents the incorporation of advanced, on-demand control/functionality (e.g. simultaneously interfacing with multiple ancillary devices enabling in-line characterization) within the printing host [92];

[1] software to generate layer-by-layer tool-paths and machine interpretable lists of commands (`g-Code`)
[2] a systems-design platform for visual programming from National Instruments
[3] the layer within software providing control over data-access and data-manipulation functionality

(c) **data analysis** – although data/commands are frequenlty logged throughout fabrication, the analysis of this data in real-time has not been exploited to any significant extent; and

(d) **language** – there is no standard for the language or style used to document printing hosts, making interfacing or constructing functional/extendable *libraries* from pre-existing hosts difficult.

Other software-related issues which follow from the slicing process, but are not specific to the printing host, include:

(e) **file restrictions** – the boundary based file type `.STL` used in most printing processes does not inherently allow for multi-material or multi-technology fabrication. Furthermore this legacy file type does not promote collaboration and unnecessarily complicates device designs by rasterizing all features with triangular facets. File types including `.3MF` and `.AMF` have been proposed to remidy some of the faults, but in practice have not been adopted as they suffer from similar issues [92].

3.2 Design requirements and implementation

App requirements The printing host, or *hybrid additive manufacturing application (hybrid-AM app)*, was designed to address some of the limitations of current printing hosts (outlined in Section 3.1.2). Table 3.2.A provides a selection of principal design specifications considered throughout development, in particular those relating to: (a-e) the user interaction with the hybrid-AM app, (f-j) the architecture of the application, i.e. the structure and hierarchy of underlying code, and (k-p) the desired app functionality, i.e. the type of tasks which were required.

Hybrid-AM app requirements	
User interaction	(a) provide an intuitive, familiar and seamless user-interaction experience
	(b) reflect the chronology of the hybrid-AM workflow (see Figure 2.3.A)
	(c) be automated where possible
	(d) prevent non-permissible/destructive actions or machine commands
	(e) provide an overview of progress/machine status at all times
Architecture	(f) facilitate modular, extensible and scalable functionality
	(g) written in verbose, self-explanatory and transparent manner
	(h) bundled such that application and file reprositories are all in one place
	(i) allow for multi-paradigm, cross-platform programming
	(j) follow a logical, hierarchical architecture
Function	(k) coordinate, analyze and log commands to/from multiple ancillary devices
	(l) allow robust and repeatable operation of the hybrid-AM machine (see Section 5)
	(m) allow for interrupt routines e.g. pause, restart, emergency stop
	(n) account for customizable machine set-up/configuration/calibration
	(o) allow for manual override/control of ancillary devices
	(p) provide overarching (system) and module specific (extensible) functionality

Table 3.2.A: A selection of principal design requirements for the hybrid-AM app related to (a-e) the user interaction, (f-j) architecture and (k-p) function.

Implementation A brief overview of how the app design requirements were implemented is given below. References to subsequent sections providing more detail are provided, while labels (a-p) refer to Table 3.2.A.

User interaction To (a) provide an intuitive, familiar and seamless user-interaction experience, a graphical user interface (GUI) with conventional, interactive user inputs such as buttons and toggle switches was designed (see Section 3.3.1). The layout of the GUI, (b) reflected the chronology of the hybrid-AM workflow (outlined in Section 2.3). Where possible, default settings were provided or (c) automatically extracted/stored/analyzed from associated files. All machine commands were screened/filtered to (d) prevent non-permissible and potentially destructive/unwanted machine actions. The GUI displayed all commands sent/received to/from ancillary devices in verbose pseudo-code[4], alongside providing an indication of the machine status at all times (see Section 3.3.1) for (e) showing at what stage of the hybrid-AM workflow the user was at.

Architecture The modular architecture of the hybrid-AM app (see Section 3.3) allowed for (f) extensible functionality. All code for the hybrid-AM app was (g) written in a verbose, self-explanatory and transparent manner (see Figure 3.3.C and Section 3.3.3). The hybrid-AM app was (h) bundled as a single, standalone application and unique file repositories (by date) were created for each build/print/experiment to provide a logical structure for the generated data (i.e. folders for printing logs and/or associated characterization/design files). The hybrid-AM app was written in *MATLAB*: (i) allowing for multi-paradigm[5] (e.g. *procedural* during fabrication, following a `g-Code` command line-by-line, *functional* when referring to recurring commands and *imperative* in the assignment/reference to global calibration values) and cross platform programming (mac and windows). Furthermore the architecture was (j) simple and hierarchical (see Section 3.3) by, for example, using mutually exclusive/non-recursive functions where possible.

[4]code that is interpretable by a user, but not necessarily executable by a machine
[5]see [106] for an introduction to programming paradigms

Function The hybrid-AM app facilitated communication with multiple ancillary devices and (k) coordinated, analyzed and logged commands by, for example, linking sensor readings with gantry position (see Figure 3.3.C). For all critical, procedural commands, confirmation was requested to (l) allow robust and repeatable machine operation. The architecture allowed for high-priority (m) interrupt routines, such as *pause*, *restart* and *emergency stop*, to suspend normal operation. The modular libraries of the hybrid-AM app, (n) accounted for varying machine configurations and calibration values. The user was able to, (o) manually override/control the ancillary devices/machines by directly sending machine command lines (`g-Code`). Support for, (p) both the overarching system requirements (e.g. gantry motion), and specific functional modules (e.g. monitoring the temperature of nozzles) was provided (see Section 3.3.2).

3.3 Software architecture

Figure 3.3.A schematically illustrates how the constituent components of the hybrid-AM app interacted, namely: (1) a GUI (see Section 3.3.1), (2) callbacks and functions (see Section 3.3.2) as well as (3) properties (see Section 3.3.3). With reference to labels in Figure 3.3.A, a series of inputs/outputs and data transfers dictated the operation of the hybrid-AM app: (i) user interaction with the GUI (i.e. graphical components) upon which (ii) relevent callbacks were prompted, (iii) executing functions/commands which could (iv) modify/generate properties or (v) interact with ancillary devices. Finally, (vi) processed information was visualized for the user in the GUI.

Programming language With foresight for the need of interfacing multiple devices/microcontrollers, alongside robustness and available support, *MATLAB* was chosen as programming language for the hybrid-AM app. *MATLAB* is a proprietary, multi-paradigm numerical computing environment based on C, C++ and Java. Principal benefits include: GUI support (easy debugging and code generation), available, mature interfacing libraries (e.g. with third party equipment), interfacing with other languages (i.e. allows subfunctions/routines written in other languages to be called/run), and cross-platform support (mac, windows).

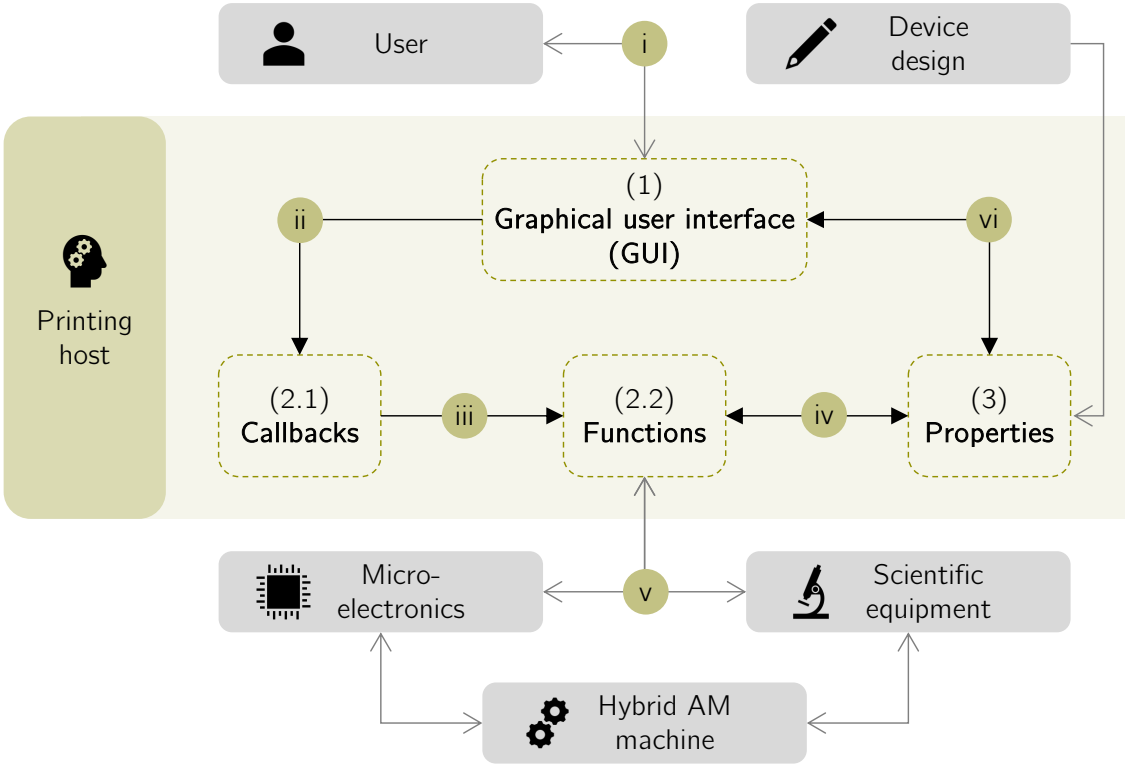

Figure 3.3.A: A flowchart of the hybrid-AM app and its constituent components: (1) the GUI, (2) callbacks & functions and (3) properties. Labels (i-vi) are referred to in the text.

3.3.1 The graphical user interface

A bespoke GUI (label 1 in Figure 3.3.A) was developed to allow for the control and monitoring of the hybrid-AM machine in a single *window*. Principally, the GUI was comprised of input fields (e.g. buttons, text or numeric inputs, toggle options) and output fields (e.g. axes/graphs, character strings). Figure 3.3.B shows how these fields were clustered: (i) a *status dashboard* provided an indication of workflow progress and which *modules* were activated (colour scheme: green – completed, orange – in progress/active, pink – requires user input, red – failed); (ii) toggles to connect/disconnect ancillary devices; (iii) an indication of print progress and a button for an emergency stop, (iv) module specific input fields for print parameters (i.e. label i in Figure 3.3.A), and (v) output fields to visualize data such as machine commands or temperature profiles.

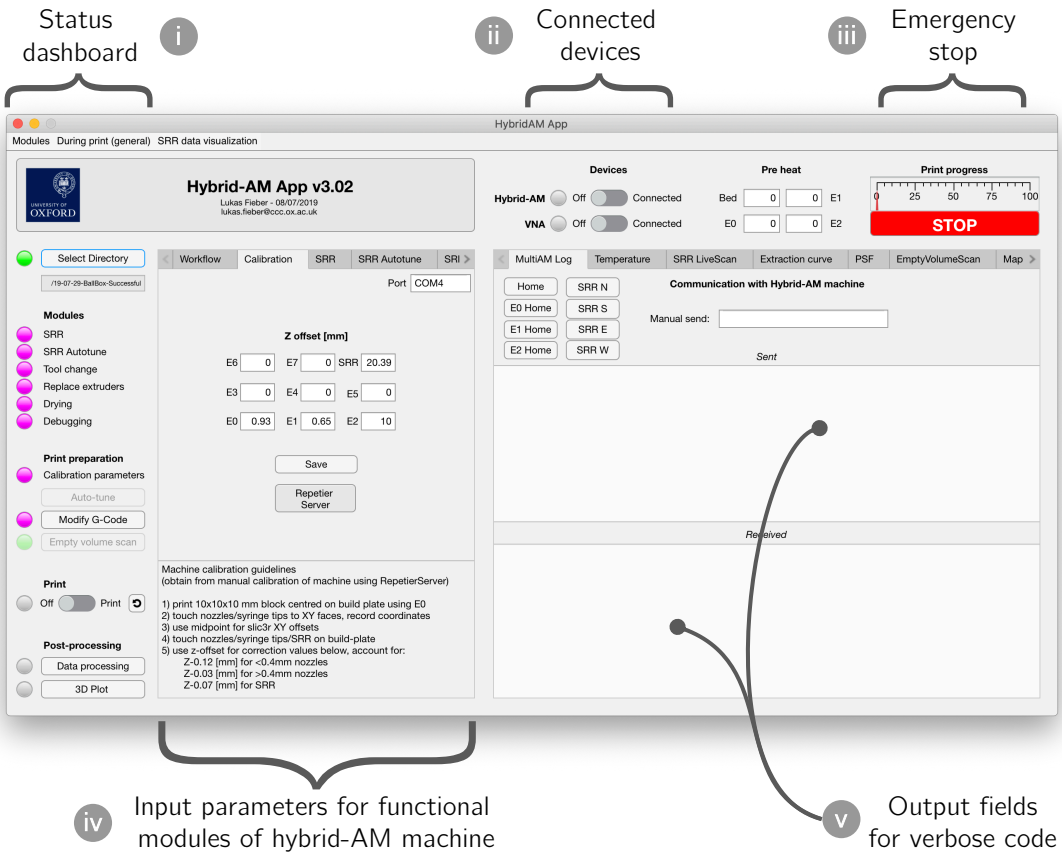

Figure 3.3.B: A screenshot of the GUI for the hybrid-AM app showing: (i) a *status dashboard*, (ii) toggles to connect/disconnect ancillary devices, (iii) an indication of print progress, (iv) module specific input fields, and (v) output fields to visualize data.

3.3.2 Callbacks and functions

Types of functions Functions (label 2 in Figure 3.3.A) are subroutines that are executed as a sequence of tasks defined by a *statement block* (example provided in Figure 3.3.C). They may have an arbitrary number (including none) of arguments/inputs and return values/outputs. Here, *callbacks* are considered to be functions which are triggered by the user and usually invoke/call further functions. The functions declared in the hybrid-AM app may be classified along multiple *dimensions* (see Table 3.3.A): (i) by functionality, (ii) location, (iii) module and (iv) trigger. In total, the hybrid-AM app referred to over 70 user-defined functions (i.e. excluding default MATLAB functions).

Dimension	Types	Description	Example
Functionality	Data processing	performs modifications to *properties*	`readLocation`
	GUI	visualizes *properties* for the user	`PlotSRR`
	Communication	interacts with ancillary devices	`fprintfMultiAM`
Location	Global	accessible from any function/application	`addpath`
	Member	accessible at any point in the hybrid-AM app	`startupFcn`
	Embedded	can only be referred to within a specified function	`insertCode`
Module	System	applicable to overarching/system operations	`gCode_MultiAM`
	Fabrication	specific to fabrication modules e.g. FFF or DIW	`DryingfieldsEnable`
	Characterization	specific to characterization modules e.g. SRR	`RecordVNA`
Trigger	User	execution prompted by user (e.g. button callbacks)	`STOPButtonPushed`
	Internal	functions called internally by hybrid-AM app	`fscanfMultiAM`

Table 3.3.A: Dimensions and types of functions used in the hybrid-AM app.

Programming style Principles from object oriented programming (OOP) were considered throughout app development, in particular relating to: (a) *encapsulation and abstraction* – functions only exposed high-level mechanisms, hiding internal implementation details. For example, the function responsible for sending a machine interpretable command solely required the command (`g-Code`) and returned a *status-flag* indicating the success or failure of command transmission, while actions such as logging or screening of commands occured automatically within; and (b) *inheritance* – functions with predominantly similar functionality were paired and differentiation for variations was provided by an *activation flag* (e.g. to account for the slight difference in procedure when starting or re-starting a print after a pause). Figure 3.3.C provides an example of a function (`RecordVNA`) which queried data from an ancillary device (VNA) and related it to the hybrid-AM machine gantry coordinates.

```
%% Record data from VNA at location XYZ
%   09-10-2018
%   Lukas Fieber
%   Input:      VNA                 serial object (VNA)
%               XYZstring           gCode of XYZ location
%               numReadings         no. readings to average
%               dataTable           pre-existing array
%   Output:     dataTable           updated array

%---
% 1) Declare function
function [dataTable] =
         RecordVNA(VNA,XYZstring,numReadings,dataTable)

%---
% 2) Initialize
    flushinput(VNA);    %clear VNA input buffer
    temp = zeros(numReadings,6);    %initialize variables
    n = length(dataTable{dataTable{:,'f0'}~=0,'f0'}) + 1;

%---
% 3) Prompt data from VNA
    for h=1:numReadings % prompt VNA [numReadings] times
        rs_send_command(VNA,':CALCULATE1:MARKER:FUNCtion:
           EXECute BFILter'); %bandfilter search
        pause(0.1); %allow VNA to respond
        [~,tempString] = rs_send_query(VNA,'CALCulate1:
           MARKer1:BWIDth?'); %query data
        temp(h,:) = str2num(tempString); %convert data type
    end; clear h tempString numReadings %clean up workspace

% ---
% 4) Extract/output data
    dataTable{n,'Time'} = datetime; %record time
    if ischar(XYZstring) %validity check
        dataTable = readLocation(dataTable,XYZstring,n);
    end
    dataTable{n,'BandWidth'}    = mean(temp(:,1));
    dataTable{n,'f0'}           = mean(temp(:,2));
    dataTable{n,'QFactor3dB'}   = mean(temp(:,3));
    dataTable{n,'Loss'}         = mean(temp(:,4));
    dataTable{n,'LowerEdge'}    = mean(temp(:,5));
    dataTable{n,'UpperEdge'}    = mean(temp(:,6));
    clear temp n  %clean up workspace

end
```

Figure 3.3.C: Example of code defining a function (`RecordVNA`) in the hybrid-AM app which queried data from an ancillary device (VNA) and related it to the machine/gantry coordinates. The function comprised: (1) declaration of the function, (2) initialization of variables, (3) prompting of data from an ancillary device and (4) extraction/outputting of data in a relevant format. Colour scheme: notes/annotations, keywords, strings and executable code.

3.3.3 Properties

Data types *Properties* (label 3 in Figure 3.3.A) contain/store data of different types. Table 3.3.B provides an overview of the types of data and corresponding class names that were used in the hybrid-AM app. Data types were initialized/defined either manually (pre-allocated to improve speed), or automatically by *MATLAB*.

Data type	**Class name**	**Description**
Structures	`struct, axes, serial object`	Fields that store arrays of varying classes and sizes (i.e. a *folder* for other data types)
Numeric	`single, double uint32`	Integer and floating-point data for signed and unsigned numbers
Characters and strings	`char, string`	Text in character arrays and string arrays
Dates and time	`datetime`	Arrays of date and time values that can be displayed in different formats
Tables	`table`	Arrays in tabular form whose named columns can have different data types
Cell arrays	`cell`	Cells store arrays of varying classes and sizes
Function handles	`function_handle`	Scalar handle i.e. pointer to a function (@) to allow a functon being invoked indirectly
Logical	`logical`	Used in relational conditions or to test state

Table 3.3.B: A selection of data types and class names used in the hybrid-AM app.

Data location Throughout operation of the hybrid-AM app, *properties* were either stored within the application (internal) or in a specified global directory on the printing host computer (external). Figure 3.3.D shows a hierarchical overview of the first two tiers of *properties*. Internal properties served the purpose of storing temporary data, whereas external properties could be referred to even after a hybrid-AM app session[6] had been terminated. For example, the `serial objects` created to enable communication between the hybrid-AM app and hybrid-AM machine were only relevant for a single hybrid-AM app session and as such were stored *internally*. Properties including calibration values of the hybrid-AM machine, e.g. `calibration offsets`, could be carried over between sessions, and as such were stored *externally*.

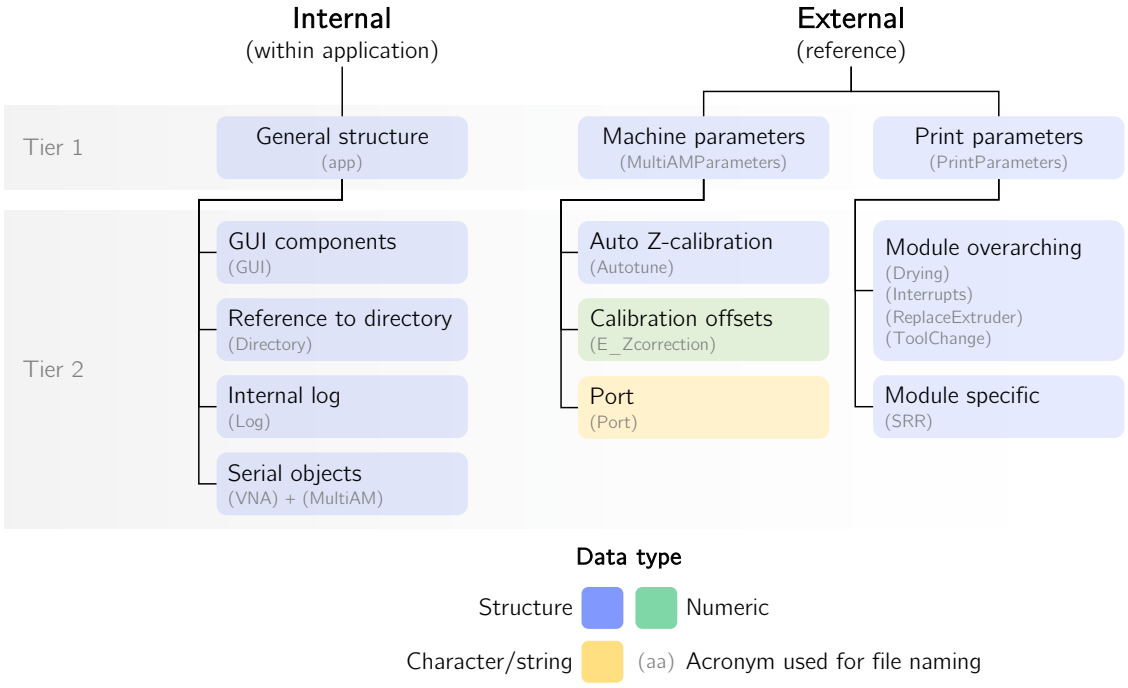

Figure 3.3.D: An overview of printing host properties (internal and external). *Structures* contain further nodes, and only the first two tiers of the hierarchy are shown here. Note, a copy of the `internal log` was stored externally for debugging purposes after completion of a print, but all other *internal* data was discarded after each session.

[6] a temporary interactive information exchange, i.e. a session begins when a user initializes the hybrid-AM app and ends when the user closes the hybrid-AM app

Data hierarchy An index of all user-controlled properties (i.e. excluding general graphical components) associated with the hybrid-AM app was declared in the form of a *code-book*: an example is provided in Figure 3.3.E. The *code-book* provided information about the hierarchy, class type and a description of the purpose of each property. The naming convention followed by all properties was hierarchical, for example, `app.Log.initLog.Command` referred to a local, tier 4 property called `Command` which was stored in the structure `initLog` etc. In total, the hybrid-AM app refers to over 130 properties in its current configuration (extendable depending on machine functionality).

Tier 1	Tier 2	Tier 3	Tier 4	Tier 5	Tier 6	Type	Description
app.	Log.	gCode.	n			uint32	gCode line counter
app.	Log.	initLog.	Command			string	String of received communication
app.	Log.	initLog.	Time			datetime	Time of received communication
app.	Log.	initLog.				table	Log for communications with MultiAM machine during initialization
app.	Log.	Receive.	n			uint32	received information line counter (MultiAM communications)
app.	Log.	Receive.	ReceiveLog.	Time		datetime	Time of received communication
app.	Log.	Receive.	ReceiveLog.			table	log of commands received from MultiAM machine
app.	Log.	Sent.	Homed			logical	Flags to indicate if MultiAM has been homed.
app.	Log.	Sent.	n			uint32	sent line counter (MultiAM communications)
app.	Log.	Sent.	SentLog.	Command		cellstr	Command sent (verbose)
app.	Log.	Sent.	SentLog.	Completed		datetime	Time SentLog.Command was completed by MultiAM
app.	Log.	Sent.	SentLog.	Confirmed		datetime	Time SentLog.Command was received/confirmed by MultiAM
app.	Log.	Sent.	SentLog.	Time		datetime	Time SentLog.Command was sent
app.	Log.	Sent.	SentLog.			table	log of commands sent to MultiAM machine
app.	Log.	SRR.	Autotune.	Air.	BandWidth	double	bandwidth of the bandpass/bandstop region [Hz]
app.	Log.	SRR.	Autotune.	Air.	f0	double	Resonance frequency of air [GHz]
app.	Log.	SRR.	Autotune.	Air.	Loss	double	Magnitude of S21 [dB]
app.	Log.	SRR.	Autotune.	Air.	LowerEdge	double	Lower band edge [Hz]
app.	Log.	SRR.	Autotune.	Air.	UpperEdge	double	Upper band edge [Hz]

Figure 3.3.E: A selection of properties as recorded in the *codebook*, showing data location/hierarchy, data type and a description of the purpose of the property.

3.4 Software operation

This section outlines some of the unusual/unconventional functionality/features the hybrid-AM app demonstrated throughout operation. Figure 3.4.A provides an overview of this sub-section, entailing: (1) app initialization (creation of the classes, graphics environment, etc.), (2) print preparation (definition of print paramters and pre-processing of machine commands), (3) build (the physical manifestation of an object on the build plate) and (4) data analysis (processing and interpreting data collected during build). Note, data analysis does not necessarily occur strictly after the build phase is completed, but may take place recurringly, *in-line* i.e. in between discrete build layers, with AM.

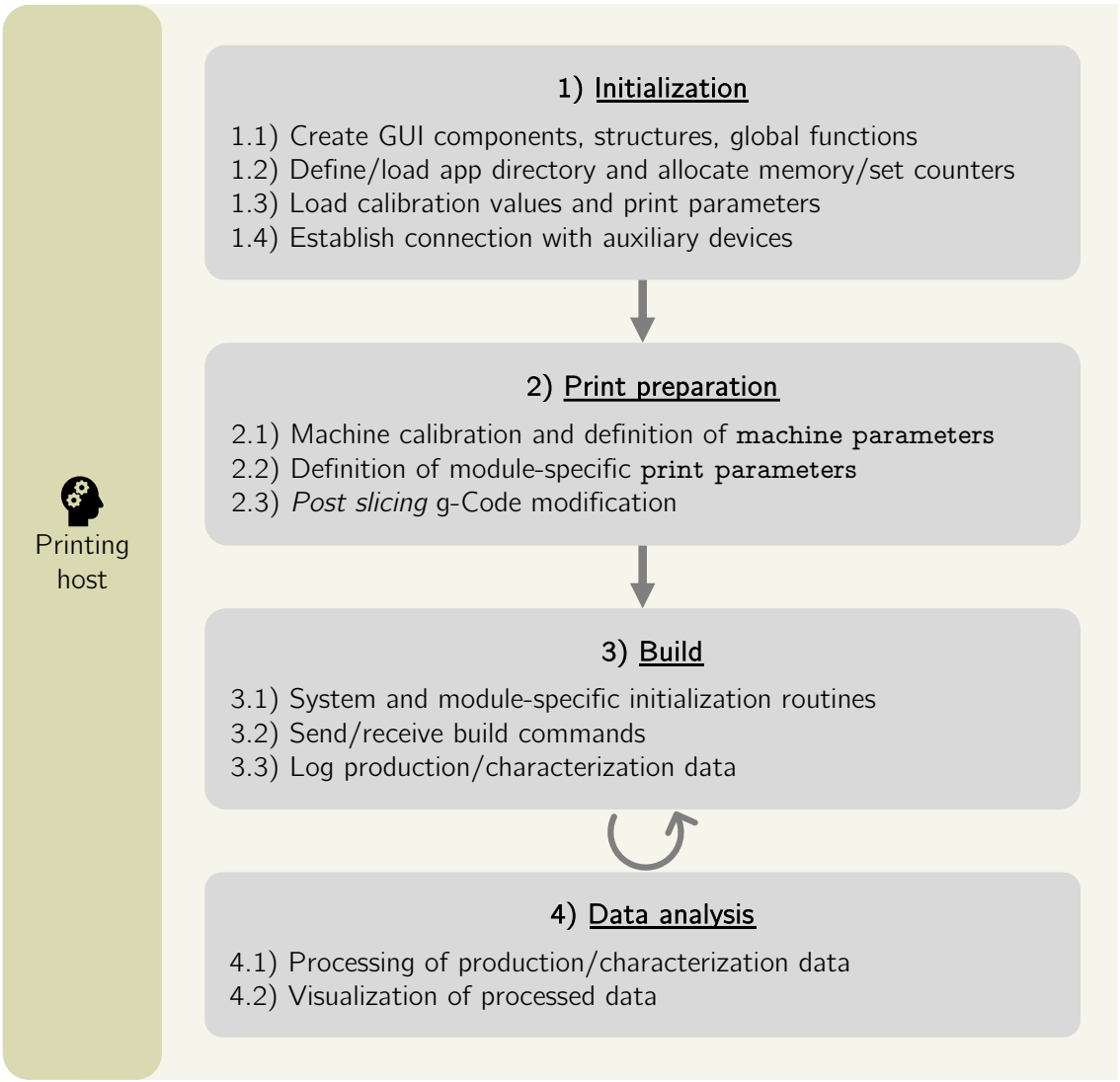

Figure 3.4.A: A flowdiagram outlining the chronology of the hybrid-AM app in operation: (1) app initialization, (2) print preparation, (3) build and (4) data analysis. Note: build and data analysis may occur simultaneously; app termination is not shown.

3.4.1 Initialization of the printing host

Launch Upon initializing the hybrid-AM app, a series of functions/commands were automatically executed (e.g. the `startupFcn`) to create GUI components (see Section 3.3.1), declaration of global callbacks and functions (see Section 3.3.2) and definition of data structures/properties (see Section 3.3.3). A directory (i.e. the location of *external* properties, see Figure 3.3.D) was specified by the user and, if available, information from previous sessions, such as calibration settings (`MultiAMParameters`) or print parameters (`PrintParameters`) was loaded. Memory was preallocated for data structures and variables (e.g. for production data logging) to prevent incremental resizing of variables and speed up subsequent operations.

Communication with ancillary devices The user could initialize and terminate serial communication with multiple ancillary devices in the hybrid-AM app GUI, for example with the hybrid-AM machine through a universal serial bus (USB) protocol or to scientific equipment, such as a VNA (see Part III), using virtual instrument software architecture (VISA) and a high-speed LAN instrument protocol (HiSLIP). All commands sent/received to/from ancillary devices were given a unique identifier (line number and timestamp) and were logged automatically for data analysis/debugging purposes. For critical, procedural commands, a confirmation of successful data transmission was required for the hybrid-AM app to proceed (e.g. by returning the command number as part of a *read receipt*).

3.4.2 Print preparation

Machine parameters The hybrid-AM machine needed to be calibrated when the machine configuration was physically modified: the calibration process was guided in dedicated GUI tabs in the hybrid-AM app and considered: (1) the microelectronics system, (2) overarching mechanical systems and (3) functional modules. Step-by-step procedures for the calibration process are provided subsequently in Section 5.6. Paramaters relating to the overall machine calibration (e.g. the vertical, Z-axis offset [mm] of nozzles/tips) were stored in an *external* property `MultiAMParameters` (see Figure 3.3.D) as input for *post slicing* `g-Code` modifications (label 2.3 in Figure 3.4.A).

Print parameters The hybrid-AM app was comprised of *libraries* (both module specific and permanent) defining *print parameters* specifically related to the machine motions/tool paths (and not the overall configuration). Some of the permanent libraries available were: (a) interrupts and logs – allowed the user to configure debugging functionality; (b) replace extruders – facilitated renaming extruder declarations in the `g-Code` (e.g. to call a tool change routine between multiple parts on the same layer); (c) drying time – for inserting pauses between tool changes; and (d) tool change – to identify tool specific parameters

when switching from idle to active (e.g. retraction distances). Some of the module specific libraries used in Part III of this thesis included: (e) split ring resonator (SRR) – defined meshing parameters for in-line characteriztion; and (f) SRR autotune – defined the scope of an automatic bed-levelling tool. All of the parameters specified in the GUI of the hybrid-AM app were stored in an *external* property `PrintParameters` (see Figure 3.3.D) as input for the *post slicing* `g-Code` modifications (see label 2.3 in Figure 3.4.A).

Post slicing g-Code modifications The *sliced* `g-Code` (from step 5.1 in the hybrid-AM workflow, see Figure 2.3.A) provided the general sequence of machine commands, and was modified/amended automatically by the app to reflect the machine parameters (`MultiAMParameters`) and print parameters (`PrintParameters`). This additional, *post slicing* step was necessary to implement the additional, unconventional functionality of the hybrid-AM machine, not supported by traditional slicing software (e.g. *in-line* characterization). The modifications (often to $> 10,000$ lines of `g-Code`) were automated within the hybrid-AM app: an overview of the steps entailed is provided in Table 3.4.A. The process followed: (1) definition/loading of parameters (`MultiAMParameters` and `PrintParameters`), (2) loading/importing of the sliced `g-Code`, (3) automatic extraction of metadata (e.g. extrusion speeds specified in the slicing software), (4) modification to incorporate additional functionality of the hybrid-AM machine, and (5) saving of the *modified* `g-Code` ready for execution. The modified `g-Code` included *flags* identifying to which serial object (e.g. the hybrid-AM machine or a VNA) each command/query should be sent to/received from.

3.4.3 During build

Initialization Prior to *building* a part, the hybrid-AM app orchestrated an initialization routine dependent on the hybrid-AM machine configuration: (1) preheating of relevant system components (e.g. heated bed and extruder nozzles), (2) *homing* of the gantry (to determine a reference position for subsequent moves), and (3) module specific initialization routines (e.g. priming of FFF nozzles or purging of DIW nozzles). Upon re-starting a paused print, a subset of the initialization routine was repeated.

Send/receive commands The hybrid-AM app thereafter sequentially followed the *modified g-Code* from Section 3.4.2, sending and receiving commands/queries to/from ancillary devices (e.g. the hybrid-AM machine or VNA). All commands were logged and received unique numbers for traceability and debugging purposes: one associated to its position in relation to the overall progress/`g-Code`, and another in relation to the chronology within the serial communication (the first line in a communication protocol was not necessarily the first line of the overall `g-Code` e.g. to account for initialization routines).

Step	Description
1) Define/load variables	identify *search strings* (keywords to recognize special actions e.g. layer/tool change)
	load hybrid-AM machine calibration values (i.e. `MultiAMParameters`)
	extract module specific parameters from the GUI (i.e. `PrintParameters`)
2) Load g-Code	locate g-Code file in directory (pop-up window if multiple files exist)
	load g-Code file into local workspace and convert into compatible data type
	screen g-Code to remove unknown/invalid commands (see Table 4.3.B)
	rename tool declarations to allow for multiple parts on a single layer
3) Extract metadata	extract slicing parameters from g-Code (i.e. amend `PrintParameters`)
	identify the location (command numbers) of layer and tool changes in g-Code
4) Modify g-Code	amend tool initialization routine (e.g. purge DIW tips or prime FFF extruders)
	amend layer change routines to account for machine calibration
	insert drying times between tool changes as specified
	amend tool change routines (e.g. drop and re-*home* build plate)
	insert g-Code interrupts and pause-ability for debugging purposes
	insert other module specific functionality
5) Save g-Code	export a copy of the modified g-Code to the identified directory for future reference

Table 3.4.A: The steps involved in automatically modifiying machine commands (i.e. the g-Code from slicing software) to incorporate the additional, unconventional functionality of the hybrid-AM machine.

Dynamic buffering Building highly resolved features required frequent machine commands (multiple per second). To allow for some latency in communication, the firmware and associated communications protocol allowed for a predefined buffer of commands to be sent. However, this systematically induced a *lag* between when a command is sent and actually executed. The implementation of *dynamic buffering* addressed this issue by altering the buffer size to match needs, e.g. during in-line measurements, where synchronizing machine location and readings is critical, the buffer could be reduced to a single command to ensure the printing host knows at which stage of execution the machine is. For printing highly resolved features, the buffer size was increased sufficiently to enable smooth, non-stoccato operation. This was achieved by automatically including action-less *pause & wait* commands (denoted by `M400` in the g-Code/firmware) where applicable.

Log Throughout build, all communication with ancillary devices was logged in an *internal* property (`Log`, see Figure 3.3.D). The commands themselves, a unique line number and timestamps indicating when a command was sent to, received by and executed by (where applicable) an ancillary device was recorded. Commands were visualized in verbose, human interpretable code in the GUI (see Figure 3.3.B), and saved *externally* when a hybrid-AM app session was terminated.

3.4.4 Data analysis

Application-dependent The extent of data analysis conducted throughout build depended on the application and desired functionality. In principle, the architecture of the hybrid-AM app allowed for advanced, in-line data analysis (within *MATLAB*), and could in principle facilitate *reactive* manufacturing. Advanced, in this context, refers to the ability to draw on information from multiple ancillary devices in real-time (e.g. raw data from sensors or pre-processed data from a VNA) while being able to use the computing power of a printing host computer as opposed to being limited to the microcontrollers on microelectronics systems. A proof-of-concept for advanced, *in-line* data analysis is explored in detail in Part III of this thesis.

3.5 Summary of the printing host

Functionality The hybrid-AM app provided a novel approach for host-based printing, specifically designed for hybrid-AM processes. Ultimately, the hybrid-AM app sent, received and logged all digital commands related to the hybrid-AM system and provided a user-friendly, centralized platform for the user/engineer to interact with the system.

Novelty Some of the main, novel ideas implemented in the hybrid-AM app included: (a) the modular, extensibile architecture – unlike conventional printing hosts, the hybrid-AM app reflects the modularity and extensibility of hybrid-AM systems, provides an open *back-end*, and the app architecture was designed specifically for easy modification/upgrades; (b) advanced pre-processing capabilities – implementation of advanced machine control which is currently not provided by conventional slicing engines/printing hosts (e.g. *smart* tool-change routines, insertion of *drying times* when transitioning from liquid to solid AM and support for an arbitrary number of functional modules); (c) simultaneous communication – support for multiple machines/devices to run side-by-side to, for example, facilitate real-time data collection during AM, including *dynamic buffering* to ensure appropriate synchronization of all devices; and (d) advanced *in-line* data analysis – being able to process and visualize large amounts of production and characterization data in real-time i.e. during manufacture.

Future work Further development of the hybrid-AM app may be considered, in particular relating to: (a) *reactive* manufacturing – finding a suitable PoC application to exploit the ability for advanced data analysis within the hybrid-AM app; (b) spatial control – integration of a closed, feedback control system for gantry motion, using linear encoders (already installed on hybrid-AM machine), and other functional modules (e.g. to allow the detection of filament breakages using a filament speed sensor); (c) libraries – development of further libraries to extend the functionality of the hybrid-AM app; (d) speed – improvements to the app architecture (e.g. which variables are passed into which functions) may further reduce latency in communication with ancillary devices; (e) remote access – integration with e.g. *octoprint* [103] to facilitate remote access of print jobs; (f) visualization – provision of a graphical preview of the printing process to detect tip-clashes and other avoidable defects (e.g. by integrating *CNviewer* [107]); (g) debugging – advance the set of rules that determines if a command line is *safe* to be sent to an ancillary device; and (h) streamlining – consider integrating the slicing process into the hybrid-AM app (i.e. unify steps 5 and 6 in Figure 2.3.A).

4

Modular microelectronics

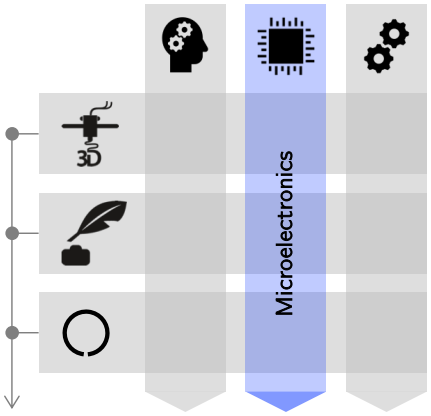

Figure 4.0.A: The microelectronics system within the hybrid-AM framework.

4.1 The microelectronics system in context 40
4.1.1 Purpose and functionality 40
4.1.2 Literature review 41
4.2 Design requirements and implementation 43
4.3 Architecture of the microelectronics system 45
4.3.1 The microcontrollers 47
4.3.2 Module specific breakout boards 49
4.3.3 Power & wiring 49
4.4 Prototyping and assembly 51
4.5 Summary of the microelectronics system 53

Section 4 outlines the design considerations for a modular microelectronics system. The system acted as electronic interface or 'bridge' between the virtual (i.e. software, see Section 3) and real components (i.e. physical machinery, see Section 5) within the hybrid-AM framework.

4.1 The microelectronics system in context

4.1.1 Purpose and functionality

The *microelectronics system* interpretted machine commands from the printing host (i.e. `g-Code` commands from the hybrid-AM app) and translated these into electrical signals to actuate the modules of the hybrid-AM machine (see Figure 2.3.A for context). This entailed: (a) interpreting the current machine status (e.g. position of actuators or temperature of components), (b) relaying the machine status to the printing host for logging purposes, (c) comparing the machine status to the desired state (i.e. the command), and (d) providing power/electrical signals to actuate motors/heaters/etc. accordingly. The decision framework necessary to conduct these actions was documented in a piece of software, the *firmware*, which operated on a microcontroller (described subsequently in Section 4.3.1) at the core of the microelectronics system.

Inputs The primary inputs to the microelectronics system were: (a) commands from the hybrid-AM app, communicated through a serial protocol (i.e. `g-Code` via USB), (b) power supply for low voltage (5 V for microelectronics and sensors) and high voltage (12 V for actuators, cooling etc.) electrical devices, (c) analog signals from the hybrid-AM machine (e.g. thermistor resistance/thermocouple voltage or switch circuitry), and (d) calibration parameters for the hybrid-AM machine.

Outputs The primary outputs of the microelectronics system were: (a) the supply of electrical signals (i.e. currents and voltages) to actuators/sensors/etc. in the hybrid-AM machine, (b) communication of status (i.e. the print log) to the hybrid-AM app, and (c) visual indication of the microelectronics system status through light emitting diodes (LEDs).

4.1.2 Literature review

Current microelectronics systems The maturity of microelectronics systems for AM systems has developed significantly in recent years: from basic one-off prototyping boards aimed at simply *getting the job done*, to sophisticated/integrated and powerful microelectronics solutions with ever increasing and even modular functionality [108]. The marketplace is competitive, with frequent innovations and new approaches being demanded by a quickly moving, tech savvy customer base. The microelectronics system can principally be split into: (1) the *control board* or hardware, and (2) the *firmware*.

Control boards Control boards are comprised of a central processor (e.g. 8-bit AVR or 32-bit ARM architecture) and a host of connectors, drivers and other electronic components. Control boards may differ based on: (a) the printer configuration (i.e. arrangement of motors, heaters etc.), (b) available communication ports (e.g. wireless, USB or ethernet), (c) the control board architecture (e.g. number of I/O pins, integrated or *breakout* drivers) and, (d) firmware compatibility. Popular control boards include: *Arduino Mega 2560* and *RAMPS* – a very common 8-bit prototyping board due to low cost [109]; *RAMBo v1.4* – integrated derivate of RAMPS, popular in commercial printers e.g. Prusa i3 MK II [110]; *Smoothieboard* – among the first 32-bit processor with proprietary firmware [111]; *Panucatt Azteeg X3 Pro* and *X5 GT* – based on smoothieboard, with built-in WiFi and high current capabilities [112]; *Duet WiFi* – expandable, allows 1/256 microstepping [113]; and *Revolve* – powerful 1 GHz microcontroller with linux support [114].

Firmware The firmware is permanent software programmed into the read-only memory of a microcontroller (on the control board) to interpret machine commands from the printing host. A variety of firmware exists, written in different programming languages (e.g. C++ or Python), compatible with a variety of hardware/control boards (e.g. 8-bit or 32-bit support), and providing different functionality (e.g. proportional-integral-derivative (PID) control, delta/cartesian/etc. support, type of implemented `g-Code` commands). Popular types of firmware optimized for AM include: *Sprinter* and *grbl* – simple firmware for single-processor microcontrollers [115, 116]; *Repetier* – very mature, compatible with 8-bit and 32-bit microcontrollers, benefits from a large user base and associated documentation/forums as well as a dedicated printing host (RepetierHost) [100]; *RepRap* – modular and wide range of functionality but only works on 32-bit ARM chips [117]; *Marlin* – support for an immense range of 8-bit boards and good for cartesian printers [118]; *Smoothieware* – easy to configure but lacks safety features of mature firmware, compatible with 32-bit control boards [111]; *Teacup* – fast/responsive, 8-bit to 64-bit compatible [119]; *Klipper* – experimental, kinematics pre-calculated [120]; and *Redeem* – primarily python based, all-in-one solution with integrated printing host [121].

Limitations of microelectronics systems Mature microelectronics systems designed specifically to account for the modularity and flexibility of hybrid-AM systems did not exist towards the end of 2017, when work for Part I of this thesis commenced. Some of the main limitations of the microelectronics systems remain valid today, in 2019, and include:

(a) **expandability** – microelectronics systems based primarily on printed circuit boards lack the flexibility for retrospective expansion and repair. Even newer, *modular* systems only provide room for expansion with predefined add-on boards by the supplier, significantly limiting the capability of such systems for novel R & D;

(b) **computational power** – the vast majority of microelectronics systems still run microcontrollers with an 8-bit architecture, intrinsically limiting the computational complexity of on-board calculations;

(c) **firmware** – for microelectronics systems that do make use of more powerful 32- or 64-bit microcontrollers, the corresponding firmware remains relatively immature (e.g. missing safety features) and cannot yet draw on the knowledge-transfer benefits of having a large user-base;

(d) **standardization** – the decentralized, open-source development of AM systems has led to countless combinations and permutations of electric devices, interfaces, firmware/bootloaders on control boards. Although superficially very similar, most microelectronics systems implement slightly different functionality or nomenclature, making it difficult to standardize slicing processes or other print-preparation steps; and

(e) **optimized for FFF** – the majority of open-source firmware is written exclusively for FFF. Although some attempts have been made to modify firmware for other AM techniques, e.g. SLA using a marlin based firmware [122], both the control parameters and structure/logic of firmware remains to be concerned with FFF only.

4.2 Design requirements and implementation

System requirements The primary aim of developing a modular microelectronics system was to provide a *distributed control network* [92], where modules may be added/-subtracted to reflect the machine configuration, instead of having to redesign an entire control board. Table 4.2.A provides a selection of principal design requirements considered throughout development, in particular those relating to: (a-c) architecture, i.e. the structure of the control board and firmware, as well as (k-j) the functionality, i.e. the type of capabilities the microelectronics system should have.

Microelectronics system requirements	
Architecture	(a) allow for easy, modular expansion of capabilities
	(b) use standard/conventional electrical components where possible
	(c) harness the available user-base knowledge for microelectronics systems
Function	(d) verify the receipt of a command line to the hybrid-AM app
	(e) compare the machine state with a command (g-Code)
	(f) provide power to actuate sensors/motors etc. on the hybrid-AM machine
	(g) allow for *microstepping* of bipolar stepper motors
	(h) allow for PID control of binary elements
	(i) allow automatic *homing* of the gantry
	(j) comply with all H&S lab requirements

Table 4.2.A: A selection of principal design requirements for the microelectronics system related to: (a-c) the architecture and (d-j) function.

Implementation A brief overview of how the microelectronics system design requirements were implemented is given below. References to subsequent sections providing more detail are provided, while labels (a-j) refer to Table 4.2.A.

Architecture The microelectronics system was constructed on solderless breadboards around a central microcontroller to (a) allow for easy, modular expansion of capabilities. Where possible, (b) standard/common electrical components for AM were used (e.g. K-type thermocouples or 1.8°/step bipolar stepper motors, refer to Table 4.3.A for a list of electrical devices used in the microelectronics system). A common, open-source firmware was used as basis for firmware development (see Section 4.3.1) to (c) harness ongoing developments of a large user-base [35].

Function The microelectronics system (d) sent a *read receipt* to the hybrid-AM app to acknowledge the successful transmission of a command. To decide what actions to make, the firmware (e) compared the machine state and command from the hybrid-AM app (see Section 4.3.1) and (f) provided appropriate actuation/power to the hybrid-AM machine using module-specific breakout boards (see Section 4.3.2). The breakout boards selected for motion control support (g) micro-stepping of bi-polar stepping motors to achieve smooth machine motion. MOSFET transistors were included to (h) facilitate PID control of binary elements (e.g. using pulse width modulation (PWM) for controlling the temperature of the heated build plate). Mechanical end-stop switches on all machine axes (i) facilitated automatic *homing* of the gantry. The microelectronics system was encased in an electronics box and all exposed wires were insulated to (j) comply with lab H&S requirements.

4.3 Architecture of the microelectronics system

Data/signal transfers Figure 4.3.A schematically illustrates the constituent components of the microelectronics system and how they interacted, namely: (1) the microcontroller, (2) module specific breakout boards and (3) power/wiring solutions. A series of inputs/outputs, i.e. data or signal transfers, dictated the operation of the microelectronics system: (i) serial communication between the printing host and microcontroller via a serial bus, (ii) instruction of the firmware, (iii) flagging/signalling of peripheral pins, (iv) communication with module specific breakout boards which were (v) powered on external circuitry (e.g. using operational amplifiers) which finally, (vi) actuated mechatronic components on the hybrid-AM machine.

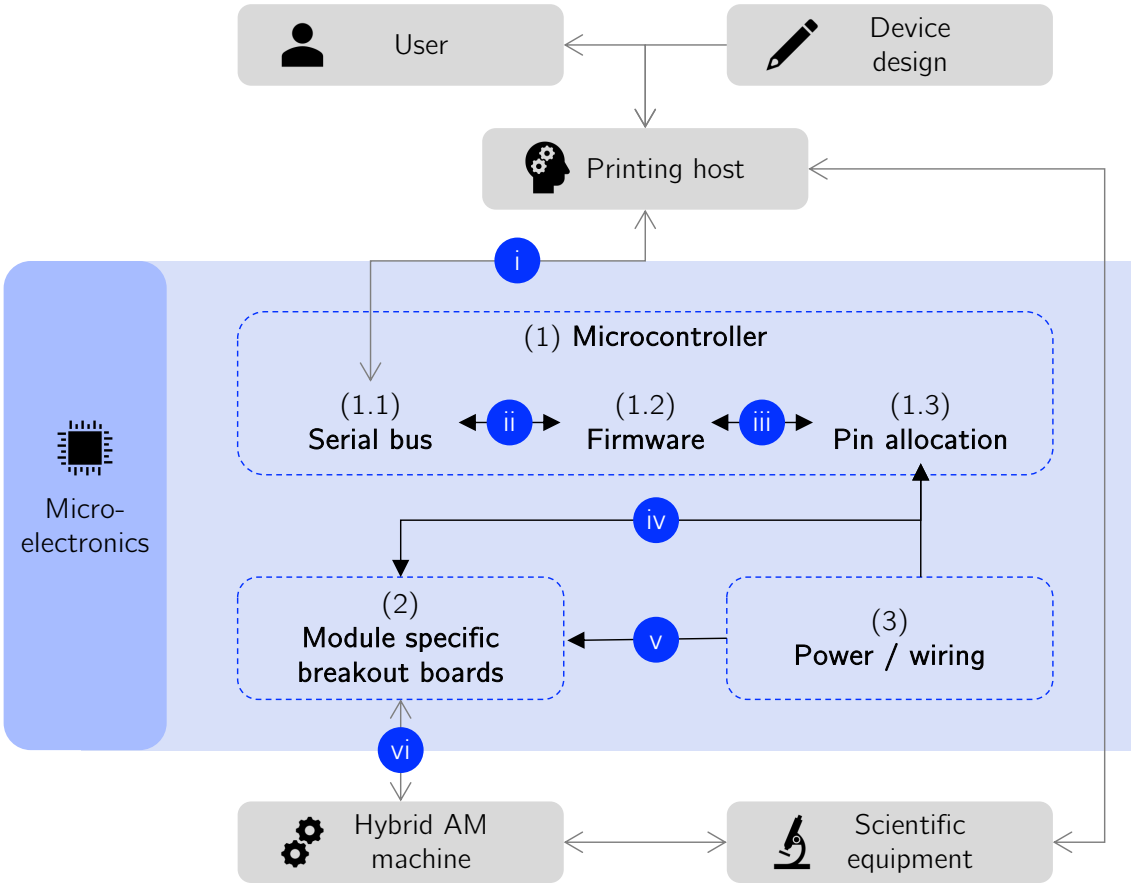

Figure 4.3.A: A flowchart of the microelectronics system and its constituent components: (1) the microcontroller, (2) module specific breakout boards and (3) power and wiring. Note, the labels (i-vi) are referred to in the text.

Constituent components Table 4.3.A outlines the purpose and examples of a selection of electronic components which were used in the microelectronics system.

	Component	Purpose	Example
(a)	Microcontroller	provide embedded logic	Arduino Mega 2560 Rev3
(b)	Stepper motor drivers	translate logic impulses to currents/voltages	Polulo A4988
(c)	Transistors	allow PWM of binary components	Pchero 25 A MOSFET
(d)	Bipolar stepper motor	actuation of gantry	RS Pro Nema 24 1.8° step
(e)	USB interface	allow serial communication with computer	Molex USB A to B
(f)	Voltage regulator	supply appropriate voltage to components	Texas Instruments 12 V
(g)	Linear encoder	feedback of system position[1]	Renishaw LM10 (1 µm)
(h)	Mechanical switch	detect machine limits and allow *homing*[2]	Omron D2F01T micro-switch
(i)	Power source (5 V)	power for logic circuitry	Weho S-300 W-5 V
(j)	Power source (12 V)	power for actuators, heating elements, etc.	Weho S-400 W-12 V
(k)	Silicon heated bed	heating of building plate	200 × 200 mm, 150 W-12 V
(l)	LED strips	lighting of overall system	Ustellar LED strips
(m)	LED	signal system status (e.g. machine busy)	DiCUNO red, blue, white
(n)	Resistors	filter and regulate currents/voltages	Various, e.g. 5 kΩ, 1 MΩ
(o)	Capacitors	filter and regulate currents/voltages	Various, e.g. 0.01 µF, 0.1 µF
(p)	Breadboard	prototyping base for motherboard	ELEGOO solderless
(q)	Electronics box	mechanical protection of microelectronics	Sourcingmap junction box
(r)	Wiring	electrical contact between components	0.5 to 13 A (insulated)
(s)	Terminal strips	simple rewiring/exchanging of modules	Saim 12 position dual row
(t)	Fans	cooling of microelectronics (e.g. motor drivers)	Xinyujie 12 V

Table 4.3.A: A selection of electronic components used in the microelectronics system, their purpose and examples.

[1] not implemented but pre-installed for potential future applications
[2] calibrating the coordinate system of the hybrid-AM machine

4.3.1 The microcontrollers

Overview Figure 4.3.B schematically depicts the microelectronics system and its central microcontroller (an 8-bit ATMega 2560), hard-wired to a smaller microcontroller (ATMega 16U2) which allowed serial communication with the hybrid-AM app. Both microcontrollers required the definiton of internal partitions (bootloader, firmware and application memory) and the allocation/declaration of peripheral pins for communication/actuation. The microcontrollers communicated to each other using transistor transistor logic (TTL).

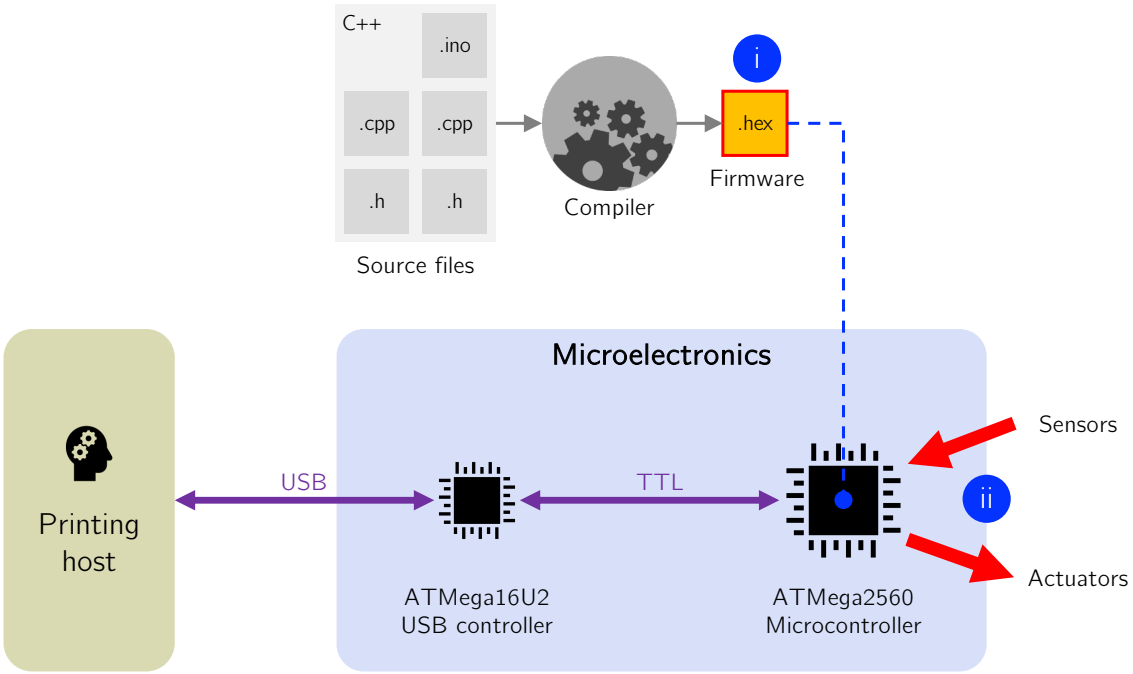

Figure 4.3.B: The (i) firmware programmed into the main microcontroller and a schematic of the (ii) data transfers between the printing host, within the microelectronics system and external sensors/actuators.

Repetier firmware The main firmware was adapted from Repetier v0.92.9 (GNU public license, open-source) [100], written in C++ and compiled using an Arduino integrated development environment (IDE) to generate a machine readable `.hex` file (label i in Figure 4.3.B). The firmware was installed on the central microcontroller (ATMega 2560) and configuration settings/variables were modified according to the hybrid-AM machine configuration. The decision framework defined in the firmware was responsible for interpreting the state of sensors (label ii in Figure 4.3.B), and actuate the relevant sub-systems to execute the command (`g-Code`) dictated by the printing host. Table 4.3.B provides a selection of common `g-Code` commands implemented in the firmware.

g-Code	Example	Description
G1	G1 X200 F100	gantry movement to coordinate X Y Z and/or extruder E at feedrate F[rate]
G4	G4 S1	wait/dwell for S[seconds] or P[milliseconds]
G28	G28 XY	home all or named axes
G92	G92 X10.00	set current position to coordinates given
M104	M104 S230 T2	set extruder target temp S[temperature] T[extruder]
M105	M105	return current temperatures
M112	M112	emergency stop
M114	M114	query current position XYZ
M116	M116	wait for all temperatures to be reached
M140	M140 S90	set bed target temperature
M400	M400	wait until previous command has been executed

Table 4.3.B: Examples of common `g-Code` commands implemented in Repetier-based firmware (based on NIST RS274NGC standard).

Firmware settings System-wide (e.g. relating to the gantry) and module-specific (e.g. relating to fabrication modules) firmware settings were optimized for use with the hybrid-AM machine (see Section 5), and principally related to: (a) motion – e.g. the number of motor *steps* (bipolar motors) required to move the gantry by 1 mm, the maximum travel speed [$\mathrm{mm\,s^{-1}}$], jerk [$\mathrm{mm\,s^{-1}}$] or acceleration [$\mathrm{mm\,s^{-1}}$] of mechanical components in the hybrid-AM machine; (b) configuration – e.g. the number and location/offset of extruders/tools, the I/O pin allocation and type of peripheral sensors or breakout boards, direction of motion/actuation and the endstop configuration; (c) safety – e.g. timeout and decoupling levels to report broken sensors when a specified temperature response has not been achieved; (d) heating – e.g. PID settings for heaters or maximum heating/cooling rates [$\mathrm{^{\circ}C\,s^{-1}}$] alongside the selection of appropriate heat managers and sensors (Semtec, Epcos100K, etc.); and (e) module-specific settings – e.g. for FFF modules the maximum extrusion speed [$\mathrm{mm\,s^{-1}}$], acceleration [$\mathrm{mm\,s^{-2}}$], extruder offset [mm], heating rate [$\mathrm{^{\circ}C\,s^{-1}}$] and steps/mm of filament or for DIW modules the number of steps/µL of ink dispensed, retraction distances [µL equivalent] etc.

Advance algorithm A rarely implemented *advance algorithm* (within the Repetier firmware [100]) was used to control the rate of extrusion in MEAM fabrication modules (e.g. FFF). The algorithm de-coupled the MEAM module motor speed from gantry motion, and instead, actuated the MEAM module to adjust its internal pressure. For example, when using DIW to print thick, viscous fluids, the algorithm instructed the DIW module to build up pressure within the dispensing syringe prior to gantry motion, to ensure ink

was being deposited as the gantry started moving. Similarly, pressure was reduced before the end of a print move (i.e. with foresight of succeeding commands, and hence the name *advance* algorithm), to allow time for the pressure within the barrel to equalize and ultimately the syringe to stop dispensing when the gantry came to a halt. The implementation of this algorithm was particularly important for enabling liquid-tight encapsulation of multi-phase devices in Part II, and to minimize the effect of *bleeding* edges when using large, experimental FFF nozzles ($\varnothing$ >1.0 mm) in Part III of this thesis.

4.3.2 Module specific breakout boards

Breakout boards are modular circuit boards which could be easily added/removed from the main control board, e.g. by means of pins or other temporary connectors (not soldered). For example, all motor controllers (i.e. the device that translated a logic impulse or *step* into actual current/voltages for the bipolar stepper motors) in the microelectronics system were breakout boards (e.g. Polulo A4988), to allow easy replacement in the case of failure as these are among the most common/predictable components that fail on AM machines. Other breakout boards included transistor assemblies for powering heaters (e.g. iS009 from PChero, China) and thermocouple amplifiers (e.g. AD8495 from Adafruit, USA).

4.3.3 Power & wiring

The software package *Eagle* was used to plan/organize wiring and power provisions related to the microelectronics system. All connections/terminals and connectors were given a unique identifier (examples provided in Appendix B.4). The design reflected the overall modularity of the hybrid-AM framework, e.g. a standardized 12 pin terminal block for communications to/from functional modules aided quick module exchanges (see Figure B.4.3). To reduce the effect of micro-electronic interference, a series of low-pass filters were included (e.g. to smooth signal tranmission for thermocouples). Figure 4.3.C provides an overview of the overall wiring schematic. Detailed schematics showing the pin allocation of the central microcontroller (label iii in Figure 4.3.C), gantry control (label viii) and an example for the wiring within a fabrication module (label ix) are given in Appendix B.4.

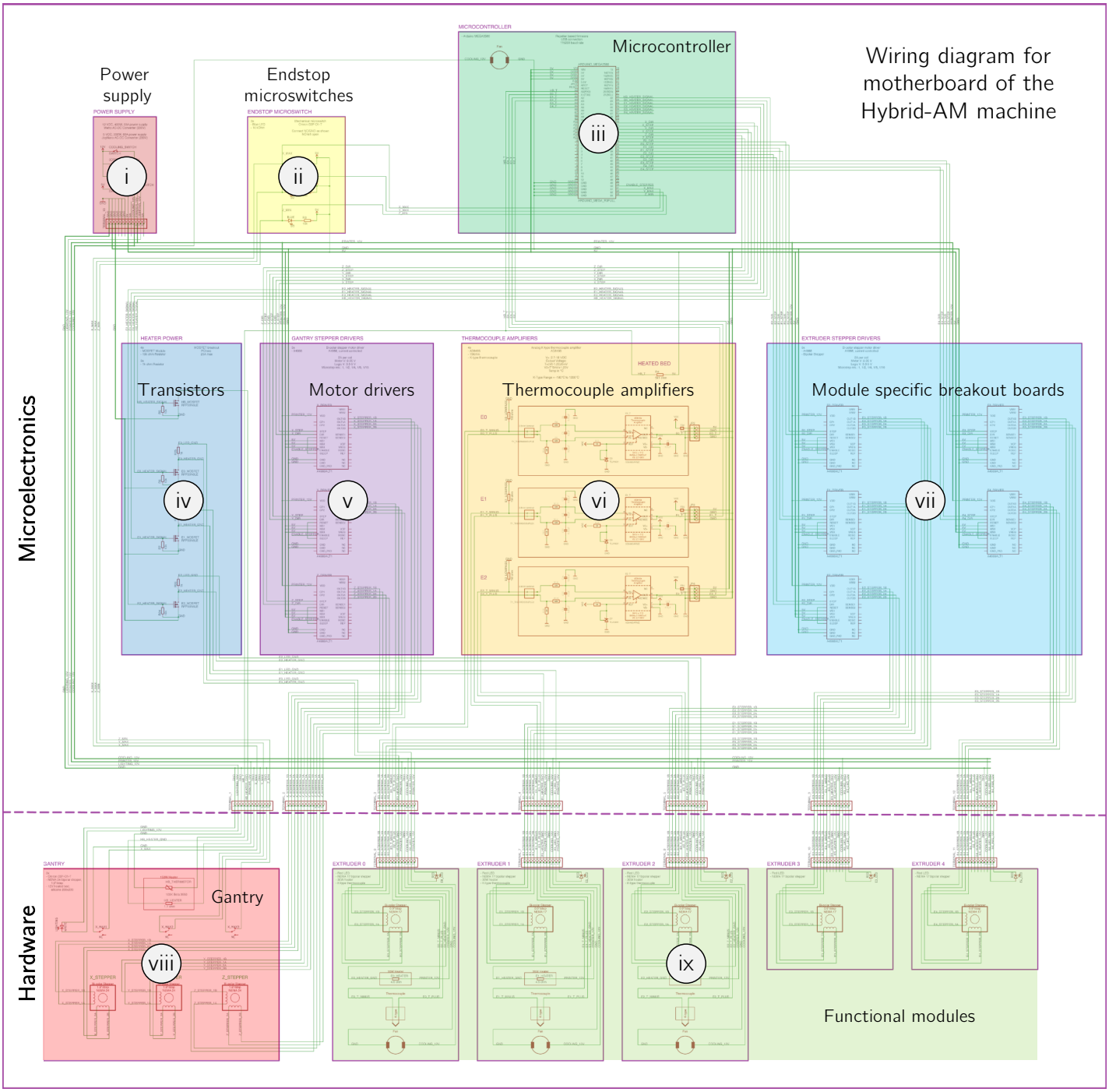

Figure 4.3.C: A overall wiring schematic for the microelectronics system showing: (i) the main power supply, (ii) endstop microswitches, (iii) the central microcontroller, (iv) MOSFET transistors for controlling heaters, (v) drivers for stepper motor, (vi) thermocouple amplifiers, (vii) module specific breakout boards, (viii) gantry and heated bed mechatronic elements, and (ix) other module-specific mechatronic elements.

4.4 Prototyping and assembly

Prototyping Figure 4.4.A shows a photograph of the *evolutionary* prototyping process (i.e. continually refined/rebuilt) as part of developing the microelectronics system. In particular the interplay between firmware and electronic devices was optimized at this stage, e.g. addressing issues associated to interference and filtering.

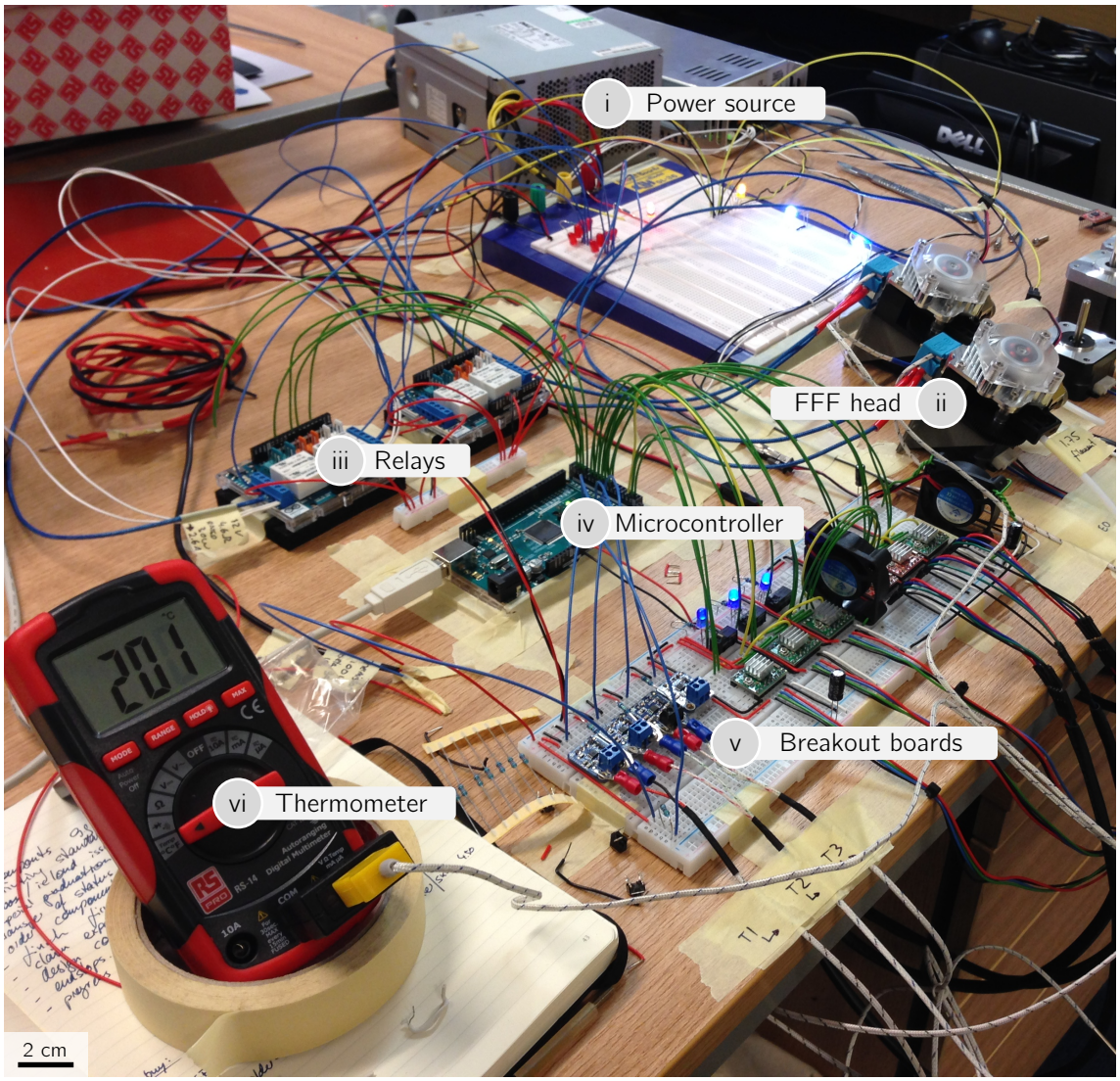

Figure 4.4.A: Photograph of the prototyping process for the microelectronics system showing: (i) 5 V and 12 V power supply, (ii) FFF modules, (iii) solid state relays for switching binary devices, (iv) the central microcontroller (Arduino Mega 2560 Rev3), (v) breakout boards on a breadboard, and (vi) a thermometer for calibrating thermocouples/thermistors.

Assembly Figure 4.4.B shows photographs of the final microelectronics system assembly on the hybrid-AM machine. The microelectronics system was connected to a host computer (label i in Figure 4.4.B) running the hybrid-AM app via USB. Terminal strips (label ii) provided a centralized interface for all wiring related to individual functional modules. The microelectronics system was assembled in a system enclosure (label iii) to provide cooling, power supplies and protection from the lab-environment.

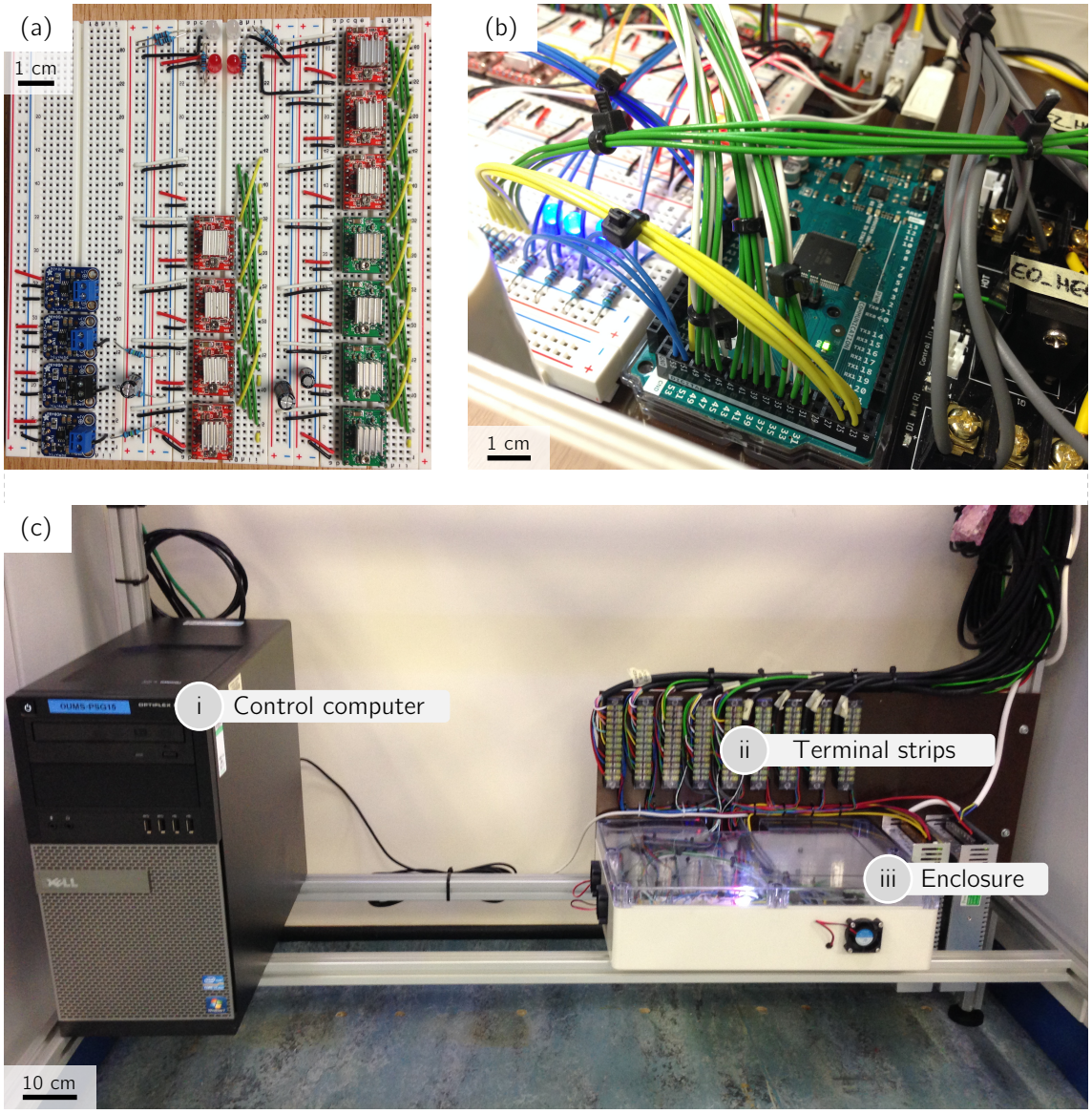

Figure 4.4.B: Photographs of the microelectronics system assembly showing: (a) breakout boards and drivers for functional modules, (b) internal wiring, and (c) the microelectronics system on the hybrid-AM machine frame: (i) the control computer running the hybrid-AM app, (ii) module-specific terminal strips and (iii) the microelectronics system enclosure

4.5 Summary of the microelectronics system

Functionality The microelectronics system provided a modular solution for translating commands (`g-Code`) into electrical signals to actuate the hybrid-AM machine. Ultimately, the microelectronics system acted as *bridge* between the hybrid-AM app (see Section 3) and the hybrid-AM machine (see Section 5).

Novelty Some of the main, novel ideas implemented in the microelectronics system included: (a) multi-tool support – the modular architecture of the microelectronics system allowed for an arbitrary amount and type of functional modules to be controlled by a central microcontroller, simply by adding more/or less breakout boards; (b) easy repairs – the breadboard based system allowed for easy repairs, i.e. the replacement of individual components as opposed to replacing the entire circuit board; and (c) advance algorithm – the implementation of the *advance algorithm* within the Repetier firmware allowed for superior control of viscous DIW.

Future work A series of upgrades may further improve the performance of the microelectronics system, including: (a) stepper drivers – an upgrade to stepper drivers with higher current carrying capabilities to facilitate faster travel times, e.g. trinamic stepper drivers such as TM2660 or DM566; (b) wireless communication protocol – to allow integration with *Octoprint* [103] and remote access/monitoring of prints; and (c) 32-bit architecture – replacement of the central microcontroller with a more powerful 32-bit chip and corresponding firmware.

Developments As mentioned in Section 4.1.2, microelectronics systems are developing at a fast pace. As such, the approach taken and described in this section would likely not coincide with one that would be taken today, in 2019. At the time of conceptualization (late 2017), virtually all commercially available microelectronics systems were running a central 8-bit microcontroller on a printed circuit board (i.e. difficult to expand functionality) and were limited to a maximum of 5 extruders. The desire to control more/an arbitrary amount of modules was ultimately the motivation to design a custom microelectronics system. Today, commercially available, modular microelectronics systems such as the Duet3D [113] would provide a good starting point and would likely form the basis of an equivalent microelectronics system.

5

Engineering design, manufacture & assembly

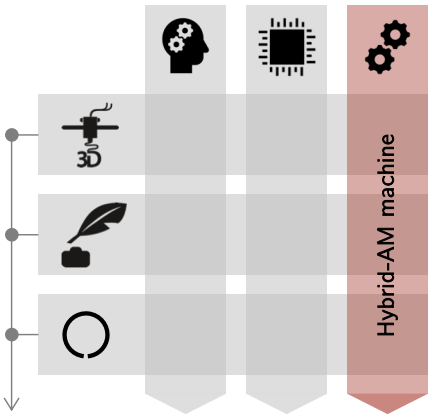

Figure 5.0.A: The hybrid-AM machine within the hybrid-AM framework.

5.1 Purpose and functionality of the hybrid-AM machine 56
5.2 Design requirements and implementation 56
5.3 Overview of the hybrid-AM machine 58
5.4 Engineering design 59
5.4.1 Frame 59
5.4.2 Gantry & build platform 59
5.4.3 Functional modules 62
5.5 Part manufacture and assembly 68
5.6 Calibration 72
5.7 Summary of the hybrid-AM machine functionality 73

Section 5 outlines the engineering design considerations for a hybrid-AM machine. The machine represented the physical/real domain within the hybrid-AM framework, and ultimately was where 3D parts were fabricated/characterized.

5.1 Purpose and functionality of the hybrid-AM machine

In the *hybrid-AM machine*, electrical signals from the *microelectronics system* (see Section 4) translated into physical actions to, for example, fabricate and/or characterize multi-material 3D parts. A *frame* acted as structural exoskeleton for all constituent sub-assemblies of the machine, namely: (a) the *gantry*, providing spatial-temporal control of (b), the *build plate*, which acted as substrate for hybrid-AM using (c), the *functional modules*, to deposit and/or characterize materials. The sub-assemblies are described in detail in Section 5.4.

Inputs The primary inputs to the hybrid-AM machine were: (a) electrical signals (i.e. currents and voltages) from the microelectronics system, and (b) material feedstock (e.g. polymer filament for FFF or functional inks for DIW).

Outputs The primary outputs of the hybrid-AM machine were: (a) *additively* manufactured, multi-material parts, and (b) analog signals (e.g. thermistor resitance or thermocouple voltage) to the microelectronics system.

5.2 Design requirements and implementation

Design requirements The hybrid-AM machine was designed and built based on experiences from a proof-of-concept, dual-extrusion prototype (see Appendix A) and the literature outlined in Section 1.3. Table 5.2.A provides a selection of principal design requirements considered throughout development, in particular those relating to: (a-e) the overall design, (f-j) spatial control, and (k, l) manufacturability of machine components. A brief overview of how the hybrid-AM machine design requirements were implemented is given below. References to subsequent sections, providing more detail are given, while labels (a-l) refer to Table 5.2.A.

Hybrid-AM machine requirements	
Design	(a) allow for easy, modular expansion of capabilities
	(b) provide support for > 5 functional modules
	(c) allow for various substrates for AM (e.g. kapton, glass or aluminum)
	(d) provide a heated build plate (20 to 130 °C) and reach desired temperature in <5 min
	(e) comply with all H&S lab requirements
Spatial control	(f) provide 3-axis spatial control with resolution <50 µm/step
	(g) provide an effective working envelope/building volume larger than $100 \times 100 \times 100$ mm
	(h) prevent backlash in spatial control mechanisms
	(i) allow simple machine and module calibration
	(j) facilitate automatic *homing* of the gantry
Manufacturability	(k) use standard/conventional mechanical components where possible
	(l) consider manufacturing capabilities at the workspace

Table 5.2.A: A selection of principal design requirements for the hybrid-AM machine.

Implementation A modifiable frame (a) allowed for easy, modular expansion of capabilities, and (b) provided support for 9 functional modules (see Section 5.4). An exchangeable build platform (c) allowed for various substrates for AM, and (d) was temperature controlled (20 to 150 °C). A polycarbonate (PC) shield around the frame and an emergency stop routine, among other things, were installed to (e) comply with H&S lab requirements (see Appendix B.1 for a risk assessment). The gantry (f) provided 3-axis spatial control (± 3.4 µm in X and Y and ± 1.5 µm in Z) for the build platform, (g) with an effective working volume of $200 \times 200 \times 175$ mm in the X, Y and Z axes respectively (see Figure B.3.4 in Appendix B.3 for axis definitions). Synchronous timing belts in the gantry system allowed for (h) precise control and provided minimal backlash. The hybrid-AM app (see Section 3) guided the user through (i) machine calibration steps, and (j) the gantry was *homed* automatically through inclusion of axis *end-stop* switches. Standard/conventional mechancial components were used to (k) facilitate interchangeability, while (l) the manufacturing capabilities within the group and department were considered (e.g. design for water-jet cutting) to ensure the majority of parts could be manufactured *in-house*.

5.3 Overview of the hybrid additive manufacturing machine

Figure 5.3.A schematically illustrates the constituent aspects of the hybrid-AM machine and how they interacted, namely: (1) the engineering design of the overall machine, (2) the manufacture and assembly of machine components and (3) the calibration thereof. The hybrid-AM machine operated/provided functionality through: (i) actuation of mechatronic components by the microelectronics system (see Section 4), and (ii) sensors delivering information to external scientific equipment.

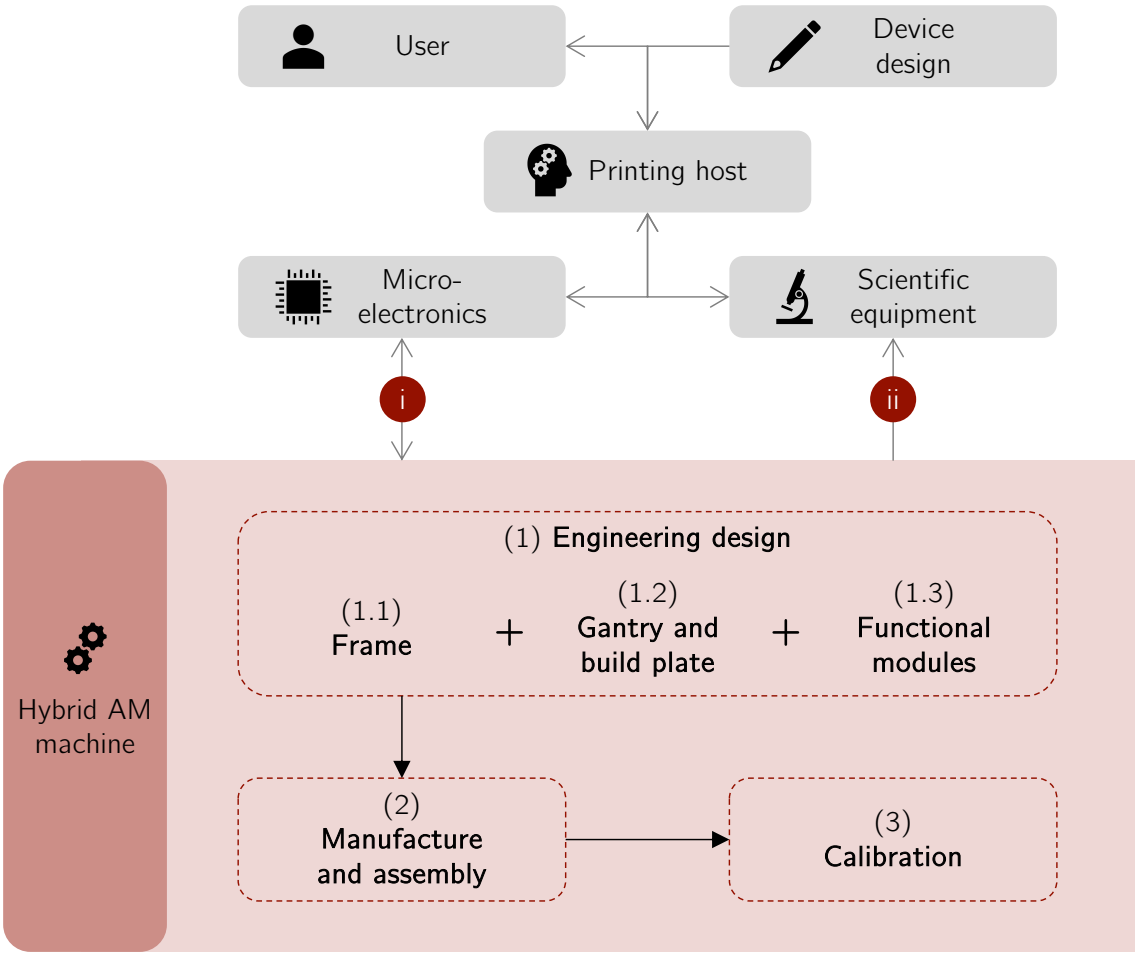

Figure 5.3.A: A flowchart of the hybrid-AM machine and constituent aspects: (1) the engineering design, (2) manufacture, assembly of machine components, and (3) calibration thereof. Note, the labels i-ii are referred to in the text.

5.4 Engineering design

General assembly Figure 5.4.A shows the general assembly of the hybrid-AM machine and its main sub-assemblies: (i) the *frame*, (ii) the *gantry & build plate* as well as (iii) *functional modules*. Figure 5.4.B shows how the *functional modules* were arranged with respect to/interacted with the *gantry & build plate*. It should be noted, that unlike most commercial MEAM machines, it was the build-plate that moves in this machine and not the nozzels/extrusion heads. All parts and assemblies of the hybrid-AM machine were designed in *SolidWorks 2017*. The assembly tree was structured in *tiers* e.g. where applicable a *tier 2* sub-assembly was comprised of *tier 3* sub-assemblies and/or *parts*. *Parts*, i.e. individual/single-material components, were considered to be the lowest/smallest element of the assembly tree. An index of all primary mechanical *parts* associated with the hybrid-AM machine is provided in the form of a *bill of materials (BOM)* in Appendix B.2. Engineering drawings are provided in Appendix B.3. In its current configuration, the hybrid-AM machine consisted of > 160 unique parts (>900 parts in total).

5.4.1 Frame

Exoskeleton The frame (label i in Figure 5.4.A) unobtrusively positioned all functional modules with sufficient positional accuracy while allowing for easy capability expansion. It acted as exoskeleton for the hybrid-AM machine and a transparent polycarbonate housing shielded the user from potential hazards. The frame was based on the *t-slot* aluminum extrusion system from Kanya, UK, and allowed height-adjustable working planes.

5.4.2 Gantry & build platform

Gantry The gantry (label iv in Figure 5.4.B) was a 3-axis, cartesian system based on profile rails with linear bearings which moved the build platform (label v). Bipolar stepper motors (NEMA 24, 1.8°/step) paired with interplanetary gear boxes (reduction ratio of 10:1) on the horizontal axes (X and Y) and a direct drive on the vertical axis (Z) achieved a resolution of 3.4 µm/step in X and Y and 1.5 µm/step in Z (see Figure B.3.4 for axis definitions). In its current configuration (i.e. with 1/16 microstepping), the gantry can move at a maximum speed of $30\,\mathrm{mm\,s^{-1}}$ over the entire working envelope of $750 \times 750 \times 200$ mm. High resolution linear magnetic encoders (1 µm, LM10 from Renishaw, UK) were installed for future positional feedback control and synchronous timing belts to minimize mechanical backlash.

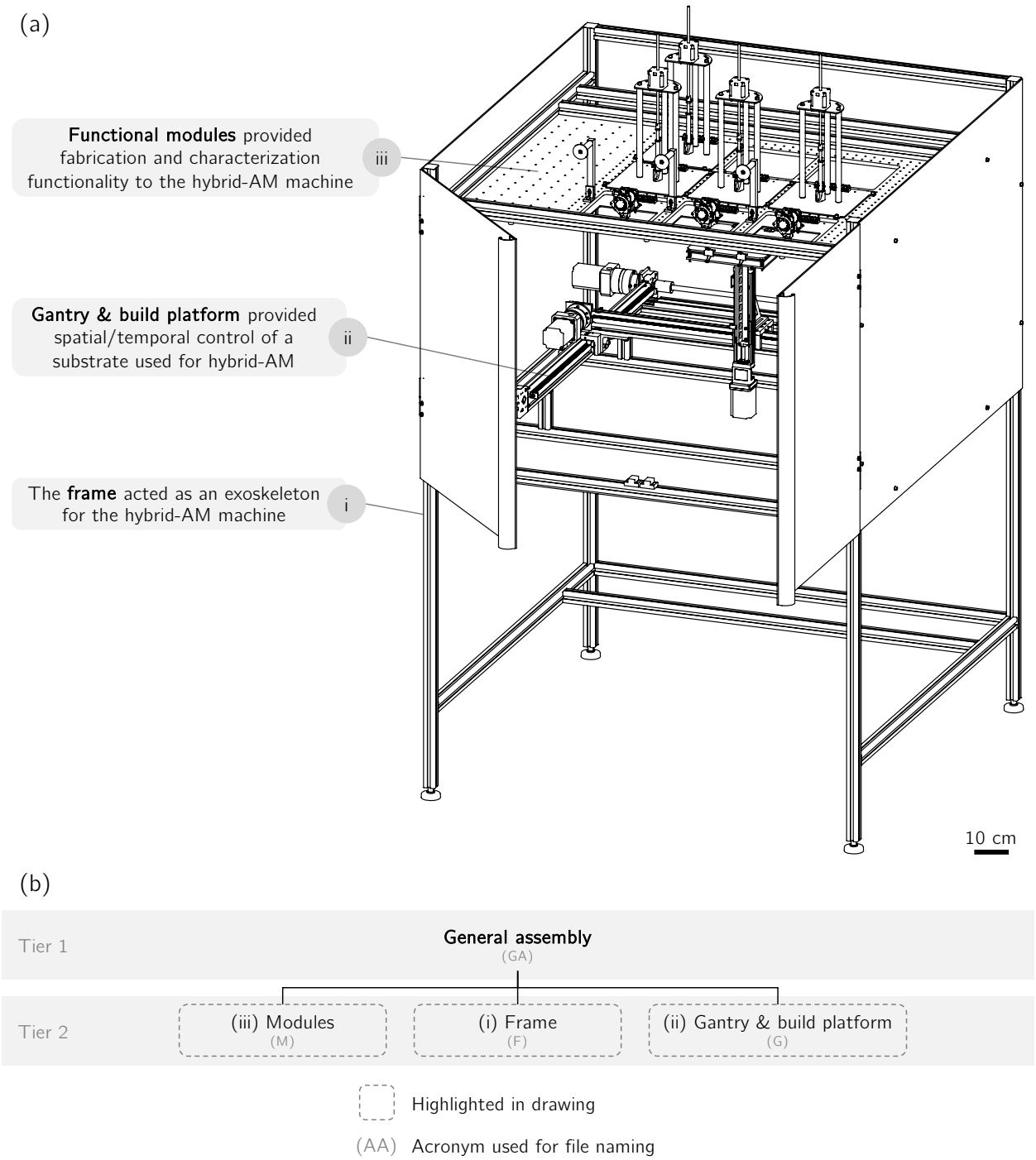

Figure 5.4.A: (a) A dimetric wireframe drawing of the hybrid-AM machine general assembly (tier 1) and (b) a hierarchical representation of constituent components: (i) the frame, (ii) the gantry & build platform and (iii) the functional modules.

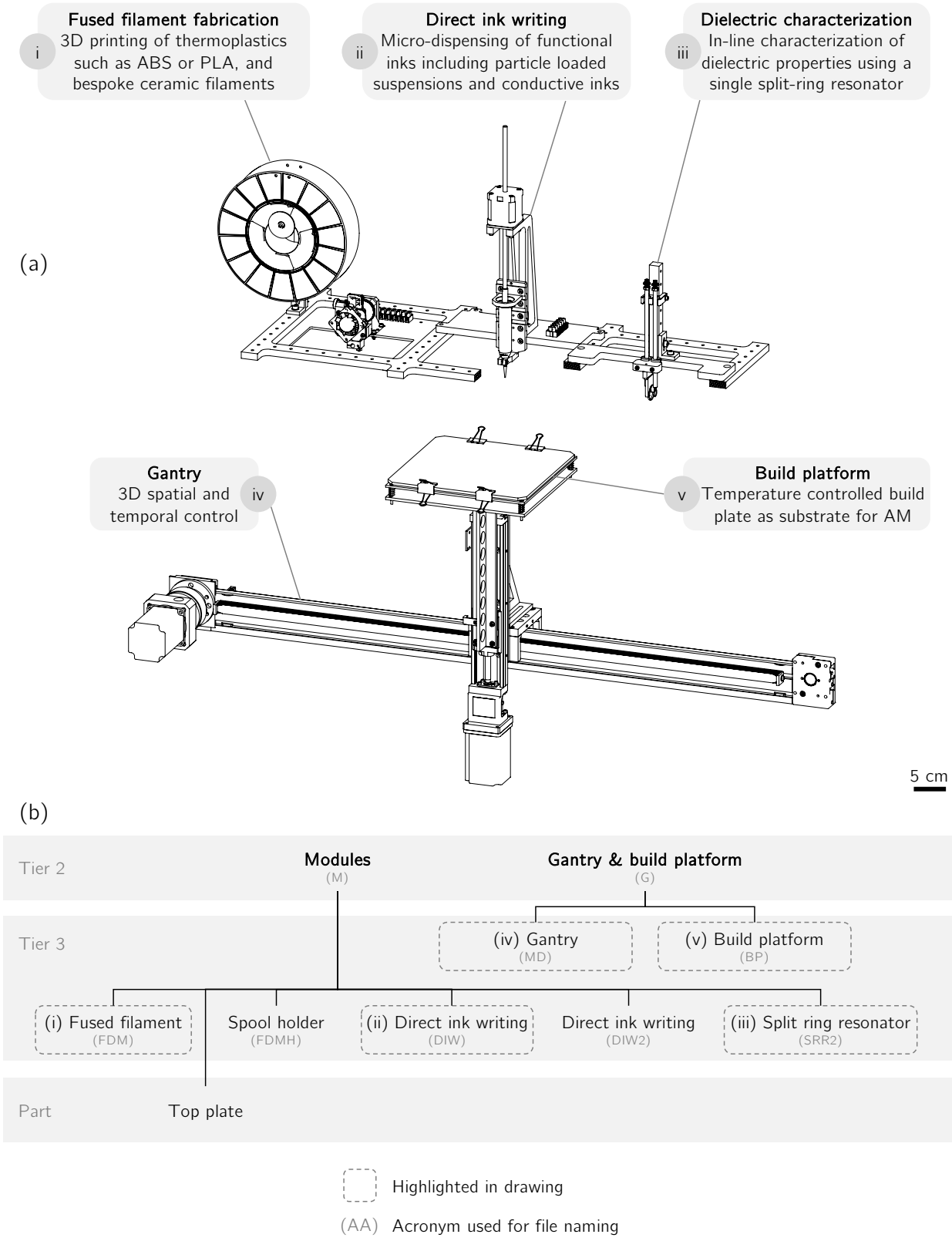

Figure 5.4.B: (a) A dimetric wireframe drawing of selected sub-assemblies (tier 3): (i) FFF, (ii) DIW, (iii) dielectric characterization, (iv) the gantry, (v) the build platform; and (b) a hierarchical representation of the constituent components of the *Modules* and *Gantry & build platform* sub-assemblies (tier 2).

Build platform The build platform (label v in Figure 5.4.B) provided a $200 \times 200\,\text{mm}$ surface for fabrication. The build surface could be easily exchanged (e.g. borosilicate glass or aluminum). A silicon heated bed (150 W) with integrated thermistor (type 100K NTC 3950) controlled the temperature of the build surface (20 to 150 °C), and copper foil underneath the build surface provided electromagnetic shielding for the applications discussed in Part III of this thesis. The build surface was levelled manually using wing-nuts at all corners. The build platform was suspended on a central Z-axis cantilever, and the design was lightweighted and stiffened (i.e. large 2nd moment of area) to allow for higher frequency printing (*jerk* up to $5\,\text{mm}\,\text{s}^{-2}$).

5.4.3 Functional modules

In principle, the functionality of *modules* for the hybrid-AM machine was unrestricted, and as such, the following examples of fabrication and characterization modules are solely indicative. Each *module* was comprised of control, mechatronic and mechanical aspects, i.e. across all of the *system components* in the hybrid-AM framework (see Figure 5.4.C). For example, a fabrication module had: (a) a library of print-parameters in the hybrid-AM app, defining nozzle temperatures, extrusion speeds and other operational parameters; (b) a sub-microelectronics system with drivers/amplifiers for motors, thermocouples and other electronic devices; and (c) a physical/mechanical sub-assembly with motors, nozzles, fixtures etc. The mechanical design and basic operating principle of selected fabrication and characterization *modules* are discussed herafter. Details regarding the underlying physics and further, detailed insight into the operating principles/limitations of the modules, as well as demonstrations of their use, are described in Parts II and III. All functional modules fitted into all *locations* on the frame (see Figure B.3.9). Modules were referred to by the hybrid-AM app (and slicing software) based on their location: 0-8, addressed by calling e.g. `E4` for the module in position 4.

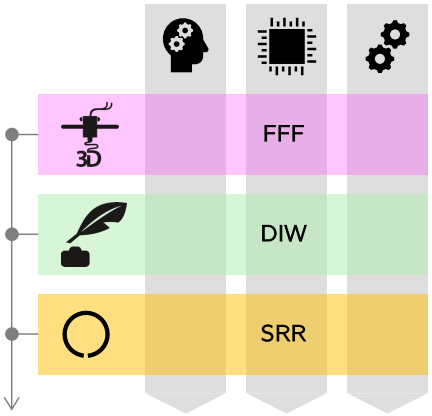

Figure 5.4.C: The functional modules within the hybrid-AM framework: fabrication (FFF and DIW) and characterization (SRR).

Fused filament fabrication Figure 5.4.D describes the FFF module and shows its sub-assembly tree. In FFF, a thermoplastic filament, such as amorphous acrylonitrile butadiene styrene (ABS) or semi-crystalline polylactic acid (PLA), is heated above its glass transition temperature in the *hot-end* i.e. *print-head* (180 to 250 °C) and pushed through a *nozzle* (⌀ 0.2 to 1.0 mm). The extrudate solidifies (through polymer crystallization and chain entanglement [123]) upon deposition onto the temperature controlled *build platform* (20 to 150 °C) to form 3D objects in a layer-by-layer manner. Principal benefits of FFF include: (a) an expanding palette of processable materials (e.g. commercial thermoplastics can be composited with functional materials [124–127]), (b) easy hybridization (through the absence of a vat or powder-bed in FFF), (c) relatively simple, fast and economical operation, (d) minimal heat input and post-processing required, and (e) good mechanical strength of printed parts [70]. Challenges related to FFF include: (a) low mass loading of functional filaments (composite functional filaments rarely exceed 30 vol% of active material [124]), (b) limited understanding of underlying processing science such as extrusion dynamics and bead spreading (wetting, rheology), (c) geometric restrictions (e.g. printing overhangs exceeding 30°), and (d) dimensional accuracy (thermal effects including shrinking and warpage are difficult to predict).

FFF process considerations and feedstock requirements FFF process parameters include print speed [mm s^{-1}], extrusion temperature [°C] and print path. Feedstock material properties include melt viscosity [Pa s] and elastic modulus [Pa]. Process and material parameters influence the quality (tolerance, pores, surface finish, distortion, etc.) of fabricated parts in a complex, and usually difficult to predict, manner [128–130]. Reviews of the FFF process include: design considerations and process models [128]; materials, dimensional accuracy and surface roughness [131]; as well as approaches to optimizing process parameters [129, 132–134]. FFF feedstock materials usually come in the form of a *filament* spool (⌀ 1.75 mm or 3.0 mm). The primary requirement for the filament is to allow for a mechanical feed mechanism to push the filament through the nozzle without breaking and to reduce the liklihood of nozzle clogging, over print periods typically of several hours.

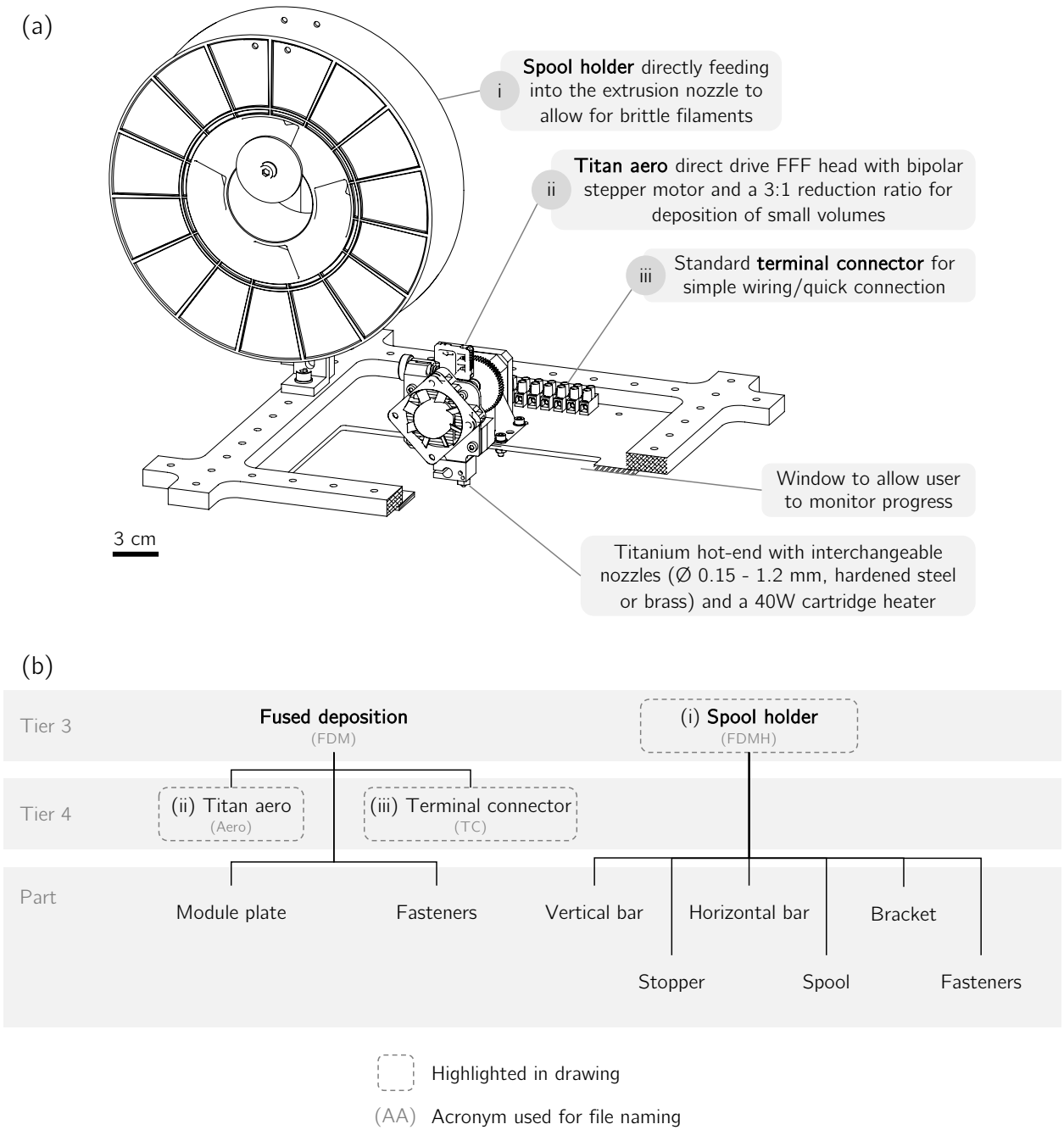

Figure 5.4.D: (a) A dimetric wireframe drawing of the FFF sub-assembly (tier 3) and (b) a hierarchical representation of constituent components.

Direct ink writing Figure 5.4.E shows the DIW module and its constituent components. In DIW (sometimes referred to as *robocasting*), a particle-loaded ink (e.g. concentrated colloidal/nano-particle suspension) is micro-dispensed using a syringe (electro-mechanical actuation through a lead-screw motor) onto the *build platform*. Principal benefits of DIW include: (a) inks with a high proportion of active/functional materials (e.g. through phase inversion, freeze gelation [135]), (b) direct deposition of liquid and/or gel materials, (c) flexible ink properties (relative to other AM technologies e.g. inkjet printing (IJP)), and (d) easy hybridization due the lack of a powder or vat bed. Challenges associated to DIW include: (a) post-processing is often required (e.g. sintering), (b) a complex and not well understood deposition/drying process, and (c) the requirement for stable suspensions/slurries which do not sediment/separate.

DIW process considerations and feedstock requirements DIW process parameters include: print speed [$\mathrm{mm\,s^{-1}}$], extrusion speed [$\mathrm{mL\,s^{-1}}$], nozzle diameter $\varnothing$ [mm] and nozzle geometry (tapered, step). Feedstock material properties include mass loading [vol%], curing parameters (thermal, UV, etc.) and rheological considerations (typically visco-elastic gels) such as viscosity [$\mathrm{mPa\,s}$] or yielding behaviour [Pa] [136]. Functional inks should allow for the formulation of stable suspensions without particle agglomoration or sedimentation. In particular, the ink-wetting properties with a variety the substrates needs to be considered (i.e. wetting substrates including paper invoke spreading of inks due to uncontrollable capillary forces whereas non-wetting substrates such as polyethylene terephthalate (PET) may lead to a *coffee-ring* effect) [137, 138].

Dielectric imaging Figure 5.4.F shows the dielectric imaging, or *SRR* module and its constituent components. The near field dielectric characterization module was developed based on a split ring resonator (SRR) probe [139]. The primary purpose of the module was to characterize the spatially varying (3D) dielectric properties of a printed device (e.g. for use in radio frequency (RF) optics) to provide insight on device manufacture, conformance to intended design and to facilitate an accelerated design cycle. Commercial, near-field magnetic field ($\vec{\mathbf{H}}$ field) probes (label i in Figure 5.4.F, RF-R 50-1 by Langer EMV, Germany) were connected to a VNA (controlled by the hybrid-AM app) and acted as emitters/receivers of electro-magnetic (EM) waves. A shift in resonance frequency of the SRR (label iii) was related to the dielectric permittivity of a printed sample (the operating principle is described in detail in Part III).

(a)

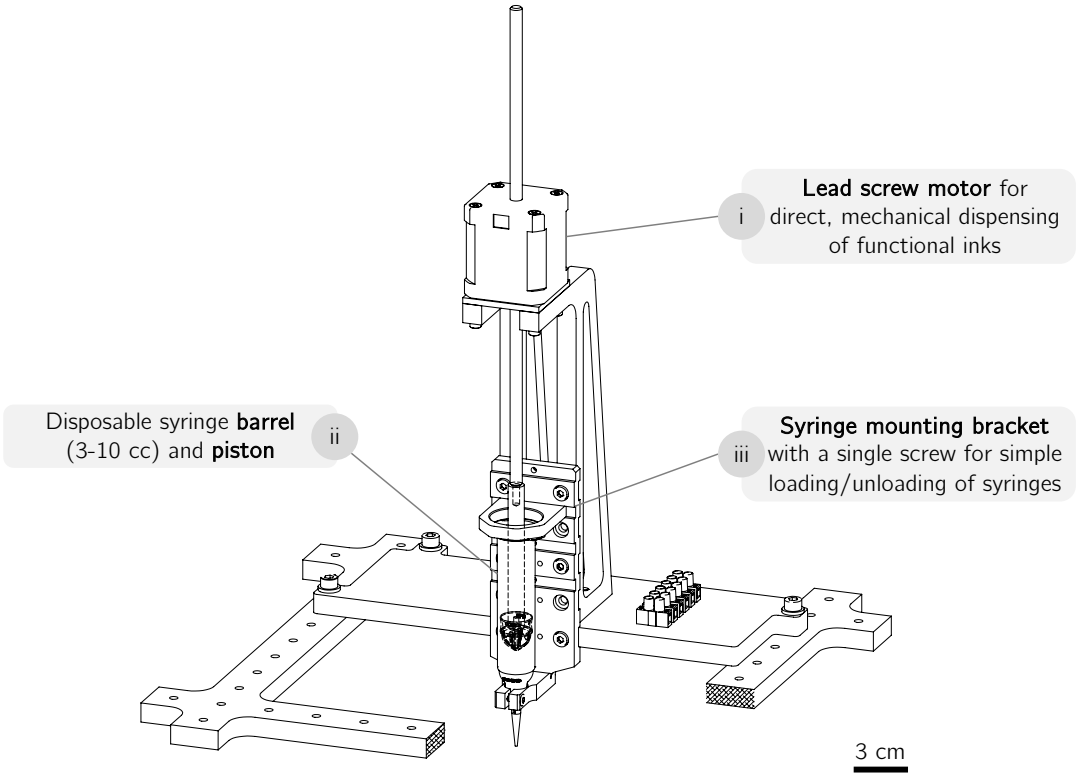

(b)

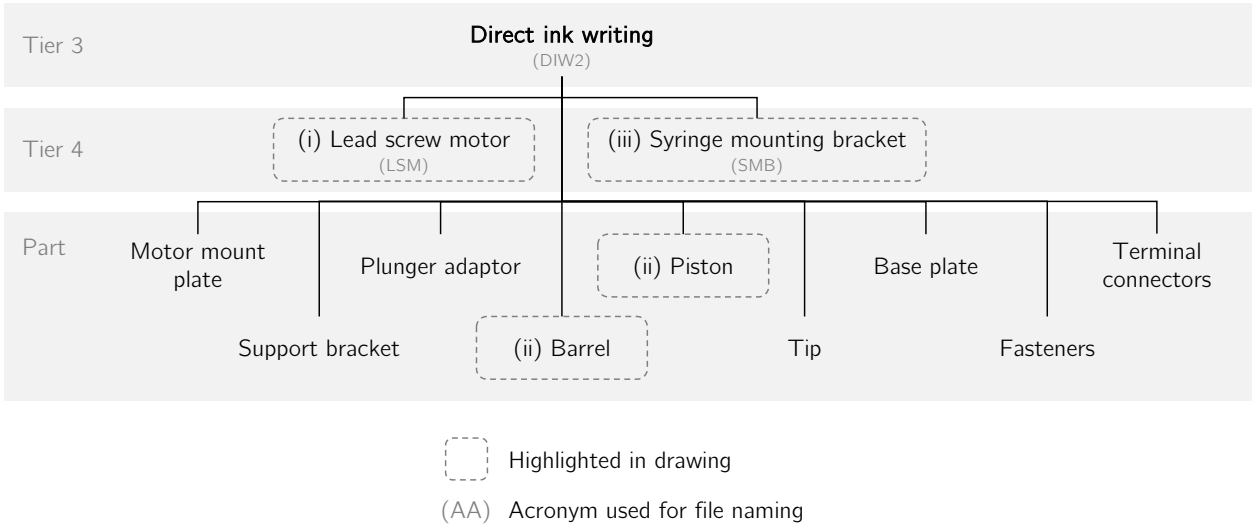

Figure 5.4.E: (a) A dimetric wireframe drawing of the DIW sub-assembly (tier 3) and (b) a hierarchical representation of constituent components.

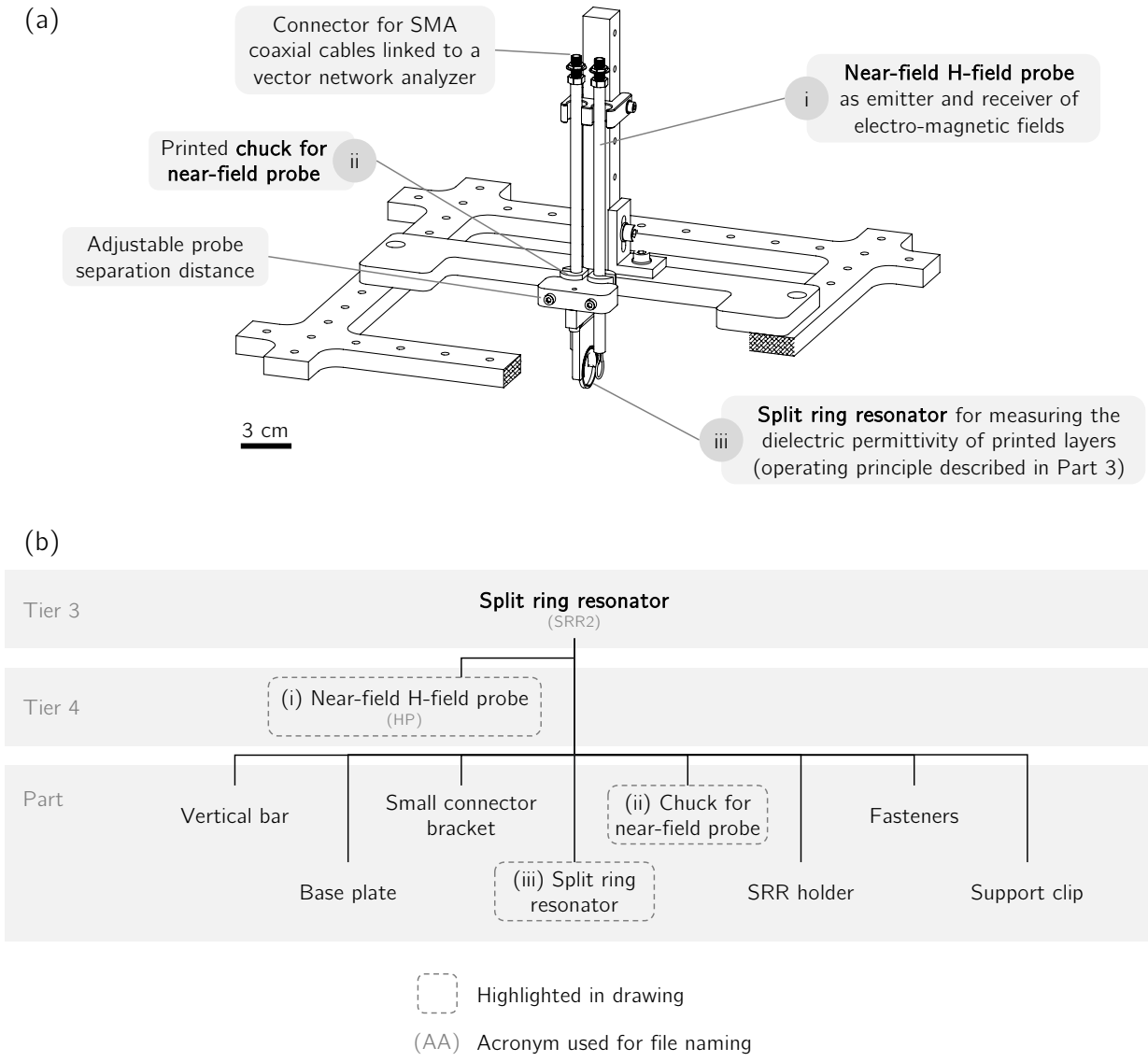

Figure 5.4.F: (a) A dimetric wireframe drawing of the SRR sub-assembly (tier 3) and (b) a hierarchical representation of constituent components.

5.5 Part manufacture and assembly

Manufacture Where possible, part manufacture was out-sourced and/or already complete/available parts were purchased. The remaining, bespoke parts of the hybrid-AM machine were fabricated *in-house* (within the Grant group). Figure 5.5.A shows photographs of the manufacturing process entailing: (a) definition of part specifications in the form of engineering drawings (see Appendix B.3 for examples), (b) *roughing* to remove the bulk of material (e.g. using a water-jet cutter), (c) finishing (e.g. tapped holes or specific surface finish requirements) and, (d) validation of component dimensions/features with the specifications from (a). Design for manufacture (DfM) was considered with respect to the available machines in our workshop: a water-jet cutter, FFF printer, CNC mill & lathe, power drills, and other conventional workshop tools. Suppliers for out-sourced parts included: E3D, UK (FFF related parts); Nordson EFD, USA (syringes and tips for DIW); Heason technology, UK (lead screw motors for the DIW module); Langer EMV, Germany (near-field H-field probes for the SRR module); Macron dynamics, USA (gantry); Taybroh Alloys, UK (cast aluminum plate for the frame); Kanya, UK (frame); and RS components, UK (electronic components and fasteners). A full list of suppliers/part names is provided in the BOM in Appendix B.2.

Assembly Figure 5.5.B shows photographs during the assembly of the hybrid-AM machine: (a) the empty frame and protective PC shielding, (b) the pre-assembled gantry as supplied from Macron Dynamics, and (c) a selection of *functional modules* mounted on the frame. Figure 5.5.C shows a photograph of the fully assembled hybrid-AM machine, representative of its configuration at the time of publication. The hybrid-AM machine is connected to a control computer (running the hybrid-AM app) and a VNA (ZNB 20 from Rohde & Schwarz, Germany). A variety of fabrication and characterization modules are mounted on the top plate of the machine.

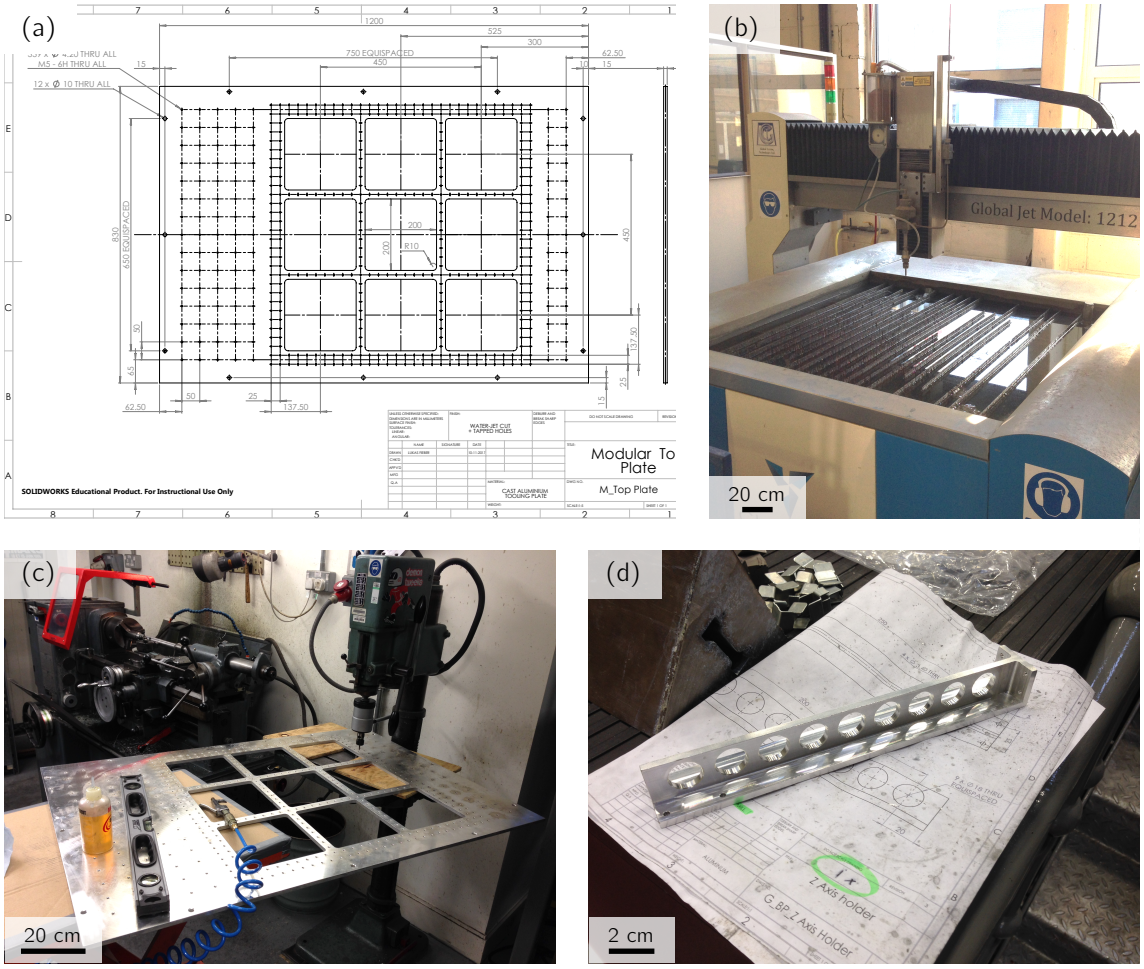

Figure 5.5.A: Photographs of the manufacturing process for in-house fabricated hybrid-AM machine parts: (a) engineering drawings (see Appendix B.3), (b) water-jet cutter for *roughing* (in particular for two dimensional (2D) parts), (c) detailing using power tools and (d) a finished, light-weight part.

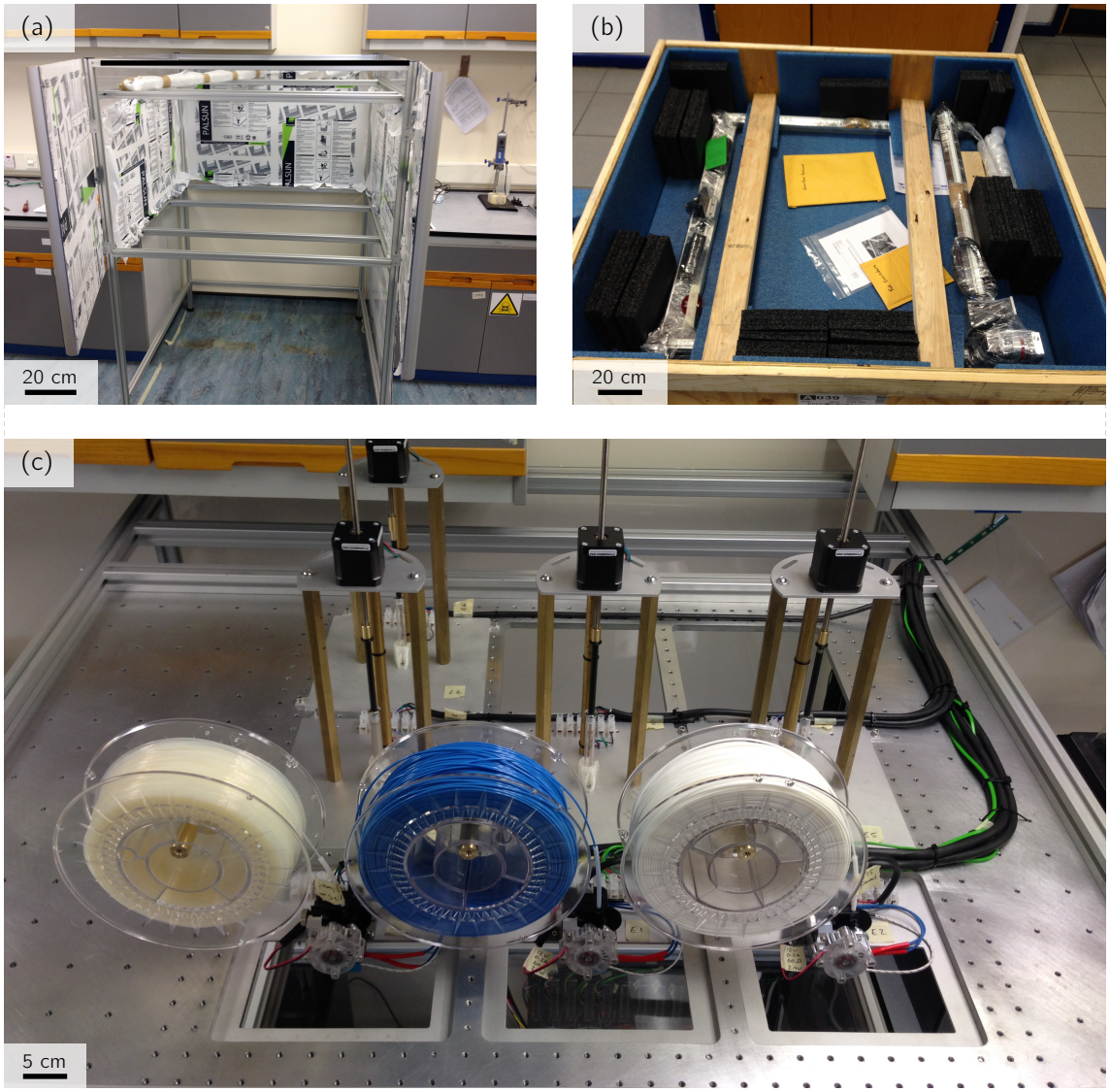

Figure 5.5.B: Photographs of the hybrid-AM machine during the assembly process: (a) sub-assembly of the frame and protective PC shield, (b) the pre-assembled gantry, and (c) a selection of fabrication modules mounted on the frame.

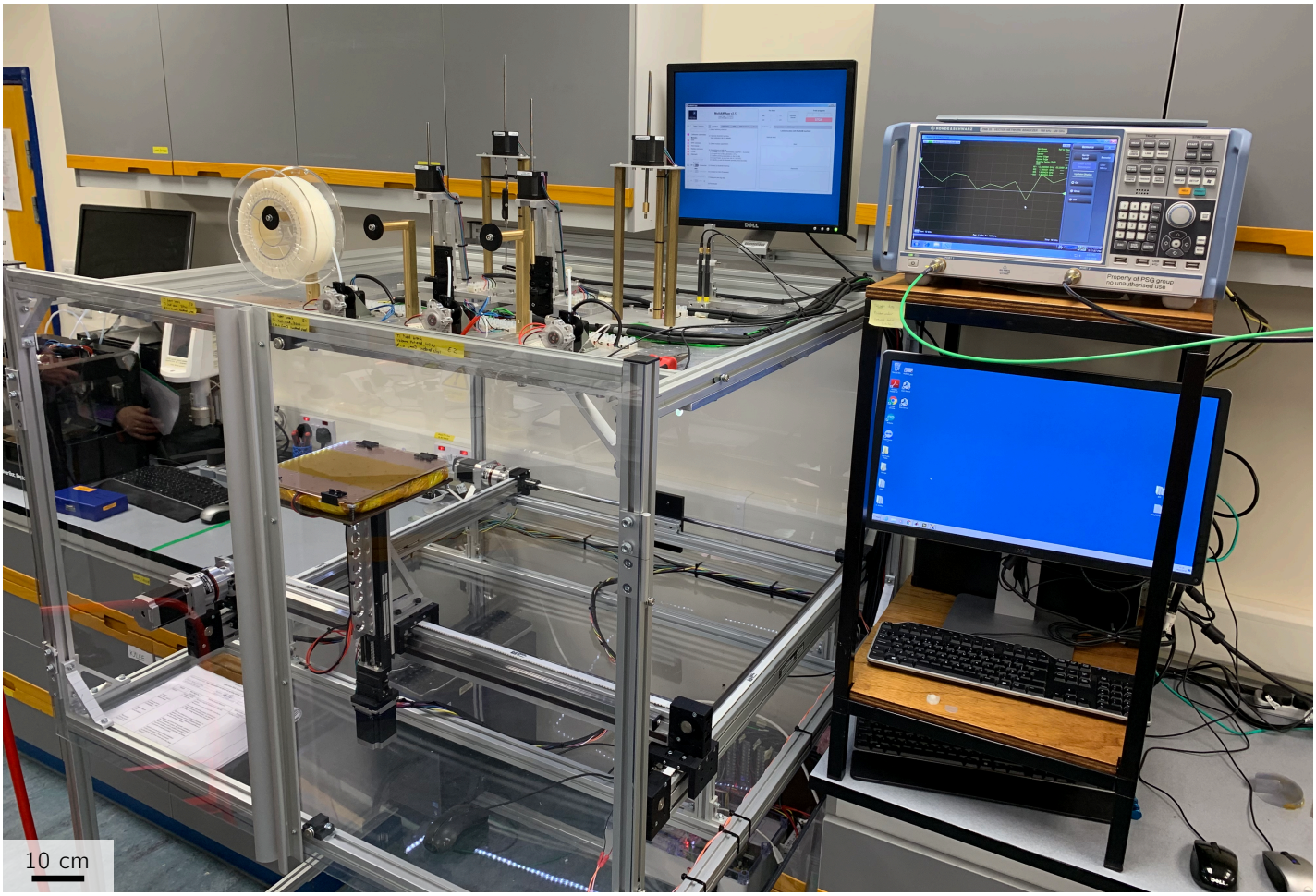

Figure 5.5.C: A photograph of the assembled hybrid-AM machine connected to a host computer (running the hybrid-AM app) and a vector network analyzer.

5.6 Calibration

Table 5.6.A provides an overview of the main calibration settings required for the hybrid-AM system. Individual parameters were stored in different locations, either: (i) the slicing engine (in a metadata file `PrintSettings.INO` in *Slic3r v1.3.0*); (ii) the hybrid-AM app (`MultiAMParameters` or `PrintParameters` entered in relevant tabs in the GUI, see Figure 3.3.D); or (iii) the firmware (in the `Configuration.h` file of the Repetier-based firmware, see Section 4.3.1). An exemplary, step-by-step instruction for evaluating the *tooling offsets* (in X, Y and Z [mm]) is provided in Appendix B.5.

	Slicing engine `PrintSettings.INO` in Slic3r	**Hybrid-AM app** `MultiAMparameters` and `PrintParameters` in MATLAB	**Firmware** `Configuration.h` in Repetier-based firmware
System	**Physical constraints** build plate dimensions [mm] and origin [mm] vibration limit [Hz] tool clearance [mm] **Start-up routine** additional g-Code	**Communication settings** ports, baud rate **Tool change routine** bed drop [mm] tool speed [mm s^{-1}] virtual-real tool replacement **Debugging** pause ability, debug console configuration	**Motion settings** max speed [mm s^{-1}] acceleration [mm s^{-2}] and jerk [mm s^{-2}] steps/mm **Safety features** decoupling [°C min^{-1}] endstop configuration **Wiring settings** pin allocation motor directions
Fabrication	**Standard print settings** infill/perimeter overlap [%] layer height [mm], etc. **Feedstock settings** tool/bed temp. [°C] **Tool configuration** retraction distances [mm] tool offset in X and Y [mm] number of virtual extruders	**Tooling parameters** Z offset [mm], tool configuration **Purge settings** tool speed [mm s^{-1}] retraction distances [mm]	**Heat manager** PID parameters sensor type **Module specific** steps/mm or steps/µL linear advance parameters
Charact-erization	**Meshing parameters** layer height distribution	**Tool settings** (X, Y and Z offsets [mm], dynamic range [GHz]) **Meshing parameters** scanning area [mm] XY frequency [mm] layer frequency Z drop [mm] number of readings	N/A

Table 5.6.A: An overview of the main calibration settings required for the hybrid-AM system relevant to: the overall system, fabrication and characterization modules and stored in the slicing engine, hybrid-AM app or the microelectronics system firmware.

5.7 Summary of the hybrid-AM machine functionality

Work achieved The hybrid-AM machine provided a modular approach for implementing multi-material, multi-technology (MMMT) manufacture at lab-scale. Ultimately, the hybrid-AM machine was where multi-material parts were built. The machine was designed from the ground up, in tandem with the printing host from Section 3 and the microelectronics system from Section 4.

Novelty Some of the main, novel ideas implemented in the hybrid-AM machine included: (a) modular, multi-tool support – a modular design with standardized inserts and interfaces for up to 9 complementary *functional modules* working side-by-side; and (b) moving build platform – unlike most available AM systems, all of motion between tool tips/nozzles and the build platform was due to the build platform moving. This approach significantly simplified the calibration process when using > 2 nozzles, systematically prevented nozzle-clashes and allowed for more sensitive and heavy extrusion heads to be used/investigated. Futhermore, the stationary extrusion heads prevented unwanted oozing or dripping from nozzles/tips during rapid machine motion/jerk (since it was not the extrusion head that was moving/vibrating, but the build platform).

Impact & applications The modular, lab-scale hybrid-AM machine may be used to further investigate concepts relating to hybrid-AM, and be of direct use for further materials science and engineering research within the Grant group. The machine formed the basis/experimental set-up for the research presented and discussed in Parts II and III of this thesis.

Future work A series of upgrades may further expand/improve the functionality of the hybrid-AM machine, including: (a) redesigning the build platform – a stiffer, even lighter build platform would allow for more jerk and faster accelerations (without vibration) to further reduce printing times, and allow more complex/rapid so-called *retract on layer-change* printing moves to be investigated; (b) a more powerful heated bed – the integration of e.g. a 500 W heated bed from E3D, UK, would speed up the response time of the build platform for faster pre-heating, and potentially more complex drying cycles for liquid-DIW prints; (c) reinforcements in the frame – further stiffening of the frame would allow for higher frequency printing without vibration/ringing; and (d) functional modules – the development of more functional modules will expand the capabilities of the hybrid-AM machine.

6

Conclusions & outlook: Hybrid-AM

The prospect of *hybridizing* individual AM technologies (and their respective benefits) in so-called *hybrid-AM* processes promises to expand the already transformative impact AM is having on high-value manufacturing: from supply chain simplification through the unison of multiple manufacturing operations, to unprecedented control of the local spatially varying material properties within printed, multi-material parts.

Novelty of work achieved An extendable, modular manufacturing *framework* was established and a functioning lab-scale MMMT machine was constructed. The research involved the interplay between the real/physical and virtual/software domain of additive manufacturing. Only a few hybrid-AM systems have been reported specifically for R & D purposes, and to the author's best understanding, the modularity/reconfigurability across hardware, software and associated digital workflows is unprecedented in academia. While specific, novel ideas which were implemented in constituent sub-systems of the hybrid-AM machine were described throughout (e.g. advanced pre-processing capabilities and *dynamic buffering* for enhanced machine control), the critical development shown here lies in the modular interplay between hardware and software, facilitating significantly more advanced data analysis, insight and control of AM. The further impact of the work will only become apparent when applied to specific applications: which now follows in Parts II and III of this thesis.

Part II
Multi-phase additive manufacturing for energy storage applications

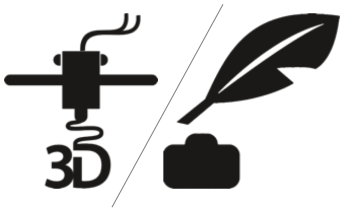

Summary

Additive manufacturing (AM) may offer a flexible, cost-effective approach to address conventional manufacturing limitations, such as time-consuming, high work-in-progress, multi-step assembly. In principle AM can also allow more novel geometric or even bespoke designs of structural and functional products. However, in terms of energy storage devices such as batteries and supercapacitors, the benefits of AM have not yet been explored to any significant extent. In Part II, multiple fabrication modules within the hybrid-AM system from Part I were used to fabricate complete energy storage devices (electro-chemical double layer capacitors, EDLCs) in a single, automated operation. The inherent flexibility of the hybrid-AM process provided an opportunity to address restrictions in geometric form factor associated with conventional planar supercapacitor manufacturing approaches. Functioning, ring-shaped EDLC devices were manufactured in a multi-material operation comprising symmetric activated carbon electrodes in a 1 M potassium hydroxide (KOH) electrolyte hydrogel. Gravimetric and areal electrode capacitances were $116.4 \pm 0.6\,\mathrm{F\,g^{-1}}$ and $599.2 \pm 3.0\,\mathrm{mF\,cm^{-2}}$ at $10\,\mathrm{mV\,s^{-1}}$, with a columbic efficiency of $99.6 \pm 0.4\,\%$ in the *as-printed* condition. These data compare sensibly with those in the literature. The work aims to accelerate progress towards monolithic integration of energy storage devices in product manufacture, offering an alternative fabrication process for applications with irregular volume/shape and mass-customization requirements.

7

Introduction: Energy storage

7.1 Capacitor technology 79
7.2 Electro-chemical double layer capacitors 82
7.3 The challenge of manufacturing EDLCs 86
7.4 The promise of AM for the manufacture of EDLCs 88
7.5 Objectives for Part II 91

7.1 Capacitor technology

Rising demand for electricity Ever-increasing demands in global energy needs ($>10 \times 10^{17}\,\mathrm{W\,h\,yr^{-1}}$, +2.1 % in 2017) have been met through the unsustainable exploitation of greenhouse gas emitting fossil fuels including oil, coal and gas (72 % of the annual increase and 81 % of the global energy consumption in 2017) [140, 141]. Meanwhile, electricity has become an indispensable form of energy, following the electrification of leading industry nations in the 1880's and then global industrialization. However, strengthening global environmental awareness and concern [142] mandates a radical rethink of how we generate, store and use electricity [143, 144]. Technological advancements, including photovoltaics and nuclear energy, aim to make electricity generation carbon-neutral [145, 146], whereas consumer electronics and ubiquitous digitization are providing us with more ways to consume electricity [147].

Capacitors To bridge both temporal and geographic *gaps* in electricity generation and consumption, various electro-chemical energy storage (EES) devices have been developed [148]. For applications with short charge/discharge times (ms to min) and long cycle-lives (>> 1000 cycles), capacitors have dominated. Capacitors are passive, two-terminal electrical devices that can store, filter and regulate electrical energy.

Types of capacitors Many types of capacitors have been developed since the original Leyden Jar in 1745 (see [149, 150] for a brief history of capacitors and supercapacitors). They are commonly classified by their: (a) internal electric field distribution (linear, asymmetric or localized), (b) size (geometric dimensions, total capacitance, or energy/power performance), (c) internal architecture (hybrid, symmetric or asymmetric), (d) primary charge storage mechanism (electrostatic, pseudocapacitive or intercalation pseudocapacitive), (e) design (coin-, wound- or pouch-cell, cylindrical or prismatic), or (f) a combination thereof (a-e). Table 7.1.A provides an overview of the main types of capacitors, a schematic of their internal electric potential distribution, their primary charge storage mechanism, specific examples of devices, the constituent components and common materials within, as well as an overview of the conventional, industrial manufacturing process to fabricate such devices.

Supercapacitors Of the available capacitor types, *supercapacitors* (sometimes referred to as *ultracapacitors*), have attracted significant attention, in particular in the pursuit of devices with simultaneously high-energy and high-power performance. Supercapacitors may provide up to 2-3 order higher energy densities than conventional electrolytic capacitors ($\sim 10^{-2}$ $\mathrm{W\,h\,kg^{-1}}$) and have power ($\sim 10^{2}$ $\mathrm{W\,kg^{-1}}$) and cycling performance ($> 10^{6}$ cycles) superior to ion-batteries [151]. The supercapacitor market has matured significantly recently, with developments including new and improved electrolytes [152], and nanostructured electroactive electrode materials [148, 153, 154]. The devices are used in applications such as regenerative braking in electric or hybrid vehicles, intermittency levelling in *smart grids*, and rapid transit rail or buses, all making use of their high power and reasonable energy density capabilities [150, 155, 156]. An overview of the performance of commercially available supercapacitors may be found elsewhere [157].

Types of supercapacitors Supercapacitors may be differentiated based on their: (a) electrolyte (organic, aqeuous or ionic), (b) electrode materials (one dimensional (1D), 2D or 3D carbons [158]; endohedral, planar or exohedral carbons; metal oxides, conducting polymers or composites [154, 159–162]), (c) application (e.g. consumer electronics, automotive or aerospace), (d) configuration (symmetric, asymmetric or hybrid), and (e) charge storage mechanism.

Charge storage mechanisms within supercapacitors The various types of supercapacitors make use of different charge-storage mechanisms: (a) *electro-static* – the physical adsorption of electrolyte ions onto a polarized electrode surface to satisfy local electrostatic equilibrium in an electric double layer (EDL); (b) *pseudocapacitive or surface redox* – reversible, fast faradaic surface reactions giving rise to a capacitive term i.e. charge $\propto$ electric potential; and (c) *intercalation pseudo-capacitive* – fast intercalation of cations

Schematic and internal electric potential distribution	Capacitors Electrostatic (non-polarized) 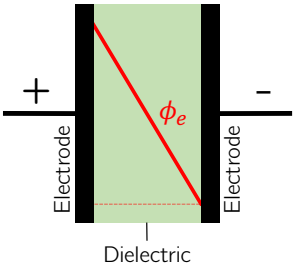 	Electrolytic (polarized) 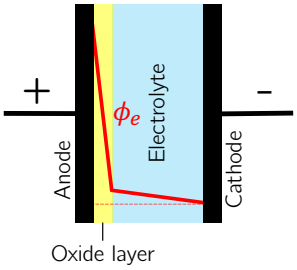 	Electrochemical (supercapacitors) 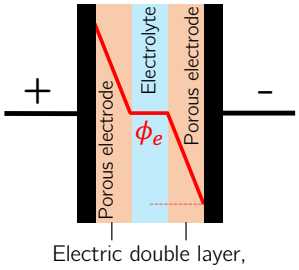
Charge storage mechanism	Electrostatic across dielectric	Electrostatic across oxide layer	Electrostatic within EDL (Pseudo-capacitive / surface redox) (Intercalation pseudo-capacitive)
Examples	Film (metalized polymer) Foil (ceramic)	Aluminum oxide Tantalum oxide Niobium oxide (solid electrolyte)	Electro-chemical double-layer (EDLC) Pseudo-capacitor Hybrid
Components and common materials	Electrodes: Al foil or metalized film Dielectric: ceramic or polymer	Electrodes: etched Al foil Dielectric: metal oxide Al_2O_3 Electrolyte: solid or non-solid Separator: cellulose	Current collector: etched Al, Ni or stainless steel foil Porous electrode: active material (activated carbon), conductive additive (carbon black), binder (PVDF/PTFE). Electrolyte: aqueous, organic or ionic Separator: cellulose or glass-fibre
Conventional manufacturing process	Film stretching/foil casting Metallization/roll-screen printing Film/foil slitting Winding/stacking (slightly offset) Compression/thermal post-treatment Attachment of terminals (shoopage) Assembly/insulation	Anode foil etching Oxide forming (anodic oxidation) Foil slitting/attachment of terminals Winding/coiling Electrolyte impregnation (vacuum) Assembly/sealing/insulation Artificial aging	Foil etching/primer Slurry casting of electrode Calendaring/drying Foil slitting/punching Winding/stacking Electrolyte impregnation Assembly/sealing/insulation Artificial aging

Table 7.1.A: A summary of the main capacitor types showing: schematics of device architecture and their internal electric potential ϕ_e distribution, the associated primary charge storage mechanisms, device examples, device components and common materials as well as the manufacturing process.

in the bulk, active electrode material but not limited by diffusion of cations within the crystalline framework of active material [163, 164]. Comprehensive reviews of the underlying physical electrochemistry [153, 163, 165] and recent advances [164, 166, 167] have been published elsewhere. It should be noted that many supercapacitors make use of a combination of charge-storage mechanisms (so-called *hybrid supercapacitors*), frequently resulting in misleading naming conventions [168]. A widely accepted publication clearly defines the boundaries [169]. In Part II of this thesis we will consider a specific type of supercapacitor, the electro-chemical double layer capacitor (EDLC), as a model EES device. When referring to EDLCs in this thesis, it means supercapacitors which predominantly store energy in an *electro-static* manner, i.e. in the EDL only.

7.2 Electro-chemical double layer capacitors

EDLC architecture & functionality Conventional EDLCs consist of (at least) two, symmetric (identical anode and cathode), ultra-high surface area electrical conductors (*porous electrodes*) separated by an ion permeable but electrically insulating membrane (*separator*). The porous electrodes are connected to an external circuit by electrical conductors (*current collectors*). The entire cell is immersed in an ion-conducting liquid or gel (*electrolyte*) and encased with an insulator (*housing*). The primary requirements of these key components are:

(a) **Porous electrode** (active material + conductive additive + binder) – to provide maximum ion-accessible surface area [$m^2\,g^{-1}$] for electro-static charge storage while retaining good electrical conductivity (intra- and inter-particle electron conductivity), alongside good chemical and mechanical stability throughout cycling. The binder provides mechanical cohesion and stability between active particles and the current collector, but may have an undermining effect on performance [170, 171];

(b) **Separator** (porous membrane) – to electrically insulate electrodes from one another while allowing electrolyte ions to shuttle between the electrodes during charge/discharge. The separator should provide [153]: mechanical stability to allow for cell assembly, high porosity (>50 %) for good electrolyte ion mobility, high thermal stability, and be as thin as is practical to reduce the length of ion pathways. Coating of the electrolyte/separator layer is often considered one of the most difficult stages in capacitor manufacture [172]. A study on the influence of separator properties on electrochemical performance of supercapacitors can be found elsewhere [173];

(c) **Electrolyte** (salt + solvent) – to provide a source of ions allowing the local electrostatic equilibrium to be satisfied at the electrode-electrolyte interfaces. The primary

requirements include high ionic concentration [$\mathrm{mol\,m^{-3}}$] and intrinsic ionic mobility, a wide operating window, or electro-chemical stability window (ESW), in terms of potential [V] and temperature [°C], and a small solvated ion radius [nm] to increase surface accessibility into porous electrodes [162]. There are a wide range of electrolytes including aqueous (e.g. polyvinyl alcohol (PVA) hydrogels [174, 175]), organic [176], and ionic liquids [177], however safety (flammability) concerns related to non-aqueous liquid and some gel-based electrolytes create an imperative for the use of solid electrolytes in some energy storage applications. Reviews of electrolyte types [152] and specifically hydrogel polymer electrolytes (frequently used in AM processes) can be found elsewhere [178];

(d) **Current collector** (electrical conductor) – to supply electrons to and from an external circuit to polarize the electrodes. The current collector should have excellent intrinsic electron conductivity [$\mathrm{S\,m^{-1}}$], good adhesion to the porous electrode to reduce internal resistance, as well as chemical inertness to the electrolyte; and

(e) **Housing** (encasing) – to encapsulate the complete cell arrangement with sufficient mechanical strength for service, and to prevent electrolyte leakage. Furthermore, this passive component should provide degradation resistance over the entirety of intended shelf and operation life.

Over-arching, general requirements applicable to all EDLC components include: minimization of H&S (e.g. toxicity of embodied materials) and environmental impact (ecological sourcing, end of life disposal), regulatory adherance (compatibility with current legislation for product manufacture), process-ability, chemical stability, cost and shelf life. Generally, EDLCs can operate over a wide range of temperatures (-40 to $85\,^{\circ}\mathrm{C}$), that is difficult to achieve for other electrochemical devices such as ion-batteries.

Energy storage in an EDLC The electric double layer (EDL) may be described as the localized accumulation of electrolyte ions in proximity to an externally polarized electrode. Given the high chemical stability of the materials, this arrangement is induced to satisfy electrostatic equilibrium (as opposed to Nernstian thermodynamic equilibrium in other EES devices). The phenomenon is schematically shown in Figure 7.2.A for a flat electrode. Note, in EDLCs the electrodes are ultra-high surface area, porous materials. A simplified[1] variation in the internal electric potential ϕ_e distribution, with distance from the electrode, is shown in Figure 7.2.A(a). The schematic shows the ϕ_e distribution based on the *Stern model* [179], combining both the *Helmholtz model* (label ii in Figure 7.2.A)

[1] excluding effects such as: ion deficiency due to diffusion, surface re-dox reactions leading to pseudo-capacitance of specifically adsorbed ions, Thomas-fermi screening distance and effects of electron spilling.

[180] and *Gouy-Chapman model* (label iii) [181, 182]. Although some energy is also stored in the orientation of molecular dipoles within the electrolyte (label i), the vast majority of energy within an EDLC is stored within the highly confined *compact layer* (as capacitance is inversely proportional to the separation distance of charge). The *compact layer* may be defined as the region between the electrode surface and the *outer Helmholtz plane*, i.e. the closest distance of approach for oppositely charged ions to reside. The resulting, effective *polarization plane separation distance* of 0.2 to 0.8 nm (a function of the solvated ion radius ∅ [nm]) gives rise to significantly higher capacitance compared with other capacitors (up to 5000 F, approximately ×100 more specific energy than electrolytic capacitors). Further away from the electrode, the *Gouy-Chapman diffuse layer* governs the distribution of electric potential. In this layer, ions are thermally distributed following the Boltzmann principle (dependent on ionic concentration, temperature etc.). The EDL exists at both electrodes, as shown in Figure 7.2.A(b), and non-ideal faradaic losses (often referred to as internal resistance, or *IR losses*) may take place in the bulk electrolyte and/or across the separator.

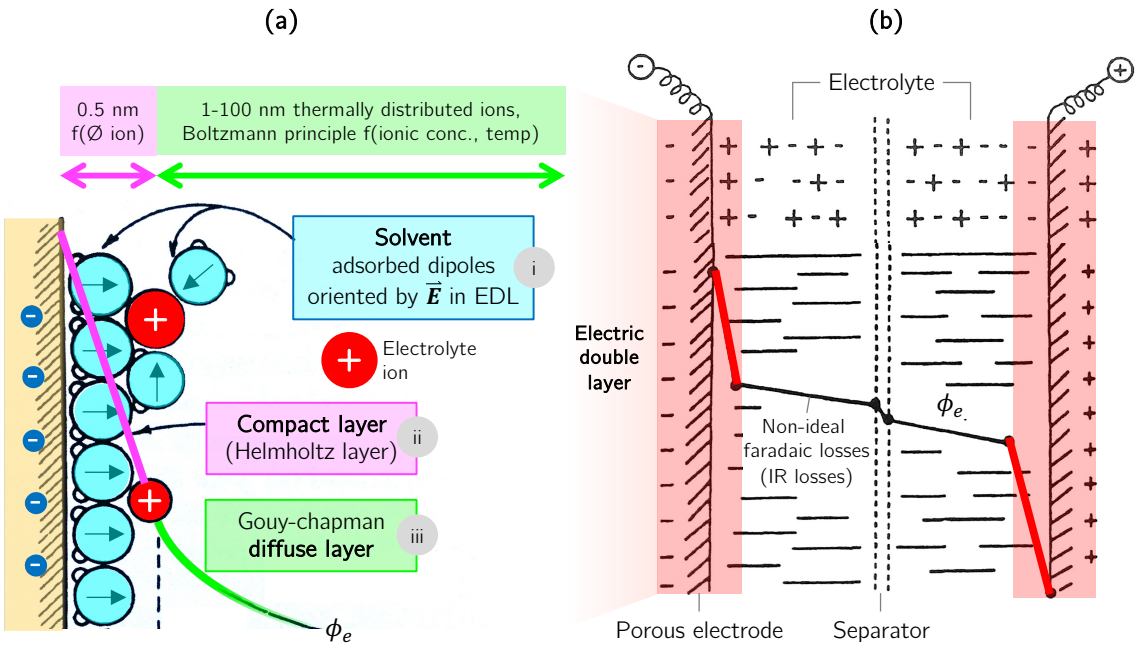

Figure 7.2.A: A schematic of: (a) the internal distribution of electric potential ϕ_e in proximity to an electrode within an EDLC, highlighting the primary charge storage mechanisms (i-iii) following Stern's model, and (b) the internal distribution of ϕ_e within the entire cell. Adapted from [163].

Key performance parameters EDLC performance parameters (also applicable to other types of capacitors) include: capacitance [F], operating voltage [V], impedance [Ω], time constant [s], energy stored [J], power [W], dissipation factor [%], cycling stability (capacitance retention [%] after >10,000 cycles), charge transfer resistance or electrical series resistance (ESR) [Ω], self-discharge behaviour [V/ min], and cost [$\$\,F^{-1}$]. Absolute performance is often normalized to active material weight (g^{-1}), electrode area (cm^{-2}) or device volume (mm^{-3}). Electrochemical parameters are frequently evaluated by: cyclic voltammetry (CV), constant current charge/discharge (CCCD), and electro-chemical impedance spectroscopy (EIS). An excellent overview of the instruments and measurements required to estimate key performance parameters, alongside common inconsistencies in evaluating these, is given in [183]. Further guidelines outlining conventional experimental methods and how to interpret data are given in [183–189].

Lack of standardization Unfortunately, performance parameters, and the evaluation thereof, are not well standardized. Therefore data in many publications can only be used to inform what AM techniques are being explored in the context of energy storage devices, and there are difficulties in making robust quantitative comparisons, particularly between research and commercial performance. International Electrotechnical Commission (IEC) norms for the standardized testing of capacitors have been published [190], however access to these and their adoption, especially in academic environments, is often limited.

7.3 The challenge of manufacturing EDLCs

Principal challenge The global capacitor market is expected to grow significantly, at ∼22 % per year, to USD 4 billion by 2022 [156]. It is a competitive, high-volume mass market with many suppliers including: Asahi Glass (Japan), Batscap (France), Maxwell Technologies (USA), Murata Manufacturing Co. Ltd. (Japan), NEC corporation (Japan), Nesscap (South Korea, Canada), Nippon Chemicon (Japan), Panasonic (Japan) and Samsung Electro-Mechanics (South Korea). Manufacturing challenges arise from the perpetual desire for increased performance (increased capacitance, lifetime and energy/power density) at reduced cost. Meanwhile, the environmental requirements (operating temperatures, exposure to stresses, device size restrictions) and regulatory environment (ecological sourcing of materials, manufacturing health/safety, end of life) are becoming more stringent/demanding. While the different types of capacitors and corresponding manufacturing approaches (outlined in Table 7.1.A) each bring their own challenges, such as effective electrolyte impregnation in supercapacitors or crack-free fabrication of thin ceramic films in multi-layer electrostatic capacitors, the principal challenge in capacitor manufacture remains the same: to engineer macroscopic components (*devices*), with designed and highly resolved, multi-material, electro-active sub-structures that cost-effectively meet the required performance [148]. The manufacturing technologies must be scalable and financially attractive to significantly penetrate the price sensitive energy storage device market.

Recent focus in advancing EDLC manufacture The majority of work concerning the manufacture of EDLCs has addressed: the synthesis of cost-effective, high-surface area electrode materials [159, 162], the improvement of interfaces between, for example, the electrode and electrolyte [191] i.e. interfacial resistance, as well as advancements in electrolyte bio-compatibility and safety [152, 192]. The *slurry casting*-based manufacturing and assembly process itself however, has received surprisingly little attention [193] and has therefore remained largely the same for many years [194].

Current manufacturing process EDLC electrodes are commercially manufactured in a mature, roll-to-roll mass-manufacturing process synonymously known as either *doctor blading*, *slurry casting* or *slot-die coating* (similar to how Li-ion batteries are fabricated) which entails [153, 194]: (1) current collector foil (e.g. Al foil 15 to 40 µm for organic electrolytes and Ni or stainless steel (SS) for aqueous electrolytes) etching, alongside the application of a conductive primer (∼1 µm carbon black), to increase the surface area and reduce ESR respectively; (2) *doctor blading* or *slurry casting* of active material (e.g. activated carbon from wood [195] or coconut [196] precursor, activated by water vapor with up to 2000 $m^2\,g^{-1}$), conductive additive (e.g. ultra-fine carbon black particulate),

binder (e.g. 10 wt% polyvinylidene fluoride (PVDF) or polytetrafluoroethylene (PTFE)) and a fugitive solvent (e.g. N-Methyl-2-pyrrolidone (NMP) and/or isopropyl alcohol (IPA)) to a preset, constant thickness (50 to 150 µm) by a passing blade; (3) drying (e.g. along a drying tunnel on a conveyor) and calendering (i.e. compression through heat pressing) of the porous electrodes; (4) electrode and current collector foil slitting or punching; (5) winding or stacking of current collector, electrodes and porous (50 to 90 % porosity) separator (e.g. 15 to 50 µm paper of solvent-spun cellulose or recycled cellulose fibres for organic [197], or 30 µm glass-fiber-based for aqueous electrolyte [198]); (6) impregnation of the cell with liquid or gel electrolyte (organic, aqueous or ionic); (7) multi-step assembly and sealing involving welding; and finally (8) artifical ageing at elevated temperatures before testing and packaging.

Limitations of current EDLC manufacturing Some of the limitations of the current, commercial EDLC manufacturing process include: (a) limited geometric design freedom – the inherent planar form-factor restrictions of *slurry casting* techniques for electrode fabrication restrict the device architectures possible (flat, wound or coin-cell configurations) [199]; (b) homogeneous electrode morphology – the intrinsically stochastic micro-porosity and tortuous pore morphology of electrodes fabricated using conventional *slurry* methods hinders optimal use of electro-active materials (especially at ultra-fast charging rates) due to limited ion mobility [148]; (c) performance hindering binders – the need for a *binder* (e.g. PVDF) to hold the porous, particulate based electrode together and onto the current collector reduces the performance theoretically achievable by the active materials [200]; and (d) expensive cell assembly – the multi-step assembly-process required to fabricate EDLCs, induce high up-front capital costs and long product lead-times [201]. Overcoming these limitations may further help exploit the attractive features of supercapacitors and secure their use in a wider range of emerging applications [202].

Novel manufacturing approaches Only recently, (since ∼2010) have initial, transformative approaches to the manufacture of supercapacitors, as a way to enhance performance, gained traction and attention in R & D [123, 148, 193, 203, 204]. To address the limitations associated with the conventional roll-to-roll manufacturing method, *printed power sources* and specifically *printed EDLCs* are being developed. AM ideas and approaches, while not yet penetrating significantly into the energy storage sector, offer opportunities to address the manufacturing limitations. Furthermore, AM may allow direct integration of the devices into printed products, alongside free-form device fabrication and even cost-effective mass-customization [204, 205]. While the full potential of AM technologies for the fabrication of capacitors is still unclear, possible advantages and disadvantages are now described.

7.4 The promise of AM for the manufacture of EDLCs

Advantages of AM for capacitor fabrication With respect to the fabrication of capacitor devices and components, the spatial and temporal material manipulation abilities of AM techniques may allow for:

(a) **Increased geometric design freedom** – the sequential, *layer-by-layer* deposition of functional materials allows for the fabrication of geometrically complex, multi-material (ceramic, plastic, metal) devices such as capacitors [130]. Such devices may demonstrate novel geometric form factors (e.g. periodic or interdigitated electrode capacitor configurations) for improved performance (through, for example, shortened ion diffusion pathways) and allow for the utilization of irregular volumes for energy storage [206];

(b) **Nano- to macro-scale control of material properties** – AM technologies may provide an economical approach to control material properties over a wide range of length scales (from e.g. aligned carbon nanotubes (CNTs) in extrudates to large hierarchically structured devices). Nano- to micro-scale architectures have already been demonstrated for other applications [207–209];

(c) **Functionally gradient devices** – the spatial control of material properties (e.g porosity and morphology) may allow AM processes to provide additional functionality of capacitors through functional gradients [78] or heterogeneous designs. The potential benefits of graded electrodes in energy storage devices [210] and Li-ion batteries specifically [211] as well as supercapacitors [212] have begun to be explored;

(d) **Direct manufacturing integration** – the direct integration of capacitor manufacture in product manufacture may facilitate novel, more compact electronic device designs. Integrated manufacture may allow for on-chip printing [213] and direct manufacture of energy storage devices on crowded micro-devices [205];

(e) **Process flexibility** – in terms of material feed-stock properties (e.g. paste, powder, laminate, filament, suspension), AM processes may provide unprecedented versatility. The shortened overall manufacturing lead times achievable with AM techniques may promote rapid prototyping for capacitor designs and allow the rapid testing of novel materials combinations.

Disadvantages of AM Some of the main drawbacks of AM technologies for the fabrication of capacitors include: (a) relatively high cost (current high-throughput, roll-to-roll techniques are highly efficient and productive), (b) intrinsic anisotropy of material properties (strength, conductivity, etc.) resulting from the line-by-line or layer-by-layer deposition and sequential integration/application of materials, (c) limited scalability (discrete machines with preset working envelopes), (d) immature technology (AM process dynamics have not yet been fully understood and in particular feedback control approaches are generally absent), and (e) low material throughput (e.g. $[m^2\,h^{-1}]$ of electrode).

Examples of AM for EDLCs Only a few, recent, top-level publications review AM for energy storage applications e.g. [123, 148, 193, 203, 204]. The author has reviewed AM technologies specifically for capacitors elsewhere [214]. Table 7.4.A provides a summary of examples, where AM techniques have been reported for the fabrication of individual capacitor components (or relevant, related applications), alongside a subjective indication of the current suitability (*suitable* - green, *unsuitable* - red) of the AM technology for fabricating individual capacitor components. MEAM processes, such as FFF [215] and DIW [216, 217], are among the most widely used processes, partly due to their relatively low capital and running costs, broad range and quickly expanding palette of processable materials, along with generally no need for significant heat input during processing or chemical post-treatment of printed parts [128, 218].

Hybrid-AM for EDLCs Capacitors are multi-material devices and as such, developing a MMMT or *hybrid-AM* approach may be desirable and arguably necessary to fabricate complete devices. Hybrid approaches allow each component to be fabricated in a preferred, optimized way, and even for entire devices to be fabricated in a single operation. Critically, they rely on a good understanding and careful study of how different AM processes interact, especially the interactions of the different materials e.g. at interfaces. General requirements for MMMT for fabricating EDLCs include: (a) materials should form good inter-particle bonds, once deposited, without the need for additional compression such as calendaring (rolling), (b) fabrication routes should not require any post-processing (e.g. thermal curing) which may degrade some already printed parts of the assembly, and (c) processes should not be vulnerable to contamination of feedstock through the introduction of a multi-material component (e.g. vat-based systems). It follows that, in general, powder-bed or vat systems are intrinsically/systematically unsuited for MMMT approaches as they are mono-material, and that nozzle/dispensing technologies such as MEAM or material jetting processes are suitable. Challenges in MMMT approaches are often associated with the sequential, layer-by-layer, deposition of compositionally discrete layers, and ensuring the right behaviour/nature of the associated material interfaces.

AM technology		Capacitor component				
		Dielectric	Current collector	Housing	Electrolyte/ separator	Porous electrode
Material extrusion	FFF	[125] PLA [219] PLA† [124] Ceramic†	[125] Thermoplastics [126, 220] Graphene-ABS†/PLA†	[221] Silicone [222] PLA [130] PP	[127] Nafion precursor [223] Ion exchange membrane*	N/A Too low mass loading achievable.
	DIW e-3D	[136] Rheology of ceramic pastes†	[130, 224] Ag ink [225] Embedded 3D printing†	[224] Silicon	[130, 224] Gel [226] Ionic liquid* [172] Solid-state PEMA*	[217] Review [227–230] Graphene [130, 221] Activated C [135, 216] CNT
Vat polymerization	SLP PμSL HL DLP	[231] PμSL: polymer-ceramic	[232] SLP: Metal-UV resin†	N/A no literature	[233] PμSL: Macro-structured polymer* [234] PμSL: Micro-structured ceramic* [235] DLP: porous†	[236] HL: Li-ion*
Powder bed fusion	SLM/ DMLS SLS EBM	[237] Ceramics†	[238] SLM: Steel [239] SLM: Ti [240] DMLS: Steel	[241] Polymer† [242] PEEK†	[243] EBM: Liquid/gas diffusion layer*	[244] Tool electrode†
Material jetting	IJP Spray	[245, 246] $BaTiO_3$ [247, 248] Polymer [249, 250] BN [251] Fe_3O_4†	[252, 253] Reviews† [245, 246, 254] Ag [249, 250] Graphene [247] Polymer	[255] Printed hydraulics†	[256] PVA, solid [257] Solid-state [258] Ionogel* [259] Spray*	[260] Graphene [256, 257, 261, 262] CNT [263] Activated C [264] $LiFePO_4$*
Binder jetting	IJP	[265] $BaTiO_3$ [266] Ceramics†	[267] Copper†	N/A Generally too porous without post-processing	N/A no literature	[268] Graphene [269] CNF plaster†

Table 7.4.A: Examples of AM technologies, split by process categories, used for the fabrication of capacitor components (dielectric, current collector, housing, electrolyte and porous electrode). The colour-code gives an indication of the overall suitability of an AM technique for the fabrication of the component, spanning from *suitable* (green) to *unsuitable* (red).
Note: * indicates that the example given is in another energy storage related application and † indicates the example is for applications further removed from capacitors but of potential relevance.

Complete capacitor devices fabricated by AM First attempts to fabricate complete capacitor devices, using only *additive* technologies have been made: (a) interdigitated solid-state electrolyte capacitor - IJP [257]; (b) thin film capacitor - IJP [246]; (c) stacked non-polarized capacitor - FFF [125]; (d) 2D material thin film capacitor - IJP [250]; and (e) hydrated graphene oxide (GO) micro-supercapacitor - direct laser write (DLW) [202]. Nevertheless, the research-scape related to MMMT AM of energy storage devices remains very immature, and the fabrication of complete capacitor devices is currently confined to proof-of-concept work. Most devices suffer from poor long-term cycling performance as well as the need for additional encapsulation (to prevent electrolyte from leaking) [257].

7.5 Objectives for Part II

Part II seeks to demonstrate how existing EDLC materials can be used in MEAM processing techniques (FFF and DIW) to fabricate or *print* functioning, form-factor free electro-chemical energy storage devices in a single operation. The following objectives are addressed:

(a) **explore multi-phase processing science** – to develop quantified understanding of underlying MEAM processing-science, such as melt and extrusion dynamics, extrudate spreading as well as bonding processes between successive layers, to enable *multi-phase* AM, i.e. the layer-by-layer deposition of solid-gel-liquid combinations;

(b) **formulate printable inks** – to demonstrate how existing EDLC materials can be used to formulate enhanced material combinations specifically designed for MEAM. The objective is to investigate the links between chemical formulation, slurry rheology and cell performance;

(c) **print an energy storage device** – to fabricate or *print* functioning, form-factor free EES devices in a single, automated manufacturing operation using MEAM techniques, and characterize their electro-chemical performance. The objective is not to achieve energy storage behaviour (e.g. gravimetric capacitance, cost, lifetime) that is superior to the mature slurry cast electrodes and devices commercially available, but to demonstrate encouraging performance in a novel form factor impossible by current approaches;

(d) **investigate various geometric form factors** – to explore novel cell arrangements and geometric form factors, and characterize the influence this has on cell performance.

8

Materials & methods

8.1 Materials & ink preparation 93
8.2 Manufacturing sequence 94
8.3 Cell characterization 96
8.3.1 Electro-chemical performance evaluation 96
8.3.2 Physical characterization 97

8.1 Materials & ink preparation

Functional inks were prepared on the day of EDLC manufacture as outlined hereafter. Unless otherwise stated, chemicals were sourced from Sigma-Aldrich UK and, where possible, industry standard materials were used.

Electrode A two-step mixing process was adopted from [270], that accounts for the typically cuboid shape of commercial activated carbon particles used in supercapacitors. A water-insoluble binder was chosen to allow for the fabrication of aqueous electrolyte EDLCs in atmospheric conditions, and the binder content was chosen as low as possible to maximize electro-chemical performance while preserving electrode stability [170]. The method was: (1) mixing of activated carbon (YP80F from Kuraray, Germany), conductive additive (carbon black 99.9 % from Alfa Aeser, UK), a solvent with high boiling point (NMP, CAS 872-50-4) and a low boiling point (IPA, CAS 67-63-0) in a weight ratio of 0.8:0.2:2.5:7.5 at 250 rpm for 20 min; (2) addition of a binder (PVDF, CAS 24937-79-9) dissolved in a solvent (NMP) to the slurry at a weight ratio of 0.05:2.5:11 and mixing at 250 rpm for 20 min. A ZrO_2 pot with 8 ZrO_2 balls ($\varnothing$1 cm) was used in a planetary ball mill (Pulverisette 6 from Fritsch GmbH) to prepare the slurry. The electrode slurry was back-loaded into a syringe (Nordson EFD Optimum 3 cc barrel) ready for DIW.

Electrolyte hydrogel A thickening agent (PVA, CAS: 9002-89-5) was mixed with deionized water and a salt (potassium chloride (KCl), CAS: 7447-40-7) at a weight ratio of 5:100:14.9 at 90 °C, 400 rpm for 1 h to synthesize a 1 M hydrogel electrolyte. The hydrogel was cooled to room temperature and back-loaded into a syringe (Hamilton 1002RN 2.5 mL barrel) ready for DIW.

Current collector A commercial conductive ink based on Ag nano-particulates (IINK-SSX from IIMAK, USA) was back-loaded into a syringe (Nordson EFD Optimum 3 cc barrel) ready for DIW.

Housing A PP filament (Centaur PP from FormFutura, The Netherlands) was used for FFF fabrication of all of the supercapacitor housing elements. The filament was dried at 50 °C for >5 h prior to printing.

8.2 Manufacturing sequence

For the purpose of printing EDLCs, the hybrid-AM machine from Part I was fitted with two FFF modules and three DIW modules. Entire EDLC (supercapacitor) devices were manufactured as follows, with an example geometry and manufacturing sequence schematically depicted in Figure 8.2.A: (1) FFF of 2 rectilinear, orthogonal base layers (each 200 µm high, 100 % infill), as well as external and internal walls (200 µm high, 800 µm and 400 µm wide respectively), to assist (2) DIW of the current collector ink which was (3) dried at a 80 °C bed temperature for 100 s yielding typical current collector thicknesses of 20 µm. Thereafter, (4) FFF of housing walls sufficiently high (600 µm) for (5) DIW of an electrode layer, before (6) drying of the electrode at a bed temperature of 70 °C for 500 s yielding typical electrode layer thicknesses of 40 to 120 µm depending on the specified extrusion multiplier. Steps 5 and 6 were repeated for the desired number of electrode layers before, (7) FFF of the housing walls to allow for, (8) DIW of the electrolyte hydrogel before finally (9) sealing of the device using FFF. The nozzles were tapered polyethylene (PE) tips ∅0.58 mm for electrode and current collector inks, a tapered PE tip Ø1.6 mm for the electrolyte hydrogel and a hardened steel ∅0.4 mm nozzle with a titanium hot-end for FFF of the housing. An animation and videos of the manufacturing sequence can be viewed at: https://youtu.be/mmDfWsusjYw

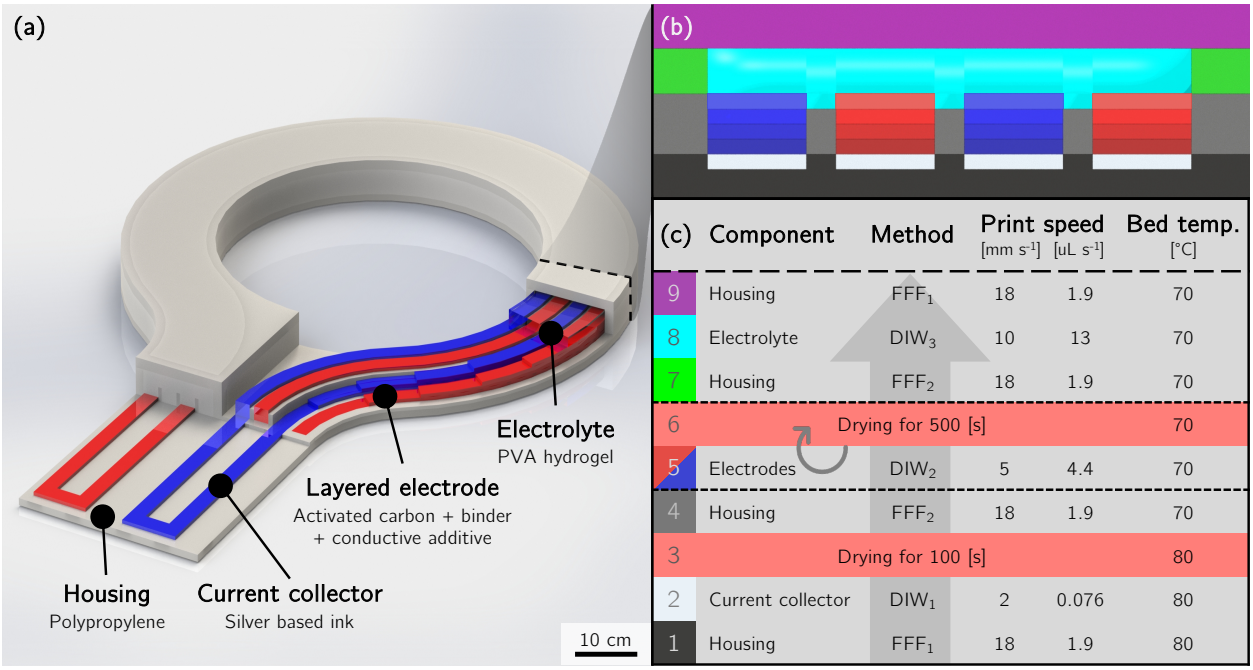

Figure 8.2.A: (a) Isometric render of the demonstration AM EDLC highlighting the unusual geometric *ring* form factor and functional elements, (b) cross-section of the EDLC orthogonal to the print direction, depicting the arrangement of different colour-coded materials, and (c) the corresponding colour-coded table showing the manufacturing sequence and a selection of key processing parameters.

8.3 Cell characterization

8.3.1 Electro-chemical performance evaluation

To evaluate key electro-chemical performance parameters, cyclic voltammetry (CV), constant current charge/discharge (CCCD) and electro-chemical impedance spectroscopy (EIS) measurements were carried out on as-printed, full-cell EDLCs using a potentiostat (Gamry 600), following the guidelines given in [183].

CV The rate performance of printed EDLCs was evaluated by applying a linear voltage ramp across working and counter electrodes over an electric potential window $\phi_e \in [V_0, V_1]$ for 10 cycles at constant scan rates $\nu \in [5, 10, 25, 50, 100]$ $\mathrm{mV\,s^{-1}}$. The current response $i(V)$ of the cell was recorded where $V_0 = 0\,\mathrm{V}$ and $V_1 = 1\,\mathrm{V}$ such that all components remained within their electro-chemical stability window (ESW). From Equation (8.1), the total cell capacitance C_{cell} was estimated by trapezoidal numerical integration (MATLAB) and normalized by active material mass, electrode footprint area and number of electrodes:

$$C_{cell} = \frac{1}{2(V_1 - V_0)\nu} \oint_{V_0}^{V_1} i(V)dV \tag{8.1}$$

The efficiency of charge-discharge cycles was evaluated by comparing the electrons required to charge Q_{charge} and received during discharge $Q_{discharge}$, expressed as $\eta = Q_{discharge}/Q_{charge}$. Cycling performance was investigated at $\nu = 25\,\mathrm{mV\,s^{-1}}$ by evaluating the columbic efficiency of charge and discharge cycles, as well as capacitance retention over 250 cycles.

CCCD After conditioning the printed EDLC cells to 0 V for >60 s, a constant current of $i \in [0.5, 1, 2]$ $\mathrm{A\,g^{-1}}$, normalized to the total mass of active material in the EDLC cell, was applied to the cell to charge to a working potential of $\phi_e > 1\,\mathrm{V}$ and then immediately, without dwelling, discharge to a working potential of $\phi_e < 0\,\mathrm{V}$. The steady-state drop in working potential ΔV_{ss} was evaluated by extrapolating the 2 to 5 % discharge states to the moment of current reversal $\Delta i = 2|i|$. An interpretation of the electrical series resistance (ESR) was derived following a conventional method ($ESR_{CCCD} = \Delta V_{ss}/\Delta i$) [183].

EIS An oscillating, time harmonic excitation wave with amplitude $V_a = 5\,\mathrm{mV}$ was applied to the EDLC cells at open circuit voltage ($V_0 = 0\,\mathrm{V}$) over a range of frequencies $f \in [10^{-2}, 10^{6}]$ Hz according to $V_i = V_0 + V_a \sin(2\pi f \times t)$. The temporal current response $i(t)$ of the EDLC was recorded and using *Ohm's Law* in complex form $V \propto [Re(Z) + Im(Z)]$, attenuation $|Z|$ and phase shift θ as function of frequency were recorded. Under the assumption that the electro-chemical system behaved pseudo-linearly

over the small excitation wave, parameters including the ESR were evaluated following [189]. A Randles equivalent circuit was fitted to EIS spectra to determine the Warburg diffusion coefficient.

8.3.2 Physical characterization

Electrode weight 250 µL of electrode ink was dispensed into a petri dish of known weight, heated above the boiling point of all solvents (250 °C)and dried for >1 h. The net dry-weight of active material [mg µL^{-1}] was used to estimate the electrode weight from relevant commands in the machine code i.e. the weight of active material in a device was estimated from the calibration of the weight dispensed per unit volume.

Rheology The rheology, in particular the shear-thinning behaviour of electrode inks, was characterized and optimized using a rheometer (Ametek Brookfield DV2-T). The cone spindle set-up was selected to: (a) apply DIW relevant shear-rates $\dot{\gamma} \in [0.5, 50]$ s^{-1}; (b) allow small sample sizes <1 mL to be evaluated; and (c) allow the use of a rheological continuum assumption [271], that is, the particle loaded ink can be considered pseudo-homogeneous.

Electrode morphology The morphology of as printed electrodes was investigated by scanning electron microscopy (SEM) (JEOL JSM-6500F). A cross-section of an EDLC printed without electrolyte, and coated with 5 nm of platinum (Pt), was used to investigate the interfaces between functional components, alongside the evaluation of electrode and current collector thickness. Whitelight confocal microscopy (NanoFocus μSurf) was used for 3D surface measurements of electrodes and printed features over areas of 1.5×1.5 mm with depth ranges of up to 250 µm.

Printed features Printed features were observed using an optical microscope (Leica M165C). X-ray tomography (XRT) (North Star Imaging Imagix 150 kV) was used to investigate the spatial arrangement of printed features within complex 3D EDLC cells at 51 µm voxel size. For improved contrast and visualization purposes, LFP, acting as a contrast agent principally due to attenuation by Fe, was added to the electrode ink and an Al filter was placed in front of the X-ray source to partially absorb low energy photons. The surface roughness and thickness of printed features was evaluated using the aforementioned confocal microscope.

9

Results & discussion

9.1 Overview of results 99
9.2 Key materials and processing considerations 100
9.2.1 Ink preparation and rheology 100
9.2.2 DIW processing parameters 101
9.2.3 Drying of DIW fabricated components 104
9.2.4 Achieving encapsulation 106
9.3 Characterization of as-printed EDLCs 109
9.3.1 Physical characterization 109
9.3.2 Electro-chemical characterization 111
9.4 Cell configuration 113
9.4.1 Thick electrodes 113
9.4.2 Parallel cell arrangements 114
9.4.3 Form factor free EDLC fabrication 116

9.1 Overview of results

Functioning EDLC devices with a variety of form factors, cell configurations and electrode thicknesses were fabricated in a single, automated hybrid FFF-DIW manufacturing operation using the hybrid-AM machine from Part I of this thesis. The fabrication process avoided the need for any cell assembly and packaging steps, potentially allowing for direct integration into 3D printed systems and components. The devices were typically fabricated in under 30 min. Key materials and processing considerations for repeatable AM of EDLCs are discussed hereafter. The characterization of as-printed devices, and exploration of electrode thickness, cell configuration and geometric form factor is also discussed.

9.2 Key materials and processing considerations

9.2.1 Ink preparation and rheology

Rheology of printed inks The relationship between rheology and printability for particle loaded inks involves the complex shear rate profiles the inks are exposed to during fabrication, which are associated with the varying print speeds and geometric features of narrowing DIW tips. Conventional cone-plate rheological characterization allowed for tuning of the ink compositions to allow for repeatable DIW fabrication. Figure 9.2.A(a) shows a plot of apparent viscosity as a function of DIW-relevant shear rates for the inks used in Part II of this thesis (see Section 8.1 for optimized compositions). The electrode ink showed significant shear-thinning behaviour, comparable with that reported for other particle loaded inks [272], whereas both the electrolyte and current collector inks behaved in a quasi-Newtonian manner.

DIW tip selection To select a DIW tip for responsive and repeatable printing of the electrode ink, the internal pressure gradient of various geometries was simulated using commercial, multi-physics finite-element software (COMSOL). A non-Newtonian power law (Equation (9.1) [271]) with consistency coefficient $m = 5700\,\mathrm{kg\,m^{-1}\,s^{-1}}$ and flow behaviour index $n = 0.265$ was used to approximate the viscosity μ response as a function of shear rate $\dot{\gamma}$ of the electrode ink according to:

$$\mu = m(\dot{\gamma})^{n-1} \tag{9.1}$$

The difference in steady-state internal pressure build-up, for tips with identical inlet/outlet cross-sections and constant volume flow-rate, is shown in Figure 9.2.A(b) for a conventional tip with a discrete, internal step, and in Figure 9.2.A(c) for the preferred, *tapered tip*. This helps to explain the experimentally observed lag/unresponsiveness during DIW printing with a standard-step tip, and the undesirable *oozing* of inks as the pressure gradient equalized when the tip was idle.

Particle size and agglomerates A critical, determining factor in the rheological behavior of particle loaded ink suspensions is the formation and structure of any agglomerates [273]. To reduce the liklihood of nozzle clogging and thereby improve printability, without increasing the DIW tip diameter to retain the print resolution, agglomerates in the electrode ink were broken down using a relatively low-energy, wet ball milling technique. Stirring balls acted to apply shear stresses in order to disperse active material and conductive additive agglomerates, while breaking up such agglomerates [270]. Figure 9.2.B shows SEM micrographs of the commercial activated carbon (YP80F), (a) before and (b)

after ball milling, confirming that particles were not significantly damaged by limited time ball milling, and larger agglomerates were substantially broken up. In a second step, ball-milling also dispersed the conductive additive (20 wt% carbon black) and binder (5 wt% PTFE), as shown in Figure 9.2.B(c). There was enhanced printability of ball-milled electrode inks when compared with inks prepared using conventional pestle and mortar [274].

9.2.2 DIW processing parameters

Factors influencing DIW Printed current collectors acted as the interface between the external circuit and the internal workings of printed EDLC cells. Current collectors had to be compatible with AM and the various other materials in the device, good electrical conductors, and provide a low contact resistance with the subsequent C-rich electrode material. Ag-nano-particulate based conductive inks have attracted significant attention for printable electronics due to their ability to sinter at low temperatures, comparable with the heated bed temperatures used in FFF processing ($< 100\,^{\circ}\mathrm{C}$), and their relatively low electronic resistivity ($< 29\,\mu\Omega\,\mathrm{cm}^{-1}$) when compared to other conductive materials suitable for AM without post-processing [253]. However, the quality of the DIW current collector *tracks* not only depended on the bonding/sintering processes between Ag particles within the conductive ink, but also on the processing parameters and repeatability of the DIW process. In particular, the: (a) surface roughness and surface energy of the substrate layer; (b) nozzle-substrate separation distance; (c) bed temperature; (d) rheology of the conductive ink; (e) DIW retraction settings; and (f) the DIW extrusion speed all had a critical impact on the quality/function of the current collectors. The effect of a selection of these parameters is shown in Figure 9.2.C, including undesirable features such as (a) smearing, (b) and (c) variable *track* width and (d) optimized conditions.

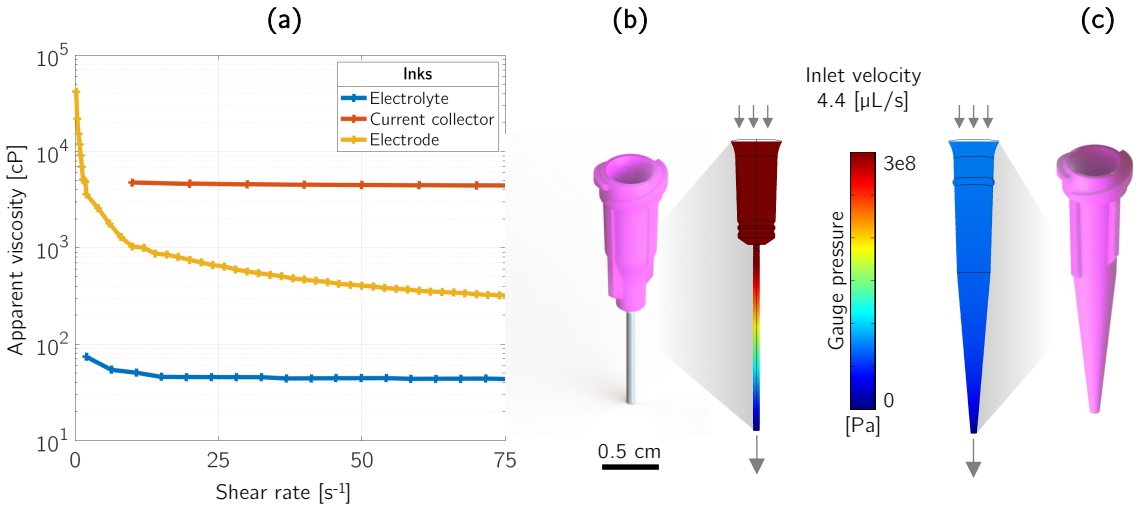

Figure 9.2.A: (a) Rheological behaviour of DIW inks for EDLC manufacture and simulation of the pressure gradient within DIW tips of different geometries: (b) standard step and (c) tapered tip.

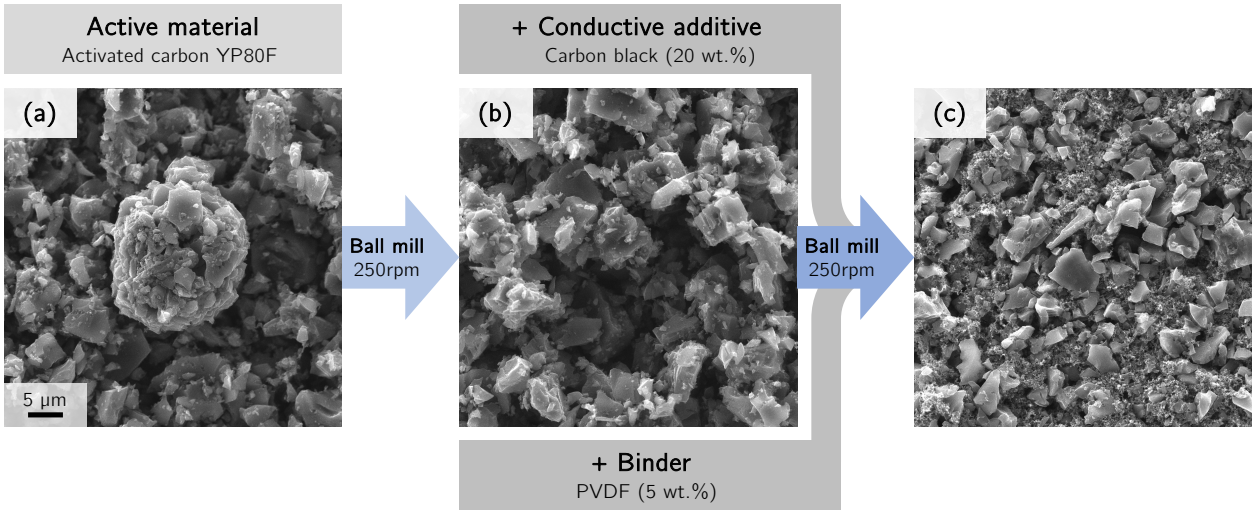

Figure 9.2.B: SEM micrographs showing (a) typical agglomerates in raw activated carbon (YP80F from Kuraray), (b) broken down activated carbon particles after low energy, wet ball milling, and (c) ink morphology including well dispersed C conductive additive and a PVDF binder.

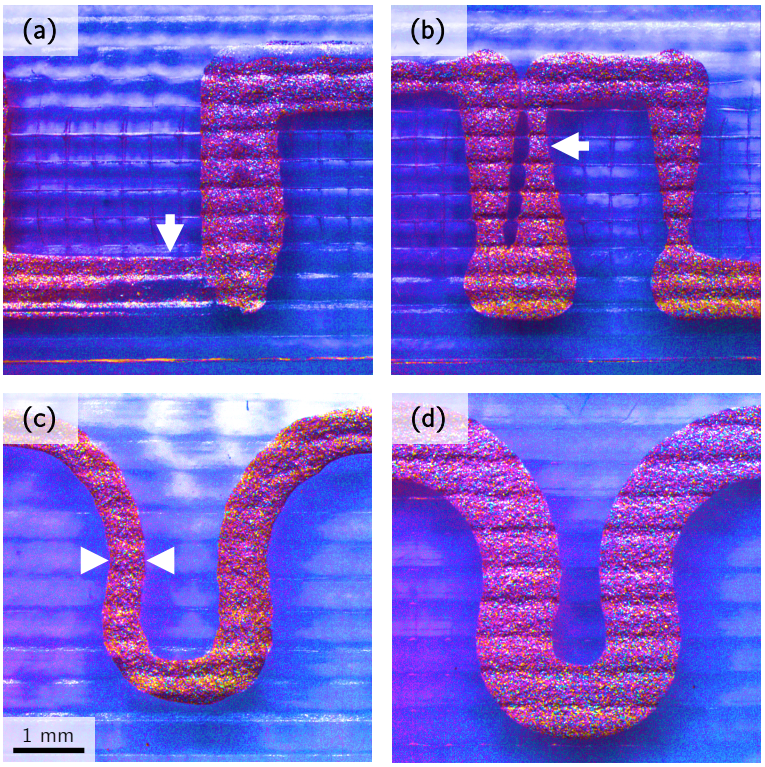

Figure 9.2.C: Micrographs highlighting printing defects of Ag-based ink printed on PP substrates as a function of DIW processing parameters: (a) nozzle-substrate separation distance too small leading to tip clash and smearing, (b) DIW print speed too fast for pressure build-up in barrel and tip to equalize, (c) unreliable retraction parameters leading to material build up at the beginning of a print, and (d) optimized print conditions.

Optimum printing parameters For a FFF fabricated PP substrate with optimized process parameters to achieve low surface roughness (R_a = 0.5 µm parallel to print direction and R_a = 6 µm perpendicular to print direction) the following DIW processing parameters yielded best results when using a tapered PE tip (⌀0.58 mm): tip-substrate separation distance 120 to 150 µm; extrusion speeds of <2 mm s^{-1} depositing <0.1 µL s^{-1}; and retraction volumes of 0.6 to 1.0 µL at 1 µL s^{-1} in between current collector track prints. For too small tip-substrate separation distances (<50 µm), DIW tip clashing with the substrate led to areas of poor quality, *smeared* prints and high electrical resistance (see Figure 9.2.C(a)), whereas with too large tip-substrate separation distances (>200 µm) the current collector tracks suffered from poor initial ink-substrate contact leading to intermittent tracks. DIW printing speeds exceeding 5 mm s^{-1} led to unrepeatable tracks, in particular in geometrically complex areas (see Figure 9.2.C(b)). A lack or excess of ink due to non-optimized retraction settings was most noticeable towards the beginning and end of a current collector track (shown in Figure 9.2.C(c)). The optimization of the DIW parameters outlined resulted in repeatable and consistent prints (shown in Figure 9.2.C(d)).

9.2.3 Drying of DIW fabricated components

Cracking of thin films Figure 9.2.D shows the effect of bed temperature, as proxy for the electrode drying rate, on electrode morphology. The electrodes were fabricated using the ink composition outlined in Section 8.1, and processing parameters adjusted to achieve dry-film thicknesses of 120 ± 20 µm. Electrodes dried at bed temperatures exceeding 90 °C showed substantial crack formation, whereas no or minimal crack formation was observed for electrodes fabricated at a bed temperature of 80 °C. Any further reduction in bed temperature, i.e. drying rate, merely resulted in longer drying times, slowing down the fabrication process. The shrinkage cracks appeared as the capillary force-induced stress profile exceeded the particle network strength [275] during the evaporation of fugitive solvents. Cracks can adversely impact device performance by, for example, increasing internal electrical resistance due to reduced contact area [276].

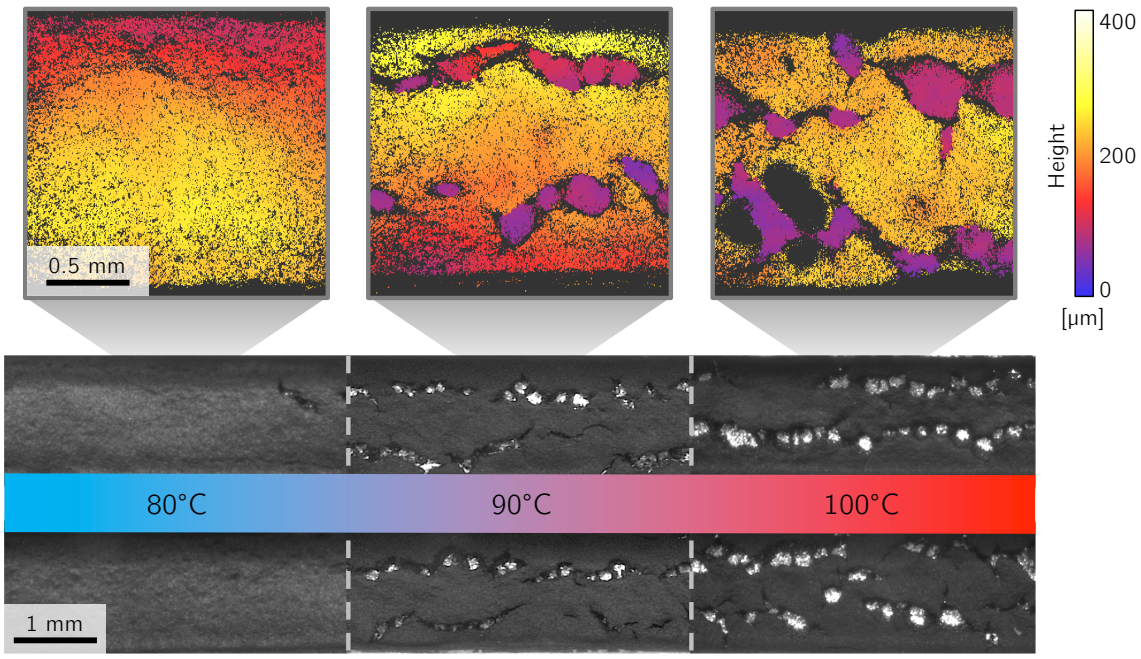

Figure 9.2.D: Optical surface roughness maps of dried electrodes at different bed-temperatures with an electrode ink equivalent solvent boiling point of 130 °C.

9.2.4 Achieving encapsulation

A comprehensive study on the impact of various FFF printing parameters on the print quality was conducted and is summarized in Figure 9.2.E. To fabricate fully encapsulated EDLCs, as schematically shown in Figure 8.2.A (step 9), it was necessary to print a liquid-tight layer of impermeable polymer directly onto the DIW processed electrolyte hydrogel, which was wet and non-rigid. A visual overview of the main FFF processing parameters impacting the print quality on this type of wet substrate is given in Figure 9.2.F.

Processing parameters The FFF extrusion speed and acceleration had to be fast enough for *bridging* of the extruding, molten filament over the gap filled with gel. However, bridging parameters must not be too fast to jeopardize extrusion stability or to prevent sufficient heat-transfer from the FFF hot-end to liquefy the filament. For a bridging gap of 10 mm i.e. over the *trench* containing the printed electrode and gel electrolyte (step 9 in Figure 8.2.A), extrusion speeds of $10\,\mathrm{mm\,s^{-1}}$ and effective acceleration (including jerk) of $50\,\mathrm{mm\,s^{-2}}$ gave best results. To compensate for the rapid cooling of the polymer extrudate on deposition onto any underlying liquid or gel (at room temperature), a slightly elevated extrusion temperature ($\approx +15\,^{\circ}\mathrm{C}$ relative to free-space prints) was required. The separation distance between nozzle tip and the gel had a strong impact on all subsequent layers printed onto the gel due to either sagging of the polymer *bridges* (too large separation distance) or excess dried electrolyte gel that caused a rough surface finish and print defects. The extent of infill overlap (label 7 in Figure 9.2.F) with existing perimeter print lines was an important parameter: overlap parameters, expressed in terms of FFF nozzle diameter, in the range 40 to 60 % yielded best bridging results.

Material selection and compatibility A thickening agent (5 wt% PVA) was used to increase the electrolyte viscosity sufficiently to support subsequent bridging, that then allowed complete encapsulation of the cell (steps 8 and 9 in Figure 8.2.A respectively). PVA was chosen because it is non-toxic, cheap and chemically compatible [178] with the underlying electrode (step 5 in Figure 8.2.A) and the over-bridging polymer (step 9 in Figure 8.2.A). PVA also acts as a hydrophilic binder [174] to maintain long-term cycling performance by binding with the water in the electrolyte gel. PP was chosen as the housing material primarily due to its favorable bridging abilities and relatively inert chemical response when compared to conventional FFF materials such as ABS and PLA. The non-polar nature of the methyl side groups in the macro-molecular chains of PP improved chemical resistance towards polar liquids such as alcohols, organic acids, ester and ketones [277], which are commonly used as solvents in electrode slurries or conductive inks, including those used here (NMP).

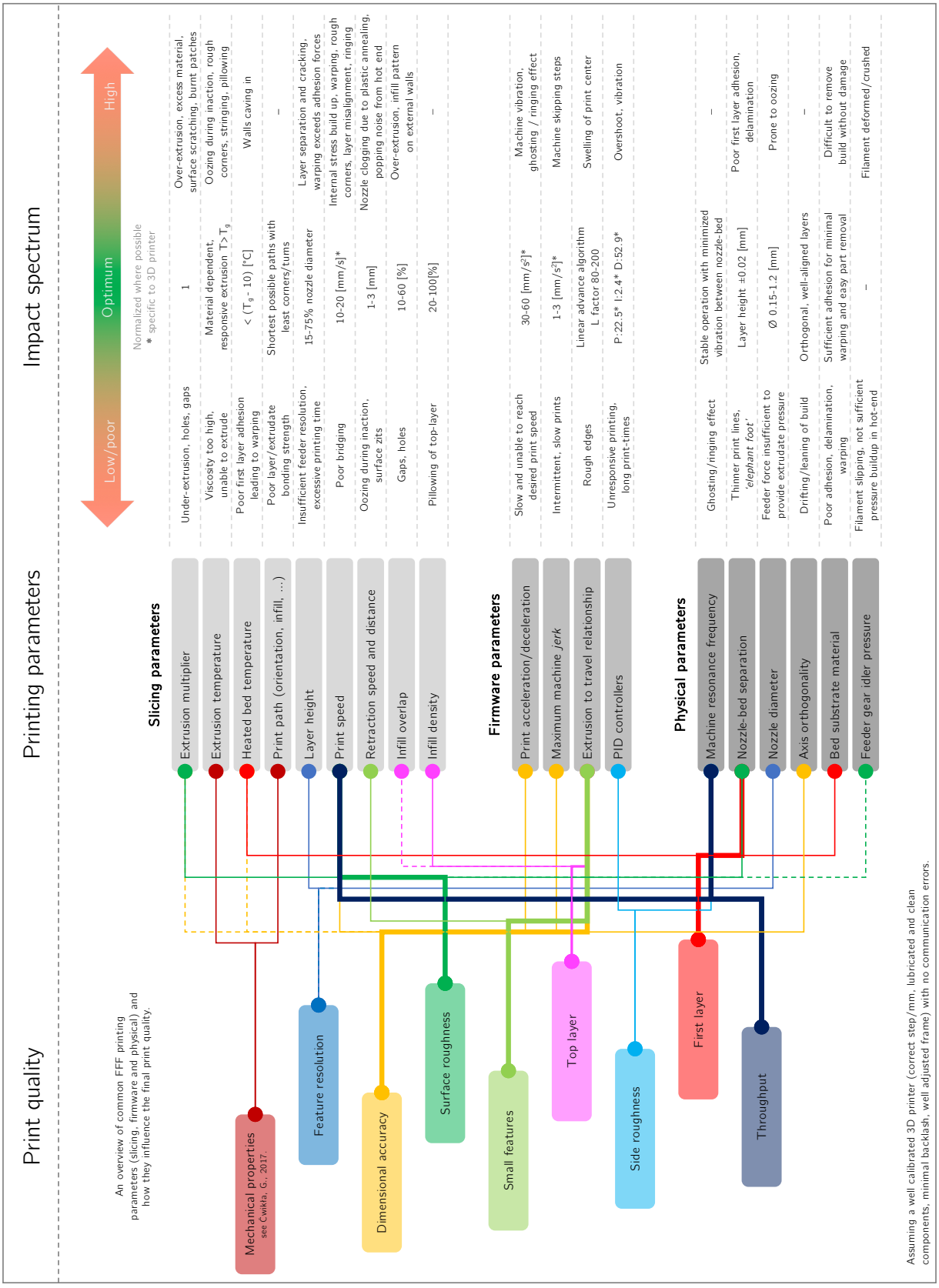

Figure 9.2.E: An overview of FFF print parameters, and their effect on print quality.

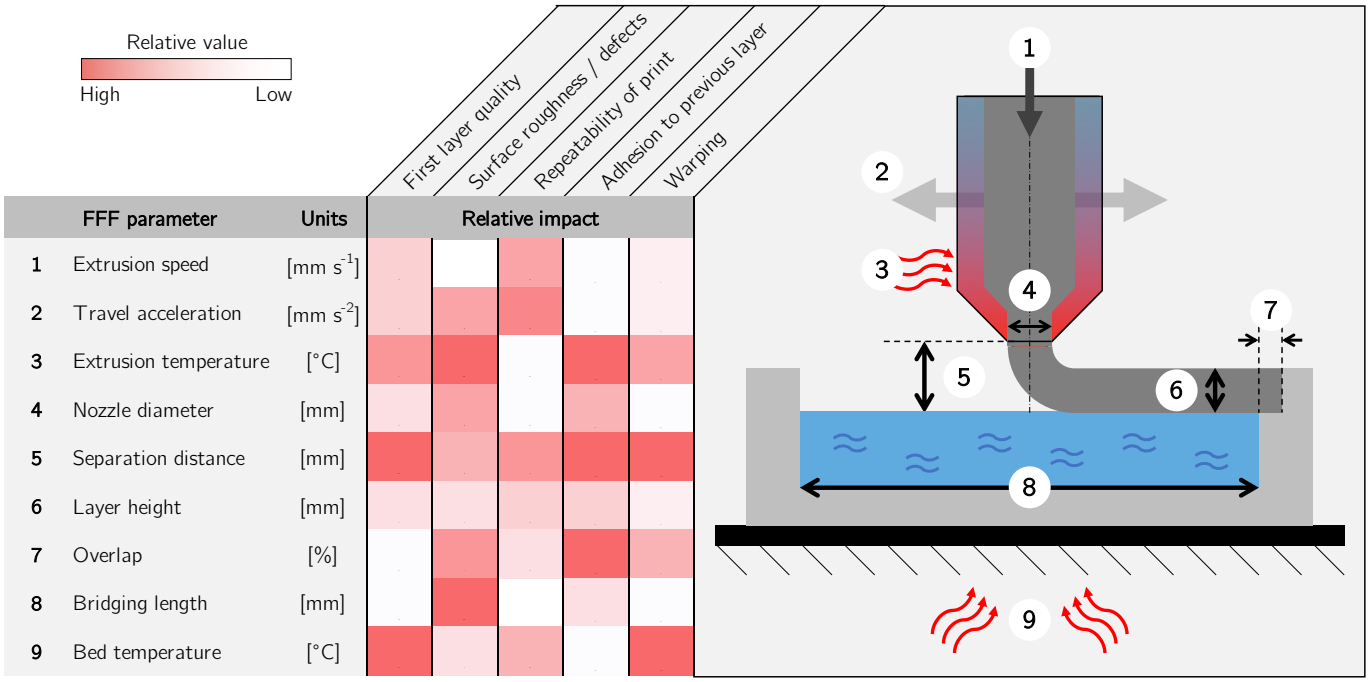

Figure 9.2.F: The relative impact of a selection of FFF processing parameters on different aspects of process stability when printing on a wet substrate.

9.3 Characterization of as-printed EDLCs

Physical and electro-chemical characterization was conducted on as-printed EDLC devices fabricated using the single operation hybrid FFF-DIW approach outlined in Section 8.2. Figure 9.3.A(a) schematically shows the *linear EDLCs* that were fabricated in order to assess basic supercapacitor behaviour (and for process optimization) before the more complex multi-layer *ring* EDLCs in Figure 8.2.A were fabricated.

9.3.1 Physical characterization

Figure 9.3.A shows SEM micrographs of (b) a cross-section of a *linear EDLC* (two parallel trenches each filled with Ag, then activated carbon, then electrolyte gel); (c) and (d) the interfaces between the PP housing – Ag-based current collector – C-based electrode. Figure 9.3.A(b) shows how K^+ and OH^- in the electrolyte hydrogel pass between the anode and cathode during operation, with short circuit avoided by the dividing *wall* of housing between the electrode tracks. Note the *bridge* printing of the housing by FFF over the top of the electrolyte hydrogel to seal the cell (see Section 9.2.4). Printing parameters were selected to achieve electrode thicknesses of $100 \pm 10\,\mu m$, similar to the thickness of commercial EDLCs, and current collector thicknesses of approximately $25\,\mu m$. Note the minimum *width* of features/components fabricated by DIW (e.g. current collector and electrode) was limited by the choice of DIW nozzle diameter (i.e. $\varnothing 0.58\,mm$ reported here) and ink spreading behaviour (determined by surface energy and substrate properties). Through the addition of fugitive solvents to dilute the functional inks, there was no observable lower limit ($< 5\,\mu m$) to the minimum layer thickness, other than ultimately the size of deposited particulates. The difference in morphology, from a relatively smooth, monolithic housing to the micron sized the Ag-flakes in the current collector led to poor contact adhesion between these two elements. Although this is likely to have little effect on the electro-chemical performance of a cell, as the housing is an inactive component, improving the current collector-housing interface should be addressed for applications where mechanical integrity is required over long life-times. Figure 9.3.A(d) shows how Ag-flake based current collector was completely dried prior to DIW of the electrode (no intermixing). The primary particles of the activated carbon in the electrode and the Ag-flakes had comparable dimensions that facilitated a well-matched inter-locking C/Ag interface.

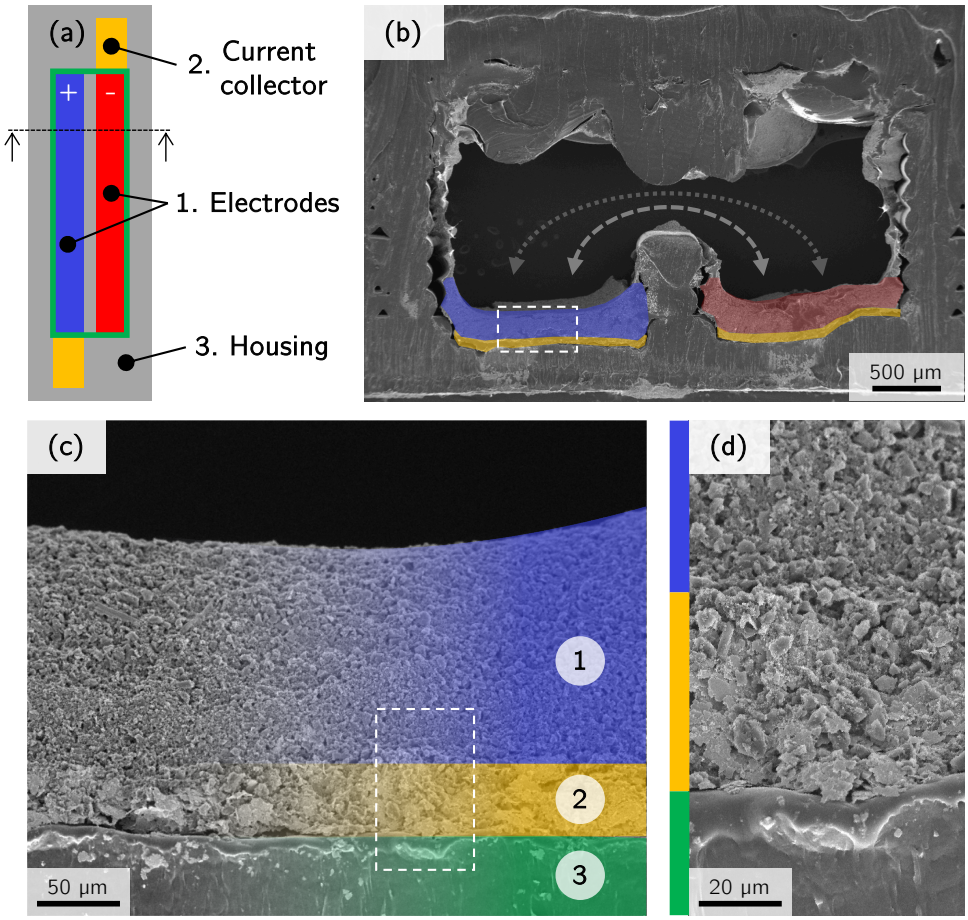

Figure 9.3.A: (a) Colour-coded schematic of the plan view of a functional supercapacitor (EDLC) in a *linear* configuration for physical and electro-chemical testing, (b) SEM micrograph of a cross-section of a *linear EDLC* (running in and out of the page) highlighting the ion diffusion paths in the electrolyte gel between electrodes, (b,c,d) show the colour-coded functional elements at different magnifications including (1) the C-based electrodes and (2) the Ag-based current collector fabricated by DIW, as well as (3) the PP housing fabricated by FFF.

9.3.2 Electro-chemical characterization

CV Figure 9.3.B(a) shows cyclic voltammograms for an as-fabricated *linear EDLC* as a function of scan rate from 5 to 100 $\mathrm{mV\,s^{-1}}$. The plots were quasi-rectangular and indicate acceptable EDLC-type behaviour (ideal EDLCs show classic rectangular cyclic voltammograms). Deviations from ideal performance arose due to internal resistances, and possible underlying non-reversible chemical reactions, the nature of which could not be resolved by similar tests on various materials in isolation but probably relate to Ag-ink/KOH hydrogel reactions. Nonetheless, their contribution was vanishingly small. By integration of the data in Figure 9.3.B(a), the gravimetric electrode capacitance was $116.4 \pm 0.6\,\mathrm{F\,g^{-1}}$ at $10\,\mathrm{mV\,s^{-1}}$ based on the total weight of active material, activated carbon (YP80F) and conductive additive (carbon black). Note that it was not possible to weigh the amount of active material in the device directly, and was instead estimated on the volume dispensed and prior calibration. The areal and volumetric electrode capacitance was $599.2 \pm 3.0\,\mathrm{mF/cm^2}$ and $61.7 \pm 0.6\,\mathrm{mF/mm^3}$ at a scan rate of 10 mV/s, normalized by electrode foot-print area and electrode volume respectively. The devices showed cycling efficiency η of $99.6 \pm 0.4\,\%$ over all tested scan rates and capacitance retention of 97.1 % over 250 cycles at $25\,\mathrm{mV\,s^{-1}}$. The performance demonstrated is comparable to reported symmetric carbon-carbon EDLCs [153, 163].

CCCD Figure 9.3.B(b) shows the corresponding galvanostatic charge/discharge behavior at 0.5, 1 and $2\,\mathrm{A\,g^{-1}}$. The inset shows the ESR_{CCCD}, often referred to as *IR* drop on voltage reversal, which was estimated at $3.2\,\Omega$ at $1\,\mathrm{A\,g^{-1}}$. Otherwise the profiles were near-linear, showing good capacitor-only (electro-static charge/discharge) behaviour, although once again with a slight deviation from linearity suggestive of possible minor underlying side-reactions.

EIS Figure 9.3.B(c) shows the EIS spectrum of a *linear EDLC* prior to cycling. A Warburg diffusion coefficient of 0.8, and an ESR of $13.2\,\Omega$ at 1 kHz was estimated. The relatively low diffusion coefficient, when compared to liquid-electrolyte cells, which may be close to the ideal coefficient of 1.0, can be explained by the use of a thickening agent (PVA) in the electrolyte hydrogel to achieve AM processability, as well as the relatively long ion diffusion paths (see Figure 9.3.A(b)) in the printed cells.

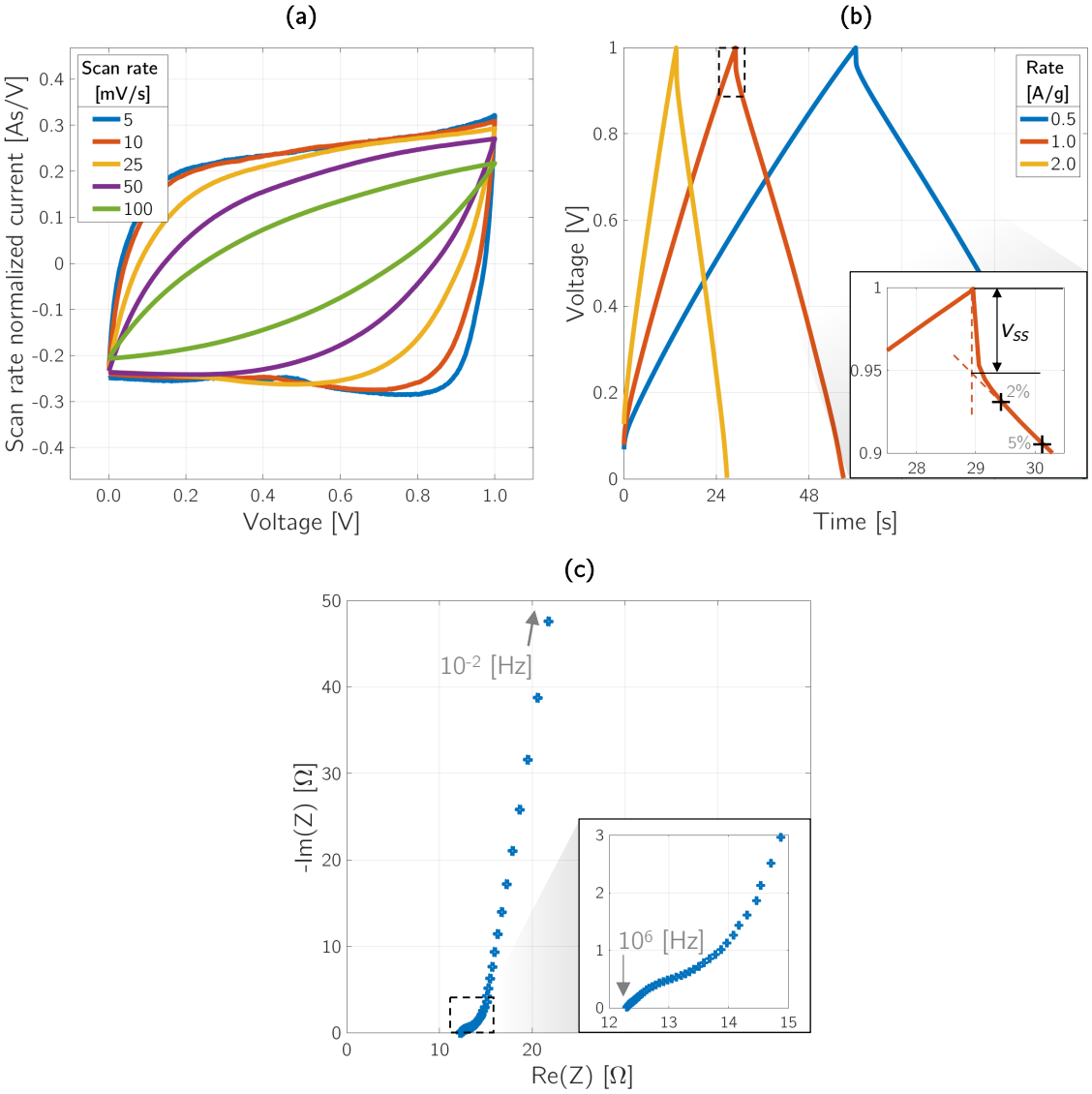

Figure 9.3.B: Electro-chemical performance of as-printed, single cell EDLCs showing (a) rate performance from CV curves, (b) CCCD profiles and (c) an EIS spectrum.

9.4 Cell configuration

The increased geometric flexibility inherent in AM processes opens a multitude of possibilities, with a vast design and parameter space, and as such the following section is by no means exhaustive and serves only to indicate what is possible by AM of energy storage devices by focusing on: (i) thick electrodes, (ii) parallel cell arrangements, and (iii) form-factor free EDLC fabrication.

9.4.1 Thick electrodes

Ion mobility within thick electrodes The electrode DIW extrusion multiplier was doubled to increase the dried electrode thickness, from 97 ± 4 to $180 \pm 5\,\mu m$, for a batch of *linear EDLCs* (Figure 9.3.A(a)). Figure 9.4.A(a) shows the resulting Nyquist diagram from EIS now with a lower gradient Warburg element for the thicker electrode (180 µm) (an extended, comparatively shallow EDL formation slope), presumably due to lengthened ion-diffusion paths within the thicker electrodes. The equivalent electrode resistance, including the current collector resistance contributions, increased from 12.8 to 16.1 Ω (+26 %) when approximately doubling the electrode thickness. This indicated that the principal resistance was probably due to the current collector-electrode interface (which was unchanged). The thicker electrodes also undermined rate performance, as shown in Figure 9.4.A(b). The columbic efficiency was not affected significantly.

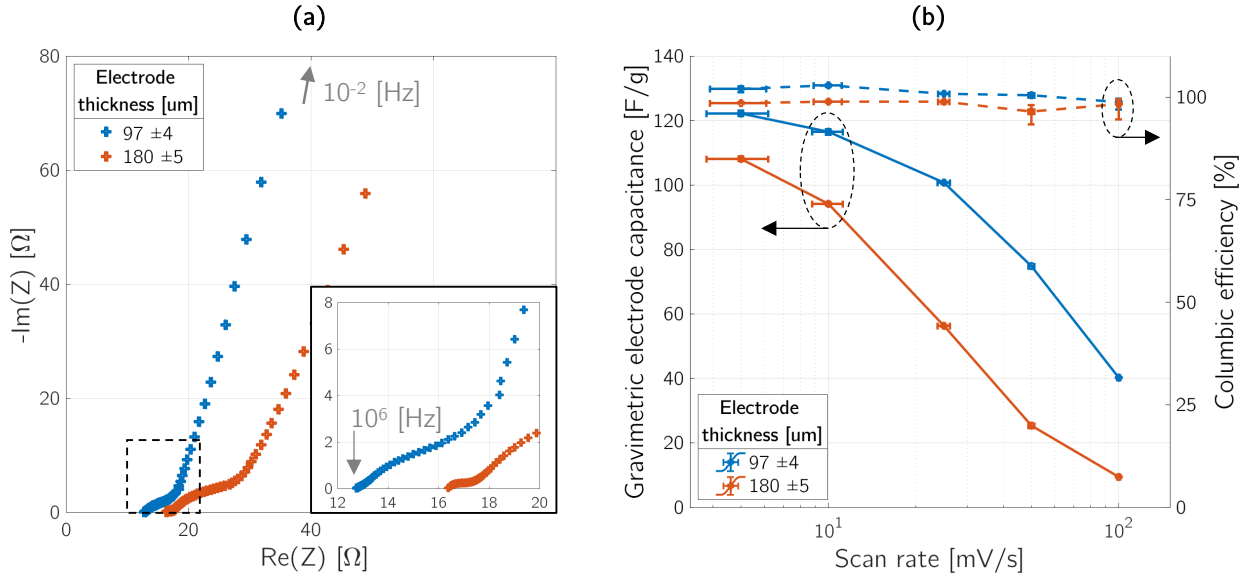

Figure 9.4.A: Effect of electrode thickness on electro-chemical performance in an AM *linear EDLC*: (a) Nyquist plot of EIS spectra and (b) rate performance.

9.4.2 Parallel cell arrangements

Internal resistance Figure 9.4.B(a) shows photographs and cross-sectional schematics of *linear EDLCs* with 1 pair of electrodes (device 1) and 2 parallel pairs of electrodes (device 2). The EIS spectra, shown in Figure 9.4.B(b), revealed that the internal resistance of the device with 2 pairs of electrodes (device 2) reduced to approximately a third of the device with 1 pair of electrodes (device 1), from 12.8 to 4.1 Ω, and not simply to a half which was observed when connecting two devices with 1 pair of electrodes in parallel (Kirchoff's law). Assuming that the electrode resistance was unchanged in both arrangements, since electrodes were fabricated using identical processing parameters, this reduction in internal resistance can be explained by the existence of a third set of ion diffusion pathways in device 2, schematically shown in the cross-sections of Figure 9.4.B(a).

Rate performance The gravimetric capacitance at relatively slow charge-discharge speeds ($\nu < 10\,\mathrm{mV\,s^{-1}}$) did not alter significantly, as expected for quasi steady-state systems where the EDL is fully saturated. However, due to the significant reduction in overall electrolyte resistance, the performance of the supercapacitor with 2 pairs of electrodes (device 2) was notably superior to the device with only 1 pair (device 1) when the scan rate was increased. The increased capacitance, indicated by a larger area enclosed by the cyclic voltammograms and highlighted by label (i) in Figure 9.4.B(d), was due to the larger available surface area (more active material) in device 2. The improved rate performance, indicated by label (ii) in Figure 9.4.B(d) was likely a result of the shortened average ion diffusion paths in the bulk electrolyte. At fast charge-discharge rates ($\nu > 100\,\mathrm{mV\,s^{-1}}$) both cell arrangements were only able to utilize a fraction of the theoretical maximum capacitance due to ion mobility limitations in the viscous electrolyte.

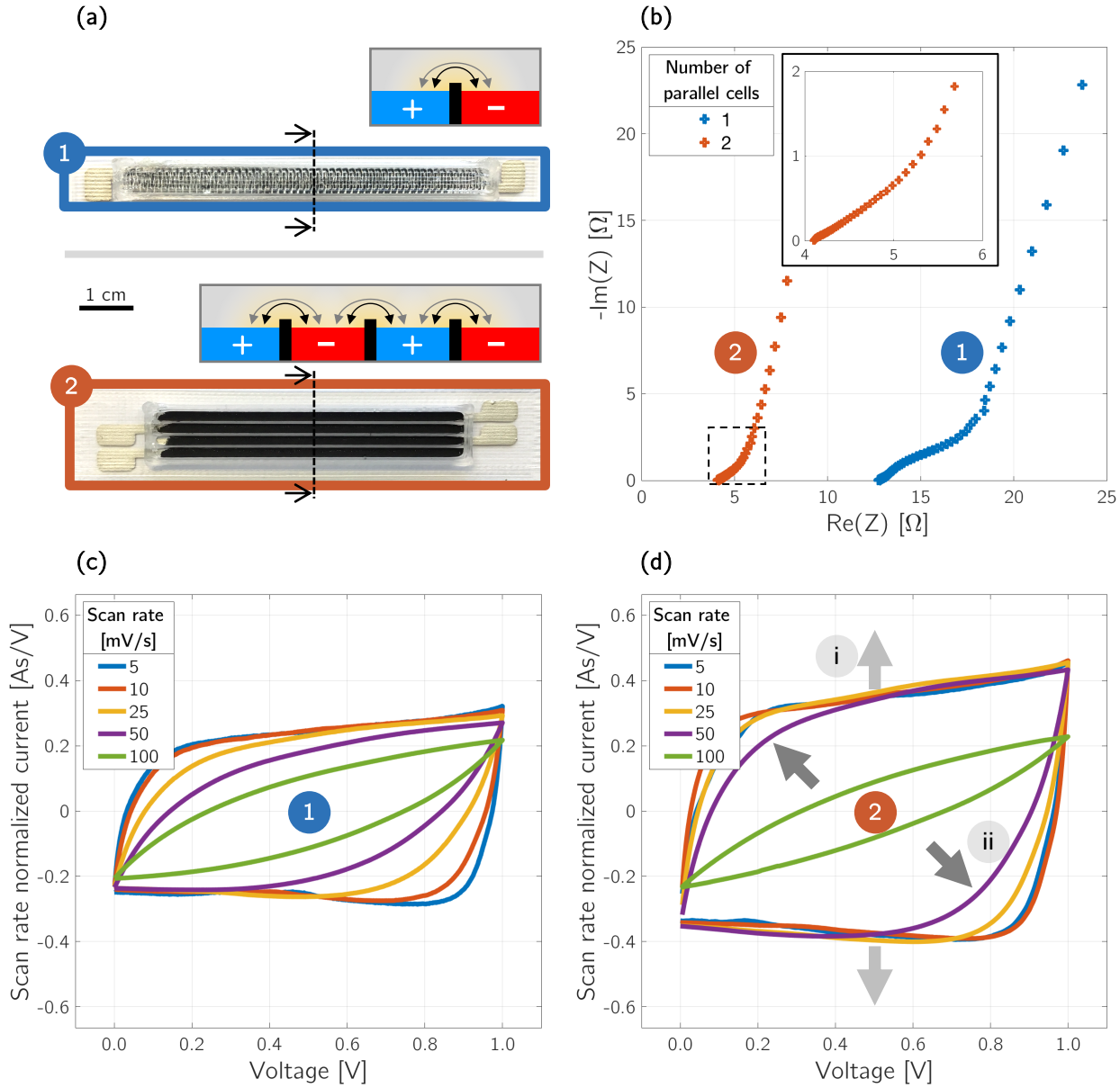

Figure 9.4.B: Electro-chemical performance of a 2-electrode *linear EDLC* (device 1) and a connected, 4-electrode *linear EDLC* (device 2): (a) photographs of a completed, enclosed device 1 and incomplete open device 2 revealing the electrode arrangement of device 2, alongside cross-sectional schematics highlighting the ion diffusion pathways, (b) Nyquist plot of EIS spectra, (c) CV rate performance for device 1 and (d) CV rate performance of device 2 showing the increased capacitance (i) and improved rate performance (ii) of a multi-cell arrangement.

9.4.3 Form factor free EDLC fabrication

An arbitrarily shaped 3D *ring EDLC*, impossible by conventional means, was fabricated in a single manufacturing operation, through the sequential manufacture of 4 and 2 electrodes (see Figure 9.4.C(a), individual manufacturing steps outlined in Section 8.2). The fully functional device was fabricated in 32 min. Through extension of this 3D fabrication approach, the geometric permutations available are endless and may offer interesting solutions for applications with irregular volumes, for example in medical implants, aerospace, defence and satellite applications. XRT scans (see Figure 9.4.C(b)) confirmed that the spatial arrangement of printed EDLC sub-components matched their intended location, with the relatively X-ray absorbing Ag-based current collectors and $LiFePO_4$ containing C-based electrodes strongly resolved by X-ray adsorption contrast.

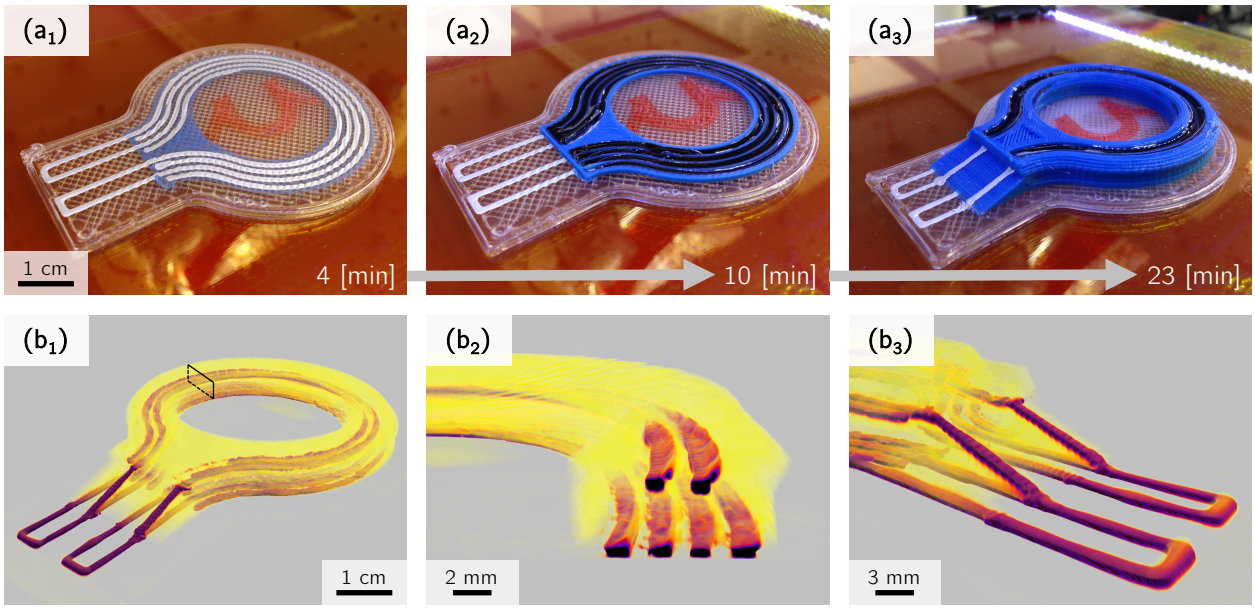

Figure 9.4.C: (a) Photographs of sequential manufacture and (b) XRT renders of 3D spatial arrangement of EDLC components. (a_1) Housing base layer (FFF) and current collectors (DIW), (a_2) electrodes (DIW) in cavities, (a_3) stacking of printed EDLCs, (b_1) complete device, (b_2) cross section showing stacked EDLC cells and (b_3) current collector bridge connecting stacked cells. An animation and videos of the manufacturing sequence can be viewed at: https://youtu.be/mmDfWsusjYw

10

Conclusions & outlook: AM of EDLCs

Impact & applications AM for the fabrication of energy storage devices, such as supercapacitors including EDLCs, may be a promising approach for high-value, niche applications where maximizing the utilisation of irregular volumes becomes desirable (e.g. powered miniature devices including medical micro-implants). Furthermore, the prospect of assembly-free, monolithic integration of printed energy storage devices in, for example, crowded micro-devices or *on-chip* applications, as well as the easy, lab-scale assessment of unconventional materials combinations and device architectures make the pursuit of fabricating functional devices through AM techniques worthwhile. AM of energy storage devices may provide opportunities in new decentralized manufacturing solutions, with emphasis on material waste minimization and reduction in part specific tooling requirements. However, in the field of mass-market, ultra high area coated electrodes for conventional supercapacitor device fabrication it is unlikely that AM will be able to rival conventional manufacturing processes in terms of economic viability, throughput and efficiency.

Novelty of work achieved In Part II of this thesis, a novel, single-operation manufacturing process to fabricate fully functioning, form-factor free supercapacitor/EDLC devices using a hybrid, multi-phase AM approach has been demonstrated. In-depth understanding of the underlying MEAM processing-science was developed and key materials/processing considerations were discussed. New functional inks were synthesized from commercial EDLC materials, and the devices fabricated by the automated hybrid-AM process were characterized. Some indicative experiments of how the inherent flexibility in AM processes may be used to explore a previously unachievable geometric parameter space was shown. The achieved performance when normalized by likely price and considering scalability

issues, cannot yet rival current mature mass-production methods, but nevertheless, the speed and ease of prototyping using hybrid-AM may allow for the development of novel materials arrangements.

Future research Remaining challenges in the field of multi-material, *multi-phase* AM for capacitors include: (a) greater understanding of the processing science (e.g. rheology, surface/interfacial energy, drying dynamics) governing individual MEAM techniques, alongside (b) insight into the interaction of materials in hybrid-AM systems, (c) the fabrication of devices with flexible, conformal substrates for new markets and applicatiosn (e.g. wearable electronics), (d) extension of the printable materials palette to advanced functional materials, and (e) in-operation quality control techniques for responsive process development. Specifically with respect to AM of energy storage devices, the development of printable separators (ion permeable, electron insulating) would allow for designs that facilitate shorter, more efficient ion diffusion pathways while allowing more freedom for the fabrication of fully/arbitrary 3D cell configurations. The ability to control the surface energy of FFF extrudates and DIW inks would allow engineering of the many interfaces between inks and polymers that are implicit to multi-material manufacturing schemes. The layer-by-layer nature of AM techniques can also facilitate the investigation of heterogeneous or *structured* electrodes with enhanced performance [212, 262].

Part III
In-line characterization of dielectric properties

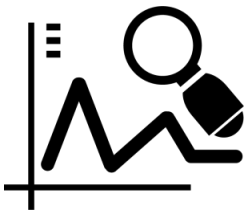

Summary

AM techniques are used increasingly for the direct fabrication of microwave devices, such as graded index lenses and dielectric resonator antennas, which have spatially-varying dielectric properties (i.e. relative permittivity) that are difficult to manufacture using traditional methods. However, there is no effective method to characterize the spatial distribution of permittivity within the printed component, either during manufacture or once the component is complete. Therefore it is not possible to confirm the extent to which the manufactured spatial distribution of permittivity meets the intended design. In Part III of this thesis, a split ring resonator (SRR) surface mapping technique is directly integrated into an AM process using the hybrid-AM environment from Part I, to make non-destructive *in-line* measurements of the local dielectric permittivity (ε_r) within 3D objects as they are formed. These data are then reconstructed into 3D dielectric "images" of the printed component. Detailed insights into the dielectric imaging principle, data processing/analysis, as well as limitations and opportunities related to the technique are described. The work aims to accelerate the design-make-test cycle for advanced microwave devices, and suggests the possibility for real-time, *closed-loop* control of dielectric properties during AM.

11

Introduction: Electro-magnetic characterization

11.1 Characterization of material properties in AM 121
11.2 Additive manufacturing of radio frequency devices 123
11.3 Electro-magnetic characterization techniques 123
11.4 Objectives for Part III 124

11.1 Characterization of material properties in AM

The need for data in AM Despite significant progress in the utility, flexibility, speed and accuracy of AM or *3D-printing* technologies, a common, un-met requirement described in review papers and by practitioners is the desire for greater availability of real-time data associated with the evolution of properties within a printed part [278, 279]. For example, in the case of powder bed fusion techniques (such as SLM that use metallic powders and a laser to selectively fuse the powder), the *in-situ* real-time distribution of temperature both at fine scale in/near the beam/powder interaction volume, and at the macro-scale over the entire developing 3D object [280–283], is considered useful to understand and ultimately control the tendency for defects such as voids and pores, stresses and distortion, and surface finish [284]. More generally, real-time data could be used to: (a) verify the integrity of parts manufactured by AM (i.e. for quality control (QC) or quality assurance) [285, 286]; and (b) facilitate *reactive manufacturing* and to *close the loop* for dynamic error mitigation by response to live production data [87, 287].

Existing techniques Measurement or metrology systems used in AM processes are generally used to either monitor the manufacturing system parameters (such as bed/nozzle temperatures, deposition speed or rheological properties of extrudates [286, 288, 289]), or characterize the properties of the printed part (e.g. relating to the internal distribution of mechanical material properties [290]). The latter techniques may be further classified as: (a) in-line/in-situ or ex-situ (e.g. integrated strain sensors [290] or post-print XRT analysis [291]), (b) destructive or non-destructive [124, 285], and (c) direct or indirect (e.g. using a proxy such as mechanical impedance for identifying build defects [292]). Different techniques may also be needed for different material classes [139, 293], speed of measurement (e.g. high-speed optical sensing for material jetting [294] or thermography for electron beam melting [287]), and depend on the property of interest, such as strain and temperature [295], tensile properties [296] or surface roughness [297].

Challenges & limitations In terms of integrating these metrology systems directly into AM processes, challenges include: (a) spatial restrictions – the physical space available to place sensors in the apparatus, especially near the deposition/build zone, is often severely constrained; (b) temporal penalty – acquiring data may be relatively slow so the production rate is undermined; (c) material restrictions – many characterization techniques are restricted to certain material classes e.g. metals [285, 293]; and (d) data analysis – there is limited understanding of the relationships between the properties that can be measured in the AM environment and the final component properties that are required.

Dielectric imaging In Part III of this thesis, the dielectric permittivity (ε_r) of just-printed polymers is investigated in real-time. The local permittivity and its spatial distribution is of interest because ε_r along with the magnetic permeability (μ_r) control the refractive index (n) of the material according to $n = \sqrt{\varepsilon_r \mu_r}$. The control of the refractive index allows the single-operation, direct fabrication (using AM) of novel optical devices for microwave or RF applications [124, 298, 299]. It should be noted, that ε_r may also be a useful proxy measurement of printed properties in other non-metallic AM applications, for example in detecting printing voids. Although there are various well-known characterization techniques for measuring ε_r, their incorporation *in-line* with an AM process has not been reported, and most are unsuitable for the AM environment.

11.2 Additive manufacturing of radio frequency devices

Microwave or RF devices that rely on the controlled spatial variation of EM properties include invisibility cloaks, graded index lenses or dielectric resonator antennas [300–303]. However, engineering progress towards realizing such devices has been slow due to the limitations imposed by conventional manufacturing approaches that are required, for example, to create periodic resonant structures (e.g. metals or ceramics) at sub-wavelength spacing and at large scale [304]. Because AM forms parts incrementally, *layer-by-layer*, it provides an opportunity to overcome these conventional limitations by depositing/building different materials at different locations and with sufficient, sub-GHz wavelength resolution. For example, FFF has been used to print selectively in different places a variety of particulate composite materials, each with a different ε_r to form a graded index lens [124]. Other approaches include IJP or assembly of heterogeneous metal-polymer composites [305]. Moreover, the layer-by-layer nature of AM can be exploited by measuring each layer, or each track within a layer, *in-line* and throughout build [87, 290], and then reconstructing these data in 3D.

11.3 Electro-magnetic characterization techniques

EM characterization Techniques for characterizing the EM properties of dielectric materials and devices have been reviewed frequently [306–308] and may generally be classified as: (a) resonant or non-resonant (e.g. split post dielectric resonator (SPDR) [309] or parallel plate capacitors [310]), (b) free-space or guided (e.g. scattering patterns [311] or waveguide measurements [312]), and (c) reflection or transmission (e.g. a 1-port coaxial probes [313] or 2-port striplines [314]). Other attributes of EM characterization techniques include: (a) the sampled frequency range (e.g. narrow- or broad-band), (b) the required resolution, (c) sample preparation requirements (e.g. surface roughness/finish or sample dimensions), (d) the nature or type of the material (i.e. solids, gels or liquids), (e) destructive or non-destructive (i.e. requiring physical modification/contact with the sampled part), and (f) cost. Novel approaches to measuring the spatial ε_r distribution of a solid surface include a 2D mapping technique using a SRR [139] and a technique based on multi-angle reflection ellipsometry [315].

Limitations of current EM characterzation techniques Of the available EM characterization techniques, only few might be considered suitable for easy, direct integration into AM processes, and limitations include: (a) danger of cross-contamination and damaging of the printed part through probe contact; (b) the need for controlled ambient EM environments; and (c) stringent requirements on surface roughness and other geometric tolerances.

11.4 Objectives for Part III

Part III shows proof-of-concept for a non-destructive, non-contact dielectric imaging technique, *in-line* with an AM process to characterize the spatial distribution of dielectric permittivity (ε_r) within a printed part. The following objectives are addressed:

(a) **engineer a non-destructive dielectric probe** – to engineer and characterize a non-destructive, non-contact probe to measure the dielectric permittivity of an as-printed substrate, suitable for direct integration *in-line* with MEAM processes; and

(b) **demonstrate 3D dielectric imaging** – to demonstrate proof-of-concept for the real-time, non-destructive acquisition of dielectric data during AM (in three dimensions), providing quantified insight into the internal distribution of the local dielectric permittivity within a printed part.

12

Materials & methods

12.1 Hybrid-AM 125
12.2 Electro-magnetic characterization techniques 128
12.3 Simulation 130

12.1 Hybrid additive manufacturing

Hybrid-AM machine With reference to the labels in Figure 12.1.A(a), the hybrid-AM machine from Part I of this thesis was fitted with: (i) an in-house built split ring resonator (SRR) module (see Section 5.4.3) connected to (ii) a VNA (ZNB20, Rohde Schwarz, Germany) and (iii) a computer running the hybrid-AM app from Section 3. Multiple (iv) fabrication modules including FFF extrusion heads were installed for the purpose of fabricating multi-material devices on (v) a temperature controlled build platform. The primary parameters describing the geometry and operation of the SRR sensor are shown in Figure 12.1.A(b) and (c).

Control software The printing host, or hybrid-AM app, (see Section 3 in Part I) was configured for simultaneous control of the hybrid-AM machine and a VNA, i.e. to send, receive and log commands or queries to/from the various micro-electronic and measurement sub-systems. The printing host provided a computer-based platform to interact with all system components and also allowed for: (a) debugging of control commands and queries (i.e. the g-Code), (b) manual machine control (e.g. for calibration purposes), and (c) analysis and visualization of production/characterization data. A screenshot of the printing host GUI showing some of the input/output tabs specifically designed for dielectric imaging, is shown in Figure 12.1.B.

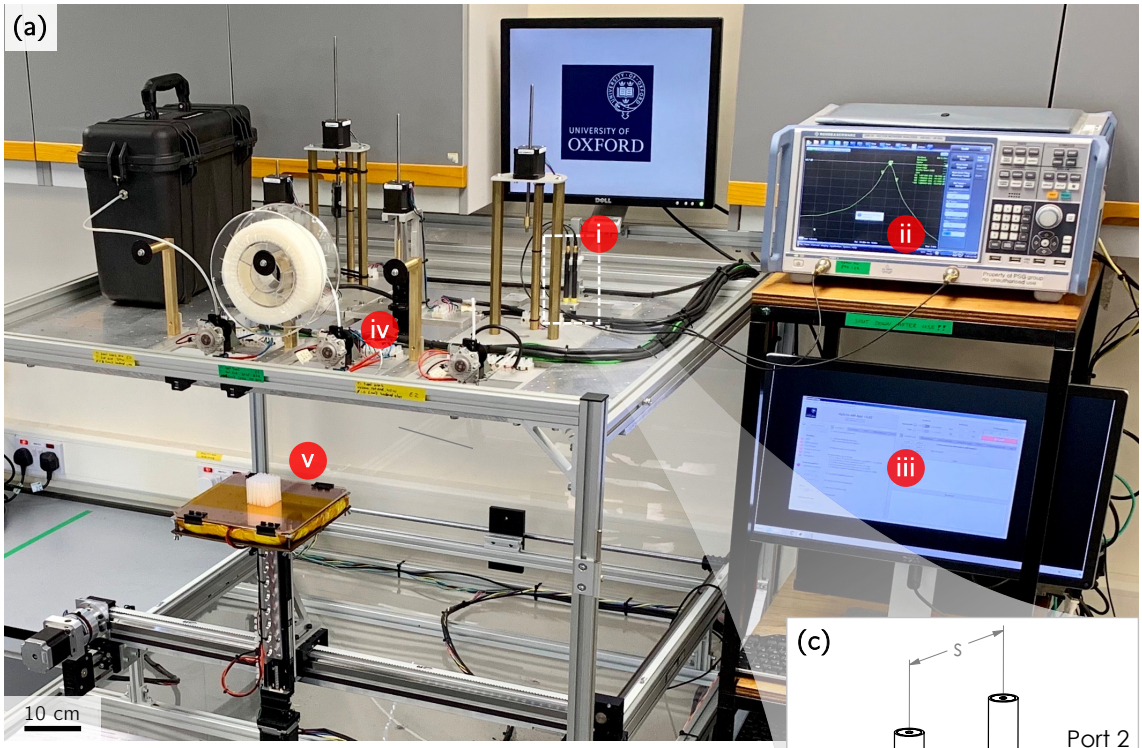

(b)

	Constant		Description
Δf	0.005	GHz	Frequency sweep resolution
g	0.55	mm	Air gap in SRR
h	1	"	Thickness of SRR ring
R	10	"	Internal radius of SRR
w	2	"	Width of SRR ring
q	0.5	"	Ring-sample separation
s	8	"	Probe separation
t	0.2	"	Layer thickness

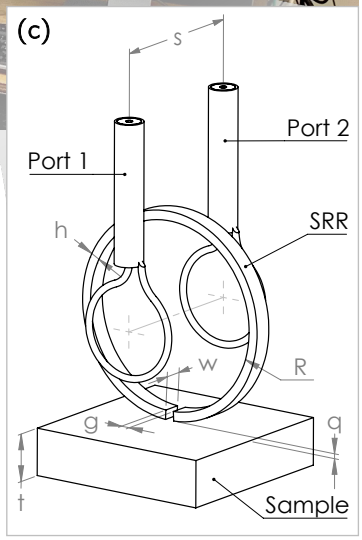

Figure 12.1.A: (a) A photograph of the hybrid-AM machine showing: (i) the SRR probe connected to (ii) a VNA, (iii) a control computer, (iv) functional modules including FFF hot-ends and (v) the temperature controlled build platform. (b-c) The primary geometric and operating parameters used for the SRR probe.

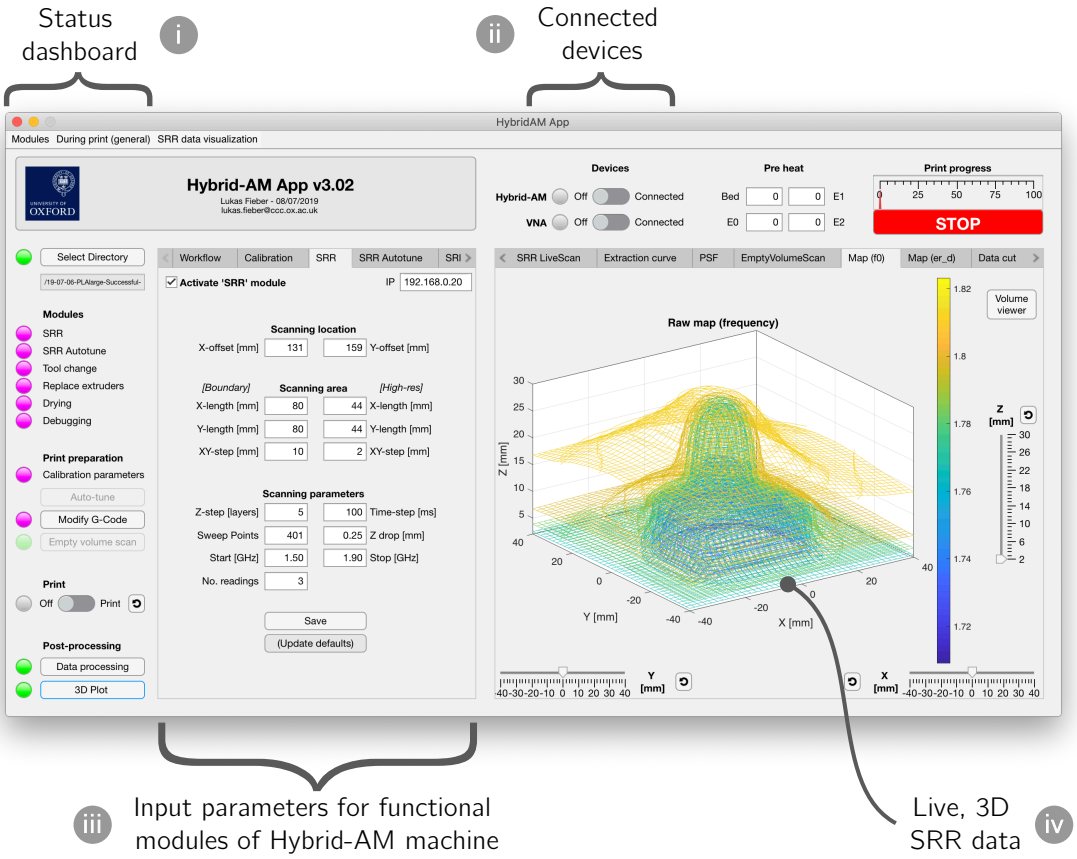

Figure 12.1.B: Screenshot of the GUI for the hybrid-AM app showing (i) the status dashboard and activated functional modules, (ii) connected devices, (iii) module specific tabs for inputting parameters and (iv) live 3D contour plots of the SRR data during print.

Device design and fabrication The hybrid-AM workflow from Section 2.3 in Part I was followed: 3D parts for AM were designed in CAD software (*SolidWorks 2017*) before being exported as surface geometries (`.STL` files). Open source slicing software (*Slic3r v1.3.0*) was used to generate a *layer-by-layer*, machine interpretable code (`g-Code`), which was thereafter automatically modified by the printing host (post-slicing modifications, see Section 3.4.2) to: (a) reflect calibration values for the hybrid-AM machine, and (b) include tool-paths and other commands for automatically characterizing the device as it formed (i.e. using the SRR probe). AM parts were fabricated using a FFF hot-end (TitanAero from E3D, UK with a $\varnothing 0.6\,\text{mm}$ brass nozzle) with a commercially available polymer filament (Natural PLA from Spoolworks, UK) with $\varepsilon_r = 2.71 \pm 0.06$ at print speeds of $30\,\text{mm}\,\text{s}^{-1}$, and nozzle/build-platform temperatures of $192\,^{\circ}\text{C}$ and $40\,^{\circ}\text{C}$ respectively. The ε_r of printed PLA was considered to be independent of temperature at frequencies in the low GHz spectrum [219].

12.2 Electro-magnetic characterization techniques

Split ring resonator probe Figure 12.2.A schematically illustrates the operating principle of the SRR probe: (a) two $\vec{\mathbf{H}}$ field probes (RF-R 50-1, Langer EMV, Germany) were placed at equal distance from a single Cu split ring resonator (SRR), at a separation distance $s = 8\,\text{mm}$ and connected to a VNA using flexible coaxial cables (1 m SMA-SMA, Langer EMV, Germany); (b) the probes induced an electric field ($\vec{\mathbf{E}}$ field) across the SRR and its fundamental resonant frequency (f_0) in free space was evaluated by searching for the local maximum in transmission (S_{21}) over a frequency sweep $f \in [1.5, 1.9]$ GHz at specified resolution $\Delta f < 1\,\text{MHz}$; (c) f_0 was then influenced by the presence of an introduced material with $\varepsilon_r > 1$ in the fringing $\vec{\mathbf{E}}$ field across the SRR air gap that resulted in; (d) a shift in f_0 that was recorded by the VNA. Finally, (e) contributions related to the sample ε_r were isolated from other factors and, (f) by post-processing of the SRR resonant frequency map $f_0(\vec{\mathbf{x}})$; a (g) spatial permittivity map $\varepsilon_r(\vec{\mathbf{x}})$ was obtained.

EM properties of printed filaments For validation, the intrinsic dielectric permittivity of the printed PLA filament was measured using conventional Nicolson-Ross-Weir (NRW) waveguide methods according to [316]. Reflection and transmission data was collected from a 2 mm thick sample (printed using FFF, 100 % infill) which was placed in a rectangular waveguide (No. 18094-SF40, Flann, UK) operating in mode $TE_{1,0}$ over the frequency range 12 to 18 GHz.

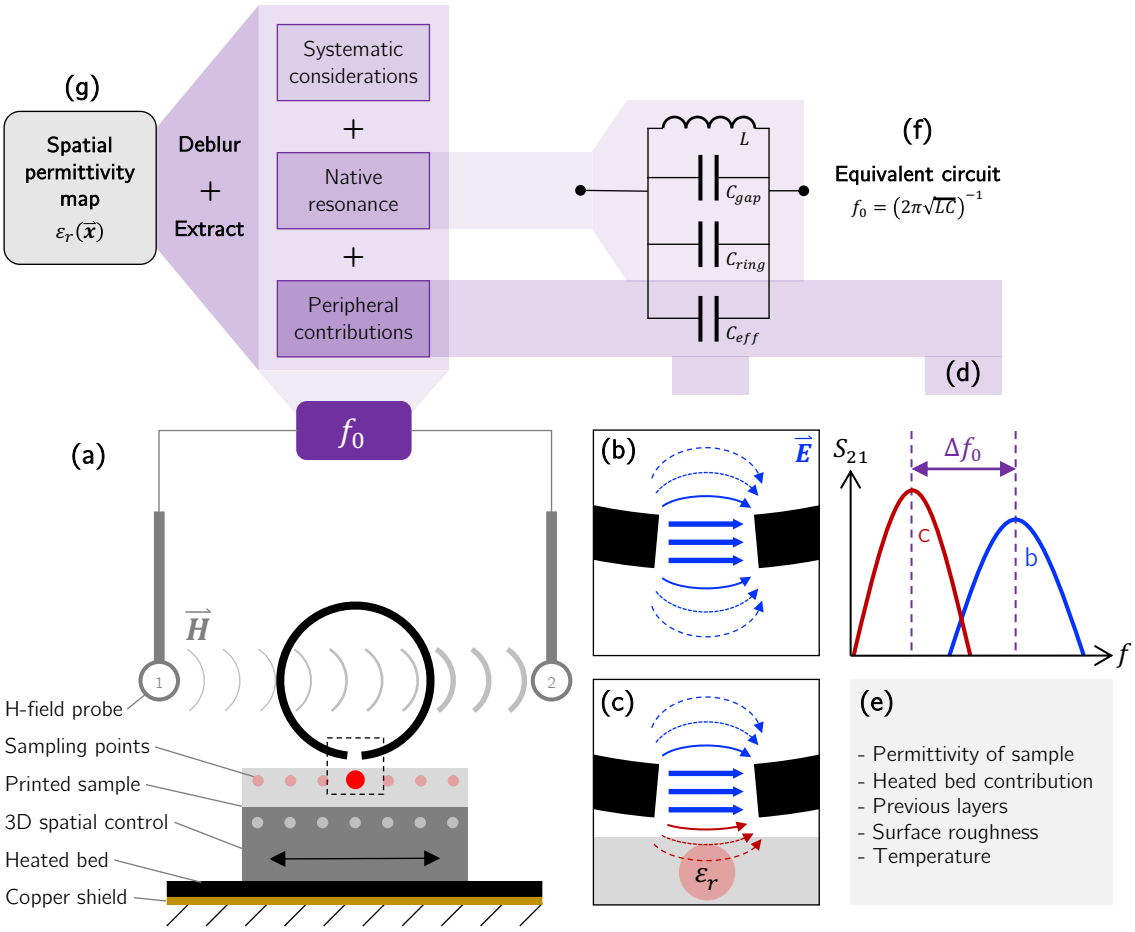

Figure 12.2.A: A schematic illustration of the SRR operating principle depicting: (a) the SRR, (b) the $\vec{\mathbf{E}}$ field in free space and (c) under the influence of a material $\varepsilon_r > 1$, (d) the resulting shift in resonant frequency Δf_0, (e) a sub-set of parameters influencing the resonant frequency, (f) an equivalent circuit for interpreting the frequency shift, and (g) the resulting spatial permittivity map.

12.3 Simulation

Full-wave EM simulations of the SRR system were conducted in *Comsol Multiphysics*. The geometry of the SRR probe was derived from a CAD model with dimensions comparable to the experimental set-up shown in Figure 12.1.A. The $\vec{\mathbf{H}}$ field probes were modelled as simplified, planar (2D) rings of $\varnothing 10\,\text{mm}$, equi-distant from the SRR with a probe-probe separation distance $s = 8\,\text{mm}$ and lumped port impedances of $50\,\Omega$ to model the coaxial, SMA connectors used in experiments. The SRR was modelled as an ideal, perfect electric conductor in free space (without the SRR holder, see Figure 12.3.A), and all surfaces were considered to be perfectly flat. The quasi-infinite, spherical finite elements model (FEM) boundary was defined as a perfectly matched layer (PML). The FEM mesh size was limited to $< \lambda/5$, and areas of interest (e.g. between the SRR gap and sample) were refined by a factor of 4 to provide mesh-independent solutions. The SRR resonant frequency f_0 was determined numerically using a coordinate search $f \in [1.5, 3]$ GHz, maximizing for the port transmission parameter S_{21}, i.e. f_0 at $max(S_{21})$, to an optimality tolerance of $S_{21,dB} < 0.005$ (approximately equal to the nearest 1 MHz to match the VNA sweep resolution used in experiments). Figure 12.3.A shows that the transmittance response $S_{21}(f)$ of the simplified, simulated SRR probe matched the experimental data closely, with experimental and simulated values of f_0 matching to within $\pm 2\,\text{MHz}$.

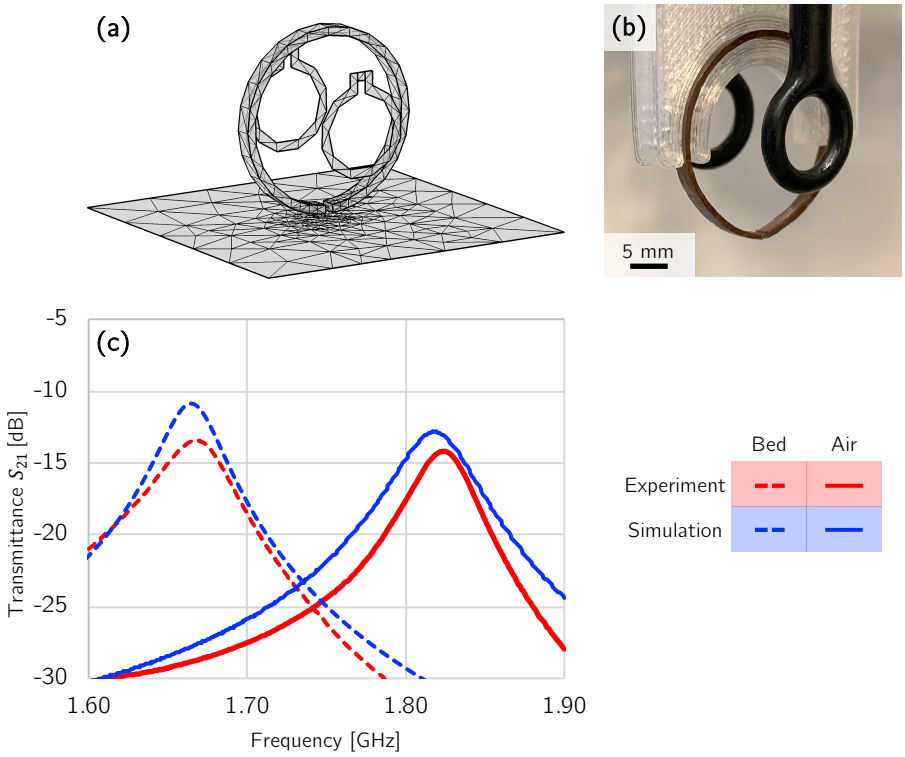

Figure 12.3.A: A comparison of the transmission parameter S_{21} between (a) simulation and (b) experiments for a SRR in free space ($\varepsilon_r = 1$) and in proximity to the build platform ($\varepsilon_r = 5.6$).

13

Results & discussion

13.1 Overview of results 133
13.2 Measurement: In-line sampled frequency map 135
13.2.1 Geometric factors influencing the intrinsic resonant frequency 137
13.2.2 Considerations related to the SRR system 139
13.2.3 Peripheral contributions 143
13.3 Deblurring: Improving spatial resolution 147
13.4 Extraction: Interpreting the resonant frequency 150

13.1 Overview of results

The key steps involved in measuring the spatial distribution of dielectric permittivity (ε_r) within printed parts were: (i) the resonant frequency (f_0) of the split ring resonator (SRR) was measured (i.e. sampled at discrete locations *layer-by-layer* and *in-line* with AM), (ii) a deblurring post-processing step was applied to enhance the spatial resolution, and finally (iii) an *extraction* model was applied to obtain a 3D, spatial $\varepsilon_r(\vec{\mathbf{x}})$ map of the printed object. Figure 13.1.A schematically shows steps (i) to (iii) above, alongside corresponding 3D contour maps of experimental data showing the resonant frequency for: (a) an empty build platform, termed $f_{ref}(\vec{\mathbf{x}})$, (b) an arbitrary 3D shape (PLA, 100 % infill), termed $f_0(\vec{\mathbf{x}})$, and (c) the same shape after deblurring, termed $f_{0d}(\vec{\mathbf{x}})$. Note that the 3D data presented in Figure 13.1.A is a reconstruction of successive X-Y imaging planes incrementing in the Z direction.

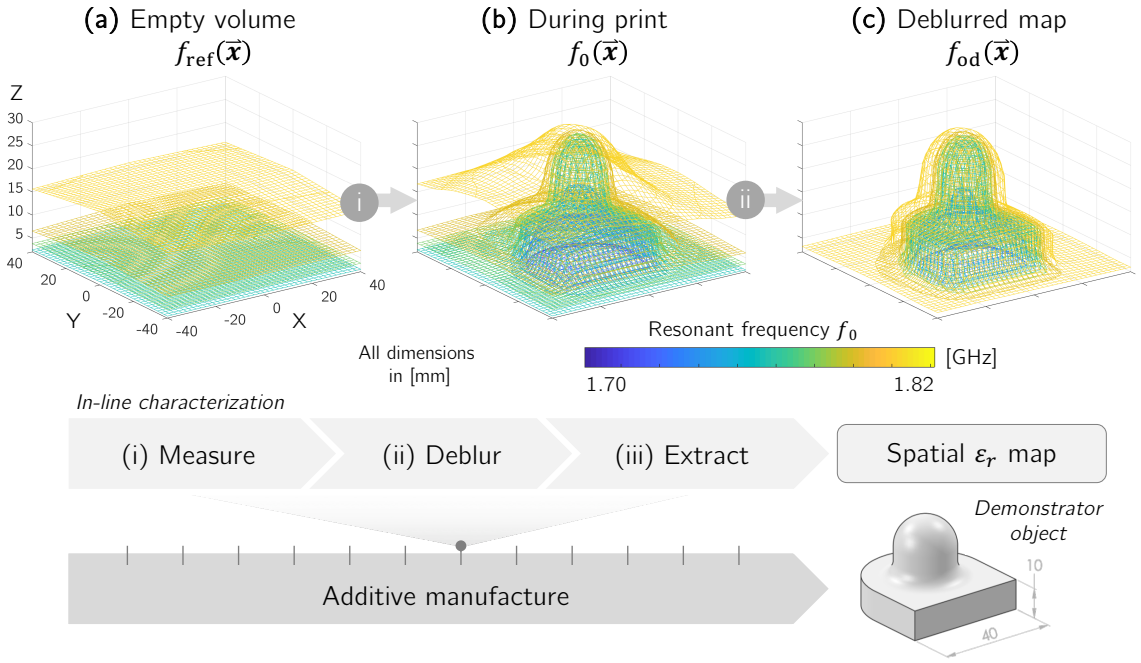

Figure 13.1.A: A schematic flowchart of the steps (i-iii) involved in the non-destructive, *in-line* dielectric characterization technique and 3D contour maps of resonant frequency (f_0) data for: (a) an empty build $f_{ref}(\vec{\mathbf{x}})$ (free space), (b) during manufacture of the demonstrator object, showing the permittivity contribution of the printed part $f_0(\vec{\mathbf{x}})$, and (c) the sample data after deblurring $f_{0d}(\vec{\mathbf{x}})$.

13.2 Measurement: In-line sampled frequency map

Figure 13.2.A(a) shows a photograph of the SRR probe in relation to a printed demonstrator during the later stages of fabrication. Figure 13.2.A(b), (c) and (d) show *raw*, unprocessed experimental resonant frequency data from *in-line* measurement: (b_1) is a Y-Z plane in free space showing only the (weak) permittivity influence of the build platform, i.e. $f_{ref}(\vec{\mathbf{x}})$, and ($b_2$) is the same Y-Z plane but now with the additional contribution/influence of the printed object, i.e. $f_0(\vec{\mathbf{x}})$; (c) is a X-Y plane of $f_0(\vec{\mathbf{x}})$, and (d) is the reconstructed data in 3D showing the location of the preceding 2D sections shown in (b) and (c). The local resonant frequency was influenced by: (i) the native or *intrinsic* f_0 of the SRR probe, (ii) contributions from the overall ambient environment/system, and (iii) a contribution from the just-printed part (referred to as *peripheral* contributions). Factors (i-iii) are now described in Sections 13.2.1 to 13.2.3 respectively.

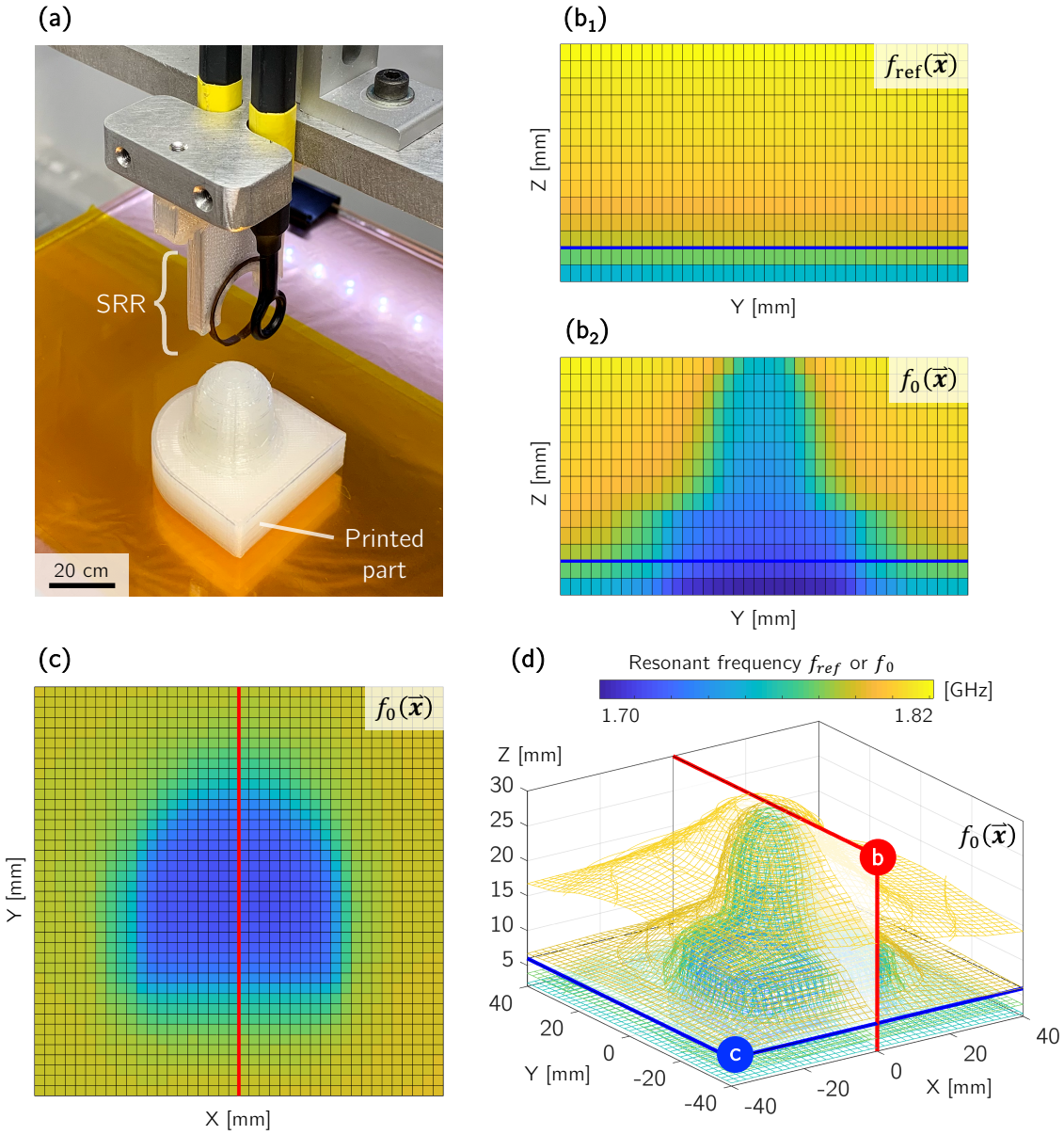

Figure 13.2.A: (a) A photograph of the SRR probe during operation and (b-d) *raw*, unprocessed experimental resonant frequency data from *in-line* measurements: (b_1) a Y-Z plane showing only the contribution of the build platform, (b_2) the same Y-Z plane with additional contributions from the printed part, (c) a X-Y plane of the frequency data in (b_2) and (d) a 3D contour map showing the location of the cross-sections in (b) and (c).

13.2.1 Geometric factors influencing the intrinsic resonant frequency

The intrinsic resonant frequency of the SRR (i.e. f_0 for an ideal, singly split ring resonator in free space with permittivity and permeability ε_0 and μ_0 respectively, excluding any peripheral contributions) may be modelled as an equivalent electronic L-C circuit as expressed in Equation (13.1). The total capacitance of the resonating system C_{tot} is given by Equation (13.2): the sum of the parallel plate capacitance C_{gap} (across the air gap), and the capacitance of the SRR surface C_{ring}. The magnetic inductance L as well as C_{gap} and C_{ring} may be expressed analytically from [317], see Equations (13.3) to (13.5), as a function of geometric SRR parameters (ring width w, thickness h, internal radius R and air gap g, defined in Figure 13.2.B(a) and (b)). Figure 13.2.B(c) shows a plot of the analytical equations for geometric parameters comparable to those used for the *in-line* dielectric characterization technique. R_m was defined as the average radius of the SRR, i.e. $R_m = R + w/2$.

$$f_{0,air} = \frac{1}{2\pi\sqrt{LC_{tot}}} \tag{13.1}$$

$$C_{tot} = C_{gap} + C_{ring} \tag{13.2}$$

$$C_{gap} = \varepsilon_0 \left(\frac{hw}{g}\right) + \varepsilon_0(h + w + g) \tag{13.3}$$

$$C_{ring} = 2\varepsilon_0 \left[\frac{h + w}{\pi} \ln\left(\frac{4R}{g}\right)\right] \tag{13.4}$$

$$L = \mu_0 R_m \left[\ln\left(\frac{8R_m}{h + w}\right) - \frac{1}{2}\right] \tag{13.5}$$

(a*)

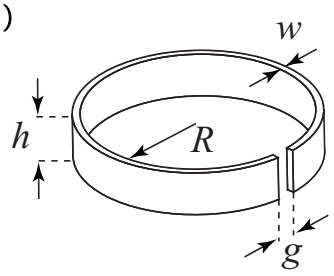

(b)

	Dimension		Description
g	0.25	mm	Air gap
h	1	"	Thickness
R	10	"	Internal radius
w	2	"	Width

*Schematic in (a) from Sydoruk et al., 2009

(c)

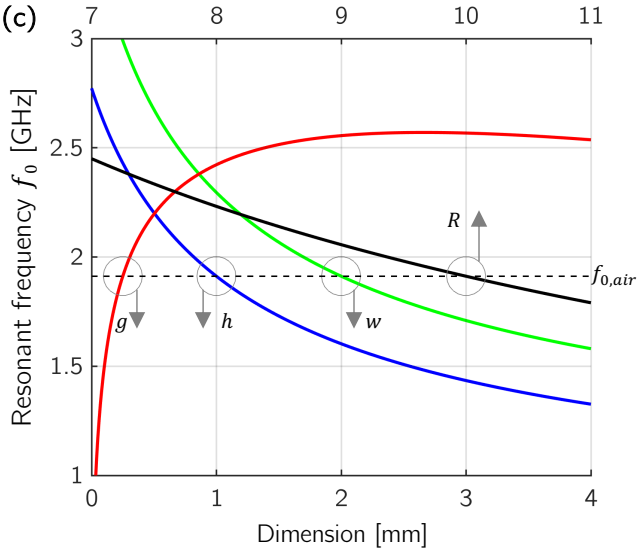

Figure 13.2.B: (a-b) Definition of the SRR parameters used, and (c) the intrinsic resonant frequency (f_0) of the SRR in free space as a function of the geometric parameters.

13.2.2 Considerations related to the SRR system

The control system (e.g. meshing distribution/density and NC parameters) as well as the calibration of the SRR system (e.g. mechanical offset, perpendicularity of the probe to the print-bed) influenced the quality of 3D SRR measurements (i.e. the *raw* data: $f_{ref}(\vec{\mathbf{x}})$ and $f_0(\vec{\mathbf{x}})$ in Figure 13.1.A).

Meshing A series of time-saving measures were implemented in the automated meshing process to speed up the sampling: (a) a *coarse*, 9-point mesh and skipping of sampling layers for the *empty volume scan* $f_{ref}(\vec{\mathbf{x}})$, and (b) a variable mesh density with a high resolution core (where the printed part was) and a coarse perimeter. Figure 13.2.C illustrates the different mesh densities. To generate a map with uniform denisty, missing data points were interpolated using a spline algorithm. Applicable metadata (e.g. the size and location of the printed part) was automatically extracted from the `g-Code` by the hybrid-AM app.

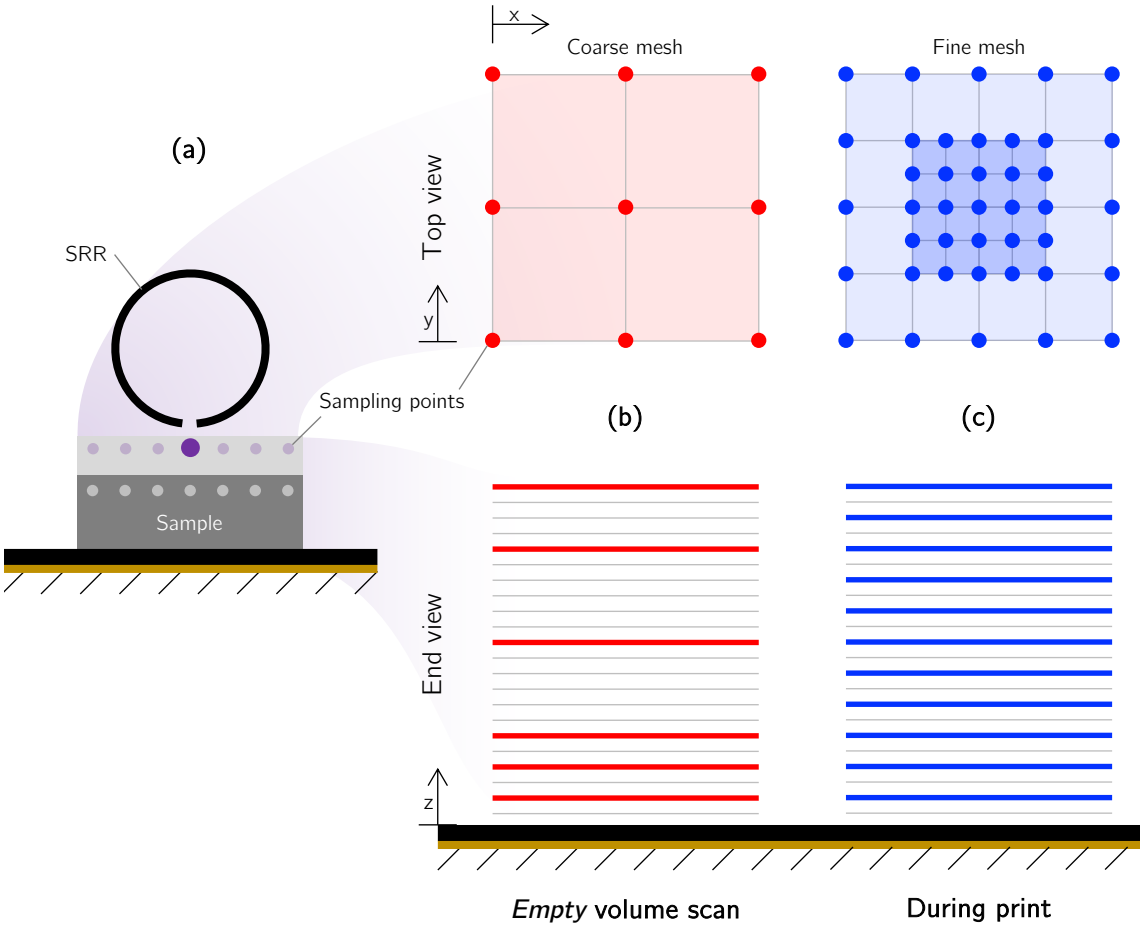

Figure 13.2.C: Schematic illustration of the meshing process showing (a) an end-view of the SRR in relation to the sample and sampling points, (b) the *coarse* mesh used for scanning $f_{ref}(\vec{\mathbf{x}})$ and (c) the *fine* mesh used for scanning $f_0(\vec{\mathbf{x}})$.

Electro-magnetic shield and equivalent bed permittivity The build platform was comprised of a glass plate (4 mm thick borosilicate glass, $\varepsilon_r = 4.6$ [318]), a heated silicone bed with internal electronics (heaters, sensors, wiring) and mechanical fixtures (e.g. Al bars and insulation material). Figure 13.2.D(a) shows that the recorded f_0 was noticably influenced by the silicon bed and fixtures which may be interpreted as unwanted *background noise* ($\sim 25\,\%$ of the dynamic range DR_{bed} for $\varepsilon_r \in [1, 5]$). An EM shield (Cu foil) was inserted between the silicon bed and glass plate to reduce this effect (see Figure 13.2.D(b)). The introduction of Cu with very high dielectric permittivity ($\varepsilon_r \to \infty$) and the influence this had on the reference frequency $f_{0,bed}$ was considered. To simplify the extraction model, the build platform was considered to have an *equivalent* permittivity of $\varepsilon_r = 5.6$ (see Figure 13.2.E).

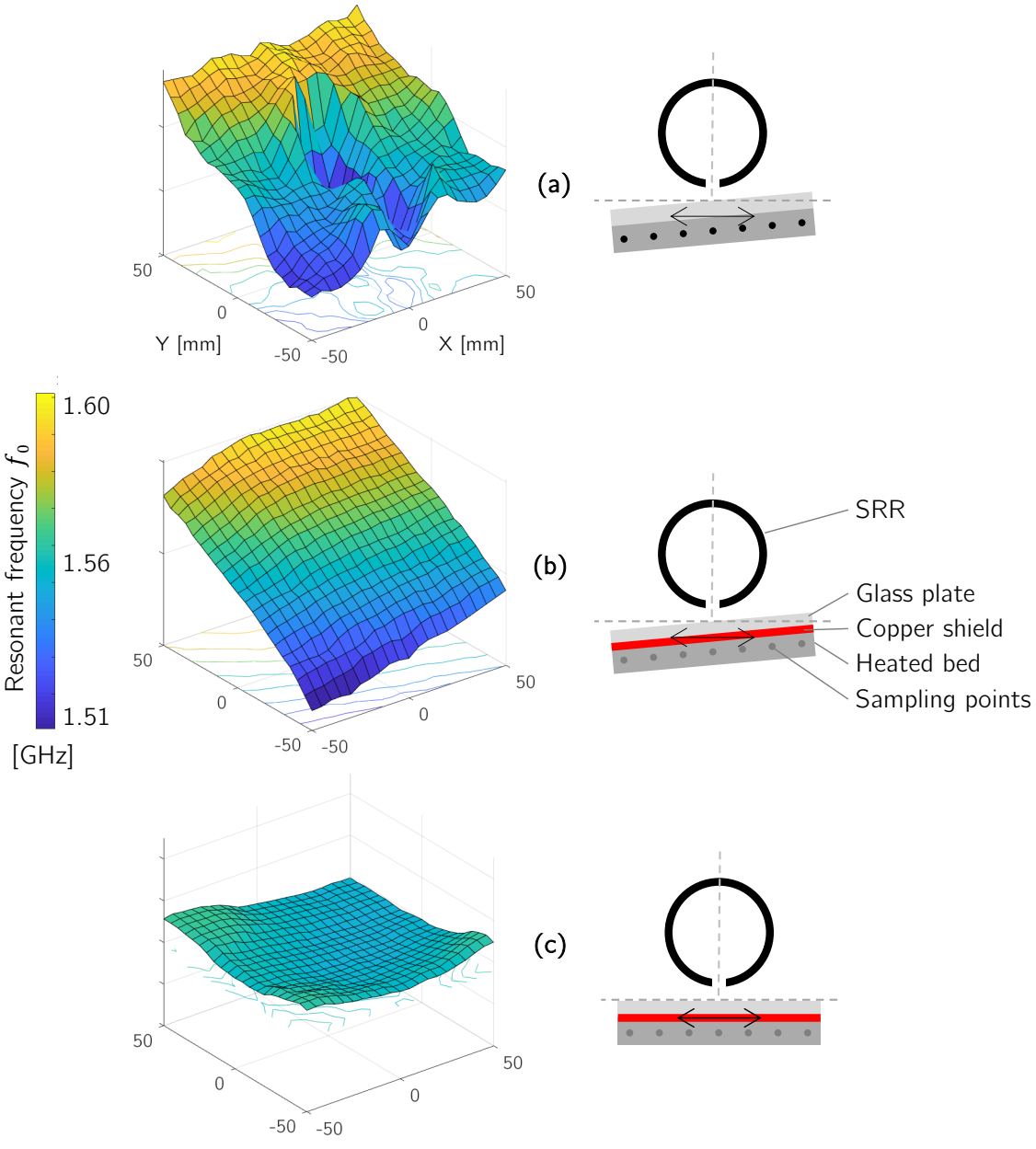

Figure 13.2.D: Experimental data for an XY-scan of SRR resonant frequency f_0 for an empty build-plate showing: (a) build plate, consisting of a glass plate and heated bed, not parallel to build-plate motion, (b) the addition of a copper shield as electric conductor and (c) build plate with copper shield parallel to motion.

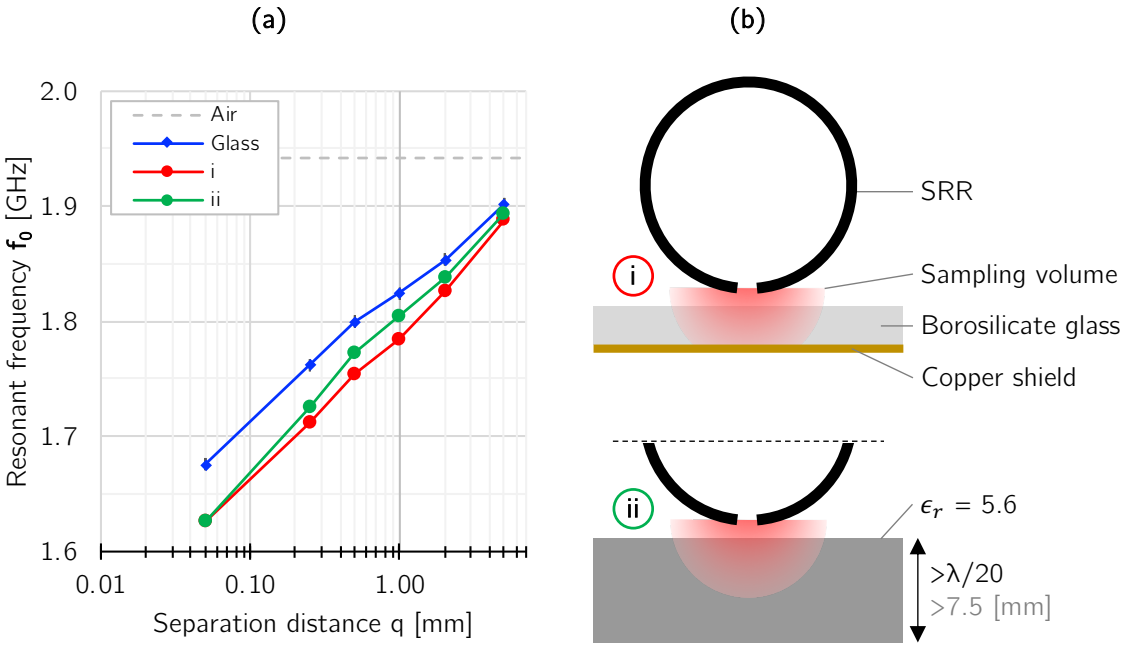

Figure 13.2.E: (a) Simulation data showing the resonant frequency (f_0) as a function of separation distance q for (b) various build-plate configurations: (i) a borosilicate glass plate with a Cu shield and (ii) a simplified build platform of quasi-infinite thickness with an overall equivalent permittivity of $\varepsilon_r = 5.6$.

13.2.3 Peripheral contributions

Permittivity dependence While both the intrinsic f_0 of the SRR, and any ambient environment/systematic contributions were considered to remain constant throughout sampling, the shift in f_0 with position, i.e. $f_0(\vec{\mathbf{x}})$ in Figure 13.2.A, was attributed to a change in the local environment (i.e. the *peripheral* conditions) sampled by the SRR. This arose due to distortion of the fringing fields associated with the induced $\vec{\mathbf{E}}$ field across the SRR gap (schematically illustrated in Figure 12.2.A(c)) when close to materials with a permittivity different from air. This may be interpreted as a change in total ring capacitance (contribution of C_{eff} in Figure 12.2.A(f)), and leads to the measured shift in f_0. By simulating the SRR close to an ideal, quasi-infinite material with user-specified, varying EM properties ($\varepsilon_r \in [1, 50]$), a logarithmic relationship between f_0 and ε_r was established:

$$\frac{\partial f_0}{\partial \varepsilon_r} \propto \frac{M_e}{\varepsilon_r} \tag{13.6}$$

where M_e was a best-fit coefficient dependent on the SRR geometry. Data to support Equation (13.6) is shown subsequently in Figure 13.4.A(b).

Probe-sample separation distance Both simulation and experiment showed the SRR resonant frequency was sensitive to the probe-sample separation distance (q). Equation (13.7) below expresses the relationship between f_0 and q that was established by simulating a quasi-infinite sample (i.e. all sample dimensions exceeding the sampling volume size) with $\varepsilon_r \in [1, 10]$ for $q > 0.05\,\text{mm}$:

$$\frac{\partial f_0}{\partial q} \propto \frac{\exp(M_q \times q^n)}{q^{1-n}} \tag{13.7}$$

where $n = 0.1$ and $M_q < 0$ were best-fit coefficients. Data to support Equation (13.7) is again shown subsequently in Figure 13.4.A(c). In other words, the closer the SRR was to the sample (i.e. $q \to 0$), the more noticable (larger Δf_0) the contribution of the sample to the frequency shift (i.e. a stronger *signal*). However in practice, when the SRR was too close to the printed part ($q < 0.2\,\text{mm}$), inevitable surface printing imperfections (e.g. stringing, blobs and zits) came into physical contact with the SRR, invalidating readings by possible deformation of the SRR. Figure 13.2.B provides an indication of the sensitivity of f_0 to changes in ring geometry. Therefore, a probe-sample separation distance $q \in [0.5, 1]\text{mm}$ was identified as a reasonable compromise between attaining sufficient signal strength (*dynamic range*) while preventing occasional surface undulations from touching the SRR. The probe-sample separation distance used for all data shown here was $q = 0.5\,\text{mm}$.

Surface roughness Given the comments above, the surface roughness of printed parts using optimized printing parameters was evaluated using whitelight confocal microscopy (NanoFocus μSurf) as $R_a = 0.7\,\mu m$ parallel to the print direction and $R_a = 6.4\,\mu m$ perpendicular to the print direction. The effect of typical surface roughness on the SRR signal was therefore considered to be negligible due to the large difference in roughness length scale when compared with the probe-sample separation distance (q) $\sim 0.5\,mm$.

Automatic calibration Let $f_{0,air}$ be the intrinsic resonant frequency of the SRR in free space, and $f_{0,bed}$ be the resonant frequency of the SRR at a separation distance q between the SRR and the build platform (see Figure 12.1.A(c) for a definition of q). Simulations indicated that for a probe-sample separation distance $q = 0.5\,mm$, the shift in f_0 (i.e. the dynamic range $DR_{bed} = f_{0,air} - f_{0,bed}$) should equal $DR_{bed} = 140\,MHz$. In order to accurately and repeatably reach the chosen probe-sample separation distance of $0.5\,mm$ in practice, the build platform approached the SRR in small increments (Z-steps of $> 3.4\,\mu m$) while monitoring the shift in f_0. Once $DR = 140\,MHz$ was reached, with knowledge of $f_{0,air}$ and $f_{0,bed}$, the best-fit coefficients M_e and M_q in Equations (13.6) and (13.7) could be obtained. Experiments showed that the desired probe-sample separation distance could be achieved repeatedly to within $\pm 5\,\mu m$. The calibration process is shown schematically in Figure 13.2.F.

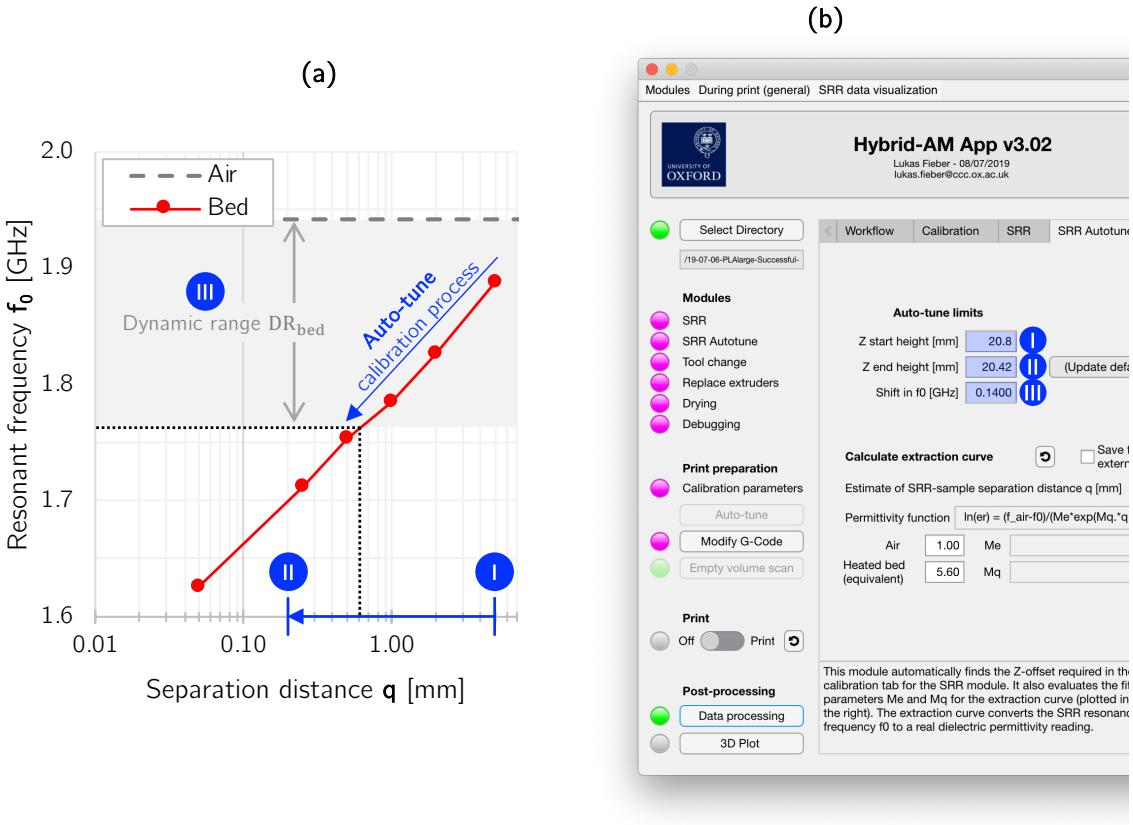

Figure 13.2.F: (a) The influence of probe-bed separation distance q on the SRR resonant frequency and (b) a screenshot of the control software GUI for initiating the automated SRR calibration process.

Sampling volume The signal (f_0) recorded at point $\vec{\mathbf{x}}$ was not only influenced by the dielectric properties of the *desired sampling point* directly below the ring split, but also by the aggregate contribution of a large, weighted *sampling volume* that influenced the $\vec{\mathbf{E}}$ field. Figure 13.2.G(a) shows the simulated SRR sampling volume, which was approximately hemi-spherical. It is this sampling volume effect that explains the *blurring* in the f_0 maps at the object edges in Figure 13.2.A. The sampling volume in Figure 13.2.G(a) was modelled as a distribution directly proportional to the simulated magnitude of the $\vec{\mathbf{E}}$ field within a dielectric material (i.e. a 3D, point spread function (PSF) $\propto |\vec{\mathbf{E}}|$). The shape/dispersion and in particular the *penetration depth* (in the vertical Z-axis) of the sampling volume was a function of the material ε_r (a higher ε_r resulted in a more shallow sampling volume). The sampling volume associated with a SRR operating at wavelength $\lambda \sim 15\,\text{cm}$ (2 GHz in free space) was approximately $\lambda/11$ (i.e. ranging from -7 to 7 mm in the PSF in Figure 13.2.G(a)). This provided a good estimate of the default spatial resolution of the characterization technique, i.e. the minimum achievable distance between two fully decoupled measurements.

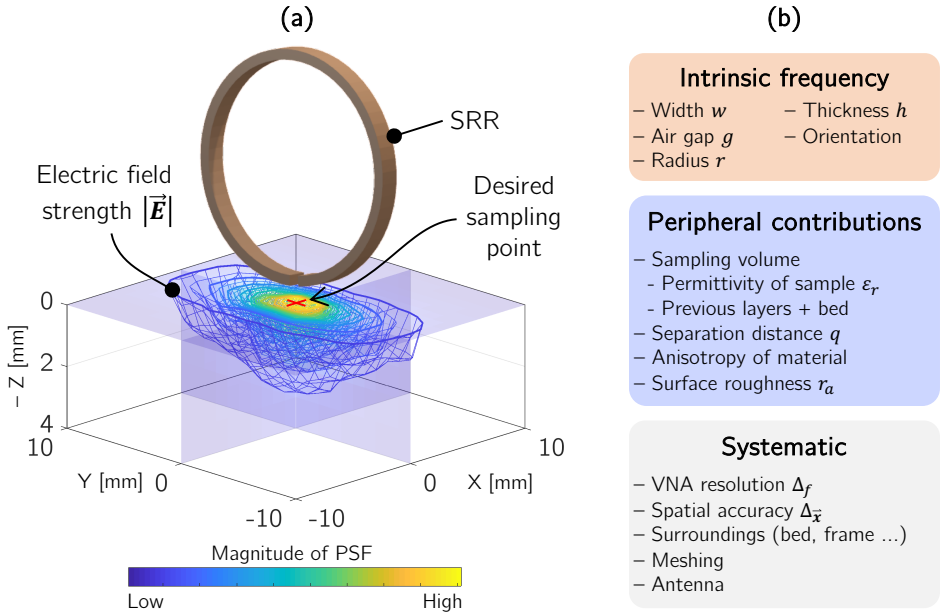

Figure 13.2.G: (a) A 3D contour-plot of simulation data showing the sampling volume (linearly proportional to the magnitude of the induced $\vec{\mathbf{E}}$ field within the sample, i.e. point spread function (PSF) $\propto |\vec{\mathbf{E}}|$) for an ideal, quasi-infinite material with $\varepsilon_r = 3$, and (b) an overview of the primary factors influencing the resonant frequency (f_0) of a SRR.

13.3 Deblurring: Improving spatial resolution

To account for the blurring and to enhance the spatial resolution of the resonant frequency map $f_0(\vec{\mathbf{x}})$ (i.e. step ii in Figure 13.1.A), a post-processing method referred to as *deblurring* was developed and entailed: (a) the expansion and enhancement of $f_0(\vec{\mathbf{x}})$ in space, (b) 3D deconvolution thereof using a single, approximated point spread function related to the shape of the sampling volume shown previously, and (c) contraction of the expanded, deconvoluted map to generate a refined frequency map $f_{0d}(\vec{\mathbf{x}})$ matching the original size of $f_0(\vec{\mathbf{x}})$.

Expansion of the measured data set To enhance the sampling resolution despite the relatively large PSF (comparable in size with the object features), it was imperative to *taper* the edges of the data set. This was necessary to minimize the ringing effect induced by deconvolution [319]. To preserve information near the edges of $f_0(\vec{\mathbf{x}})$, the data set was expanded/extrapolated before being tapered. Figure 13.3.A shows an expanded data-set (prior to deconvolution) and highlights how data from an empty volume scan (f_{ref} in Figure 13.1.A), alongside $f_{0,air}$ and $f_{0,bed}$ (from the automatic calibration process described in Section 13.2), was used to extrapolate the data.

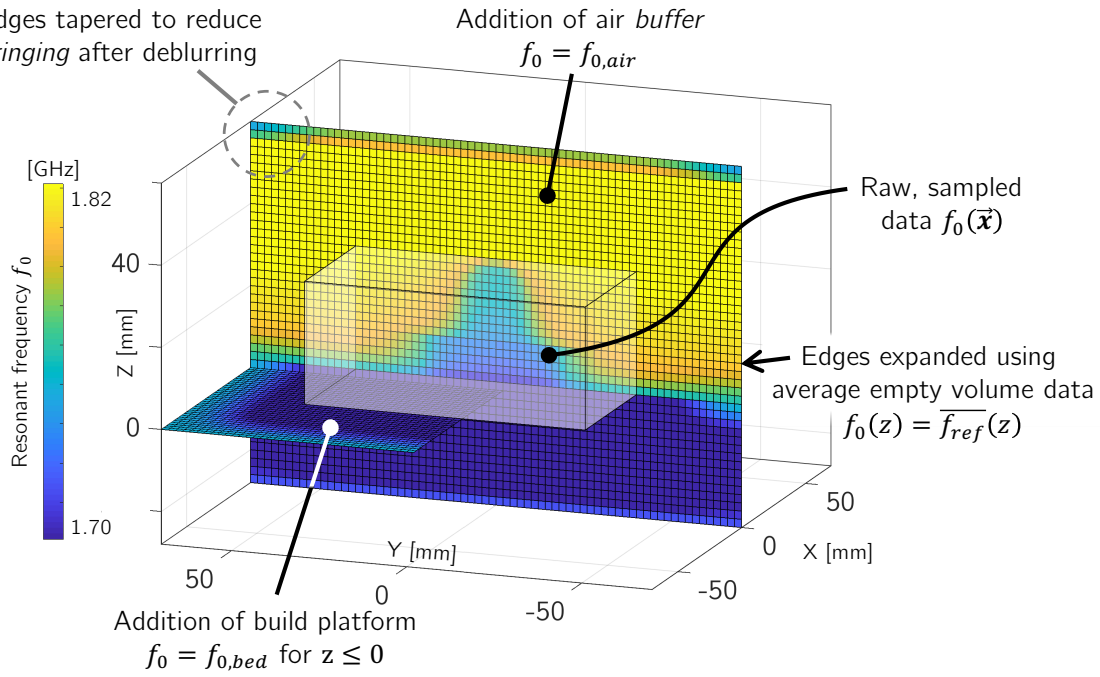

Figure 13.3.A: The expansion and enhancement of 3D experimental data ($f_0(\vec{\mathbf{x}})$) with tapered edges, addition of air and build platform buffers alongside extrapolation of edges using reference data for an empty scan (f_{ref}).

Deconvolution The PSF from Figure 13.2.G(a) was used to deconvolute the newly expanded, tapered frequency map from Figure 13.3.A in a single iteration. It should be noted that the sampling volume in Figure 13.2.G(a) was truncated in the vertical Z-axis to account solely for the contribution of already printed layers (i.e. beneath the SRR at the time of measurement) resulting in an asymmetric PSF with a step-function: PSF= 0 for $Z > 0$. Figure 13.3.B(a) shows a plot of f_0 as a function of X for the X-Z section shown in Figure 13.3.B(b), indicating the effect of deconvolution in the resulting maps for $f_{0,d}(\vec{\mathbf{x}})$. With reference to the labels in Figure 13.3.B, deconvolution led to: (i) a reduction in the range of resonant frequency within a single material, and (ii) much improved dielectric isolation of the build-platform contribution.

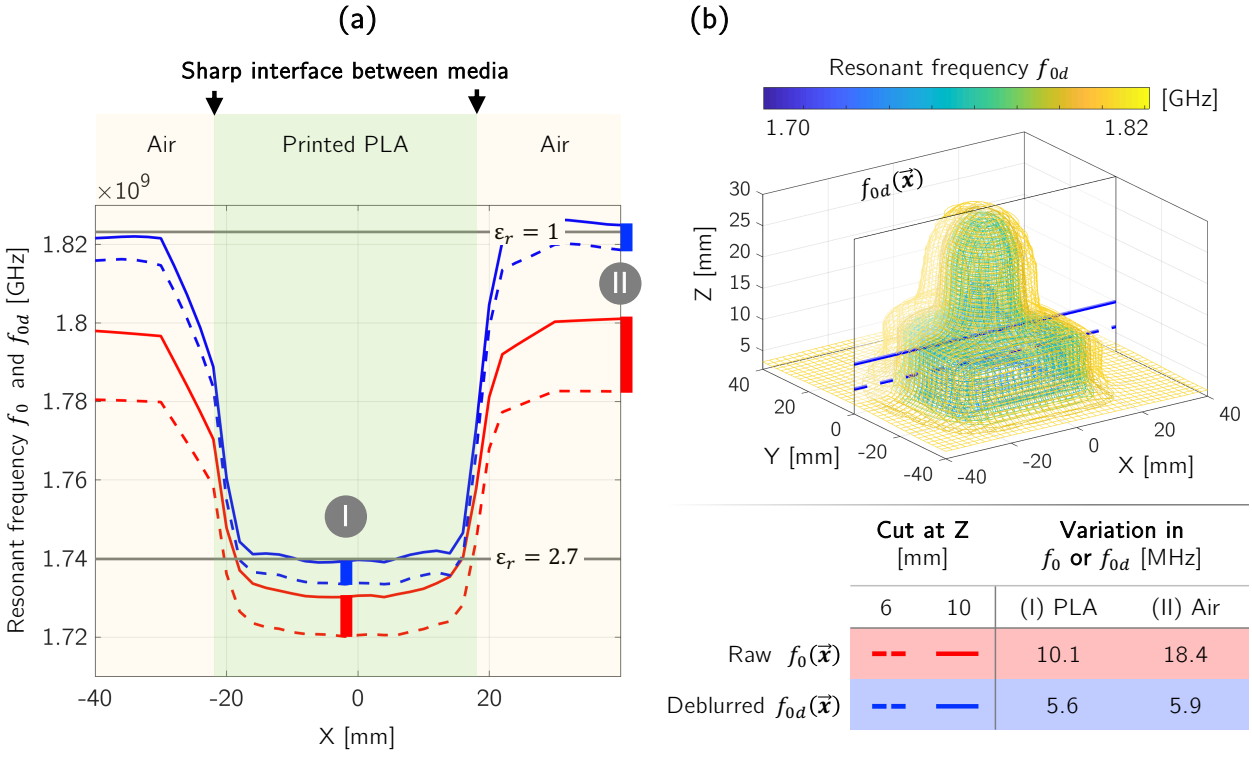

	Cut at Z [mm]		Variation in f_0 or f_{0d} [MHz]	
	6	10	(I) PLA	(II) Air
Raw $f_0(\vec{x})$	- -	—	10.1	18.4
Deblurred $f_{0d}(\vec{x})$	- -	—	5.6	5.9

Figure 13.3.B: Deblurring of experimental data showing: (a) various sections of data (raw/unprocessed f_0 data and deblurred f_{0d} data) at different heights and (b) the location of the X-Z sections taken from the 3D reconstruction.

Resolution limit To quantify the improvement in spatial resolution due to *deblurring*, consider the SRR with resonant frequency $f_{0,air}$ in free space, and with $f_{0,s}$ when in proximity to a large sample ($\varepsilon_r > 1$ and all dimensions exceeding the size of the PSF). The dynamic range (DR) for this system is defined as $DR = |f_{0,air} - f_{0,s}|$. We define the spatial resolution of the SRR technique as the step (in $\vec{\mathbf{x}}$) required to resolve a 10 % shift in f_0 when transitioning across a physically sharp interface between the sample and air, i.e. $\Delta f_0 = 0.1 \times DR$. Using this definition, for a sample with $\varepsilon_r = 10$, deblurring achieved a spatial resolution improvement of at least $\times 1.6$, from $\pm 6.4\,\text{mm}$ or $\lambda/11$ to $\pm 4.0\,\text{mm}$ or $\lambda/18$ where λ is the resonance wavelength of the SRR. Figure 13.3.C shows supporting simulation data to assess the spatial resolution limit of an ideal SRR. It should be noted that the spatial resolution was dependent on ε_r because the simplified PSF function used in deblurring was itself related to the fringing $\vec{\mathbf{E}}$ fields of the SRR, which were again dependent on ε_r.

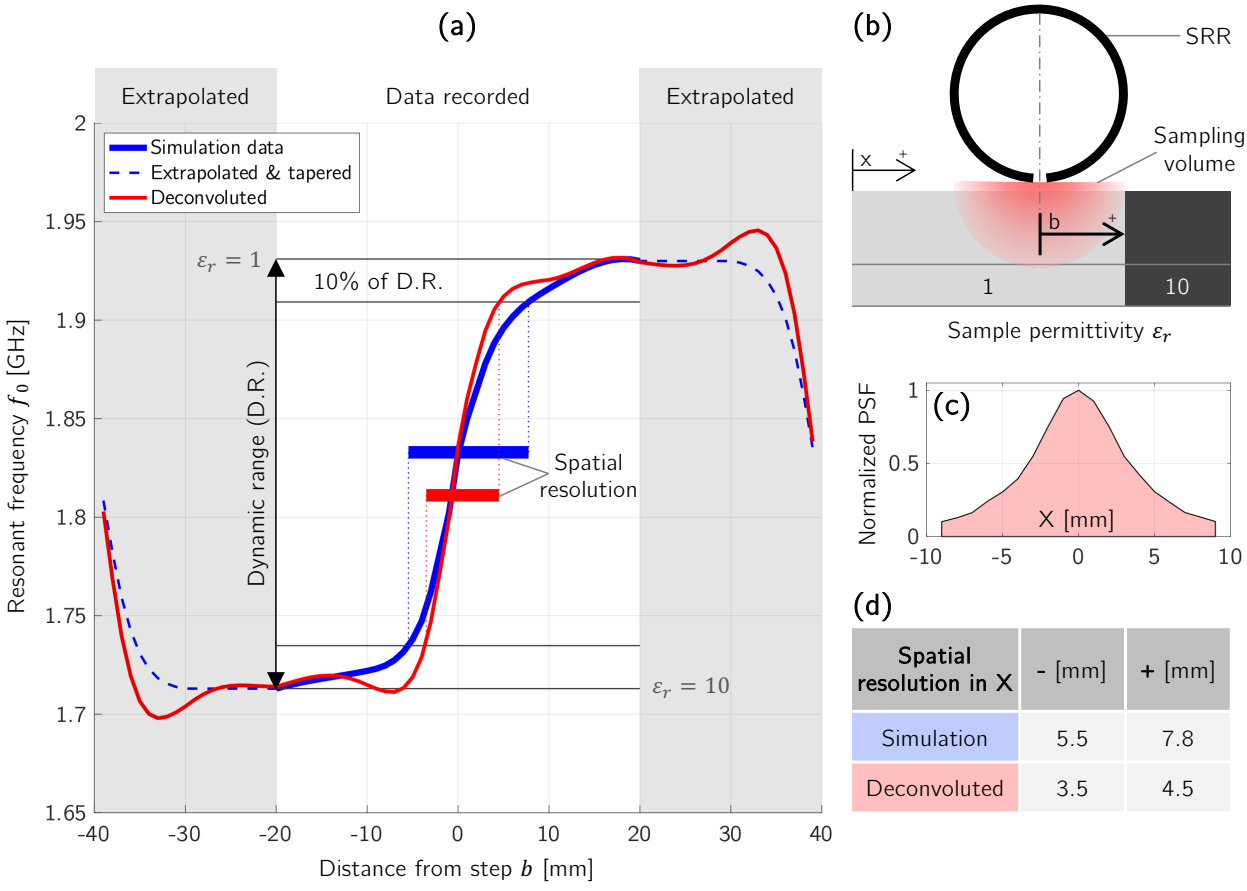

Figure 13.3.C: (a) Simulation data showing the spatial resolution limit of the SRR in the x-axis, (b) a schematic of the experimental setup used for simulation, (c) the PSF used for deconvolution and (d) an indication of the impact deconvolution had on spatial resolution.

13.4 Extraction: Interpreting the resonant frequency

Extraction model A model to translate the frequency maps to dielectric permittivity (ε_r) maps (i.e. step iii in Figure 13.1.A), while taking into account the SRR probe-sample separation distance q, was derived from Equations (13.6) and (13.7). The *extraction model* is expressed in Equations (13.8) and (13.9) below and is shown graphically in Figure 13.4.A:

$$f_{0d} = f_{0,air} - DR \times \exp\left(M_q \times q^{0.1}\right) \tag{13.8}$$

$$DR = M_e \ln(\varepsilon_r) \tag{13.9}$$

where $f_{0,air}$ is the intrinsic resonant frequency of the SRR in free space (see Figure 13.2.B), DR is the dynamic range as a function of dielectric permittivity (ε_r), q is the sample-SRR separation distance, and M_q and M_e are sensitivity factors related to q and ε_r respectively. Combining Equations (13.8) and (13.9) yields:

$$\ln(\varepsilon_r) = \frac{f_{0,air} - f_{0d}}{M_e \times \exp\left(M_q \times q^{0.1}\right)} \tag{13.10}$$

The *extraction model* allowed for an extraction curve (i.e. $\varepsilon_r(f_0)$ at constant q, see label i in Figure 13.4.A(a)) to be deduced for any specified experimental set-up. The dynamic range DR in Equation (13.9) is a logarithmic best-fit over a sample permittivity range $\varepsilon_r \in [1, 50]$ and is shown for $q \in [0.5, 2]$mm in Figure 13.4.A(b). The relationship between resonant frequency f_0 and probe-sample separation distance q is shown in Figure 13.4.A(c).

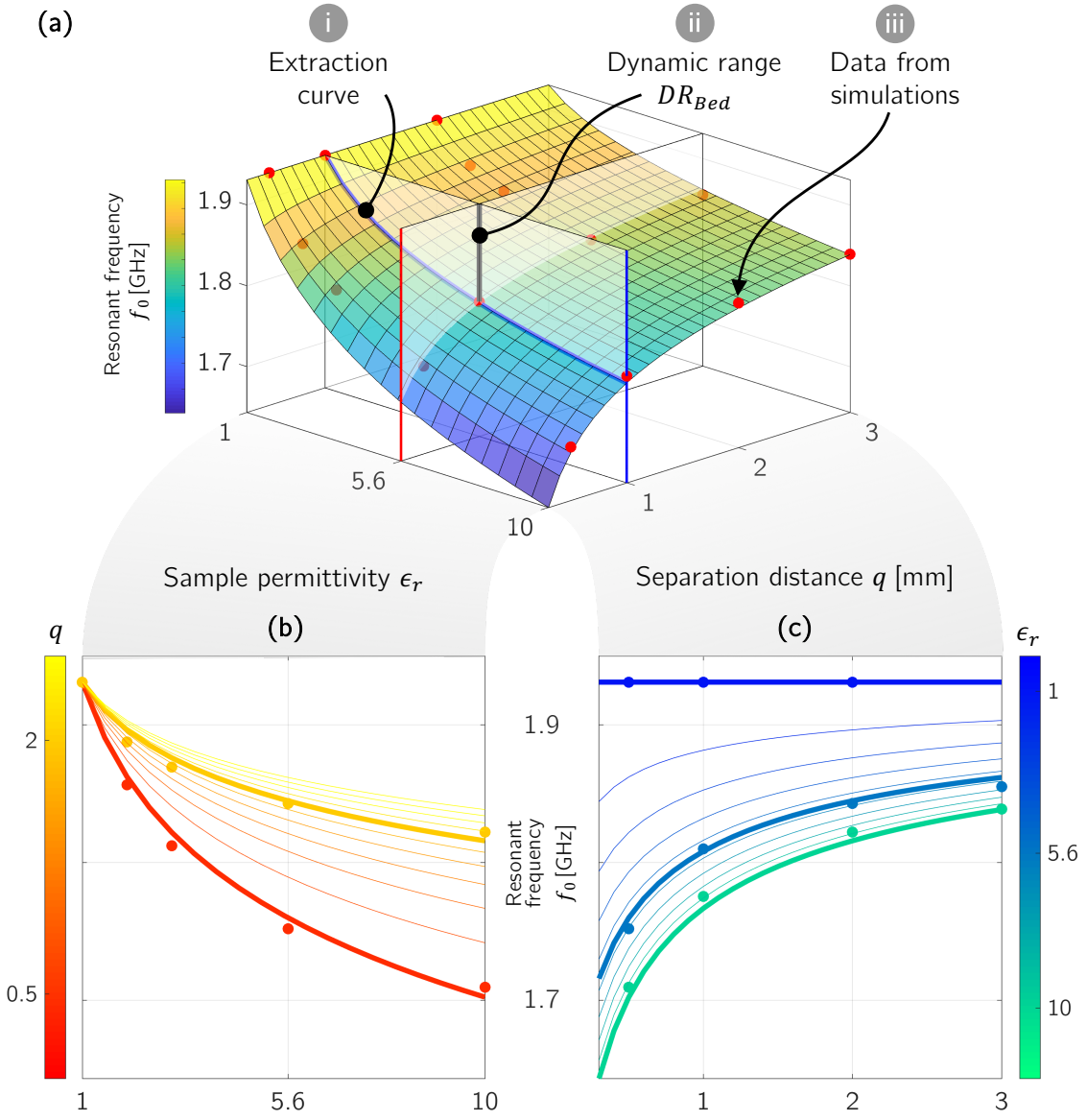

Figure 13.4.A: (a) A 3D surface plot showing the *extraction function* for converting SRR resonant frequency f_{0d} into permittivity ε_r while accounting for SRR probe-sample separation distance q. An indicative (I) extraction curve at $q = 1\,\text{mm}$ is highlighted, alongside (II) the dynamic range DR_{Bed} associated to the build platform and (III) data points from simulations. Cross-sections highlighting contours at (b) $q = [0.5, 2]\text{mm}$ and (c) $\varepsilon_r = [1, 5.6, 10]$ are also shown.

Demonstration Figure 13.4.B shows a 3D spatial $\varepsilon_r(\vec{\mathbf{x}})$ map of a printed demonstrator with deliberately varying local fill density to provide a range of local ε_r, between air ($\varepsilon_{r,air} = 1$) and printed PLA ($\varepsilon_{r,PLA} = 2.71$). The demonstrator, shown in Figure 13.4.B(a) and (b), comprised a ⌀20 mm sphere (100 % infill) centered within a 40 mm cube (25 % infill). The dimensions of printed features could be deduced from the ε_r map in Figure 13.4.B(c) and (d) to an accuracy of ±2 mm. The average ε_r measured for the 25 % dense box around the sphere was 1.46, in excellent agreement with a Wiener's formula based estimate of 1.43 [320].

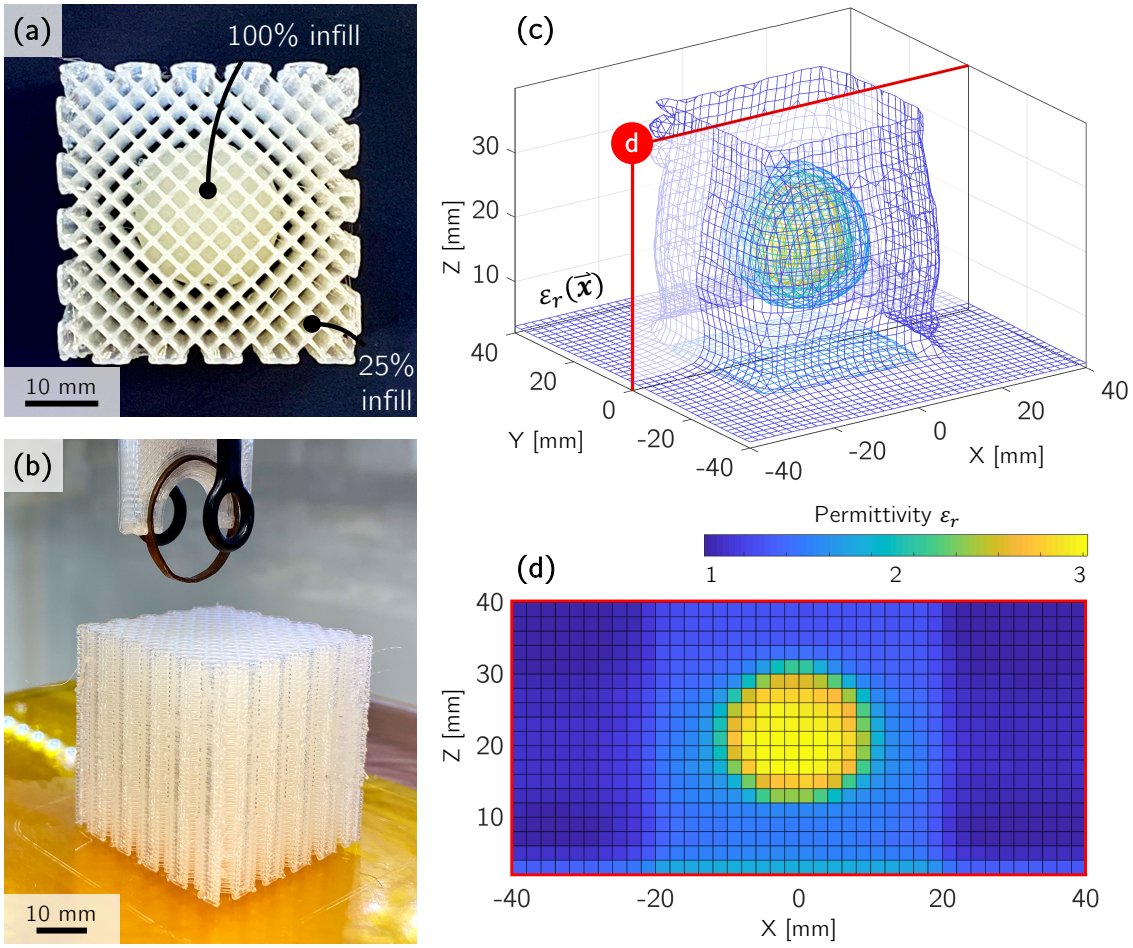

Figure 13.4.B: Photographs showing (a) a printed object with varying infill density, and (b) the dielectric imaging module/sensor and object during the later stages of fabrication. Experimental data showing (c) the measured spatial permittivity map $\varepsilon_r(\vec{\mathbf{x}})$ using SRR measurements of f_0 only, and (d) a typical X-Z planar cross-section of $\varepsilon_r(\vec{\mathbf{x}})$.

14

Conclusions & outlook: In-line characterization

Novelty of work achieved The *layer-by-layer* nature of AM processes presented an opportunity to integrate a surface-based characterization technique *in-line* with device fabrication. In Part III of this thesis, the automated integration of a novel, non-destructive dielectric characterization technique *in-line* with FFF has been demonstrated. Using data obtained during manufacture, it was possible to reconstruct 3D images of the spatial distribution of dielectric permittivity within a printed part. The non-contact, sub-wavelength EM characteriztion technique was based on a split ring resonator (SRR) and allowed for real-time assessment of local material properties, which could immediately provide a form of quality control to validate part conformance to intended design, at least in terms of the permittivity design. To the authors best knowledge, this is the first reported dielectric imaging technique specifically designed for integration *in-line* with AM, and is the first technique capable of measuring/visualizing the 3D variation in dielectric permittivity within a printed part. The imaging principle and its limitations have been discussed in detail and proof-of-concept experimental data presented.

Impact & application The methodology shown here could be easily extended to integrate other surface-based techniques *in-line* with AM processes. In particular, the non-contact/non-destructive nature of the dielectric imaging technique may offer opportunities for other AM applications e.g. for monitoring deposition, curing or defects in soft materials, or mapping property changes due to combinations of materials. However, the resolution of the current technique, even after post-processing, was insufficient to detect sub-mm features or small printing defects. Where high spatial resolution is needed, the time penalty from point-by-point scanning over a surface may become significant (approximately 1 sec per point using the apparatus reported here). However, both constraints are likely amenable to further optimization through hardware/software improvement.

Future research This proof-of-concept study has shown that there are some generic challenges related to integrating characterization techniques into AM, and in particular include: (a) the need for open, accessible control software that readily allows for *plug and play* sensor integration and data sampling, (b) a greater range of characterization probes compatible with a wider range of materials and AM processes, and (c) the need for sensor/hardware/software strategies that avoid slow point-by-point scanning of the printed area. Specifically with respect to 3D dielectric imaging using a SRR *in-line* with AM described in this paper, a proof-of-concept demonstration of closed-loop feedback control, i.e. immediately responding to potential (relatively large) printing defects, could now be realistically considered. The investigation of other EM material properties, such as the dielectric loss tangent, may be considered by, for example, relating the quality factor of the resonant transmission signal S_{21} to the loss tangent in an analogous manner to the method described in Part III for relating f_0 to ε_r. Furthermore, increasing the operating frequency of the SRR system (i.e. using a smaller ring) will lead to improved spatial resolution and may allow the detection of smaller printing defects.

15

Research summary: Parts I to III

The following objectives were addressed in this thesis:

Part I – Hybrid additive manufacturing framework

(a) **Construct a versatile hybrid-AM system** – an extendable, modular manufacturing *framework* was established and a functioning, lab-scale multi-material, multi-technology (MMMT) machine was designed, built and commissioned. The critical development lied in the modular interplay between the real/physical and virtual/-software domain of additive manufacturing (AM). The hybrid-AM system facilitated significantly more advanced data analysis, insight and control of AM processes.

Part II – Multi-phase additive manufacture for energy storage applications

(b) **Investigate *multi-phase* AM processing science** – in-depth understanding of underlying material extrusion additive manufacturing (MEAM) processing-science was developed, and key AM materials/processing considerations were discussed. The new insights enabled controlled, layer-by-layer deposition of solid-liquid-gel combinations using fused filament fabrication (FFF) and direct ink writing (DIW) techniques;

(c) **Print a complete energy storage device** – a novel, single-operation manufacturing process to fabricate fully functioning, form-factor free supercapacitor devices (electro-chemical double layer capacitors, EDLCs) using a *multi-phase* AM approach was demonstrated. The technique provided an opportunity to address inherent restrictions in geometric form factor associated with conventional planar supercapacitor manufacturing approaches, and provides an alternative fabrication process for applications with irregular volume/shape and mass-customization requirements.

(d) **Engineer a non-destructive dielectric probe** – a dielectric probe based on a split ring resonator (SRR) was extended to operate without contact (non-destructive) and *in-line* with material extrusion additive manufacturing (MEAM) processes. The probe enables measurement of the dielectric permittivity (ε_r) of as-printed polymers;

(e) **Demonstrate 3D dielectric imaging** – proof-of-concept for the real-time, non-destructive acquisition of dielectric data (in three dimensions) during AM was demonstrated. The technique provided quantified insights into the internal distribution of the local ε_r within 3D objects as they are formed and suggests the possibility for real-time, *closed-loop* control of dielectric properties during AM.

Future research While specific recommendations for future research associated to the inidvidual objectives were outlined throughout, the following over-arching ideas may be considered: (a) to extend the functionality of the hybrid-AM machine by developing and integrating further functional modules (e.g. a fabrication module to deposit photo-sensitive materials, or a characterization technique to monitor the surface roughness or thermal stresses during AM), (b) to explore the vast unexplored parameter space in printed energy storage devices (e.g. associated with geometric form-factor, heterogeneous electrodes or complex materials-processing combinations), and (c) to harness the additional, advanced data-processing capabilities during AM to demonstrate *closed-loop* manufacturing (e.g. to improve compliance of a printed part with its intended design).

Afterword

Hybrid-AM is an exciting field of research, with new ideas and approaches emerging frequently, and an endless pool of potential applications to target. It has been shown that entire functional devices consisting of multiple, different materials can be manufactured in a single, automated manufacturing operation. The full implications this may have in terms of new technologies being developed, and on the manufacturing value chain as a whole, remains impossible to predict.

This thesis has sought to answer most of the questions raised in the preface, including: *'can we print an energy storage device?'* (yes), and *'can we characterize the internal material properties of a part as it is being printed?'* (also, yes). However, after dedicating 3 years of research to the field of hybrid-AM, I am now left with a new set of queries. The questions have shifted from *'is it possible to..'* and *'can we..'*, to wondering what the implications of emerging hybrid-AM processes will be. Where will the impact of hybrid-AM be most noticable? How will hybrid-AM methods be integrated into conventional value chains? Who will be the first to utilize the additional functionality of hybrid-AM? When will 'design for *hybrid*-AM' become an area of interest? And is single-operation manufacture really what we should be aiming for?

As mentioned early on in this thesis, we are merely beginning to understand the impact fabricating parts *additively*, as opposed to *subtractively* may have (not to mention the potential impact of any *hybrid* systems). And while I cannot claim that this thesis has changed that to any significant extent, I do hope that the work provides a step in the right direction, providing ideas and tools for the further exploration of novel manufacturing concepts, and perhaps inspiring new applications and technologies related to hybrid-AM.

Appendix A

Conceptualization of the hybrid additive manufacture machine

Dual-extrusion prototype Figures A.1 and A.2 schematically depict a prototype built for proof-of-concept of dual-extrusion. Lessons learned were implemented in the hybrid-AM system outlined in Sections 3 to 5 of this thesis. The prototype was comprised of a FFF and DIW nozzle and was designed, built and calibrated to fit onto an existing, commercial FFF printer (Makerbot Replicator). The general assembly consisted of 66 components, 36 unique parts and cost approximately 300£.

General assembly Successful design features included: (a) combining FFF fabricated components (e.g. irregularly shaped fixtures) with purchased/pre-fabricated parts (e.g. bipolar stepping motors), and (b) the overall system functionality/integration with existing firmware. Design flaws included: (a) cooling and choice of materials in the assembly, (b) vibration and resonance for small movements (e.g. infill), (c) tip-clash and contamination issues between the 2 nozzles, (d) not robust wiring and (e) a heated bed which did not remain flat at high temperatures due to polymer cantilevers. The hybrid-AM machine (outlined in Section 5) addresses these issues, for example: tip-clash is prevented by moving the build platform as opposed to the functional modules, a significantly more robust/revised wiring system (outlined in Section 4), and a central axis for supporting the build platform, preventing cantilever issues.

FFF With respect to the FFF nozzle, the hot-end from E3D worked well and the modular ecosystem of heaters, nozzle tips etc. proved useful. However the module suffered from oozing during inaction, no filament force control and a temperature limit of 250 °C. The FFF module in the hybrid-AM machine (outlined in Section 5.4.3) is based on an improved extruder system by E3D (Titan Aero) with titanium hot-ends and a more robust setup, e.g. to allow printing up to 300 °C.

DIW Syringe loading worked well using the FFF fabricated fixtures and controlling extrusion through a stepper motor by manipulating the `g-Code` also worked. However, DIW suffered from significant backlash and issues related to the drying of ink at the nozzle tip. The DIW modules in the hybrid-AM machine outlined in Section 5.4.3 have a direct lead screw motor attached to minimize issues with backlash, and the printing routine includes a syringe purging step to prevent dry ink to influence the print quality.

Demonstrators The successful fabrication of complex arrangements of 2-materials in different phases, such as the enclosure of a liquid in a polymer housing in single manufacturing operation (see Figure A.2(b)) ultimately formed the basis for Part II of this thesis.

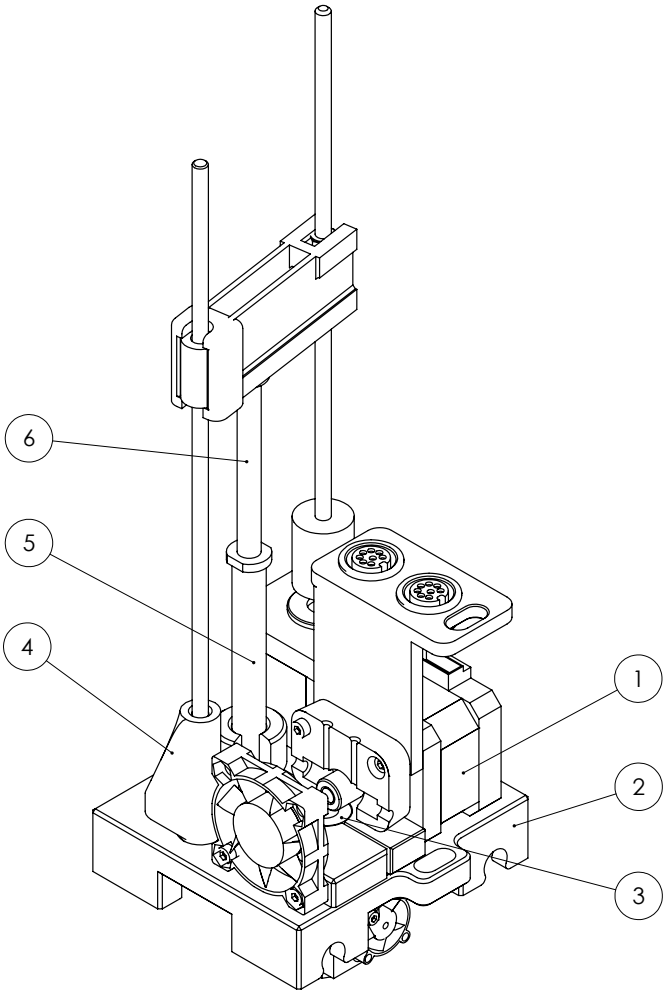

Figure A.1: Isometric wireframe drawing of the general assembly for a dual-extrusion prototype showing: (1) bipolar stepper motor for FFF, (2) base plate sub-assembly, (3) plastic extruder sub-assembly (E3D, UK), (4) bipolar stepper motor for DIW, (5) syringe barrel 2.5 mL, and (6) syringe plunger.

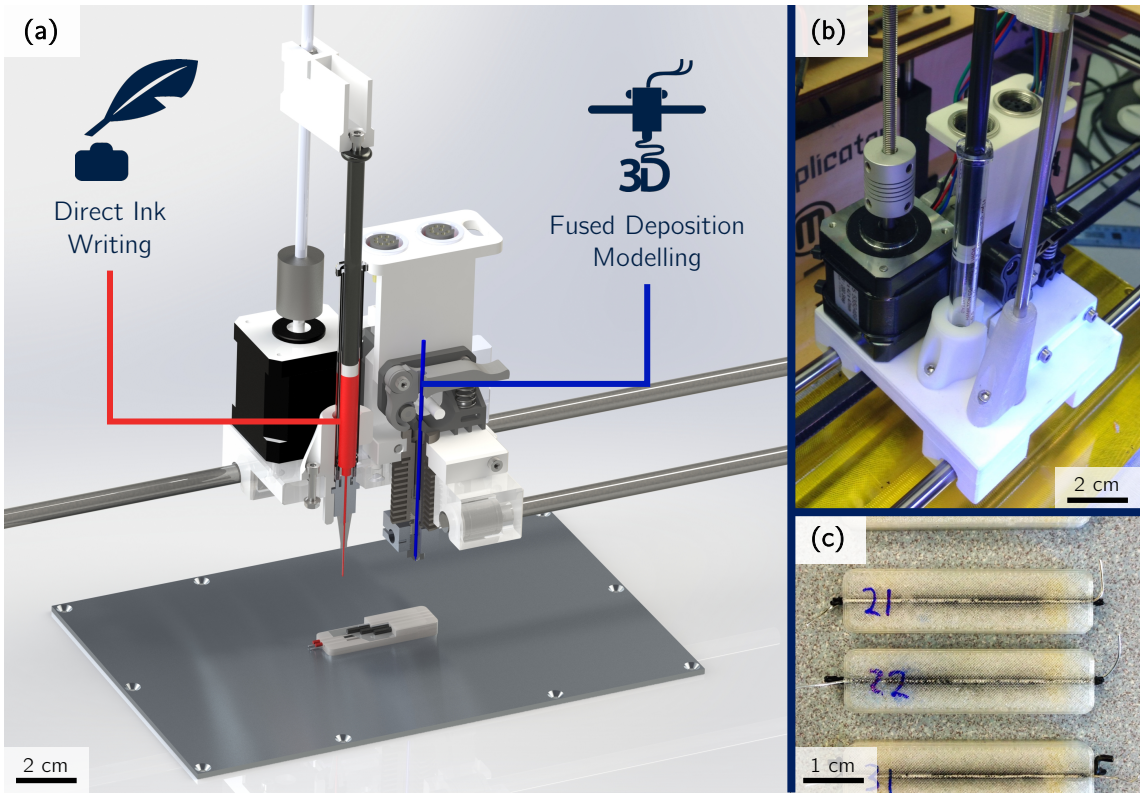

Figure A.2: (a) A cross-sectional render of the multi-phase (FFF-DIW) extrusion head developed for prototyping, (b) a photograph of the dual extrusion head on a commercial AM machine and (c) initial demonstrators showing liquid (printed by DIW) enclosed in a polymer (printed by FFF).

Appendix B

Technical documentation

B.1 Risk assessment

Outline of Work/Activity: **Fused deposition and direct ink writing additive manufacture**			**Review date:**	
			Location: 195.20.08	
Assessor Name: Lukas Fieber	Signature:		**Date: 11/12/17**	
Authorised By: Prof. Grant	Signature:		**Date:**	
Hazard	**Who Might Be Harmed?**	**Existing Control Measures**	**What Further Action is Required?**	**By Whom/When?**
General	Students, staff and post docs	All users must be trained to operate this process. No work can be carried out after work hours.	Training of users	Lukas Fieber – as appropriate
Electrical hazards – risk of electric shock		Low voltage operating system, all electronics contained within insulated box / no free wire showing / wiring mounted away from user.		
Airborne fumes or powder – risk of inhalation		Refer to COSHH form of specific chemicals, in general materials will not be heated beyond their safe processing temperature and there is no risk of airborne fumes.		
Heat – risk of skin burn/irritation		Engineering control for hot ends – protected from accidental contact. Hot bed temperatures will not exceed 120*C, additive manufacture machine contained within PC frame to prevent accidental contact.		
Mechanical moving parts – risk of injury		Additive manufacture machine contained within polycarbonate frame to prevent accidental contact. Parts move very slow (max 40mm/s).		

Table B.1.1: Apparatus risk assessment form for the hybrid-AM machine.

B.2 Bill of materials

PART NUMBER	DESCRIPTION	SUPPLIER
SA_FrameKanya	Frame Sub Assembly	P-KANYA 17-7871
M_Top Plate	Modular Top Plate	M-TAYBROH
M_SRR2_VerticalBar	Vertical bar for probe support	M-STORES
M_SRR2_Support Clip	Support clip for probes	M-PRINTED IN LAB
M_SRR2_SRR Holder	Holder for SRR	M-PRINTED IN LAB
M_SRR2_Split Ring	Split ring resonator (SRR)	M-STORES
M_SRR2_SA_Coax Probe	Near-field H Probe (co-axial)	P-Langer RF-R 50-1
M_SRR2_ProbeChuck	Chuck for near-field probe	M-PRINTED IN LAB
M_SRR2_Horizontal Bar	Base plate for SRR2 module	M-STORES
M_SRR_SplitRing Fixture	Fixture for SRR	M-PRINTED IN LAB
M_SRR_HorizontalBar	Base plate for SRR module	M-STORES
M_SA_Terminal Connectors	Terminal Connectors	P-AMAZON B00O7P08VK
M_FDMH_Vertical Bar	FDM Holder Vertical Bar	M-STORES
M_FDMH_Stopper	FDM Holder Stopper	M-PRINTED IN LAB
M_FDMH_Horizontal Bar	FMD Holder Horizontal Bar	M-STORES
M_FDM_SA_Titan Aero 1.75	E3D Titan Aero 1.75mm filament Sub Assembly	P-E3D TITAN-AERO-ST-175-12V
M_FDM_Aero Holder	Module Plate for Titan Aero Extruder	M-STORES
M_DIW2_Piston10cc_NordsonEFD_7012025	10cc Piston	P-NORDSON 7012025
M_DIW2_Motor Mount Plate	Motor Mount Plate	M-STORES
M_DIW2_Plunger adaptor	Plunger Adaptor	M-StORES
M_DIW2_Module Support	Support Bracket	M-STORES
M_DIW2_Module Base Bar	Base Plate	M-STORES
M_DIW2_Tip20GA TT 023_NordsonEFD_7018	Tip gauge 20	P-NORDSON 7018216
M_DIW2_Barrel10cc_NordsonEFD_7012007	10cc Barrel	P-NORDSON 7012007
M_DIW_SA_Lead Screw Motor	Lead Screw Motor with NEMA 17 motor	P-HEASON 207-08332
M_DIW_S2.5_Syringe Short Needle	Needle, Kahnetics 18 or 21 Gauge	P-RS 400-3895 / 400-3889
M_DIW_S2.5_Syringe Luer Lock Adapter	Male Luer Lock Adapter, Hamilton	P-SIGMA 26293
M_DIW_S2.5_Syringe 2.5mL Body	Syringe Body, Hamilton 1002RN 2.5mL	P-SIGMA 2219-3-U
M_DIW_S2.5_Base Plate Syringe Holder	Syringe Holder, Printed in Lab	M-PRINTED IN LAB
M_DIW_Plunger Adaptor	Plunger Adaptor for Lead Screw	M-STORES
M_DIW_Motor Mount Plate	Motor Mount Plate	M-STORES
M_DIW_Module Base Plate	Module Base Plate for Syringe	M-STORES
M_DIW_Column	Column for Motor mount Plate	M-STORES
G_SA_Macron MCS-R15-750-750-750-200	Gantry from Macron Dynamics 750x750x200	P-OLSEN ACTUATION PODJ2017550
G_M_Z Endstop Probe	Probe for Z endstop	M-PRINTED IN LAB
G_M_Z Endstop Holder	Holder for Z endstop	M-PRINTED IN LAB
G_M_Y Endstop Holder	Holder for Y endstop	M-PRINTED IN LAB
G_M_X Endstop Holder	Holder for X endstop	M-PRINTED IN LAB
G_M_Split Ring Collar	Split Ring Collar	M-STORES
G_M_NEMA23	Motor for Gantry	P-RS 535-0445
G_M_LB_Z Axis L-Bracket Vertical Plate	Z Axis L-Bracket Vertical Plate	M-STORES
G_M_LB_Z Axis L-Bracket Triangle	Z Axis L-Bracket Triangle	M-STORES
G_M_LB_Z Axis L-Bracket Base Plate	Z Axis L-Bracket Base Plate	M-STORES
G_M_Kanya Small L-Bracket	Small connector bracket Kanya	P-KANYA
G_BP_Z Axis Holder	Z Axis holder	M-STORES
G_BP_Spring M3	M3 Spring	P-E3D M-SPRING
G_BP_SA_Clip	Binder Clip	P-AMAZON B000KJKIH6
G_BP_Heated Bed Heater	Silicon Heater 200 x 200150W	P-E3D E-HEATER-MAT-SQUARE200
G_BP_Heated Bed Glass	Print Surface	P-E3D M-BED-GLASS-214x214x4mm
G_BP_Heated Bed Base	Platform for Heated Bed	M-RS 194-1132
G_BP_Heated Bed	Conductive Plate for Heated Bed Heater	M-STORES

Table B.2.1: A bill of materials (BOM) showing major mechanical components of the hybrid-AM machine. Note: fasteners and control components have been excluded. In the *supplier* information: parts with `P` refer to purchased/outsourced components whereas `M` refer to parts which were fabricated in-house.

B.3 Engineering drawings

Figure B.3.1 schematically highlights a selection of engineering drawings for the hybrid-AM machine which are shown in this section (Figures B.3.2 to B.3.9). The assembly tree is structured in *tiers* e.g. where applicable a *tier 2* sub-assembly is comprised of *tier 3* sub-assemblies and/or *parts*. For example, the part *M_FDM_Aero holder* is a *part* in the tier 3 sub-assembly *FDM* which in turn is part of a tier 2 sub-assembly *modules*. File names including the acronym *SA* refer to a sub-assembly (independent of tier). Note, reference to the tier 1 *general assembly* is omitted, as all files refer to this. In the *supplier* information provided for all sub-assemblies (tier 2 and below), parts with `P` refer to purchased/outsourced components whereas `M` refer to parts which were fabricated in-house.

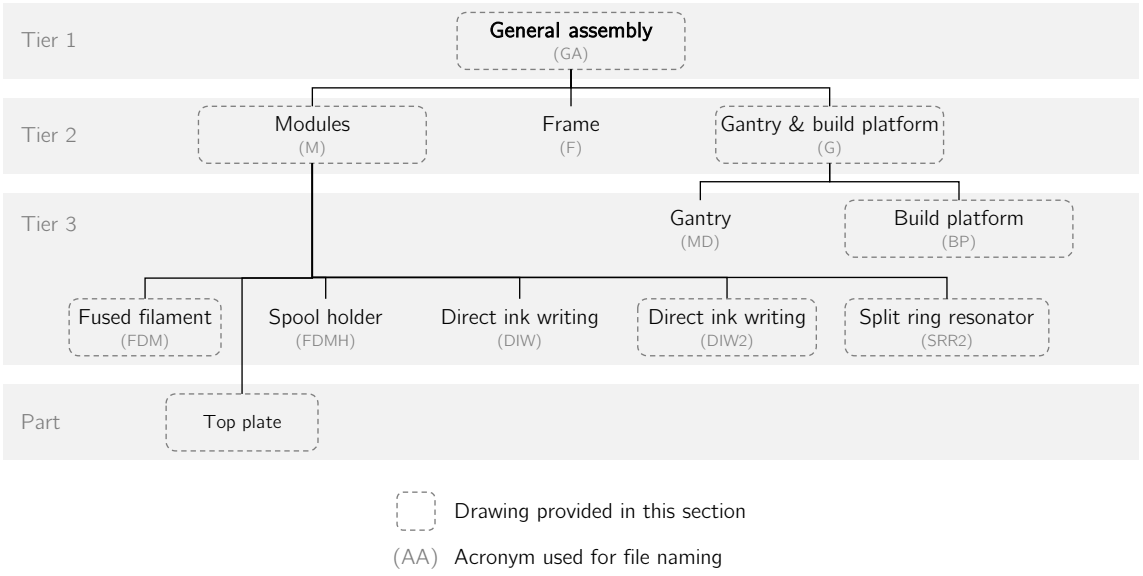

Figure B.3.1: An overview of the engineering drawings shown in this section.

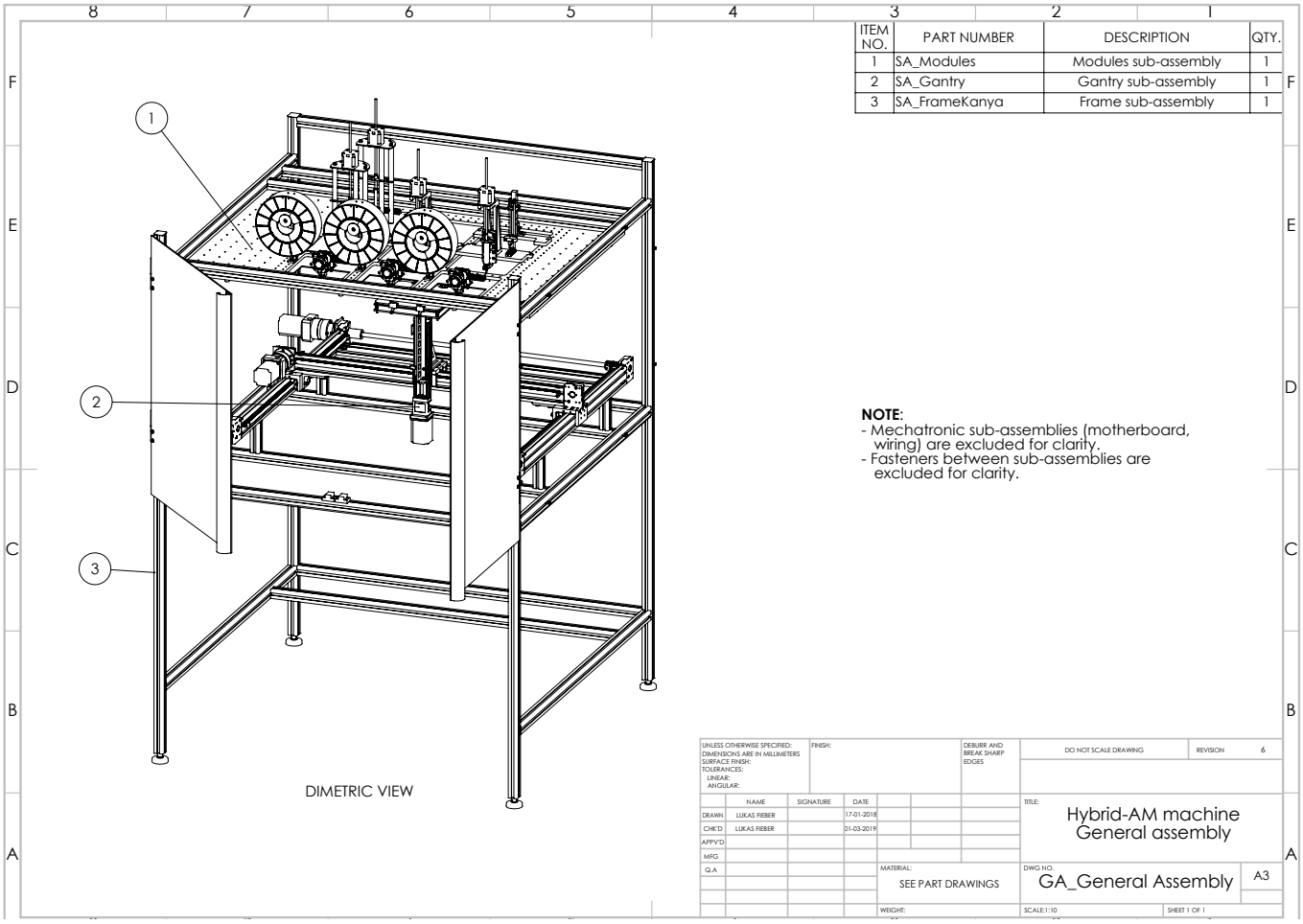

Figure B.3.2: Engineering drawing of the *hybrid-AM machine* general assembly (acronym used for file naming `GA`, tier 1).

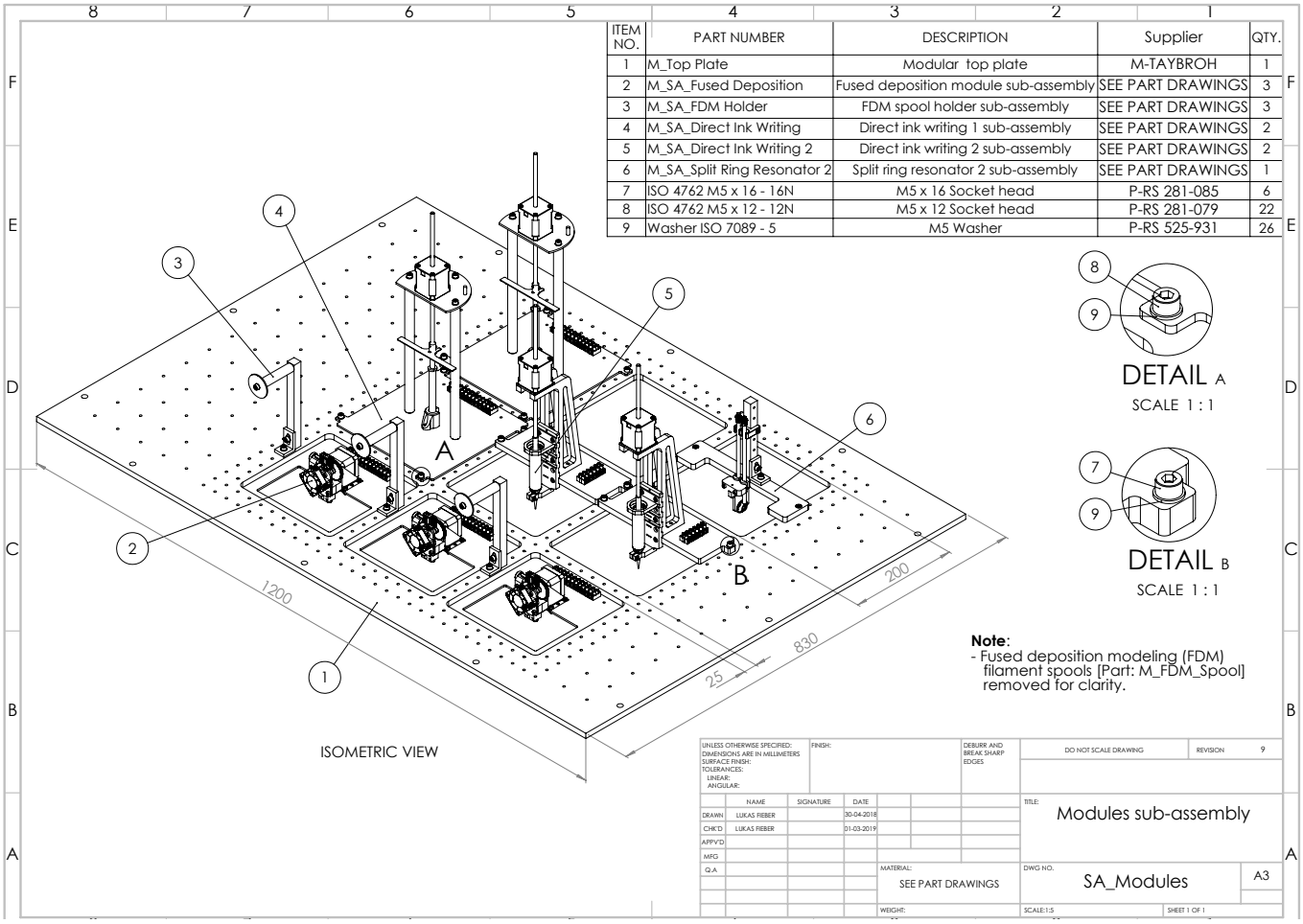

Figure B.3.3: Engineering drawing of the *modules* sub-assembly (acronym used for file naming `M`, tier 2).

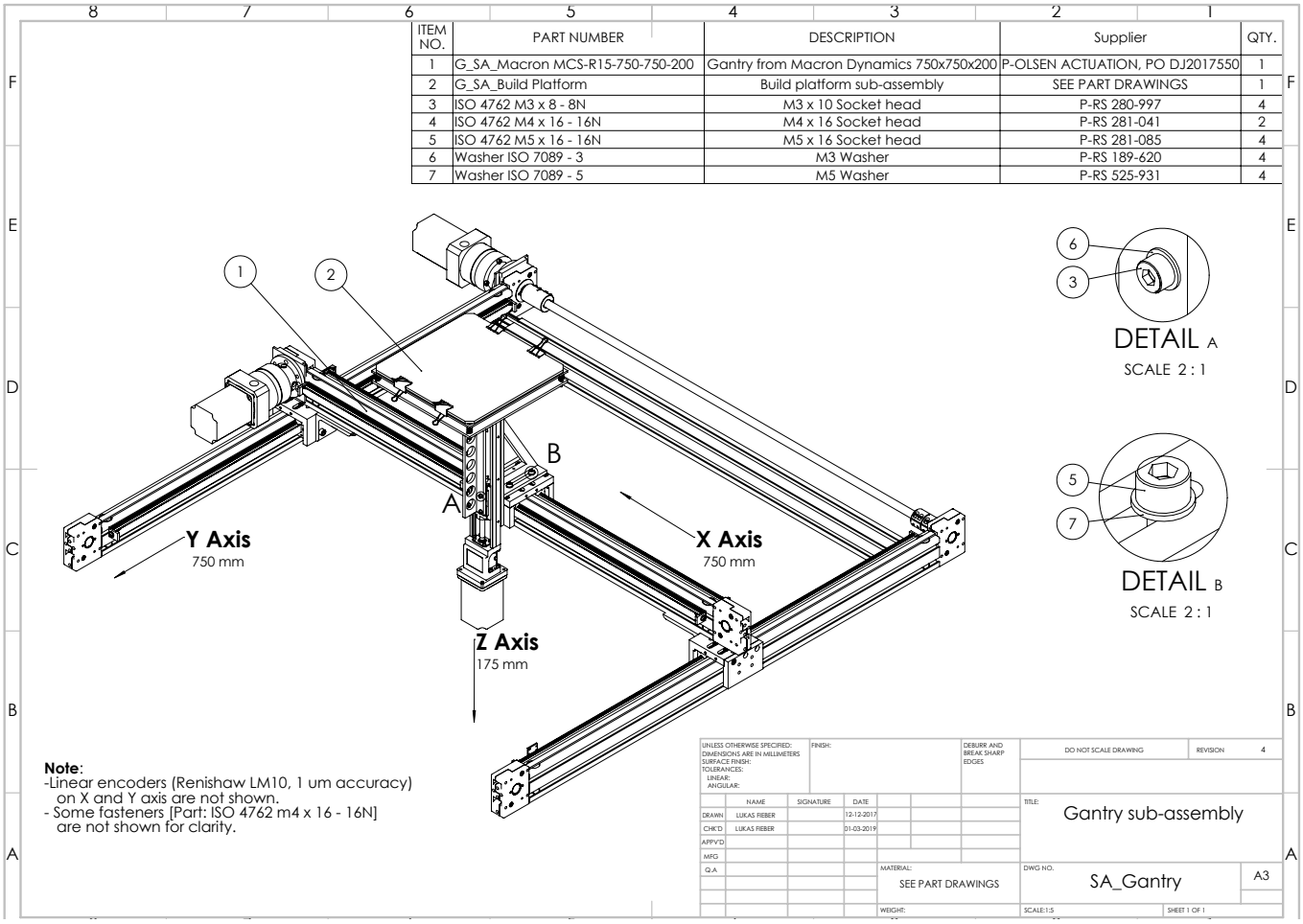

Figure B.3.4: Engineering drawing of the *gantry* sub-assembly (acronym used for file naming `G`, tier 2).

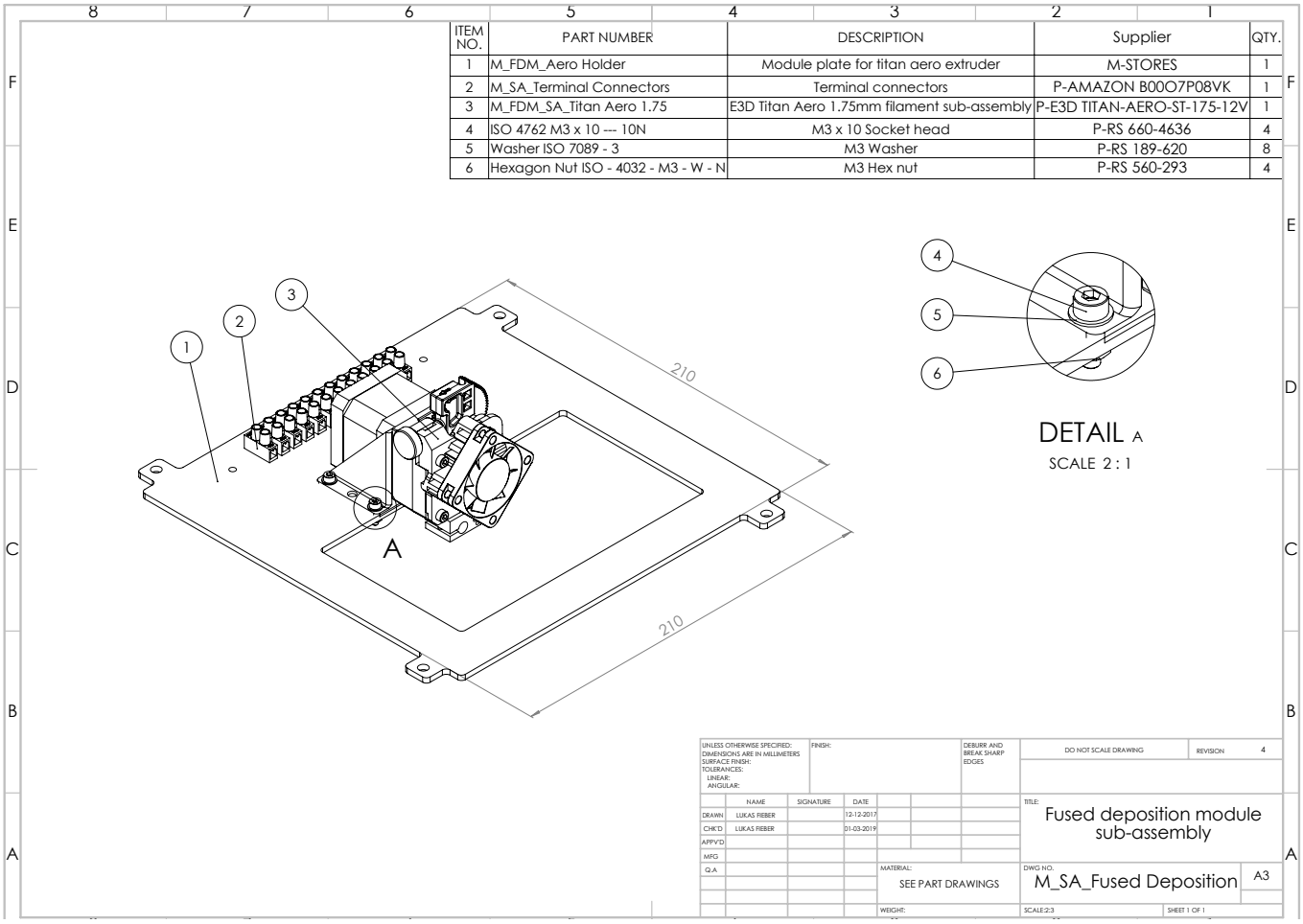

Figure B.3.5: Engineering drawing of the *fused filament fabrication (FFF)* sub-assembly (acronym used for file naming `FDM`, tier 3).

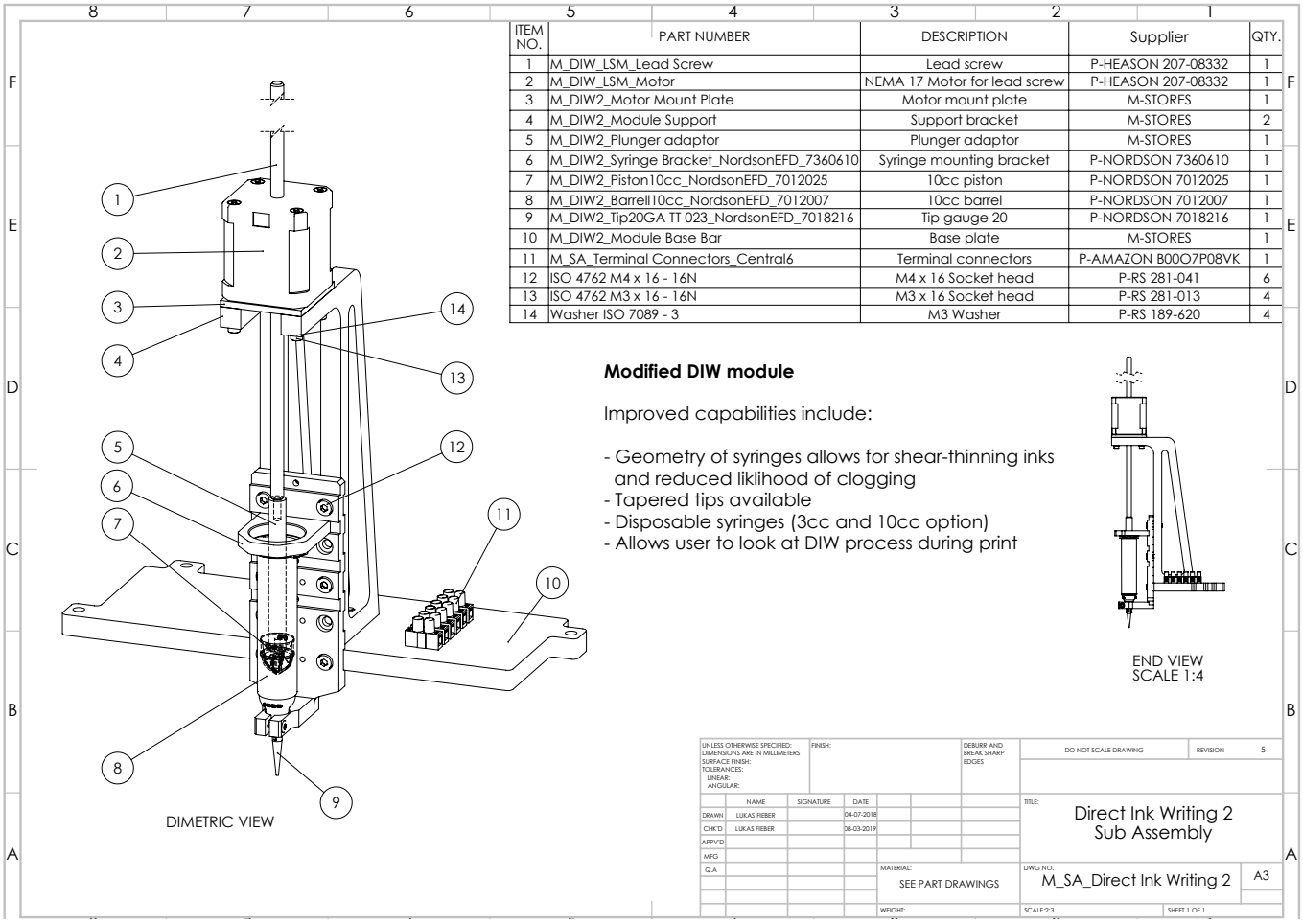

Figure B.3.6: Engineering drawing of the *direct ink writing (DIW)* sub-assembly (acronym used for file naming `DIW2`, tier 3).

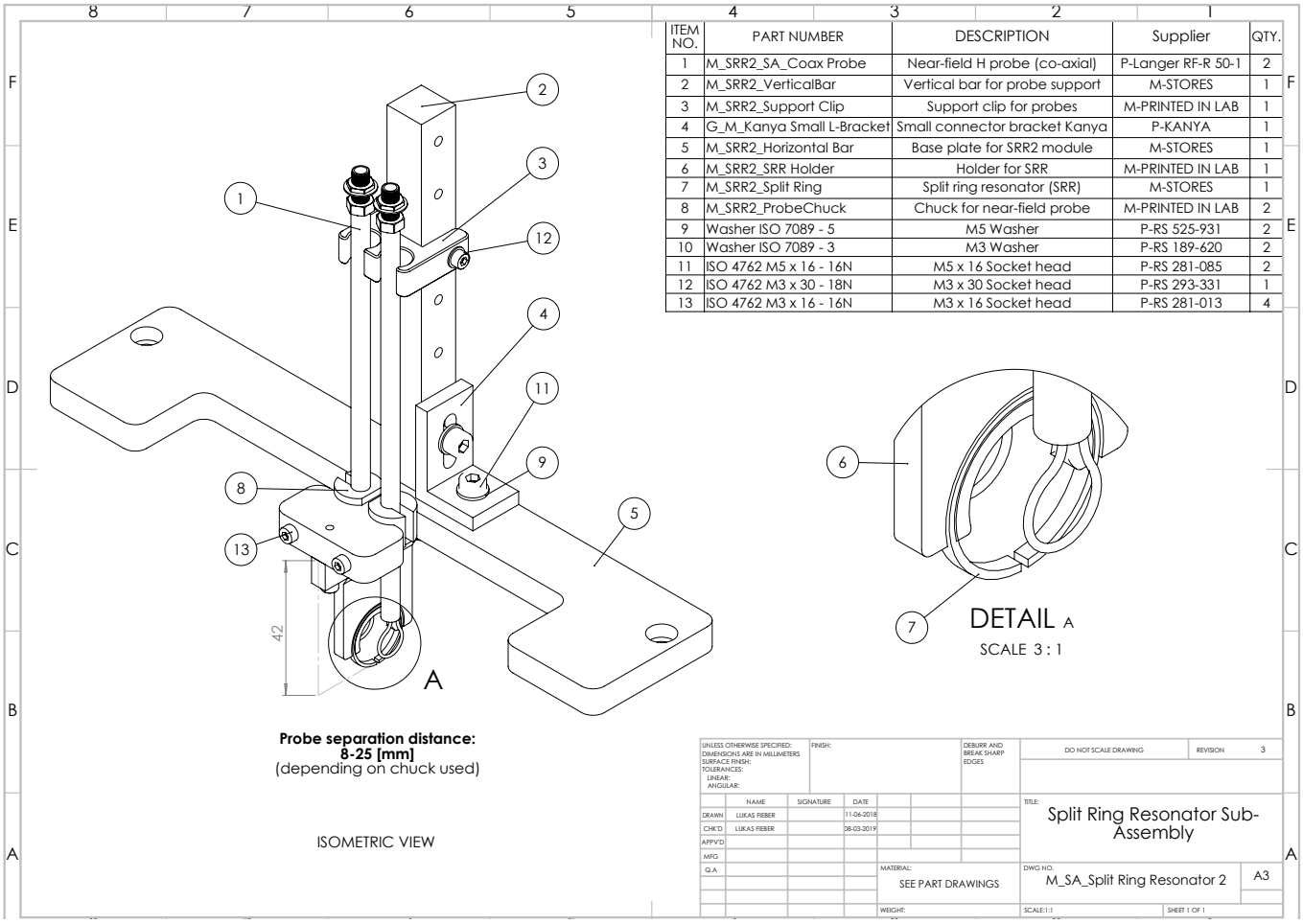

Figure B.3.7: Engineering drawing of the *split ring resonator (SRR)* sub-assembly (acronym used for file naming `SRR2`, tier 3).

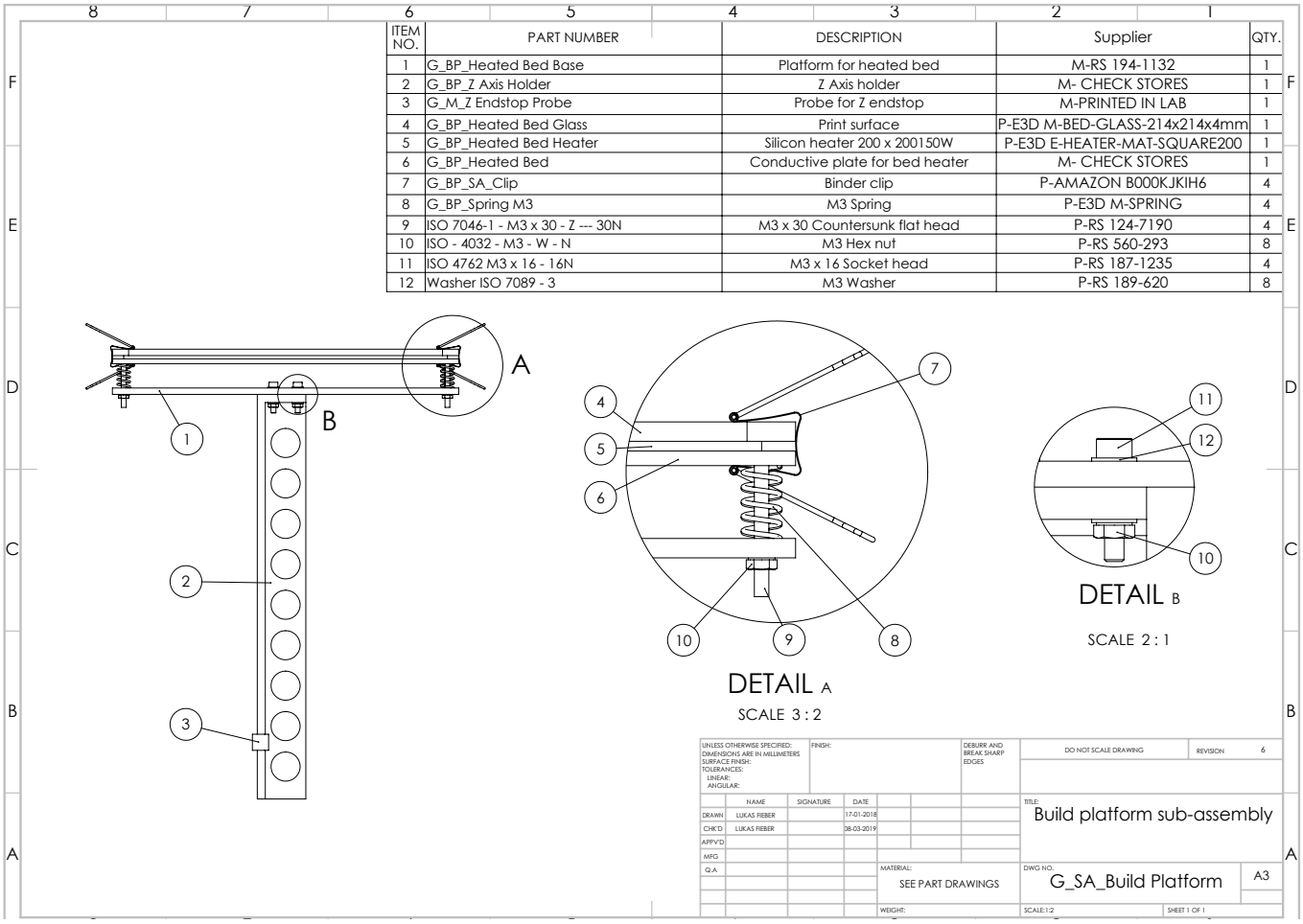

Figure B.3.8: Engineering drawing of the *build platform* sub-assembly (acronym used for file naming `BP`, tier 3).

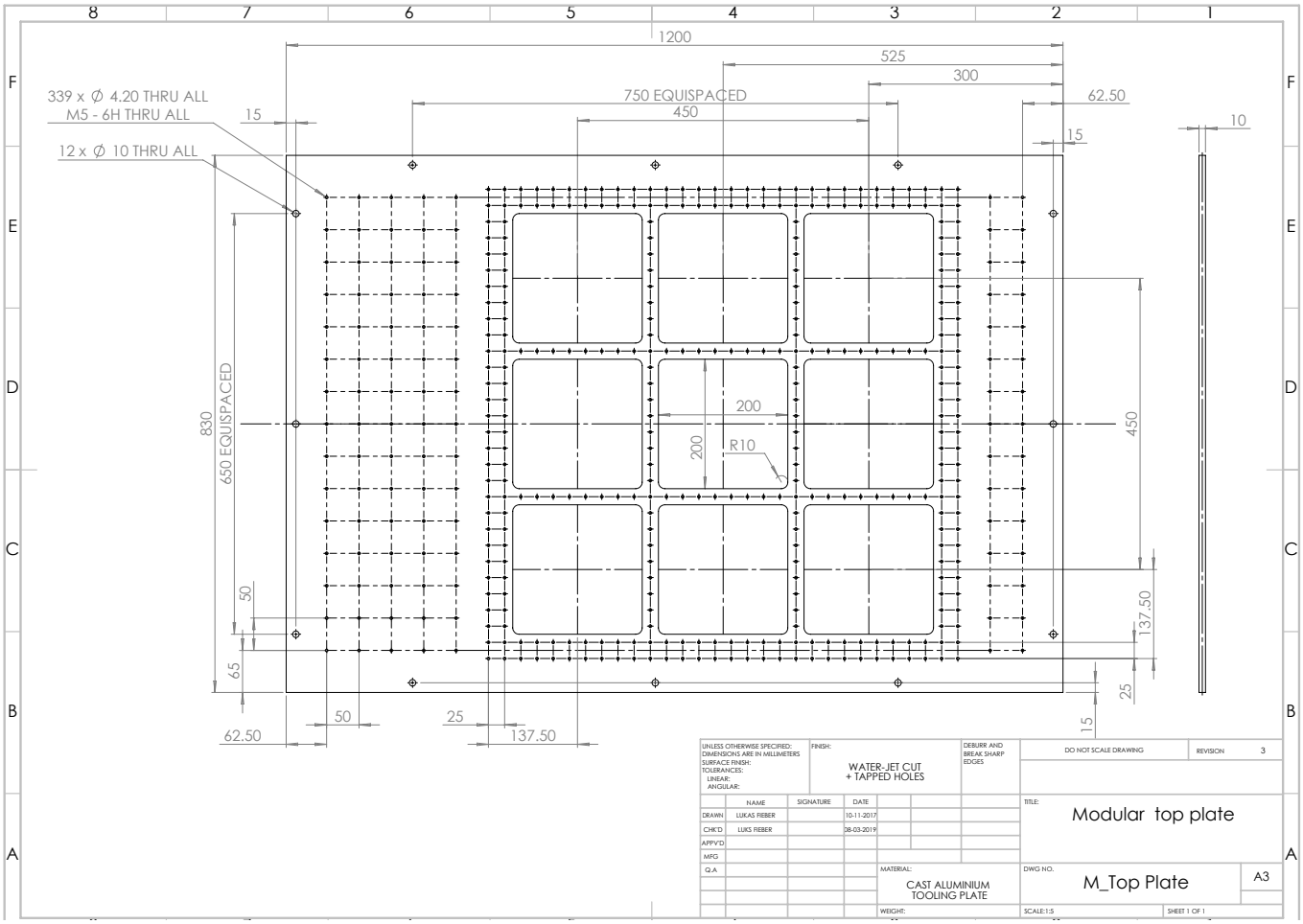

Figure B.3.9: Engineering drawing of the *top plate* part.

B.4 Control circuit diagrams

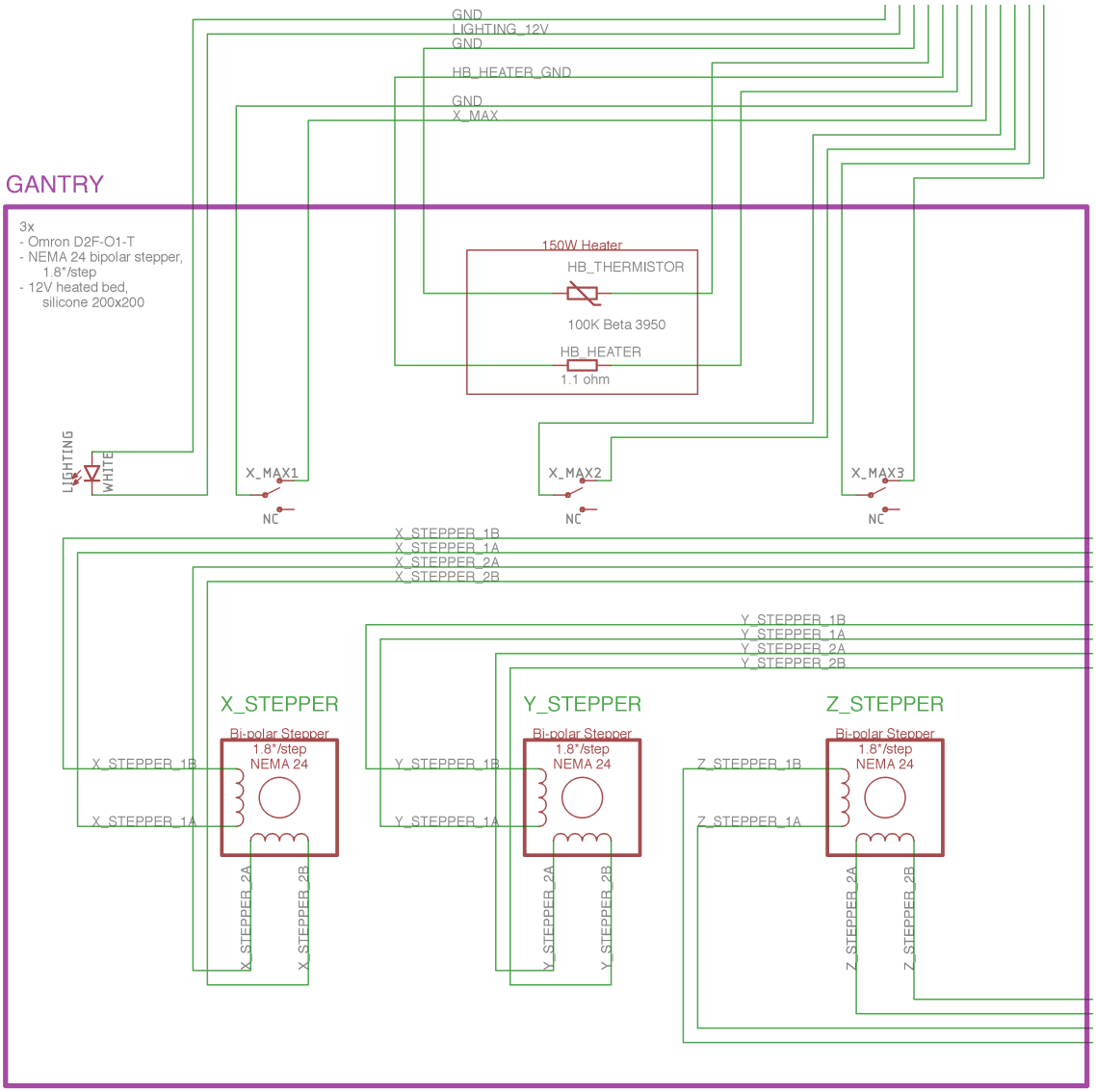

Figure B.4.1: Control circuit diagram of the *gantry and build platform* sub-assembly.

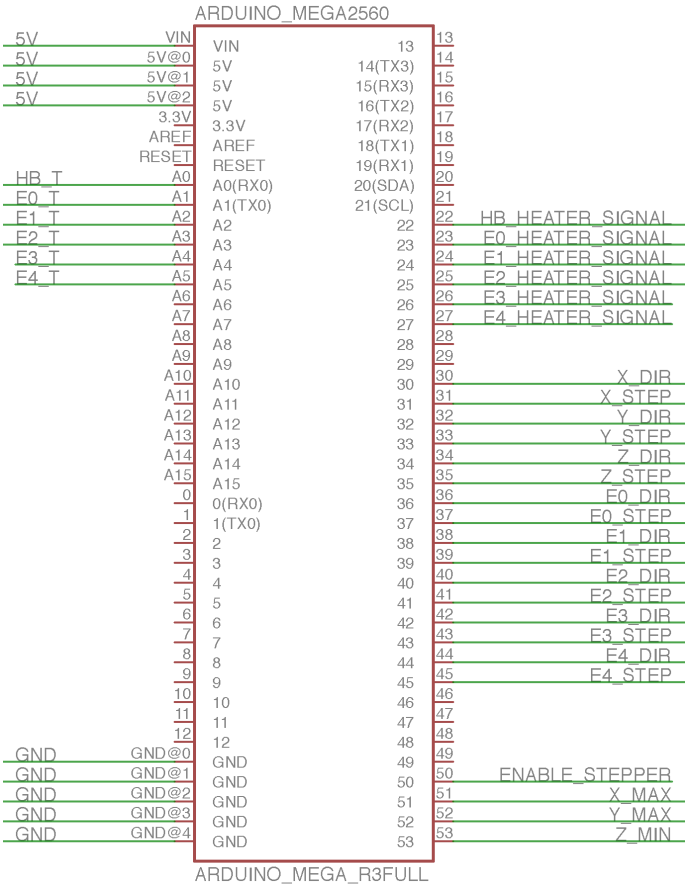

Figure B.4.2: Control circuit diagram showing the pin allocation of the main microcontroller (ATMega 2560) in the microelectronics system.

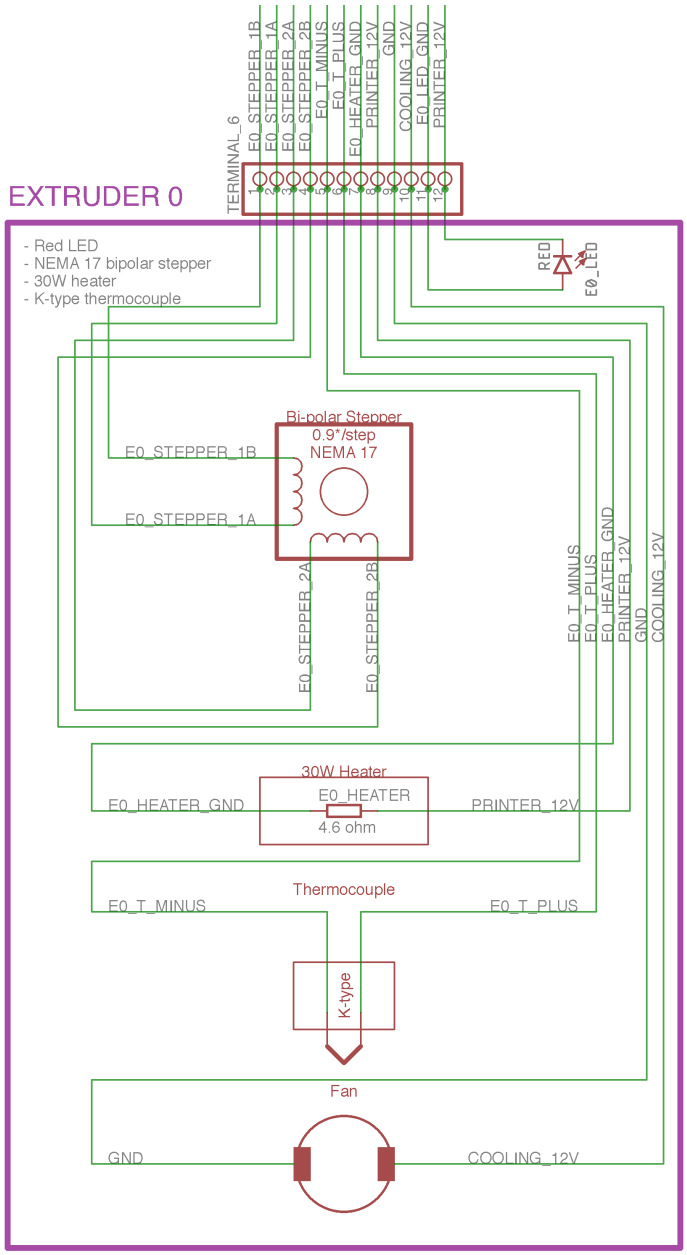

Figure B.4.3: Control circuit diagram of a FFF module.

B.5 Calibration of functional modules

X-Y-Z offset of functional modules To determine the location of module heads/tips/etc. with respect to each other, the following calibration process was conducted: (1) *homing* of the gantry (i.e. `g-Code` command `G28 XYZ`), (2) calibration of a FFF module following best-practice [321] (usually the module in *position 0*), (3) printing of a $10 \times 10 \times 10$ mm cube (FFF) centered on the build platform, (4) recording of the XY location where nozzles/syringe tips/etc. of all other modules come in contact with all vertical faces (Y-Z and X-Z) of the printed cube, (5) using the midpoints of of the measurements from (4) as X and Y offsets in the slicing engine or hybrid-AM app (see Table 5.6.A), and finally (6) recording the Z coordinate (in the hybrid-AM app) where the nozzle/syringe tip/etc. of all modules touch the build plate following best-practice [321].

Bibliography

[1] ASTM International. "F2792-12a - Standard Terminology for Additive Manufacturing Technologies". In: *Rapid Manufacturing Association* (2013), pp. 10–12. DOI: 10.1520/F2792-12A. arXiv: arXiv:1011.1669v3.

[2] Kaiyan Qiu et al. "3D Printed Organ Models with Physical Properties of Tissue and Integrated Sensors". In: *Advanced Materials Technologies* 3.3 (2018), p. 1700235. DOI: 10.1002/admt.201700235. URL: http://doi.wiley.com/10.1002/admt.201700235.

[3] Siemens. *Fast, efficient, flexible: Additive Manufacturing (3D-printing) in the energy sector*. 2019. URL: https://new.siemens.com/global/en/products/energy/services/maintenance/parts/additive-manufacturing.html (visited on 04/30/2019).

[4] David H. Autor, David Dorn, and Gordon H. Hanson. "The China Shock: Learning from Labor-Market Adjustment to Large Changes in Trade". In: *Ssrn* (2016). DOI: 10.1146/annurev-economics-080315-015041. arXiv: arXiv:1011.1669v3.

[5] (Chartered Institute of Management Accountants). "The global manufacturing sector : current issues". In: *Economic Policy* (2010).

[6] "Rethinking innovation in industrial manufacturing". In: *(PWC)* (2013), p. 92767436.

[7] Gregory Tassey. "Competing in Advanced Manufacturing: The Need for Improved Growth Models and Policies". In: *Journal of Economic Perspectives* 28.1 (2014), pp. 27–48. DOI: 10.1257/jep.28.1.27. URL: http://pubs.aeaweb.org/doi/10.1257/jep.28.1.27.

[8] (ASQ). *Shortage of Skilled Workers Tops Economy for Anticipated Challenge in 2018, according to ASQ Survey*. 2017. URL: http://asq.org/newsroom/news-releases/2017/20171128-manufacturing-outlook-survey.html (visited on 01/16/2019).

[9] Kim Zetter. *Serious security holes found in Siemens control systems targeted by Stuxnet*. 2011. URL: https://arstechnica.com/information-technology/2011/08/serious-security-holes-found-in-siemens-control-systems-targeted-by-stuxnet/.

[10] (Check Point Software Technologies LTD). *Cyber Attack Trends*. Tech. rep. 2018, p. 23.

[11] Ateeq Khan and Klaus Turowski. "A Survey of Current Challenges in Manufacturing Industry and Preparation for Industry 4.0". In: *Proceedings of the First International Scientific Conference "Intelligent Information Technologies for Industry" (IITI'16)*. Ed. by Ajith Abraham et al. Cham: Springer International Publishing, 2016, pp. 15–26.

[12] Marian Mueller et al. "Industrial Manufacturing Trends 2018-19". In: *PWC* (2018). URL: https://www.strategyand.pwc.com/media/file/Industrial-Manufacturing-Trends-2018-19.pdf{\%}0Ahttps://www.strategyand.pwc.com/trend/2018-manufacturing.

[13] Nicolas Hunke et al. *Winning in IoT*. Tech. rep. 2017.

[14] Henning Kagermann, Wolfgang Wahlster, and Johannes Helbig. "Recommendations for implementing the strategic initiative INDUSTRIE 4.0: Final report of the Industrie 4.0 Working Group". In: *Final report of the Industrie 4.0 WG* April (2013), p. 82. DOI: 10.13140/RG.2.2.14480.20485.

[15] George Q. Huang, YF Zhang, and PY Jiang. "RFID-based wireless manufacturing for real-time management of job shop WIP inventories". In: *The International Journal of Advanced Manufacturing Technology* 36.7-8 (2008), pp. 752–764. DOI: 10.1007/s00170-006-0897-4. URL: http://link.springer.com/10.1007/s00170-006-0897-4.

[16] Bernard Schmidt and Lihui Wang. "Cloud-enhanced predictive maintenance". In: *The International Journal of Advanced Manufac-*

turing Technology 99.1-4 (2018), pp. 5–13. DOI: 10.1007/s00170-016-8983-8. URL: http://link.springer.com/10.1007/s00170-016-8983-8.

[17] Daniel R. Eyers and Andrew T. Potter. "Industrial Additive Manufacturing: A manufacturing systems perspective". In: *Computers in Industry* 92-93 (2017), pp. 208–218. DOI: 10.1016/j.compind.2017.08.002.

[18] David Bourell et al. "Materials for additive manufacturing". In: *CIRP Annals* 66.2 (2017), pp. 659–681. DOI: 10.1016/j.cirp.2017.05.009. URL: http://dx.doi.org/10.1016/j.cirp.2017.05.009.

[19] H. Bikas, P. Stavropoulos, and G. Chryssolouris. "Additive manufacturing methods and modelling approaches: a critical review". In: *The International Journal of Advanced Manufacturing Technology* 83.1-4 (2016), pp. 389–405. DOI: 10.1007/s00170-015-7576-2. URL: http://link.springer.com/10.1007/s00170-015-7576-2.

[20] Sunpreet Singh, Seeram Ramakrishna, and Rupinder Singh. "Material issues in additive manufacturing: A review". In: *Journal of Manufacturing Processes* 25 (2017), pp. 185–200. DOI: 10.1016/j.jmapro.2016.11.006. URL: http://dx.doi.org/10.1016/j.jmapro.2016.11.006.

[21] Tuan D. Ngo et al. "Additive manufacturing (3D printing): A review of materials, methods, applications and challenges". In: *Composites Part B: Engineering* 143.December 2017 (2018), pp. 172–196. DOI: 10.1016/j.compositesb.2018.02.012. URL: https://doi.org/10.1016/j.compositesb.2018.02.012.

[22] Samuel Clark Ligon et al. "Polymers for 3D Printing and Customized Additive Manufacturing". In: *Chemical Reviews* 117.15 (2017), pp. 10212–10290. DOI: 10.1021/acs.chemrev.7b00074. arXiv: NIHMS150003.

[23] John J. Lewandowski and Mohsen Seifi. "Metal Additive Manufacturing: A Review of Mechanical Properties". In: *Annual Review of Materials Research* 46.1 (2016), pp. 151–186. DOI: 10.1146/annurev-matsci-070115-032024. URL: http://www.annualreviews.org/doi/10.1146/annurev-matsci-070115-032024.

[24] Nahum Travitzky et al. "Additive manufacturing of ceramic-based materials". In: *Advanced Engineering Materials* 16.6 (2014), pp. 729–754. DOI: 10.1002/adem.201400097.

[25] B Redwood et al. *The 3D Printing Handbook: Technologies, Design and Applications*. Unknown Publisher, 2018. URL: https://books.google.co.uk/books?id=R3OvswEACAAJ.

[26] Sebastian Mohr and Omera Khan. "3D Printing and Its Disruptive Impacts on Supply Chains of the Future". In: *Technology Innovation Management Review* 5.11 (2015), p. 45. DOI: 10.5437/08956308X5606193.

[27] Eric MacDonald et al. "3D printing for the rapid prototyping of structural electronics". In: *IEEE Access* 2 (2014), pp. 234–242. DOI: 10.1109/ACCESS.2014.2311810.

[28] Sheng Yang and Yaoyao Fiona Zhao. "Additive manufacturing-enabled design theory and methodology: a critical review". In: *The International Journal of Advanced Manufacturing Technology* 80.1-4 (2015), pp. 327–342. DOI: 10.1007/s00170-015-6994-5. URL: http://link.springer.com/10.1007/s00170-015-6994-5.

[29] Christiane Beyer. "Strategic Implications of Current Trends in Additive Manufacturing". In: *Journal of Manufacturing Science and Engineering* 136.6 (2014), p. 064701. DOI: 10.1115/1.4028599. URL: http://manufacturingscience.asmedigitalcollection.asme.org/article.aspx?doi=10.1115/1.4028599.

[30] Malte Gebler, Anton J.M. Schoot Uiterkamp, and Cindy Visser. "A global sustainability perspective on 3D printing technologies". In: *Energy Policy* 74.C (2014), pp. 158–167. DOI: 10.1016/j.enpol.2014.08.033. arXiv: arXiv:1011.1669v3. URL: http://dx.doi.org/10.1016/j.enpol.2014.08.033.

[31] Irene J. Petrick and Timothy W. Simpson. "Point of View: 3D Printing Disrupts Manufacturing: How Economies of One Create New Rules of Competition". In: *Research-Technology Management* 56.6 (2013), pp. 12–16. DOI: 10.5437/08956308X5606193. URL: http://openurl.ingenta.com/content/xref?genre=article{\&}issn=0895-6308{\&}volume=56{\&}issue=6{\&}spage=12.

[32] Stephen Mellor, Liang Hao, and David Zhang. "Additive manufacturing: A framework for implementation". In: *International Journal of Production Economics* 149 (2014), pp. 194–201. DOI: 10.1016/j.ijpe.2013.07.008. arXiv: /dx.doi.org/10.1108/BIJ-10-2012-0068 [http:].

[33] John Manners-Bell and Ken Lyon. "The Implications of 3D Printing for the Global Logistics Industry". In: (2012), pp. 1–6.

[34] Tomas Kellner. *An Epiphany Of Disruption: GE Additive Chief Explains How 3D*

Printing Will Upend Manufacturing. 2017. URL: https://www.ge.com/reports/epiphany-disruption-ge-additive-chief-explains-3d-printing-will-upend-manufacturing/.

[35] Adrian Bowyer and Vik Olliver. *RepRap*. 2019. URL: https://reprap.org/.

[36] Rhys Jones et al. "Reprap - The replicating rapid prototyper". In: *Robotica* 29.1 SPEC. ISSUE (2011), pp. 177–191. DOI: 10.1017/S026357471000069X.

[37] Simon Bradshaw, Adrian Bowyer, and Patrick Haufe. "The Intellectual Property Implications of Low-Cost 3D Printing". In: *Scripted* 7.1 (2010). DOI: https://doi.org/10.2966/scrip.070110.5.

[38] S. Scott Crump. *Apparatus and method for creating three-dimensional objects*. 1992.

[39] *High Value Manufacturing Catapult - HVM*. 2019. URL: http://hvm.catapult.org.uk (visited on 04/26/2019).

[40] *America Makes - National Additive Manufacturing Innovation Institute*. 2019. URL: https://www.americamakes.us (visited on 04/26/2019).

[41] *Frauenhofer Additive Manufacturing Alliance*. 2019. URL: https://www.fraunhofer.de/en/institutes/institutes-and-research-establishments-in-germany/fraunhofer-alliances/additive-manufacturing.html (visited on 04/26/2019).

[42] AMFG. *The Additive Manufacturing Landscape 2019*. Tech. rep. 2019.

[43] Halil L. Tekinalp et al. "Highly oriented carbon fiber-polymer composites via additive manufacturing". In: *Composites Science and Technology* 105 (2014), pp. 144–150. DOI: 10.1016/j.compscitech.2014.10.009. URL: http://dx.doi.org/10.1016/j.compscitech.2014.10.009.

[44] Michael Wehner et al. "An integrated design and fabrication strategy for entirely soft, autonomous robots". In: *Nature* 536.7617 (2016), pp. 451–455. DOI: 10.1038/nature19100. URL: http://dx.doi.org/10.1038/nature19100.

[45] Eleonora Atzeni and Alessandro Salmi. "Economics of additive manufacturing for end-usable metal parts". In: *International Journal of Advanced Manufacturing Technology* 62.9-12 (2012), pp. 1147–1155. DOI: 10.1007/s00170-011-3878-1.

[46] Emily Kennedy et al. "Biomimicry: A Path to Sustainable Innovation". In: *Design Issues* 31.3 (2015), pp. 66–73. DOI: 10.1162/DESI_a_00339. URL: http://www.mitpressjournals.org/doi/10.1162/DESI{_}a{_}00339.

[47] (DHL Trend Research). *3D Printing and the future of supply chains*. Tech. rep. 2016. URL: http://www.dhl.com/content/dam/downloads/g0/about{_}us/logistics{_}insights/dhl{_}trendreport{_}3dprinting.pdf.

[48] John C. Steuben, Athanasios P. Iliopoulos, and John G. Michopoulos. "Implicit slicing for functionally tailored additive manufacturing". In: *Computer-Aided Design* 77 (2016), pp. 107–119. DOI: 10.1016/j.cad.2016.04.003. URL: http://dx.doi.org/10.1016/j.cad.2016.04.003https://linkinghub.elsevier.com/retrieve/pii/S001044851630015X.

[49] Julien Gardan. "Smart materials in additive manufacturing: state of the art and trends". In: *Virtual and Physical Prototyping* 14.1 (2019), pp. 1–18. DOI: 10.1080/17452759.2018.1518016. URL: https://www.tandfonline.com/doi/full/10.1080/17452759.2018.1518016.

[50] General Fabb. *3D Printer Manufacturers: Who's In The Lead?* 2019. URL: https://www.fabbaloo.com/blog/2018/4/16/3d-printer-manufacturers-whos-in-the-lead (visited on 01/16/2019).

[51] Joe Hiemenz. *Additive Manufacturing Trends in Aerospace*. Tech. rep. Stratasys, 2014, p. 6. URL: www.stratasys.com.

[52] R L Harmon. *Reinventing the factory. Productivity breakthroughs in manufacturing today*. Reinventing the Factory. Free Press, 1990. URL: https://books.google.co.uk/books?id=NSNNtAEACAAJ.

[53] B. Nau, A. Roderburg, and F. Klocke. "Ramp-up of hybrid manufacturing technologies". In: *CIRP Journal of Manufacturing Science and Technology* 4.3 (2011), pp. 313–316. DOI: 10.1016/j.cirpj.2011.04.003. URL: http://dx.doi.org/10.1016/j.cirpj.2011.04.003.

[54] Eypor Runar Eiriksson. "Computer Vision for Additive Manufacturing". PhD. Technical University of Denmark, 2018.

[55] Neri Oxman. "Variable property rapid prototyping: Inspired by nature, where form is characterized by heterogeneous compositions, the paper presents a novel approach to layered manufacturing entitled variable property rapid prototyping". In: *Virtual and Physical Prototyping* 6.1 (2011), pp. 3–31. DOI: 10.1080/17452759.2011.558588.

[56] Xiling Yao et al. “A multi-material part design framework in additive manufacturing”. In: *The International Journal of Advanced Manufacturing Technology* 99.9-12 (2018), pp. 2111–2119. DOI: 10.1007/s00170-018-2025-7. URL: http://link.springer.com/10.1007/s00170-018-2025-7.

[57] Patrik Spalt and Thomas Bauernhansl. “A Framework for Integration of Additive Manufacturing Technologies in Production Networks”. In: *Procedia CIRP* 57 (2016), pp. 716–721. DOI: 10.1016/j.procir.2016.11.124. URL: http://dx.doi.org/10.1016/j.procir.2016.11.124.

[58] Ismet P. Ilyas. “3D Machine Vision and Additive Manufacturing: Concurrent Product and Process Development”. In: *IOP Conference Series: Materials Science and Engineering* 46.1 (2013). DOI: 10.1088/1757-899X/46/1/012029. URL: http://stacks.iop.org/1757-899X/46/i=1/a=012029?key=crossref.b7a53e9b1856e72778fda9201b245fdd.

[59] Hybrid Manufacturing Technologies. *AMBIT Series 7 multi-task system*. 2019. URL: http://www.hybridmanutech.com (visited on 03/05/2019).

[60] Joseph M. Flynn et al. “Hybrid additive and subtractive machine tools – Research and industrial developments”. In: *International Journal of Machine Tools and Manufacture* 101 (2016), pp. 79–101. DOI: 10.1016/j.ijmachtools.2015.11.007. URL: http://dx.doi.org/10.1016/j.ijmachtools.2015.11.007.

[61] Marion Merklein et al. “Hybrid Additive Manufacturing Technologies – An Analysis Regarding Potentials and Applications”. In: *Physics Procedia* 83 (2016), pp. 549–559. DOI: 10.1016/j.phpro.2016.08.057. URL: https://linkinghub.elsevier.com/retrieve/pii/S187538921630164X.

[62] Lin Li, Azadeh Haghighi, and Yiran Yang. “A novel 6-axis hybrid additive-subtractive manufacturing process: Design and case studies”. In: *Journal of Manufacturing Processes* 33.September 2017 (2018), pp. 150–160. DOI: 10.1016/j.jmapro.2018.05.008. URL: https://doi.org/10.1016/j.jmapro.2018.05.008.

[63] Wei Du, Qian Bai, and Bi Zhang. “A Novel Method for Additive/Subtractive Hybrid Manufacturing of Metallic Parts”. In: *Procedia Manufacturing* 5 (2016), pp. 1018–1030. DOI: 10.1016/j.promfg.2016.08.067. URL: http://dx.doi.org/10.1016/j.promfg.2016.08.067.

[64] Taku Yamazaki. “Development of A Hybrid Multi-tasking Machine Tool: Integration of Additive Manufacturing Technology with CNC Machining”. In: *Procedia CIRP* 42.Isem Xviii (2016), pp. 81–86. DOI: 10.1016/j.procir.2016.02.193. URL: http://dx.doi.org/10.1016/j.procir.2016.02.193.

[65] R.J. Friel and R.A. Harris. “Ultrasonic Additive Manufacturing – A Hybrid Production Process for Novel Functional Products”. In: *Procedia CIRP* 6.1 (2013), pp. 35–40. DOI: 10.1016/j.procir.2013.03.004. URL: http://dx.doi.org/10.1016/j.procir.2013.03.004.

[66] Solidscape. *Wax 3D printers*. 2019. URL: https://www.solidscape.com (visited on 03/05/2019).

[67] Makerbot. *Replicator+*. 2019. URL: https://www.makerbot.com/3d-printers/replicator/ (visited on 03/05/2019).

[68] David Espalin et al. “Multi-material, multi-technology FDM: exploring build process variations”. In: *Rapid Prototyping Journal* 20.3 (2014), pp. 236–244. DOI: 10.1108/RPJ-12-2012-0112. URL: http://www.emeraldinsight.com/doi/10.1108/RPJ-12-2012-0112.

[69] Xiaoyong Tian et al. “Interface and performance of 3D printed continuous carbon fiber reinforced PLA composites”. In: *Composites Part A: Applied Science and Manufacturing* 88 (2016), pp. 198–205. DOI: 10.1016/j.compositesa.2016.05.032. URL: http://dx.doi.org/10.1016/j.compositesa.2016.05.032.

[70] Markforged. *Mark Two Desktop Carbon Fibre 3D Printer for Manufacturing*. 2019. URL: https://markforged.com/mark-two/ (visited on 04/25/2019).

[71] Cel-robox. *RoboxPro*. 2019. URL: http://www.cel-robox.com/roboxpro/ (visited on 03/05/2019).

[72] Jae Won WChoi, Ho Chan Kim, and Ryan Wicker. “Multi-material stereolithography”. In: *Journal of Materials Processing Technology* 211.3 (2011), pp. 318–328. DOI: 10.1016/j.jmatprotec.2010.10.003. URL: http://dx.doi.org/10.1016/j.jmatprotec.2010.10.003.

[73] Alt LLC. *3Dalt*. 2019. URL: https://www.3dalt.com (visited on 03/05/2019).

[74] Next Dynamics. *NexD1*. 2019. URL: https://www.next-dynamics.com (visited on 03/05/2019).

[75] Qi Ge et al. "Active origami by 4D printing". In: *Smart Materials and Structures* 23.2014 (2014). DOI: 10.1088/0964-1726/23/9/094007.

[76] Stratasys. *Stratsys J735 and J750 fullcolor, multimaterial printer*. 2019. URL: https://www.stratasys.com/3d-printers/j735-j750 (visited on 04/25/2019).

[77] A. Yakovlev et al. "Laser-assisted direct manufacturing of functionally graded 3D objects". In: *Surface and Coatings Technology* 190.1 (2005), pp. 15–24. DOI: 10.1016/j.surfcoat.2004.07.070.

[78] W.K. Chiu and K.M. Yu. "Direct digital manufacturing of three-dimensional functionally graded material objects". In: *Computer-Aided Design* 40.12 (2008), pp. 1080–1093. DOI: 10.1016/j.cad.2008.10.002. URL: http://dx.doi.org/10.1016/j.cad.2008.10.002.

[79] Amit Bandyopadhyay and Bryan Heer. "Additive manufacturing of multi-material structures". In: *Materials Science and Engineering: R: Reports* 129.April (2018), pp. 1–16. DOI: 10.1016/j.mser.2018.04.001. URL: https://doi.org/10.1016/j.mser.2018.04.001.

[80] Eric MacDonald and Ryan Wicker. "Multiprocess 3D printing for increasing component functionality". In: *Science* 353.6307 (2016), aaf2093–aaf2093. DOI: 10.1126/science.aaf2093. URL: http://www.sciencemag.org/cgi/doi/10.1126/science.aaf2093.

[81] (Aether). *Aether*. 2019. URL: https://discoveraether.com (visited on 01/30/2019).

[82] Dongping Deng et al. "Three-dimensional circuit fabrication using four-dimensional printing and direct ink writing". In: *International Symposium on Flexible Automation, ISFA 2016* (2016), pp. 286–291. DOI: 10.1109/ISFA.2016.7790176.

[83] Guo Liang Goh et al. "Additively manufactured multi-material free-form structure with printed electronics". In: *International Journal of Advanced Manufacturing Technology* 94.1-4 (2018), pp. 1309–1316. DOI: 10.1007/s00170-017-0972-z.

[84] Snapmaker. *3-in-1 3D printer*. 2019. URL: https://snapmaker.com (visited on 03/05/2019).

[85] A. Lopes et al. "Expanding Rapid Prototyping for Electronic Systems Integration of Arbitrary Form". In: *Proceedings of the 2006 Solid Freeform Fabrication Symposium* (2006), pp. 644–655. DOI: 10.1017/CBO9781107415324.004. arXiv: arXiv:1011.1669v3.

[86] Alexander D. Valentine et al. "Hybrid 3D Printing of Soft Electronics". In: *Advanced Materials* 29.40 (2017), p. 1703817. DOI: 10.1002/adma.201703817. arXiv: arXiv:1011.1669v3. URL: http://doi.wiley.com/10.1002/adma.201703817.

[87] Pitchaya Sitthi-Amorn et al. "MultiFab". In: *ACM Transactions on Graphics* 34.4 (2015), 129:1–129:11. DOI: 10.1145/2766962. URL: http://dl.acm.org/citation.cfm?doid=2809654.2766962.

[88] R. Ponche et al. "A new global approach to design for additive manufacturing: A method to obtain a design that meets specifications while optimizing a given additive manufacturing process is presented in this paper". In: *Virtual and Physical Prototyping* 7.2 (2012), pp. 93–105. DOI: 10.1080/17452759.2012.679499.

[89] Ajit Panesar et al. "Design framework for multifunctional additive manufacturing: Coupled optimization strategy for structures with embedded functional systems". In: *Additive Manufacturing* 16 (2017), pp. 98–106. DOI: 10.1016/j.addma.2017.05.009. URL: http://dx.doi.org/10.1016/j.addma.2017.05.009.

[90] H. Wargnier et al. "Proposal for a multimaterial design procedure". In: *Materials and Design* 56 (2014), pp. 44–49. DOI: 10.1016/j.matdes.2013.11.004. URL: http://dx.doi.org/10.1016/j.matdes.2013.11.004.

[91] Erin Blackwell et al. "The great re-make : Manufacturing for modern times". In: *McKinsey & Company* June (2017), p. 134. DOI: 10.1016/j.newideapsych.2011.10.001.

[92] Nadya Peek. "Making Machines that Make: Object-Oriented Hardware Meets Object-Oriented Software". PhD. MIT, 2016.

[93] GitHub. *Ultimaker-CuraEngine: a powerful, fast and robust engine for processing 3D models into 3D printing instruction*. 2019. URL: https://github.com/Ultimaker/CuraEngine (visited on 03/25/2019).

[94] Alessandro Ranellucci. *Slic3r - Open source 3D printing toolbox*. 2019. URL: https://slic3r.org (visited on 03/25/2019).

[95] Fabmetheus. *Skeinforge*. 2019. (Visited on 07/03/2018).

[96] Markforged. *Eiger software*. 2019. URL: https://www.eiger.io/ (visited on 04/22/2019).

[97] Formlabs. *PreForm software*. 2019. URL: https://formlabs.com/software/ (visited on 04/22/2019).

[98] Replicat. *ReplicatorG is a simple, open source 3D printing program*. 2019. (Visited on 03/22/2019).

[99] Simplify3D. *3D printing software*. 2019. URL: https://www.simplify3d.com (visited on 03/22/2019).

[100] Repetier. *Repetier Software*. 2019. URL: https://www.repetier.com (visited on 03/29/2019).

[101] Ultimaker. *Ultimaker Cura - Advanced 3D printing software, made accessible*. 2019. URL: https://ultimaker.com/en/products/ultimaker-cura-software (visited on 03/29/2019).

[102] Pronterface. *Printrun - pure python print host software*. 2019. URL: http://www.pronterface.com (visited on 03/29/2019).

[103] Gina Haeussige. *Octoprint - the snappy webinterface for your 3D printer*. 2019. URL: https://octoprint.org.

[104] Siemens. *Siemens NX software for manufacturing*. 2019. (Visited on 04/26/2019).

[105] Autodesk. *Additive manufacturing and deisgn software*. 2019. URL: https://www.autodesk.com/products/netfabb/overview (visited on 03/29/2019).

[106] (LMU). *Programming paradigm*. 2019. URL: https://cs.lmu.edu/{~}ray/notes/paradigms/ (visited on 09/07/2019).

[107] NCviewer. *GCode Viewer and Machine Simulator*. 2019. URL: https://ncviewer.com (visited on 04/29/2019).

[108] Mika Yeap. *5 Fantastic 3D Printer Controller Boards in 2019*. 2019. URL: https://all3dp.com/2/5-fantastic-3d-printer-controller-boards/.

[109] Arduino. *Arduino Mega2560*. 2019. URL: https://store.arduino.cc/mega-2560-r3 (visited on 04/15/2019).

[110] Ultimachine. *RAMBo-1.4 control board*. URL: https://github.com/ultimachine/RAMBo-1.4 (visited on 04/15/2019).

[111] Smoothieware. *Smoothieware firmware*. 2019. URL: http://smoothieware.org/ (visited on 04/15/2019).

[112] Panucatt. *Panucatt control board*. 2019. URL: http://www.panucatt.com/category{_}s/1819.htm (visited on 04/15/2019).

[113] Duet3D. *Duet3D control board*. 2019. URL: https://www.duet3d.com (visited on 04/15/2019).

[114] Thing-printer. *Revolve control board*. 2019. URL: https://www.thing-printer.com/revolve/ (visited on 04/15/2019).

[115] Kliment. *Sprinter firmware*. 2019. URL: https://github.com/kliment/Sprinter (visited on 04/15/2019).

[116] Gnea. *Grbl firmware*. URL: https://github.com/gnea/grbl (visited on 04/15/2019).

[117] RepRap. *RepRap firmware*. 2019. URL: https://reprap.org/wiki/RepRap{_}Firmware (visited on 04/15/2019).

[118] Marlin. *Marlin firmware*. URL: http://marlinfw.org (visited on 04/15/2019).

[119] Traumflug. *Teacup firmware*. 2019. URL: https://github.com/Traumflug/Teacup{_}Firmware (visited on 04/15/2019).

[120] Kevin OConnor. *Klipper firmware*. 2019. URL: https://github.com/KevinOConnor/klipper (visited on 04/15/2019).

[121] Elias Bakken. *Redeem firmware*. 2019. URL: https://bitbucket.org/intelligentagent/redeem (visited on 04/15/2019).

[122] Flavio Ansovini. *FSLA printer firmware*. 2019. URL: https://github.com/flavioansovini/FSLAprinter (visited on 04/15/2019).

[123] Peng Chang et al. "3D printed electrochemical energy storage devices". In: *Journal of Materials Chemistry A* 7.9 (2019), pp. 4230–4258. DOI: 10.1039/C8TA11860D. URL: http://xlink.rsc.org/?DOI=C8TA11860D.

[124] Yingwei Wu, Dmitry Isakov, and Patrick Grant. "Fabrication of Composite Filaments with High Dielectric Permittivity for Fused Deposition 3D Printing". In: *Materials* 10.10 (2017), p. 1218. DOI: 10.3390/ma10101218. URL: http://www.mdpi.com/1996-1944/10/10/1218.

[125] Patrick F. Flowers et al. "3D printing electronic components and circuits with conductive thermoplastic filament". In: *Additive Manufacturing* 18.2017 (2017), pp. 156–163. DOI: 10.1016/j.addma.2017.10.002. URL: http://dx.doi.org/10.1016/j.addma.2017.10.002.

[126] Di Zhang et al. "Fabrication of highly conductive graphene flexible circuits by 3D printing". In: *Synthetic Metals* 217 (2016), pp. 79–86. DOI: 10.1016/j.synthmet.2016.03.014. URL: http://dx.doi.org/10.1016/j.synthmet.2016.03.014.

[127] James D. Carrico et al. "Fused filament 3D printing of ionic polymer-metal composites

(IPMCs)". In: *Smart Materials and Structures* 24.12 (2015), p. 125021. DOI: 10.1088/0964-1726/24/12/125021. URL: http://stacks.iop.org/0964-1726/24/i=12/a=125021?key=crossref.8695bca7caf6c1fd8d1e9b0e89dbcd15.

[128] Brian N. Turner, Robert Strong, and Scott A. Gold. "A review of melt extrusion additive manufacturing processes: I. Process design and modeling". In: *Rapid Prototyping Journal* 20.3 (2014), pp. 192–204. DOI: 10.1108/RPJ-01-2013-0012. URL: http://dx.doi.org/10.1108/RPJ-01-2013-0012.

[129] Omar A. Mohamed, Syed H. Masood, and Jahar L. Bhowmik. "Optimization of fused deposition modeling process parameters: a review of current research and future prospects". In: *Advances in Manufacturing* 3.1 (2015), pp. 42–53. DOI: 10.1007/s40436-014-0097-7. arXiv: 1011.1669v3. URL: http://link.springer.com/10.1007/s40436-014-0097-7.

[130] Lukas Fieber et al. "Single-operation, multiphase additive manufacture of electrochemical double layer capacitor devices". In: *Additive Manufacturing* 28.August (2019), pp. 344–353. DOI: 10.1016/j.addma.2019.05.001. URL: https://linkinghub.elsevier.com/retrieve/pii/S2214860419301319.

[131] Brian N. Turner and Scott A. Gold. "A review of melt extrusion additive manufacturing processes: II. Materials, dimensional accuracy, and surface roughness". In: *Rapid Prototyping Journal* 21.3 (2015), pp. 250–261. DOI: 10.1108/RPJ-02-2013-0017. arXiv: arXiv:1011.1669v3. URL: http://www.emeraldinsight.com/doi/10.1108/RPJ-02-2013-0017.

[132] R. Anitha, S. Arunachalam, and P. Radhakrishnan. "Critical parameters influencing the quality of prototypes in fused deposition modelling". In: *Journal of Materials Processing Technology* 118.1-3 (2001), pp. 385–388. DOI: 10.1016/S0924-0136(01)00980-3. URL: http://linkinghub.elsevier.com/retrieve/pii/S0924013601009803.

[133] G. Ćwikła et al. "The influence of printing parameters on selected mechanical properties of FDM/FFF 3D-printed parts". In: *IOP Conference Series: Materials Science and Engineering* 227.1 (2017), p. 012033. DOI: 10.1088/1757-899X/227/1/012033. URL: http://stacks.iop.org/1757-899X/227/i=1/a=012033?key=crossref.355a546adfa7c7f968ed4fc6be1ae0d6.

[134] Ala'aldin Alafaghani et al. "Experimental Optimization of Fused Deposition Modelling Processing Parameters: A Design-for-Manufacturing Approach". In: *Procedia Manufacturing* 10 (2017), pp. 791–803. DOI: 10.1016/j.promfg.2017.07.079. URL: http://dx.doi.org/10.1016/j.promfg.2017.07.079.

[135] Yue Lin et al. "Pristine Graphene Aerogels by Room-Temperature Freeze Gelation". In: *Advanced Materials* 28.36 (2016), pp. 7993–8000. DOI: 10.1002/adma.201602393. URL: http://doi.wiley.com/10.1002/adma.201602393.

[136] B H King et al. "Influence of rheology on deposition behavior of ceramic pastes in direct fabrication systems". In: *Solid Freeform Fabrication Proceedings, August* (1998), pp. 391–398.

[137] Minxuan Kuang, Libin Wang, and Yanlin Song. "Controllable Printing Droplets for High-Resolution Patterns". In: *Advanced Materials* 26.40 (2014), pp. 6950–6958. DOI: 10.1002/adma.201305416. URL: http://doi.wiley.com/10.1002/adma.201305416.

[138] Joshua Lessing et al. "Inkjet Printing of Conductive Inks with High Lateral Resolution on Omniphobic "R F Paper" for Paper-Based Electronics and MEMS". In: *Advanced Materials* 26.27 (2014), pp. 4677–4682. DOI: 10.1002/adma.201401053. URL: http://doi.wiley.com/10.1002/adma.201401053.

[139] Dmitry Isakov et al. "A Split Ring Resonator Dielectric Probe for Near-Field Dielectric Imaging". In: *Scientific Reports* 7.1 (2017), pp. 1–9. DOI: 10.1038/s41598-017-02176-3. URL: http://dx.doi.org/10.1038/s41598-017-02176-3.

[140] (International Energy Agency). *Global Energy and CO2 Status Report 2017*. Tech. rep. March. International Energy Agency, 2017. URL: https://www.iea.org/publications/freepublications/publication/GECO2017.pdf.

[141] (Enerdata). *Global Energy Trends, 2018 edition. A step backward for the energy transition?* Tech. rep. Enerdata - intelligence + consulting, 2018, p. 1. URL: https://www.enerdata.net/publications/reports-presentations/2018-world-energy-trends-projections.html.

[142] Marija Ham et al. "Insights for Measuring Environmental Awareness". In: *Ekonomski Vjesnik Econviews* (2016), pp. 159–176.

[143] Naomi Klein. *This Changes Everything*. Simon & Schuster, 2014.

[144] Mathew Aneke and Meihong Wang. "Energy storage technologies and real life applications – A state of the art review". In: *Applied Energy* 179 (2016), pp. 350–377. DOI: 10.1016/j.apenergy.2016.06.097. URL: http://dx.doi.org/10.1016/j.apenergy.2016.06.097.

[145] Ibrahim Dincer and Canan Acar. "A review on clean energy solutions for better sustainability". In: *International Journal of Energy Research* 39.5 (2015), pp. 585–606. DOI: 10.1002/er.3329. URL: http://doi.wiley.com/10.1002/er.3329.

[146] Javid Mohtasham. "Review Article-Renewable Energies". In: *Energy Procedia* 74 (2015), pp. 1289–1297. DOI: 10.1016/j.egypro.2015.07.774. URL: http://dx.doi.org/10.1016/j.egypro.2015.07.774.

[147] (JEITA). *Production forecasts for the global electronics and information technology industries*. Tech. rep. Japan Electronics and Information Technology Indusgtries Association, 2017, p. 6. URL: https://www.jeita.or.jp/english/topics/2017/1219{_}en.pdf.

[148] Cheng Zhu et al. "3D printed functional nanomaterials for electrochemical energy storage". In: *Nano Today* (2017), pp. 1–14. DOI: 10.1016/j.nantod.2017.06.007. URL: http://www.sciencedirect.com/science/article/pii/S1748013217302426.

[149] Janet Ho, T.R. Jow, and Steven Boggs. "Historical introduction to capacitor technology". In: *IEEE Electrical Insulation Magazine* 26.1 (2010), pp. 20–25. DOI: 10.1109/MEI.2010.5383924. arXiv: arXiv:1011.1669v3. URL: http://ieeexplore.ieee.org/document/5383924/.

[150] John Miller. "A brief history of supercapacitors". In: *Battery + energy technologies* 21.52 (2007), pp. 61–78.

[151] Patrice Simon and Yury Gogotsi. "Materials for electrochemical capacitors". In: *Nature Materials* 7.11 (2008), pp. 845–854. DOI: 10.1038/nmat2297. URL: http://www.nature.com/articles/nmat2297.

[152] Cheng Zhong et al. "A review of electrolyte materials and compositions for electrochemical supercapacitors". In: *Chemical Society Reviews* 44.21 (2015), pp. 7484–7539. DOI: 10.1039/C5CS00303B. URL: http://xlink.rsc.org/?DOI=C5CS00303B.

[153] Francois Beguin. *Supercapacitors*. Ed. by François Béguin and Elżbieta Frąckowiak. Weinheim, Germany: Wiley-VCH Verlag GmbH & Co. KGaA, 2013, p. 539. DOI: 10.1002/9783527646661. URL: http://doi.wiley.com/10.1002/9783527646661.

[154] Yong Zhang et al. "Progress of electrochemical capacitor electrode materials: A review". In: *International Journal of Hydrogen Energy* 34.11 (2009), pp. 4889–4899. DOI: 10.1016/j.ijhydene.2009.04.005. URL: http://dx.doi.org/10.1016/j.ijhydene.2009.04.005.

[155] Jeff Emmerich. *Technical summary: Supercapacitors*. 2017. URL: https://www.design-concepts.com/insights/supercapacitors (visited on 02/07/2019).

[156] Market Research Future. *Super capacitor Market Research Report- Forecast 2022*. Tech. rep. Global: Market Research Future, 2019. URL: https://www.marketresearchfuture.com/reports/super-capacitor-market-2548.

[157] Mazen Yassine and Drazen Fabris. "Performance of Commercially Available Supercapacitors". In: *Energies* 10.9 (2017), p. 1340. DOI: 10.3390/en10091340. URL: http://www.mdpi.com/1996-1073/10/9/1340.

[158] Zenan Yu et al. "Supercapacitor electrode materials: nanostructures from 0 to 3 dimensions". In: *Energy & Environmental Science* 8.3 (2015), pp. 702–730. DOI: 10.1039/C4EE03229B. URL: http://xlink.rsc.org/?DOI=C4EE03229B.

[159] Elzbieta Frackowiak. "Carbon materials for supercapacitor application". In: *Physical Chemistry Chemical Physics* 9.15 (2007), p. 1774. DOI: 10.1039/b618139m. URL: http://xlink.rsc.org/?DOI=b618139m.

[160] Li Li Zhang, Rui Zhou, and X. S. Zhao. "Graphene-based materials as supercapacitor electrodes". In: *Journal of Materials Chemistry* 20.29 (2010), p. 5983. DOI: 10.1039/c000417k. arXiv: 0706.1062v1. URL: http://xlink.rsc.org/?DOI=c000417k.

[161] C Z Yuan et al. "Hierarchically structured carbon-based composites: Design, synthesis and their application in electrochemical capacitors". In: *Nanoscale* 3.2 (2011), pp. 529–545. DOI: 10.1039/C0NR00423E. URL: http://xlink.rsc.org/?DOI=C0NR00423E.

[162] Guoping Wang, Lei Zhang, and Jiujun Zhang. "A review of electrode materials for electrochemical supercapacitors". In: *Chem. Soc. Rev.* 41.2 (2012), pp. 797–828. DOI: 10.1039/C1CS15060J. arXiv: 1005.0853. URL: http://xlink.rsc.org/?DOI=C1CS15060J.

[163] B. E. Conway. *Electrochemical Supercapacitors, Scientific Fundamentals and Techno-*

logical Applications. New York: Kluwer Academic, Plenum Publishers, 1999, p. 698.

[164] Yonggang Wang, Yanfang Song, and Yongyao Xia. "Electrochemical capacitors: mechanism, materials, systems, characterization and applications". In: *Chemical Society Reviews* 45.21 (2016), pp. 5925–5950. DOI: 10.1039/C5CS00580A. URL: http://xlink.rsc.org/?DOI=C5CS00580A.

[165] Alexander C. Forse et al. "New Perspectives on the Charging Mechanisms of Supercapacitors". In: *Journal of the American Chemical Society* 138.18 (2016), pp. 5731–5744. DOI: 10.1021/jacs.6b02115. URL: http://pubs.acs.org/doi/10.1021/jacs.6b02115.

[166] Pawan Sharma and T.S. Bhatti. "A review on electrochemical double-layer capacitors". In: *Energy Conversion and Management* 51.12 (2010), pp. 2901–2912. DOI: 10.1016/j.enconman.2010.06.031. URL: http://dx.doi.org/10.1016/j.enconman.2010.06.031.

[167] Ander González et al. "Review on supercapacitors: Technologies and materials". In: *Renewable and Sustainable Energy Reviews* 58 (2016), pp. 1189–1206. DOI: 10.1016/j.rser.2015.12.249. URL: https://linkinghub.elsevier.com/retrieve/pii/S1364032115016329.

[168] P. Simon, Y. Gogotsi, and B. Dunn. "Where Do Batteries End and Supercapacitors Begin?" In: *Science* 343.6176 (2014), pp. 1210–1211. DOI: 10.1126/science.1249625. URL: http://www.sciencemag.org/cgi/doi/10.1126/science.1249625.

[169] Thierry Brousse, Daniel Bélanger, and Jeffrey W. Long. "To Be or Not To Be Pseudocapacitive?" In: *Journal of The Electrochemical Society* 162.5 (2015), A5185–A5189. DOI: 10.1149/2.0201505jes. URL: http://jes.ecsdl.org/lookup/doi/10.1149/2.0201505jes.

[170] Zhentao Zhu. "Effects of Various Binders on Supercapacitor Performances". In: *International Journal of Electrochemical Science* 11.10 (2016), pp. 8270–8279. DOI: 10.20964/2016.10.04. URL: http://www.electrochemsci.org/abstracts/vol11/111008270.pdf.

[171] Hawaiah Imam Maarof, Wan Mohd Ashri Wan Daud, and Mohamed Kheireddine Aroua. "Effect of varying the amount of binder on the electrochemical characteristics of palm shell activated carbon". In: *IOP Conference Series: Materials Science and Engineering* 210.1 (2017), p. 012011. DOI: 10.1088/1757-899X/210/1/012011. URL: http://stacks.iop.org/1757-899X/210/i=1/a=012011?key=crossref.7a88e59f34a1db78c483ab596fdb5762.

[172] Aaron J. Blake et al. "3D Printable Ceramic-Polymer Electrolytes for Flexible High-Performance Li-Ion Batteries with Enhanced Thermal Stability". In: *Advanced Energy Materials* 7.14 (2017), p. 1602920. DOI: 10.1002/aenm.201602920. URL: http://doi.wiley.com/10.1002/aenm.201602920.

[173] K. Tõnurist et al. "Influence of separator properties on electrochemical performance of electrical double-layer capacitors". In: *Journal of Electroanalytical Chemistry* 689 (2013), pp. 8–20. DOI: 10.1016/j.jelechem.2012.11.024. URL: https://linkinghub.elsevier.com/retrieve/pii/S1572665712004894.

[174] Christie M Hassan and Nikolaos a Peppas. "Structure and Applications of Poly(vinyl alcohol) Hydrogels Produced by Conventional Crosslinking or by Freezing/Thawing Methods". In: *Biopolymers · PVA Hydrogels, Anionic Polymerisation Nanocomposites*. Vol. 153. Berlin, Heidelberg: Springer Berlin Heidelberg, 2000, pp. 37–65. DOI: 10.1007/3-540-46414-X_2. URL: http://link.springer.com/10.1007/3-540-46414-X{_}2.

[175] Gengzhi Sun et al. "Layer-by-layer printing of laminated graphene-based interdigitated microelectrodes for flexible planar micro-supercapacitors". In: *Electrochemistry Communications* 51 (2015), pp. 33–36. DOI: 10.1016/j.elecom.2014.11.023. URL: http://dx.doi.org/10.1016/j.elecom.2014.11.023.

[176] Evgeniya Kovalska and Coskun Kocabas. "Organic electrolytes for graphene-based supercapacitor: Liquid, gel or solid". In: *Materials Today Communications* 7 (2016), pp. 155–160. DOI: 10.1016/j.mtcomm.2016.04.013. URL: http://dx.doi.org/10.1016/j.mtcomm.2016.04.013.

[177] Maral P S Mousavi et al. "Ionic Liquids as Electrolytes for Electrochemical Double-Layer Capacitors: Structures that Optimize Specific Energy". In: *ACS Applied Materials & Interfaces* 8.5 (2016), pp. 3396–3406. DOI: 10.1021/acsami.5b11353. URL: http://pubs.acs.org/doi/10.1021/acsami.5b11353.

[178] N. A. Choudhury, S. Sampath, and A. K. Shukla. "Hydrogel-polymer electrolytes for electrochemical capacitors: an overview". In: *Energy Environ. Sci.* 2.1 (2009), pp. 55–67. DOI: 10.1039/B811217G. URL: http://xlink.rsc.org/?DOI=B811217G.

[179] O. Stern. "Zur theorie der elektrolytischen doppelschicht". In: *Z. Elektrochem. Angew. Phys. Chem.* 30 (1924), pp. 508–516.

[180] H. v. Helmholtz. "Legacy Paper". In: *Natural philosophy* (1853), p. 114.

[181] M Gouy. "Sur la constitution de la charge electrique la surface d'un electrolyte". In: *J. Phys. Theor. Appl.* 9 (1910), pp. 457–468.

[182] David Leonard Chapman. "A contribution to the theory of electrocapillarity". In: *Philosophical Magazine Series 6* 25.148 (1913), pp. 475–481. DOI: 10.1080/14786440408634187. URL: http://www.tandfonline.com/doi/abs/10.1080/14786440408634187.

[183] Sanliang Zhang and Ning Pan. "Supercapacitors Performance Evaluation". In: *Advanced Energy Materials* 5.6 (2015), p. 1401401. DOI: 10.1002/aenm.201401401. URL: http://doi.wiley.com/10.1002/aenm.201401401.

[184] Andrew Burke. "Testing of Supercapacitors: Capacitance, Resistance, and Energy Energy and Power Capacity". In: *ISEE'Cap09 June*. Nantes, France, 2009, pp. 1–42.

[185] Meryl D Stoller and Rodney S Ruoff. "Best practice methods for determining an electrode material's performance for ultracapacitors". In: *Energy & Environmental Science* 3.9 (2010), p. 1294. DOI: 10.1039/c0ee00074d. arXiv: 1005.0805. URL: http://xlink.rsc.org/?DOI=c0ee00074d.

[186] Dr.N. Stryzhakova. *SC Testing methodology manual*. Tech. rep. IAPP Energy Caps, 2012, pp. 1–30. URL: http://www.energycaps.eu/wp-content/uploads/2013/09/Testing-Methodologies-Manual.pdf.

[187] Anis Allagui et al. "Reevaluation of Performance of Electric Double-layer Capacitors from Constant-current Charge/Discharge and Cyclic Voltammetry". In: *Scientific Reports* 6.1 (2016), p. 38568. DOI: 10.1038/srep38568. URL: http://www.nature.com/articles/srep38568.

[188] A. Balducci et al. "Perspective—A Guideline for Reporting Performance Metrics with Electrochemical Capacitors: From Electrode Materials to Full Devices". In: *Journal of The Electrochemical Society* 164.7 (2017), A1487–A1488. DOI: 10.1149/2.0851707jes. URL: http://jes.ecsdl.org/lookup/doi/10.1149/2.0851707jes.

[189] Bing-Ang Mei et al. "Physical Interpretations of Nyquist Plots for EDLC Electrodes and Devices". In: *The Journal of Physical Chemistry C* 122.1 (2018), pp. 194–206. DOI: 10.1021/acs.jpcc.7b10582. URL: http://pubs.acs.org/doi/10.1021/acs.jpcc.7b10582.

[190] British Standards Institution (BSI). *BSI Standards Publication Fixed resistors for use in electronic equipment Part 1 : Generic specification*. Tech. rep. BSI, 2015.

[191] Mingyuan Zhang et al. "Improving the electrochemical performances of active carbon-based supercapacitors through the combination of introducing functional groups and using redox additive electrolyte". In: *Journal of Saudi Chemical Society* 22.8 (2018), pp. 908–918. DOI: 10.1016/j.jscs.2018.02.001. URL: https://linkinghub.elsevier.com/retrieve/pii/S1319610318300188.

[192] Xu Peng et al. "A zwitterionic gel electrolyte for efficient solid-state supercapacitors". In: *Nature Communications* 7.1 (2016), p. 11782. DOI: 10.1038/ncomms11782. URL: http://www.nature.com/articles/ncomms11782.

[193] Feng Zhang et al. "3D printing technologies for electrochemical energy storage". In: *Nano Energy* 40.May (2017), pp. 418–431. DOI: 10.1016/j.nanoen.2017.08.037. URL: http://dx.doi.org/10.1016/j.nanoen.2017.08.037.

[194] Irving Erlichman. *Method for manufacturing flat batteries*. 1976.

[195] John A. Alford and Goose Creek. *High power density double layer energy storage devices*. 1999.

[196] Shuichi Ishida et al. *Activated carbon and process for production thereof, nonaqueous type polarizable electrodes and electric double-layer capacitors*. 2008.

[197] Taiji Mizobuchi, Teruyuki Shinsenji, and Masaaki Yanase. *Separator, and electrolytic capacitor, electric double layer capacitor, nonaqueous battery using the separator*. 1999.

[198] Manabu Tsushima et al. *Electric double layer capacitor and separator thereof*. 2000.

[199] Kena Zhang et al. "Fabrication and dielectric properties of Ba0.6Sr0.4TiO3 / acrylonitrile–butadiene–styrene resin composites". In: *Journal of Materials Science: Materials in Electronics* 28.12 (2017), pp. 8960–8968. DOI: 10.1007/s10854-017-6626-y. URL: http://link.springer.com/10.1007/s10854-017-6626-y.

[200] Ye Shi, Xingyi Zhou, and Guihua Yu. "Material and Structural Design of Novel Binder Systems for High-Energy, High-

Power Lithium-Ion Batteries". In: *Accounts of Chemical Research* 50.11 (2017), pp. 2642–2652. DOI: 10.1021/acs.accounts.7b00402. URL: http://pubs.acs.org/doi/10.1021/acs.accounts.7b00402.

[201] Hemadri Chadalavada et al. "Production Lead Time Reduction in a Battery Manufacturing Unit using Lean Manufacturing". In: *International Journal of Engineering Research & Technology* 4.04 (2015), pp. 842–847.

[202] Wei Gao et al. "Direct laser writing of micro-supercapacitors on hydrated graphite oxide films". In: *Nature Nanotechnology* 6.8 (2011), pp. 496–500. DOI: 10.1038/nnano.2011.110. URL: http://www.nature.com/articles/nnano.2011.110.

[203] Adriano Ambrosi and Martin Pumera. "3D-printing technologies for electrochemical applications". In: *Chemical Society Reviews* 45.10 (2016), pp. 2740–2755. DOI: 10.1039/C5CS00714C. URL: http://dx.doi.org/10.1039/C5CS00714C.

[204] Xiaocong Tian et al. "Emerging 3D-Printed Electrochemical Energy Storage Devices: A Critical Review". In: *Advanced Energy Materials* 7.17 (2017), p. 1700127. DOI: 10.1002/aenm.201700127. URL: http://doi.wiley.com/10.1002/aenm.201700127.

[205] Keun-Ho Choi, David B. Ahn, and Sang-Young Lee. "Current Status and Challenges in Printed Batteries: Toward Form Factor-Free, Monolithic Integrated Power Sources". In: *ACS Energy Letters* 3.1 (2018), pp. 220–236. DOI: 10.1021/acsenergylett.7b01086. URL: http://pubs.acs.org/doi/10.1021/acsenergylett.7b01086.

[206] Jintao Zhang and X. S. Zhao. "On the Configuration of Supercapacitors for Maximizing Electrochemical Performance". In: *ChemSusChem* 5.5 (2012), pp. 818–841. DOI: 10.1002/cssc.201100571. URL: http://doi.wiley.com/10.1002/cssc.201100571.

[207] Katsuhiko Ariga et al. "Layer-by-layer Nanoarchitectonics: Invention, Innovation, and Evolution". In: *Chemistry Letters* 43.1 (2014), pp. 36–68. DOI: 10.1246/cl.130987. URL: http://www.journal.csj.jp/doi/10.1246/cl.130987.

[208] Quan Xu et al. "Three-dimensional micro/nanoscale architectures: fabrication and applications". In: *Nanoscale* 7.25 (2015), pp. 10883–10895. DOI: 10.1039/C5NR02048D. URL: http://xlink.rsc.org/?DOI=C5NR02048D.

[209] Jordan R. Raney and Jennifer A. Lewis. "Printing mesoscale architectures". In: *MRS Bulletin* 40.11 (2015), pp. 943–950. DOI: 10.1557/mrs.2015.235. URL: http://www.journals.cambridge.org/abstract{_}S0883769415002353.

[210] Yu Li, Zheng-Yi Fu, and Bao-lian Su. "Hierarchically Structured Porous Materials for Energy Conversion and Storage". In: *Advanced Functional Materials* 22.22 (2012), pp. 4634–4667. DOI: 10.1002/adfm.201200591. URL: http://doi.wiley.com/10.1002/adfm.201200591.

[211] Yanbo Qi et al. "Is There a Benefit in Employing Graded Electrodes for Lithium-Ion Batteries?" In: *Journal of The Electrochemical Society* 164.13 (2017), A3196–A3207. DOI: 10.1149/2.1051713jes. URL: http://jes.ecsdl.org/lookup/doi/10.1149/2.1051713jes.

[212] Chuan Cheng et al. "Micro-scale graded electrodes for improved dynamic and cycling performance of Li-ion batteries". In: *Journal of Power Sources* 413 (2019), pp. 59–67. DOI: 10.1016/j.jpowsour.2018.12.021. URL: https://linkinghub.elsevier.com/retrieve/pii/S0378775318313727.

[213] Nana Amponsah Kyerematen, Thierry Brousse, and David Pech. "Microsupercapacitors as miniaturized energy-storage components for on-chip electronics". In: *Nature Nanotechnology* 12.1 (2016), pp. 7–15. DOI: 10.1038/nnano.2016.196. URL: http://www.nature.com/doifinder/10.1038/nnano.2016.196.

[214] Lukas Fieber and Patrick S Grant. "C.2 Capacitors". In: *Current state of 3D printing technologies & materials*. Ed. by Albert Tarancón Rubio and Vincenzo Esposito. Wiley, 2019.

[215] Di Zhang et al. "Fabrication of highly conductive graphene flexible circuits by 3D printing". In: *Synthetic Metals* 217 (2016), pp. 79–86. DOI: 10.1016/j.synthmet.2016.03.014. URL: http://dx.doi.org/10.1016/j.synthmet.2016.03.014.

[216] Wei Yu et al. "3D Printing of Carbon Nanotubes-Based Microsupercapacitors". In: *ACS Applied Materials & Interfaces* 9.5 (2017), pp. 4597–4604. DOI: 10.1021/acsami.6b13904. URL: http://pubs.acs.org/doi/10.1021/acsami.6b13904.

[217] Min Wei et al. "3D direct writing fabrication of electrodes for electrochemical storage devices". In: *Journal of Power Sources* 354 (2017), pp. 134–147. DOI: 10.1016/j.jpowsour.2017.04.042. URL: http://dx.doi.org/10.1016/j.jpowsour.2017.04.042.

[218] Kaufui V. Wong and Aldo Hernandez. "A Review of Additive Manufacturing". In: *ISRN Mechanical Engineering* 2012 (2012), pp. 1–10. DOI: 10.5402/2012/208760. arXiv: 208760. URL: https://www.hindawi.com/archive/2012/208760/.

[219] Claudius Dichtl, Pit Sippel, and Stephan Krohns. "Dielectric Properties of 3D Printed Polylactic Acid". In: *Advances in Materials Science and Engineering* 2017 (2017), pp. 1–10. DOI: 10.1155/2017/6913835. URL: https://www.hindawi.com/journals/amse/2017/6913835/.

[220] Xiaojun Wei et al. "3D Printable Graphene Composite". In: *Scientific Reports* 5.1 (2015), p. 11181. DOI: 10.1038/srep11181. URL: http://www.nature.com/articles/srep11181.

[221] Milad Areir et al. "A study of 3D printed active carbon electrode for the manufacture of electric double-layer capacitors". In: *Journal of Manufacturing Processes* 25 (2017), pp. 351–356. DOI: 10.1016/j.jmapro.2016.12.020. URL: http://dx.doi.org/10.1016/j.jmapro.2016.12.020.

[222] Anan Tanwilaisiri et al. "Design and fabrication of modular supercapacitors using 3D printing". In: *Journal of Energy Storage* 16 (2018), pp. 1–7. DOI: 10.1016/j.est.2017.12.020. URL: http://linkinghub.elsevier.com/retrieve/pii/S2352152X17303602.

[223] Hemma Philamore et al. "Cast and 3D printed ion exchange membranes for monolithic microbial fuel cell fabrication". In: *Journal of Power Sources* 289 (2015), pp. 91–99. DOI: 10.1016/j.jpowsour.2015.04.113. URL: https://linkinghub.elsevier.com/retrieve/pii/S0378775315007703.

[224] Milad Areir et al. "3D printing of highly flexible supercapacitor designed for wearable energy storage". In: *Materials Science and Engineering: B* 226.August (2017), pp. 29–38. DOI: 10.1016/j.mseb.2017.09.004. URL: http://linkinghub.elsevier.com/retrieve/pii/S0921510717302246.

[225] Joseph T. Muth et al. "Embedded 3D Printing of Strain Sensors within Highly Stretchable Elastomers". In: *Advanced Materials* 26.36 (2014), pp. 6307–6312. DOI: 10.1002/adma.201400334. arXiv: 1111.4970. URL: http://doi.wiley.com/10.1002/adma.201400334.

[226] C C Ho, J W Evans, and P K Wright. "Direct write dispenser printing of a zinc microbattery with an ionic liquid gel electrolyte". In: *Journal of Micromechanics and Microengineering* 20.10 (2010), p. 104009. DOI: 10.1088/0960-1317/20/10/104009. URL: http://stacks.iop.org/0960-1317/20/i=10/a=104009?key=crossref.0c94b23205d5795c822cc235f5129aad.

[227] Teressa Nathan-Walleser et al. "3D Micro-Extrusion of Graphene-based Active Electrodes: Towards High-Rate AC Line Filtering Performance Electrochemical Capacitors". In: *Advanced Functional Materials* 24.29 (2014), pp. 4706–4716. DOI: 10.1002/adfm.201304151. URL: http://doi.wiley.com/10.1002/adfm.201304151.

[228] Zhuxian Yang et al. "Preparation of 3D graphene-based architectures and their applications in supercapacitors". In: *Progress in Natural Science: Materials International* 25.6 (2015), pp. 554–562. DOI: 10.1016/j.pnsc.2015.11.010. URL: http://dx.doi.org/10.1016/j.pnsc.2015.11.010.

[229] Cheng Zhu et al. "Supercapacitors Based on Three-Dimensional Hierarchical Graphene Aerogels with Periodic Macropores". In: *Nano Letters* 16.6 (2016), pp. 3448–3456. DOI: 10.1021/acs.nanolett.5b04965. URL: http://pubs.acs.org/doi/10.1021/acs.nanolett.5b04965.

[230] Bin Yao et al. "Efficient 3D Printed Pseudocapacitive Electrodes with Ultrahigh MnO2 Loading". In: *Joule* 3.2 (2019), pp. 459–470. DOI: 10.1016/j.joule.2018.09.020. URL: https://linkinghub.elsevier.com/retrieve/pii/S2542435118304586.

[231] Yang Yang et al. "Three dimensional printing of high dielectric capacitor using projection based stereolithography method". In: *Nano Energy* 22 (2016), pp. 414–421. DOI: 10.1016/j.nanoen.2016.02.045. URL: http://dx.doi.org/10.1016/j.nanoen.2016.02.045.

[232] P.J. Bartolo and J. Gaspar. "Metal filled resin for stereolithography metal part". In: *CIRP Annals* 57.1 (2008), pp. 235–238. DOI: 10.1016/j.cirp.2008.03.124. URL: https://linkinghub.elsevier.com/retrieve/pii/S0007850608000942.

[233] Qiming Chen et al. "Printing 3D Gel Polymer Electrolyte in Lithium-Ion Microbattery Using Stereolithography". In: *Journal of The Electrochemical Society* 164.9 (2017), A1852–A1857. DOI: 10.1149/2.0651709jes. URL: http://jes.ecsdl.org/lookup/doi/10.1149/2.0651709jes.

[234] Stefanie Zekoll et al. "Hybrid electrolytes with 3D bicontinuous ordered ceramic and polymer microchannels for all-solid-state

batteries". In: *Energy & Environmental Science* 11.1 (2018), pp. 185–201. DOI: 10.1039/C7EE02723K. URL: http://xlink.rsc.org/?DOI=C7EE02723K.

[235] I. Cooperstein, M. Layani, and S. Magdassi. "3D printing of porous structures by UV-curable O/W emulsion for fabrication of conductive objects". In: *Journal of Materials Chemistry C* 3.9 (2015), pp. 2040–2044. DOI: 10.1039/C4TC02215G. URL: http://xlink.rsc.org/?DOI=C4TC02215G.

[236] Hailong Ning et al. "Holographic patterning of high-performance on-chip 3D lithium-ion microbatteries". In: *Proceedings of the National Academy of Sciences* 112.21 (2015), pp. 6573–6578. DOI: 10.1073/pnas.1423889112. URL: http://www.pnas.org/lookup/doi/10.1073/pnas.1423889112.

[237] Swee Leong Sing et al. "Direct selective laser sintering and melting of ceramics: a review". In: *Rapid Prototyping Journal* 23.3 (2017), pp. 611–623. DOI: 10.1108/RPJ-11-2015-0178. arXiv: /dx.doi.org/10.1108/BIJ-10-2012-0068 [http:]. URL: http://www.emeraldinsight.com/doi/10.1108/RPJ-11-2015-0178.

[238] Adriano Ambrosi, James Guo Sheng Moo, and Martin Pumera. "Helical 3D-Printed Metal Electrodes as Custom-Shaped 3D Platform for Electrochemical Devices". In: *Advanced Functional Materials* 26.5 (2016), pp. 698–703. DOI: 10.1002/adfm.201503902. URL: http://doi.wiley.com/10.1002/adfm.201503902.

[239] Chen Zhao et al. "Three dimensional (3D) printed electrodes for interdigitated supercapacitors". In: *Electrochemistry Communications* 41 (2014), pp. 20–23. DOI: 10.1016/j.elecom.2014.01.013. URL: http://dx.doi.org/10.1016/j.elecom.2014.01.013.

[240] Xinhua Liu et al. "3D-Printed Structural Pseudocapacitors". In: *Advanced Materials Technologies* 1.9 (2016), p. 1600167. DOI: 10.1002/admt.201600167. URL: http://doi.wiley.com/10.1002/admt.201600167.

[241] R.D. Goodridge, C.J. Tuck, and R.J.M. Hague. "Laser sintering of polyamides and other polymers". In: *Progress in Materials Science* 57.2 (2012), pp. 229–267. DOI: 10.1016/j.pmatsci.2011.04.001. URL: http://dx.doi.org/10.1016/j.pmatsci.2011.04.001.

[242] M. Schmidt, D. Pohle, and T. Rechtenwald. "Selective Laser Sintering of PEEK". In: *CIRP Annals* 56.1 (2007), pp. 205–208. DOI: 10.1016/j.cirp.2007.05.097. URL: https://linkinghub.elsevier.com/retrieve/pii/S0007850607000510.

[243] Jingke Mo et al. *Development of Liquid/-Gas Diffusion Layers with Low-Cost Additive Manufacturing*. Tech. rep. 2014.

[244] Tomohiro Koyano et al. "Electrochemical machining using porous electrodes fabricated by powder bed fusion additive manufacturing process". In: *CIRP Annals* 66.1 (2017), pp. 213–216. DOI: 10.1016/j.cirp.2017.04.127. URL: http://dx.doi.org/10.1016/j.cirp.2017.04.127.

[245] Byung Ju Kang, Chang Kyu Lee, and Je Hoon Oh. "All-inkjet-printed electrical components and circuit fabrication on a plastic substrate". In: *Microelectronic Engineering* 97.4023 (2012), pp. 251–254. DOI: 10.1016/j.mee.2012.03.032. URL: http://dx.doi.org/10.1016/j.mee.2012.03.032.

[246] Jongwoo Lim et al. "All-inkjet-printed Metal-Insulator-Metal (MIM) capacitor". In: *Current Applied Physics* 12.SUPPL. 1 (2012), e14–e17. DOI: 10.1016/j.cap.2011.04.035. URL: http://dx.doi.org/10.1016/j.cap.2011.04.035.

[247] Yi Liu, Tianhong Cui, and Kody Varahramyan. "All-polymer capacitor fabricated with inkjet printing technique". In: *Solid-State Electronics* 47.9 (2003), pp. 1543–1548. DOI: 10.1016/S0038-1101(03)00082-0. URL: http://linkinghub.elsevier.com/retrieve/pii/S0038110103000820.

[248] Neil Graddage et al. "Inkjet printed thin and uniform dielectrics for capacitors and organic thin film transistors enabled by the coffee ring effect". In: *Organic Electronics* 29 (2016), pp. 114–119. DOI: 10.1016/j.orgel.2015.11.039. URL: http://dx.doi.org/10.1016/j.orgel.2015.11.039.

[249] Adam G. Kelly et al. "All-printed capacitors from graphene-BN-graphene nanosheet heterostructures". In: *Applied Physics Letters* 109.2 (2016), p. 023107. DOI: 10.1063/1.4958858. URL: http://aip.scitation.org/doi/10.1063/1.4958858.

[250] Robyn Worsley et al. "All-2D Material Inkjet-Printed Capacitors: Toward Fully Printed Integrated Circuits". In: *ACS Nano* 13.1 (2019), pp. 54–60. DOI: 10.1021/acsnano.8b06464. URL: http://pubs.acs.org/doi/10.1021/acsnano.8b06464.

[251] Ehab Saleh et al. "3D inkjet-printed UV-curable inks for multi-functional electromagnetic applications". In: *Additive Manufacturing* 13 (2017), pp. 143–148. DOI: 10.1016/

j.addma.2016.10.002. URL: http://dx.doi.org/10.1016/j.addma.2016.10.002.

[252] Jolke Perelaer et al. "Printed electronics: the challenges involved in printing devices, interconnects, and contacts based on inorganic materials". In: *Journal of Materials Chemistry* 20.39 (2010), p. 8446. DOI: 10.1039/c0jm00264j. URL: http://xlink.rsc.org/?DOI=c0jm00264j.

[253] Krishna Rao R. Venkata et al. "Conductive silver inks and their applications in printed and flexible electronics". In: *RSC Advances* 5.95 (2015), pp. 77760–77790. DOI: 10.1039/C5RA12013F. URL: http://xlink.rsc.org/?DOI=C5RA12013F.

[254] V. Correia et al. "Design and fabrication of multilayer inkjet-printed passive components for printed electronics circuit development". In: *Journal of Manufacturing Processes* 31 (2018), pp. 364–371. DOI: 10.1016/j.jmapro.2017.11.016. URL: http://dx.doi.org/10.1016/j.jmapro.2017.11.016.

[255] Robert MacCurdy et al. "Printable hydraulics: A method for fabricating robots by 3D co-printing solids and liquids". In: *2016 IEEE International Conference on Robotics and Automation (ICRA)*. Vol. 2016-June. IEEE, 2016, pp. 3878–3885. DOI: 10.1109/ICRA.2016.7487576. arXiv: 1512.03744. URL: http://ieeexplore.ieee.org/document/7487576/.

[256] Martti Kaempgen et al. "Printable Thin Film Supercapacitors Using Single-Walled Carbon Nanotubes". In: *Nano Letters* 9.5 (2009), pp. 1872–1876. DOI: 10.1021/nl8038579. URL: http://pubs.acs.org/doi/abs/10.1021/nl8038579.

[257] Keun-Ho Choi et al. "All-inkjet-printed, solid-state flexible supercapacitors on paper". In: *Energy & Environmental Science* 9.9 (2016), pp. 2812–2821. DOI: 10.1039/C6EE00966B. URL: http://xlink.rsc.org/?DOI=C6EE00966B.

[258] P.-E. Delannoy et al. "Toward fast and cost-effective ink-jet printing of solid electrolyte for lithium microbatteries". In: *Journal of Power Sources* 274 (2015), pp. 1085–1090. DOI: 10.1016/j.jpowsour.2014.10.164. URL: http://dx.doi.org/10.1016/j.jpowsour.2014.10.164.

[259] Neelam Singh et al. "Paintable Battery". In: *Scientific Reports* 2.1 (2012), p. 481. DOI: 10.1038/srep00481. URL: http://www.nature.com/articles/srep00481.

[260] Jiantong Li et al. "Efficient Inkjet Printing of Graphene". In: *Advanced Materials* 25.29 (2013), pp. 3985–3992. DOI: 10.1002/adma.201300361. URL: http://doi.wiley.com/10.1002/adma.201300361.

[261] Chun Huang and Patrick S. Grant. "One-step spray processing of high power all-solid-state supercapacitors". In: *Scientific Reports* 3.1 (2013), p. 2393. DOI: 10.1038/srep02393. URL: http://www.nature.com/articles/srep02393.

[262] Chun Huang et al. "Solid-state supercapacitors with rationally designed heterogeneous electrodes fabricated by large area spray processing for wearable energy storage applications". In: *Scientific Reports* 6.1 (2016), p. 25684. DOI: 10.1038/srep25684. URL: http://www.nature.com/articles/srep25684.

[263] David Pech et al. "Elaboration of a microstructured inkjet-printed carbon electrochemical capacitor". In: *Journal of Power Sources* 195.4 (2010), pp. 1266–1269. DOI: 10.1016/j.jpowsour.2009.08.085. URL: https://linkinghub.elsevier.com/retrieve/pii/S0378775309015250.

[264] P.-E. Delannoy et al. "Ink-jet printed porous composite LiFePO 4 electrode from aqueous suspension for microbatteries". In: *Journal of Power Sources* 287 (2015), pp. 261–268. DOI: 10.1016/j.jpowsour.2015.04.067. URL: http://dx.doi.org/10.1016/j.jpowsour.2015.04.067.

[265] S.M. Gaytan et al. "Fabrication of barium titanate by binder jetting additive manufacturing technology". In: *Ceramics International* 41.5 (2015), pp. 6610–6619. DOI: 10.1016/j.ceramint.2015.01.108. URL: https://linkinghub.elsevier.com/retrieve/pii/S0272884215001558.

[266] J.A. Gonzalez et al. "Characterization of ceramic components fabricated using binder jetting additive manufacturing technology". In: *Ceramics International* 42.9 (2016), pp. 10559–10564. DOI: 10.1016/j.ceramint.2016.03.079. URL: http://dx.doi.org/10.1016/j.ceramint.2016.03.079.

[267] Yun Bai and Christopher B Williams. *An Exploration of Binder Jetting of Copper*. Tech. rep. 2014, pp. 793–814.

[268] Amir Azhari et al. "Binder-jet powder-bed additive manufacturing (3D printing) of thick graphene-based electrodes". In: *Carbon* 119 (2017), pp. 257–266. DOI: 10.1016/j.carbon.2017.04.028. URL: http://dx.doi.org/10.1016/j.carbon.2017.04.028.

[269] J. Czyżewski et al. "Rapid prototyping of electrically conductive components using 3D printing technology". In: *Journal of*

Materials Processing Technology 209.12-13 (2009), pp. 5281–5285. DOI: 10.1016/j.jmatprotec.2009.03.015. URL: https://linkinghub.elsevier.com/retrieve/pii/S092401360900106X.

[270] Alexander Kraytsberg and Yair Ein-Eli. "Conveying Advanced Li-ion Battery Materials into Practice The Impact of Electrode Slurry Preparation Skills". In: *Advanced Energy Materials* 6.21 (2016), p. 1600655. DOI: 10.1002/aenm.201600655. URL: http://doi.wiley.com/10.1002/aenm.201600655.

[271] Rajendra P. Chhabra. "Non-Newtonian Fluids: An Introduction". In: *Rheology of Complex Fluids*. New York, NY: Springer New York, 2010, pp. 3–34. DOI: 10.1007/978-1-4419-6494-6_1. URL: http://link.springer.com/10.1007/978-1-4419-6494-6{_}1.

[272] Cheng Zhu et al. "Highly compressible 3D periodic graphene aerogel microlattices". In: *Nature Communications* 6.1 (2015), p. 6962. DOI: 10.1038/ncomms7962. URL: http://www.nature.com/articles/ncomms7962.

[273] E. Behzadfar et al. "Effect of solid loading and aggregate size on the rheological behavior of pdms/calcium carbonate suspensions". In: *Brazilian Journal of Chemical Engineering* 26.4 (2009), pp. 713–721. DOI: 10.1590/S0104-66322009000400010.

[274] Madeleine F. Dupont and Scott W. Donne. "A Step Potential Electrochemical Spectroscopy Analysis of Electrochemical Capacitor Electrode Performance". In: *Electrochimica Acta* 167 (2015), pp. 268–277. DOI: 10.1016/j.electacta.2015.03.137. URL: http://dx.doi.org/10.1016/j.electacta.2015.03.137.

[275] Peng Xu, A. S. Mujumdar, and B. Yu. "Drying-Induced Cracks in Thin Film Fabricated from Colloidal Dispersions". In: *Drying Technology* 27.5 (2009), pp. 636–652. DOI: 10.1080/07373930902820804. URL: http://www.tandfonline.com/doi/abs/10.1080/07373930902820804.

[276] Zhijia Du et al. "Enabling aqueous processing for crack-free thick electrodes". In: *Journal of Power Sources* 354 (2017), pp. 200–206. DOI: 10.1016/j.jpowsour.2017.04.030. URL: https://linkinghub.elsevier.com/retrieve/pii/S0378775317305153.

[277] Vinny R. Sastri. "Commodity Thermoplastics". In: *Plastics in Medical Devices*. Elsevier, 2010, pp. 73–119. DOI: 10.1016/B978-0-8155-2027-6.10006-6. URL: https://linkinghub.elsevier.com/retrieve/pii/B9780815520276100066.

[278] Mahesh Mani et al. *Measurement Science Needs for Real-time Control of Additive Manufacturing Powder Bed Fusion Processes*. Tech. rep. Gaithersburg, MD: National Institute of Standards and Technology, 2015. DOI: 10.6028/NIST.IR.8036. URL: https://nvlpubs.nist.gov/nistpubs/ir/2015/NIST.IR.8036.pdf.

[279] Eujin Pei et al. "Investigating the impact of additive manufacturing data exchange standards for re-distributed manufacturing". In: *Progress in Additive Manufacturing* 4.3 (2019), pp. 331–344. DOI: 10.1007/s40964-019-00085-7. URL: https://doi.org/10.1007/s40964-019-00085-7.

[280] S. Clijsters et al. "In situ quality control of the selective laser melting process using a high-speed, real-time melt pool monitoring system". In: *International Journal of Advanced Manufacturing Technology* 75.5-8 (2014), pp. 1089–1101. DOI: 10.1007/s00170-014-6214-8.

[281] Tom Craeghs et al. "Detection of Process Failures in Layerwise Laser Melting with Optical Process Monitoring". In: *Physics Procedia* 39 (2012), pp. 753–759. DOI: 10.1016/j.phpro.2012.10.097. URL: http://dx.doi.org/10.1016/j.phpro.2012.10.097.

[282] V. Gunenthiram et al. "Experimental analysis of spatter generation and melt-pool behavior during the powder bed laser beam melting process". In: *Journal of Materials Processing Technology* 251.February 2017 (2018), pp. 376–386. DOI: 10.1016/j.jmatprotec.2017.08.012. URL: http://dx.doi.org/10.1016/j.jmatprotec.2017.08.012.

[283] Yingjie Zhang et al. "Extraction and evaluation of melt pool, plume and spatter information for powder-bed fusion AM process monitoring". In: *Materials & Design* 156 (2018), pp. 458–469. DOI: 10.1016/j.matdes.2018.07.002. URL: https://doi.org/10.1016/j.matdes.2018.07.002.

[284] Q. Sun et al. "Effect of processing conditions on the bonding quality of FDM polymer filaments". In: *Rapid Prototyping Journal* 14.2 (2008), pp. 72–80. DOI: 10.1108/13552540810862028. URL: http://www.emeraldinsight.com/doi/10.1108/13552540810862028.

[285] Matthias Hirsch et al. "Assessing the capability of in-situ nondestructive analysis during layer based additive manufacture". In: *Additive Manufacturing* 13 (2017), pp. 135–142. DOI: 10.1016/j.addma.2016.10.004. URL: http://dx.doi.org/10.1016/j.addma.2016.10.004.

[286] Hoejin Kim, Yirong Lin, and Tzu-Liang Bill Tseng. "A review on quality control in additive manufacturing". In: *Rapid Prototyping Journal* 24.3 (2018), pp. 645–669. DOI: 10.1108/RPJ-03-2017-0048. arXiv: /doi.org/10.1108/RPJ-03-2017-0048 [https:]. URL: http://www.emeraldinsight.com/doi/10.1108/RPJ-03-2017-0048.

[287] Jorge Mireles et al. "Analysis and correction of defects within parts fabricated using powder bed fusion technology". In: *Surface Topography: Metrology and Properties* 3.3 (2015), p. 034002. DOI: 10.1088/2051-672X/3/3/034002. URL: http://stacks.iop.org/2051-672X/3/i=3/a=034002?key=crossref.490c370d521de90fec67fe4be136c2a7.

[288] Prahalad K. Rao et al. "Online Real-Time Quality Monitoring in Additive Manufacturing Processes Using Heterogeneous Sensors". In: *Journal of Manufacturing Science and Engineering* 137.6 (2015), p. 061007. DOI: 10.1115/1.4029823. URL: http://manufacturingscience.asmedigitalcollection.asme.org/article.aspx?doi=10.1115/1.4029823.

[289] Timothy J. Coogan and David O. Kazmer. "In-line rheological monitoring of fused deposition modeling". In: *Journal of Rheology* 63.1 (2019), pp. 141–155. DOI: 10.1122/1.5054648. URL: http://sor.scitation.org/doi/10.1122/1.5054648.

[290] Charoula Kousiatza, Dimitris Tzetzis, and Dimitris Karalekas. "In-situ characterization of 3D printed continuous fiber reinforced composites: A methodological study using fiber Bragg grating sensors". In: *Composites Science and Technology* 174.November 2018 (2019), pp. 134–141. DOI: 10.1016/j.compscitech.2019.02.008. URL: https://doi.org/10.1016/j.compscitech.2019.02.008.

[291] A. Thompson, I. Maskery, and R. K. Leach. "X-ray computed tomography for additive manufacturing: A review". In: *Measurement Science and Technology* 27.7 (2016). DOI: 10.1088/0957-0233/27/7/072001.

[292] Logan D. Sturm et al. "In situ monitoring of material jetting additive manufacturing process via impedance based measurements". In: *Additive Manufacturing* 28.February (2019), pp. 456–463. DOI: 10.1016/j.addma.2019.05.022. URL: https://linkinghub.elsevier.com/retrieve/pii/S2214860419300909.

[293] Sarah K. Everton et al. "Review of in-situ process monitoring and in-situ metrology for metal additive manufacturing". In: *Materials and Design* 95 (2016), pp. 431–445. DOI: 10.1016/j.matdes.2016.01.099. URL: http://dx.doi.org/10.1016/j.matdes.2016.01.099.

[294] Xiao-Shan Jiang et al. "Research on accurate droplet generation for micro-droplet deposition manufacture". In: *The International Journal of Advanced Manufacturing Technology* 49.5-8 (2010), pp. 535–541. DOI: 10.1007/s00170-009-2403-2. URL: http://link.springer.com/10.1007/s00170-009-2403-2.

[295] Charoula Kousiatza and Dimitris Karalekas. "In-situ monitoring of strain and temperature distributions during fused deposition modeling process". In: *Materials and Design* 97 (2016), pp. 400–406. DOI: 10.1016/j.matdes.2016.02.099. URL: http://dx.doi.org/10.1016/j.matdes.2016.02.099.

[296] Thomas S. Lumpe, Jochen Mueller, and Kristina Shea. "Tensile properties of multi-material interfaces in 3D printed parts". In: *Materials and Design* 162 (2019), pp. 1–9. DOI: 10.1016/j.matdes.2018.11.024. URL: https://doi.org/10.1016/j.matdes.2018.11.024.

[297] Alberto Boschetto and Luana Bottini. "Roughness prediction in coupled operations of fused deposition modeling and barrel finishing". In: *Journal of Materials Processing Technology* 219 (2015), pp. 181–192. DOI: 10.1016/j.jmatprotec.2014.12.021. URL: http://dx.doi.org/10.1016/j.jmatprotec.2014.12.021.

[298] Dmitry Isakov et al. "3D-Printed High Dielectric Contrast Gradient Index Flat Lens for a Directive Antenna with Reduced Dimensions". In: *Advanced Materials Technologies* 1.6 (2016), p. 1600072. DOI: 10.1002/admt.201600072. URL: http://doi.wiley.com/10.1002/admt.201600072.

[299] Yingwei Wu. "Additive Manufacturing of Graded and Anisotropic Materials for Applications at Microwave Frequencies". In: *University of Oxford* (2018).

[300] Ulf Leonhardt. "Optical Conformal Mapping". In: *Science* 312 (2013), pp. 1777–1780. DOI: 10.1126/science.1126493. arXiv: arXiv:1308.5367. URL: http://doi.wiley.com/10.1002/9781118343371.refs.

[301] J B Pendry, D Schurig, and D R Smith. "Controlling electromagnetic fields". In: *Science* 312.5781 (2006), pp. 1780–1782. DOI: 10.1126/science.1125907. arXiv: 0602092 [physics].

[302] Do Hoon Kwon and Douglas H. Werner. "Transformation electromagnetics: An

overview of the theory and applications". In: *IEEE Antennas and Propagation Magazine* 52.1 (2010), pp. 24–46. DOI: 10.1109/MAP.2010.5466396.

[303] Paul Deffenbaugh et al. "Fully 3D Printed 2.4 GHz Bluetooth/Wi-Fi Antenna". In: *International Symposium on Microelectronics* 2013.1 (2013), pp. 000914–000920. DOI: 10.4071/isom-2013-THP53. URL: http://imapsource.org/doi/10.4071/isom-2013-THP53.

[304] Raymond C. Rumpf et al. "Spatially variant periodic structures in electromagnetics". In: *Philosophical Transactions of the Royal Society A: Mathematical, Physical and Engineering Sciences* 373.2049 (2015). DOI: 10.1098/rsta.2014.0359.

[305] Korey Kirschenmann, Keith W. Whites, and Stephen M. Woessner. "Inkjet printed microwave frequency multilayer antennas". In: *2007 IEEE Antennas and Propagation Society International Symposium*. 1. IEEE, 2007, pp. 924–927. DOI: 10.1109/APS.2007.4395646. URL: https://ieeexplore.ieee.org/document/4395646/.

[306] M.N. Afsar et al. "The measurement of the properties of materials". In: *Proceedings of the IEEE* 74.1 (1986), pp. 183–199. DOI: 10.1109/PROC.1986.13432. URL: http://ieeexplore.ieee.org/document/1457700/.

[307] James Baker-Jarvis, Michael Janezic, and Donald Degroot. "High-frequency dielectric measurements". In: *IEEE Instrumentation & Measurement Magazine* 13.2 (2010), pp. 24–31. DOI: 10.1109/MIM.2010.5438334. URL: http://ieeexplore.ieee.org/document/5438334/.

[308] Graham Brodie, Mohan V. Jacob, and Peter Farrell. "6 Techniques for Measuring Dielectric Properties". In: *Microwave and Radio-Frequency Technologies in Agriculture*. Warsaw, Poland: De Gruyter Open, 2015. DOI: 10.1515/9783110455403-007. URL: https://www.degruyter.com/view/books/9783110455403/9783110455403-007/9783110455403-007.xml.

[309] F. Castles et al. "Microwave dielectric characterisation of 3D-printed BaTiO3/ABS polymer composites". In: *Scientific Reports* 6.March (2016), pp. 1–8. DOI: 10.1038/srep22714. URL: http://dx.doi.org/10.1038/srep22714.

[310] T. T. Grove, M. F. Masters, and R. E. Miers. "Determining dielectric constants using a parallel plate capacitor". In: *American Journal of Physics* 73.1 (2005), pp. 52–56. DOI: 10.1119/1.1794757. URL: http://aapt.scitation.org/doi/10.1119/1.1794757.

[311] D.K. Ghodgaonkar, V.V. Varadan, and V.K. Varadan. "Free-space measurement of complex permittivity and complex permeability of magnetic materials at microwave frequencies". In: *IEEE Transactions on Instrumentation and Measurement* 39.2 (1990), pp. 387–394. DOI: 10.1109/19.52520. URL: http://ieeexplore.ieee.org/document/52520/.

[312] Filippo Costa et al. "Electromagnetic Characterisation of Materials by Using Transmission/Reflection (T/R) Devices". In: *Electronics* 6.4 (2017), p. 95. DOI: 10.3390/electronics6040095. URL: http://www.mdpi.com/2079-9292/6/4/95.

[313] T.W. Athey, M.A. Stuchly, and S.S. Stuchly. "Measurement of Radio Frequency Permittivity of Biological Tissues with an Open-Ended Coaxial Line: Part I". In: *IEEE Transactions on Microwave Theory and Techniques* 30.1 (1982), pp. 82–86. DOI: 10.1109/TMTT.1982.1131021. URL: http://ieeexplore.ieee.org/document/1131021/.

[314] Heping Yue, Kathleen L. Virga, and John L. Prince. "Dielectric constant and loss tangent measurement using a stripline fixture". In: *IEEE Transactions on Components, Packaging, and Manufacturing Technology: Part B* 21.4 (1998), pp. 441–446. DOI: 10.1109/96.730430. URL: http://ieeexplore.ieee.org/document/730430/.

[315] Amir Cenanovic and Lorenz Peter Schmidt. "Space-resolved measurement and 2D-mapping of material parameters using multi-angle reflection ellipsometry in W-band". In: *IEEE MTT-S International Microwave Symposium Digest* (2013), pp. 1–4. DOI: 10.1109/MWSYM.2013.6697797.

[316] Alexandre Nata Vicente, Gustavo Maciulis Dip, and Cynthia Junqueira. "The step by step development of NRW method". In: *2011 SBMO/IEEE MTT-S International Microwave and Optoelectronics Conference (IMOC 2011)*. IEEE, 2011, pp. 738–742. DOI: 10.1109/IMOC.2011.6169318. URL: http://ieeexplore.ieee.org/document/6169318/.

[317] O. Sydoruk et al. "Analytical formulation for the resonant frequency of split rings". In: *Journal of Applied Physics* 105.1 (2009), p. 014903. DOI: 10.1063/1.3056052. URL: http://aip.scitation.org/doi/10.1063/1.3056052.

[318] Azom. *Properties of Borosilicate Glass*. 2019. URL: https://www.azom.com/

article.aspx?ArticleID=4765 (visited on 05/16/2019).

[319] Renting Liu and Jiaya Jia. "Reducing boundary artifacts in image deconvolution". In: *Proceedings - International Conference on Image Processing, ICIP* (2008), pp. 505–508. DOI: 10.1109/ICIP.2008.4711802.

[320] O Wiener. "Zur theorie der refraktionskonstanten". In: *Berichte ueber Verhandlungen Koeniglich-Saechsischen Gesellschaft Wisseschaften Leipzig*. 1910, pp. 256–277.

[321] Noah Halford. *3D Printer Calibration Guide - How to Calibrate Your 3D Printer*. 2018. URL: https://all3dp.com/2/how-to-calibrate-a-3d-printer-simply-explained/ (visited on 04/12/2019).